CONTINUUM-BASED CONSTITUTIVE MODELING OF COUPLED OXIDATIVE AGING-MECHANICAL RESPONSE OF ASPHALT CONCRETE

A Dissertation

by

EISA RAHMANI

Submitted to the Office of Graduate and Professional Studies of
Texas A&M University
in partial fulfillment of the requirements for the degree of

DOCTOR OF PHILOSOPHY

Chair of Committee,	Dallas N. Little
Co-Chair of Committee,	Eyad A. Masad
Committee Members,	Mary Beth Hueste
	Charles Glover
	David H. Allen
	Masoud K. Darabi
Head of Department,	Robin Autenrieth

May 2015

Major Subject: Civil Engineering

ABSTRACT

Oxidative aging is known to be one of the main contributors to reducing the service life of asphalt pavements. Asphalt concrete becomes stiffer and more brittle when it reacts with oxygen. The aged asphalt pavement is more susceptible to crack development and damages when subjected to repeated traffic loading. The aim of this dissertation is to develop and validate a mechanistic-based aging constitutive relationship based on an aging state variable.

Oxidative aging of asphalt concrete involves a thermodynamic process between reactive molecules of asphalt and oxygen. The repercussion of such a process is a change in mechanical, macroscopic properties of the material. This phenomenon is accounted for in this study by formulating an aging constitutive equation, based on continuum theory, in which the aging state variable is correlated with oxygen content via an evolution function. In this aging constitutive equation, the rate of change of the aging variable and oxygen content are formulated as conjugate variables. In other words, oxygen content is considered as the driving force for the rate of change of the aging variable. The rate of change of the aging state variable is expressed as a function of oxygen content, temperature, and level of aging at any given time.

The behavior of asphalt concrete is modeled using the PANDA (Pavement Analysis Using a Nonlinear Damage Approach) framework, which accounts for the viscoelastic, viscodamage, and viscoplastic behavior of the materials. The time-dependent response of aged asphalt concrete is investigated by introducing the aging

state variable to Schapery's viscoelastic model. The aging state variable causes an increase in the stiffness and viscosity of the aged material by decreasing the compliance terms and the retardation times. Because the viscoelastic, viscodamage, and viscoplastic components of PANDA are coupled or interrelated, the change in the viscoelastic properties, because of aging, affects the overall mechanical behavior of asphalt concrete.

The aging constitutive equation is calibrated using data obtained from laboratory experiments, and then its predictions are validated against independent experimental data. It is shown that the proposed model is capable of predicting mechanical response of aged asphalt concrete specimens subjected to different loading conditions.

DEDICATION

To my dearest **parents**, great **brother**, and wonderful **sister**

for their patience and unconditional support

To my dear **Gilda**

for her endless love and encouragement

ACKNOWLEDGEMENTS

I am sincerely grateful to many people who helped me to complete this strenuous journey. First of all, I would like to thank my committee co-chairs, Drs. Dallas Little and Eyad Masad, for providing me with opportunities and shaping my career, and for their precious guidance, encouragement, and support throughout the course of this research.

I would like to thank my advisory committee members, Drs. Mary Beth Hueste and Charles Glover, for their pertinent comments and their patience in reading my dissertation. I would also like to express my gratitude toward Dr. David Allen for his constructive and fruitful comments at the later stages of this work, and for being on my defense committee. I thank Dr. Abu Al-Rub for his instructive comments during the early stages of this work.

I also take this opportunity to express my deepest appreciation for Dr. Masoud Darabi, whose expertise and advice truly flattened the road to completing this research. Without him, this work would never be accomplished.

Thanks also go to my fellow colleagues, Drs. Maryam Shakiba, Taesun You, Sun-Myung Kim, and John Rushing, who were supportive and very insightful. I also wish to extend my gratitude toward Drs. Richard Kim and Emad Kassem for providing data to us from a wide range of experimental tests.

Last, but not least, I gratefully acknowledge Qatar National Research Fund (QNRF) and Asphalt Research Consortium through the US Federal Highway

Administration, which provided the financial support for various elements of this research.

TABLE OF CONTENTS

Page

Page

Page

LIST OF FIGURES

Page

Page

Page

Page

Page

Page

Page

Page

LIST OF TABLES

Page

1. INTRODUCTION AND LITERATURE REVIEW

1.1 Problem Statement

Asphalt concrete is the most widely used material in constructing roadways, pavements, and airport runways globally. Asphalt pavements are designed to endure different mechanical and environmental actions until treatment or replacement. Asphalt concrete is subjected to oxidative aging, which is known to be one of the prime reasons for shortening the service life of asphalt pavements.

There are two common load-related distresses governing the serviceability of the asphalt concrete: rutting and fatigue cracking. Rutting is the longitudinal depression or permanent deformation in roadways caused primarily by shear stresses induced in the asphalt mixture. Fatigue cracking occurs as a result of micro cracks nucleation and propagation under the effects of repeated traffic loading. In addition to traffic loading, environmental factors such as temperature variations, moisture diffusion, and oxidative aging play substantial roles in structural integrity, overall functionality, and durability of asphalt pavements. In particular, oxidative aging has received significant attention in the last decade among scientists, experimentalists, and the asphalt community in general.

Oxidative aging in asphalt concrete occurs when the air oxygen reacts with components of asphalt binder. Such chemical reactions significantly alter the physical and rheological properties of asphalt concrete. The research work of Dr. Charles Glover and his co-workers at Texas A&M University offers in-depth examination of the oxygen

transport into the asphalt pavement and the chemical reactions that lead to binder and mixture aging (Glover et al., 2014; Jin et al., 2013; Prapaitrakul et al., 2009).

Aging results in hardening and embrittlement of the asphalt concrete, making it susceptible to develop more cracks (Glover et al., 2008; Hajj et al., 2005; Hintz et al., 2011; Walubita et al., 2006). Hence, better knowledge of asphalt oxidation and its repercussions on the fatigue performance is critical to cost-effective pavement design and efficient maintenance plans for roadways.

There are numerous studies that investigate oxidative aging in a variety of aspects, from chemical reactions and mechanisms occurring at the molecular level, to its impact on the overall functionality at the macro scale. However, there are very few studies in the literature to incorporate the oxidation phenomenon to mechanistic-based models that have predictive capabilities. Any predictive model ought to consider the general loading condition and environmental factors that considers multi-axial state of stress; should not have extensive material parameters; and has to be straight forward to calibrate. As a result, it is essential to develop a robust computational scheme founded on a phenomenon-based constitutive relationship that can efficiently simulate the performance of asphalt concrete under traffic load and environmental actions during its service life. This study is outlined to close the existing gap between the experimental observations and the constitutive modeling involving oxidative aging.

Asphalt concrete is a composite material, and the oxygen transport phenomenon and the way that an aged asphalt concrete responds to mechanical loading greatly depend on its microstructural features, such as air void distribution, aggregate size, and spatial

distributions; volume fraction of the binder; and physical-chemical properties of the components. Obviously, characterizing the microstructural response of asphalt concrete under the influence of each of those microstructural features by experimental testing is cumbersome and time-consuming. Therefore, it is preferred to develop a microstructural model that utilizes an appropriate chemo-mechanical constitutive relationship that explains the effect of asphalt constituents at the microstructural level on the response of the aged asphalt concrete at the macro-scale.

In this dissertation, a phenomenon-based oxidative aging constitutive relationship is developed and incorporated in a continuum damage mechanics framework. The evolutionary effect of oxidative aging on the mechanical behavior of asphalt concrete is governed by the occurring mechanisms of oxidation, oxygen content, and temperature. The proposed oxidative aging constitutive relationship is implemented in the Pavement Analysis using Nonlinear Damage Approach (PANDA) finite element package to account for effects of oxidative aging on the mechanical response of the aged asphalt pavements.

A major contribution of this dissertation is the development of a systematic procedure to identify the material properties associated with the constitutive relationships. Moreover, the developed framework is validated against a variety of experimental measurements under different loading conditions. Finally, comprehensive microstructural simulations are performed on representations of asphalt concrete microstructures to identify the combined effects of aging and mechanical loading.

1.2 Background

Asphalt binder is a complex mixture of relatively high molecular weight molecules. The complex chemical structure of asphalt made it difficult to study oxidative aging, particularly at the molecular level. One important task in constitutive modeling of aging effects on the continuum scale is to properly understand this phenomenon and the mechanisms associated with it at the molecular level. Despite the complicated nature of asphalt oxidation and the material itself, scientists have put forth significant efforts to essentially describe the mechanism, kinetics, and the chemistry behind the asphalt oxidation. This section first looks into the background and summary of the major work and findings on the complex mechanism of asphalt oxidation and the kinetics behind it, and then provides the background on the limited work on the constitutive modeling of aging effects on mechanical behavior of viscoelastic materials in general. These previous works are considered as the foundation and essential knowledge of developing the new oxidative aging constitutive relationship in this work.

1.2.1 Oxidation Models and Kinetics of Oxidative Aging

Asphalt is composed primarily of carbon and hydrogen, with nitrogen, sulfur, and many other elements at lower percentages. These elements combine to form the main fractions of asphalt, being asphaltenes, saturates, naphtene, and polar aromatics. Saturates and aromatics together make the maltene phase. In other words, asphalt can be deemed as the dispersion of asphaltene particles in the continuous maltene phase. Asphaltene is considered as the viscosity agent in the asphalt composition, so the greater amount of asphaltene molecules in asphalt leads to a higher viscosity.

Lin et al. (1995) investigated the effects of the chemical composition of asphalt fractions on the oxidation. They stated that the maltene phase is the most active contributor to the formation of new asphaltenes in the oxidation products. In which case, the newly formed asphaltenes showed the same effects on the physical changes as the original ones. Based on this study, an increase in the oxygen content in the asphalt molecules is linearly correlated with an increase in carbonyl area. They expressed that the formation of these high-polar carbonyl functional groups leads to formation of new asphaltenes, mostly in the maltene phase. They finally concluded that the presence of more fractions of asphaltene in asphalt composition results in progressive hardening and an increase in viscosity of the material.

The mechanism of oxidative aging was also investigated by Petersen and co-workers (Petersen et al., 1993; Petersen and Glaser, 2011; Petersen and Harnsberger, 1998). They suggested a dual, sequential mechanism for asphalt oxidation. Based on that, the oxidation rapidly initiates with oxidation of a limited amount of hydrocarbons, and then proceeds with a less energetic reaction of benzylic carbon. They identified ketones and sulfoxides to be the major functional group types formed during oxidation reactions. It was also reported that change in the asphalt viscosity is mainly governed by concentration of ketones functional groups with high dependency on oxygen pressure and temperature.

In other studies, Herrington et al. (1994) and Herrington (1998) explored the mechanism deriving the oxidation and concluded the same oxidation products, with carbonyl and sulfoxides functional groups as the major ones. They confirmed that the

temperature of oxidation has a significant effect on the reaction rate and the final product composition. Moreover, the association of more polar molecules reducing the mobility of the molecular components is one of the primary consequences of asphalt oxidation.

Domke et al. (1999) studied the oxidation kinetics, focusing on the effect of oxidation pressure on the rate of change in oxidation and the sensitivity of the kinetics parameters on oxygen pressure in general. Later, Domke et al. (2000) utilized an Arrhenius type function to correlate the constant rate oxidation to the oxygen pressure. They were able to define the pressure dependencies by proposing a molecular diffusion model for asphalt oxidation, in which at low pressure, oxidation occurs primarily at the maltene and polar aromatics phase leading to carbonyl formation. In this particular model, as pressure increases, oxygen is able to diffuse in the asphaltene particles that are coated by lighter asphaltenes or so-called quasi-asphaltenes. The reaction product of oxygen with these lighter coatings is the large amount of carbonyl groups, as well as new asphaltenes. When the material is exposed to further oxygen pressure driving force, the large cores of asphaltene aggregates will be the target of reaction, leading to the formation of more carbonyl area. During each of the mentioned oxidation steps, the significant increase in viscosity of the material was attributed to the formation of either new asphaltenes molecules or carbonyl groups.

Several research efforts have been devoted to correlate the formation of oxidation products with oxygen uptake during asphalt oxidation. Researchers have found that the rate of carbonyl formation in the aging asphalt follows the Arrhenius equation, such that carbonyl formation rate could be a predictor of the changes in mechanical properties

(Lau et al., 1992; Liu et al., 1996; Martin et al., 1990). Liu et al. (1998) reported that there is a linear correlation between the oxygen weight percentage and the carbonyl content in an aged asphalt, and such correlation is independent of the aging temperature and oxygen pressure. Lunsford (1994) was first to combine an oxygen diffusion and reaction model in a differential volume with Fick's first law of diffusion in order to develop an oxygen transport model that could be used to predict the oxidation in an asphalt film. Using this model, the oxygen partial pressure in the asphalt film was obtained as a function of time, temperature, and depth below the film surface. However, the proposed transport model was defined in a single dimension and assumed oxygen transports only in vertical direction. Later, Prapaitrakul et al. (2009) extended Lunsford's model to a cylindrical coordinate system. The improved model was able to include pavement temperature profile, binder kinetics, and diffusion parameters, as well as air void characteristics. Their calculated carbonyl area (the measured area under the carbonyl absorption band in the infrared spectrometer) showed a fair agreement with the extracted carbonyl rate from field data, especially at upper layers of the pavement. Afterwards, Jin et al. (2011) developed an improved oxidative kinetics model to account for both fast-rate and constant-rate oxidation, and later Jin et al. (2013) included the kinetics model in the previously developed oxygen transport-reaction model. They were able to validate the pavement oxidation against laboratory measurements on specimens data extracted from the field cores.

In addition to the numerous studies determining the oxidation kinetics and the factors affecting the kinetic-related parameters, several others have made efforts to

investigate the influence of the asphalt oxidation on the mechanical and rheological properties, and the overall functionality of the aged material. One general observation of the field asphalt pavement is that the top asphalt layers undergo a much faster rate of viscosity increase (Coons, 1965). Lee and Huang (1973) correlated the durability with the viscosity change of asphalt. They stated that the carbonyl index increase results in greater viscosity, which is inversely related to the durability of the material. Chen and Huang (2000) showed the increase in viscosity of asphalt mainly through formation of sulfoxide area during the oxidation process. In another study, Lu and Isacsson (2002) also stated the typical chemical changes due to oxidation, including increase in polar aromatics, asphaltenes, molecular association, and molecular weight. Such chemical alterations essentially result in physical changes such as increased viscosity or transformation to a solid-like behavior, increased complex modulus, and decreased phase angle.

In another study, ductility was viewed as a measure of durability of asphalt (Ruan et al., 2003). They developed a correlation between ductility and the dynamic shear rheometer (DSR) function: storage modulus/(complex viscosity/storage modulus). It was shown that the ductility of asphalt dramatically decreases as a result of oxidation due to increase in both stiffness and viscosity. Several others have also conducted researches showing the capability of DSR function to characterize the ductility changes due to oxidation and therefore prediction of age-related cracking (Al-Azri et al., 2006; Juristyarini et al., 2011). Such studies were developed based on empirical relationships being useful in material characterization. However, the major issue with such models is

that they cannot be utilized to effectively predict the response of the material under general conditions (mechanical loading and environmental factors). Therefore, one of the most important contributions of this research is to develop a model that can be used for more general cases and not only the conditions under which the testing has been conducted.

In previous mentioned studies, majority of the researchers used the Infrared Spectroscopy techniques to measure the area under the absorption band of the oxygen-containing functional groups to find a surrogate for oxidative aging phenomenon. In recent years, the atomic-level description of the oxidative aging phenomenon using molecular dynamic simulations and quantum-based chemistry has accelerated because of the power of advanced computers and parallel computing. To name a few, Tarefder and Arisa (2011) used molecular dynamic simulations to study the behavior of individual components of asphalt when exposed to oxygen. They analyzed asphaltene phase and resin phase of the asphalt in different simulation matrices where each contained several molecules. They were able to conduct simulations in different conditions, including varying temperatures and amount of oxygen atoms. Their simulations showed that at a low oxidation level, the asphaltene density increases, while it decreases at a high oxidation level. The opposite trend was found for resins. This indicates that at low oxidation and early ages, more asphaltenes are possibly being formed due to the reaction of oxygen with resin-based components containing polar aromatics. As asphalt undergoes more aging with a higher oxidation level, the asphaltene content seems to be consumed to form more carbonyl groups.

Pan et al. (2012b) and also Pan et al. (2012a) developed an atomistic-based chemophysical environment to simulate the chemical reactions that occur during asphalt oxidation using a quantum-based chemistry method. In these studies, asphalt contained three functional groups: asphaltenes, resins, and saturates. A bulk asphalt model was made by mixing a typical fraction of each component under the general service condition. Their simulations showed that asphalt oxidation initiates with a rapid reaction of oxygen, leading to a high chain-breaking trend in saturates and the formation of ketones and sulfoxides, which then is followed by a slower rate of oxidation and hardening. They concluded that ketonization and sulfoxidation account for most of the oxidative aging reactions in the simulated asphalt.

To summarize this subsection, the oxidative aging phenomenon has been extensively studied by researchers, and several mechanisms have been proposed. Due to many factors affecting the oxidation, it still seems that the exact and accurate process of asphalt aging occurring in the service life of pavements is not fully understood. However, based on the previous findings on the influences of oxidation on chemical composition, which alters the mechanical properties, one can summarize the aging process as follows:

- Asphalt binder is composed primarily of carbon and hydrogen, with nitrogen, sulfur, and other elements at a lower percentage. These components combine to form the main fractions of asphalt binder: asphaltenes, saturates, naphtene, and polar aromatics.

- Asphaltene particles tend to absorb the polar aromatics on their surfaces. The absorption of polar aromatics on the surface of the asphaltenes results in the formation of a coat around the asphaltene particles, which greatly influences the oxidation mechanism.
- When exposed to oxygen, asphalt binder undergoes a fast-rate oxidation, and then is followed by a slower constant-rate reaction. Saturates are mainly unaffected by oxidation. At the early stages, the maltene phase reacts with oxygen, forming more polar bonds. The result is mainly carbonyl and sulfoxides functional groups. Due to the high polarity provided by these functional groups, new asphaltene components are formed. The new asphaltenes may oxidize more with oxygen to form more carbonyl groups, leading to a progressive increase in viscosity. As the material undergoes more oxidation, the original asphaltene fractions, which somehow were protected previously by the polar coating, tend to oxidize and likewise produce more oxygen-containing functional groups. As asphalt oxidizes, the maltene phase, which is responsible for the rubber-like behavior of the material, is consumed and, instead, more insoluble fractions are formed. Thus, mainly carbonyl, and to some extent sulfoxides, are the major contributors to increase the viscosity of the binder.
- The carbonyl formation is linearly correlated with the increase in oxygen content during oxidation. As a result, the carbonyl formation can be a surrogate to study the oxidative aging phenomenon in asphalt concrete.

- The major contribution of oxidative aging in changing the mechanical properties of the material can be seen as: increased viscosity, increased stiffness, and reduced ductility, or increased brittleness. Such alterations will cause the material to transform from more viscoelastic behavior to more solid-like behavior.

1.2.2 Constitutive Modeling

There has been extensive research on the kinetics and the chemical mechanism of asphalt oxidation at the molecular level, and the effects of aging on physical and rheological properties of asphalt. However, there is very little work on mechanistic-based constitutive modeling of oxidative aging effects on the mechanical response of aging susceptible materials. All matter is composed of molecules which, being discontinuous, in some degree obviates the assumption that the body is continuous. Nonetheless, there are many aspects of material behavior that can be described and predicted with continuum theories without detailed regard to the molecular structure of materials. Such theories aim to explain the relationship between macroscale phenomena in a way that is consistent with the behavior of the material on the molecular scale. Therefore, within the continuum mechanics approach it is customary to consider a statistically homogeneous (but nonetheless small compared to the object of interest) representative volume element (RVE) of material, and this approach is normally considered to represent a material point within the continuum. A fundamental assumption of continuum mechanics is that it is possible to define a length that is large relative to molecular length scales and at the same time much smaller than the length scale associated with variations in the continuum scale field variables. Therefore, it is

necessary to justify the continuum approach on the basis of the molecular scale behavior only in a general sense. Accordingly, it is considered acceptable by many researchers to infer the quantities that are necessary to model the continuum scale response of an object without detailed congruence to a certain molecular theory so long as the model is shown to be accurate at the continuum scale. It should be noted that while molecular theories can and often do enhance the understanding at the continuum scale, the justification of a continuum theory in a particular situation is a matter of experimental validation.

Using an age-time shift factor has been a common practice to include the aging effects on the viscoelastic properties of an aging-susceptible material. This approach, which has been widely used in polymer engineering, mainly to incorporate physical reversible hardening effects, was first introduced by Struik (1977). In this method, the effect of aging is to shift the viscoelastic compliance along the log-time axis while assuming that the shape of the curve remains the same. By measuring the viscoelastic compliance at multiple ages and selecting one age to be the master, the retardation or relaxation times for the other ages are simply shifted by a constant factor such that they fall in line with the master curve. Many other researchers also applied the age-time shift concept for polymers, such as Pasricha et al. (1997), Haj-Ali and Muliana (2004), Guo et al. (2009), and Arao et al. (2012); and for asphalt concrete, such as Masad et al. (2008). The age-time shift mainly assumes a constant rate for aging. Therefore, it is unable to accurately predict the viscoelastic behavior of aging asphalt over a broad time span. Moreover, the age-time shift is not linked to any specific fundamental aging mechanism.

The aging effects in the viscoelastic formulation could be considered by modifying creep compliance or stress relaxation functions, such that they are functions of the aging and loading time (Bykov and Martynova, 2011; Chazal and Pitti, 2009; Masson et al., 2012; Sensale et al., 2001). In other words, the integral form of the viscoelastic functions are expressed in two time domains, aging time and loading time. Solving such integrations that are defined in two different time domains requires a great deal of computational cost and time. On the other hand, the aforementioned approaches only considered the aging viscoelastic material that is not coupled with the viscodamage and viscoplastic behavior of asphalt concrete. Therefore, it is imperative to develop a robust mechanistic-based constitutive relationship to model the detrimental effects of oxidative aging on mechanical behavior of asphalt concrete. It is noted that the time scale during which oxidative aging occurs is much longer than the loading time. Therefore, in this model, aging effects have been sequentially coupled with loading effects without losing accuracy. Moreover, the developed model does not possess extensive material parameters and is applicable to general loading conditions. Further, the procedure to identify material parameters associated with this model is straightforward. Finally, the developed aging constitutive relationship has been implemented in a way to consider the effect of aging on distress development in a simple, yet general manner.

1.3 Research Objectives

The primary objective of this dissertation is to develop, calibrate, validate and apply a coupled aging-mechanical constitutive relationship. The word “coupled” refers

to the interrelated effects of the aging phenomenon and mechanical models that describe the constitutive behavior of asphalt concrete (i.e. viscoelastic, viscoplastic, and viscodamage). The developed constitutive relationship is used to simulate and predict the mechanical response asphalt concrete subjected to various levels of oxidative aging. The proposed aging constitutive model is developed within the continuum mechanics framework.

As it is the case in continuum mechanics of a homogeneous system, the spatial heterogeneity of a material is not considered explicitly. Instead, the effects of heterogeneity on the macroscopic response is captured through development of proper constitutive relationships and identification of parameters through comparing with experimental measurements (measured for the same heterogeneous material). The state variables are used to describe the mathematical state of a transient system. When asphalt concrete undergoes oxidative aging, there is a chemical process in between reactive molecules of asphalt and oxygen. The repercussions of such a progressive process on macroscopic scale is a change in mechanical material properties or change in a state that the material has reached due to aging. In this study this phenomenon is described by aging state variable.

The coupled aging-mechanical constitutive modeling refers to predicting the mechanical response of asphalt concrete that is subjected to aging. In this case, the hardening effect of aging of asphalt concrete is sequentially coupled (or related) to the mechanical properties. The sequential coupling is referred to combination of analyses from different engineering disciplines which interact to solve a global engineering

problem. When the coupling is one-way, results of one analysis change the input of the second analysis. In this research, the result of the aging analysis alters the material properties of asphalt concrete which are the inputs for analysis under mechanical loading.

1.3.1 Development of the Aging-Mechanical Constitutive Relationship

This subsection briefly describes the development of a continuum-based oxidative aging constitutive relationship based on evolution of the so-called aging state variable. The aging constitutive relationship is formulated based on continuum theory such that the aging state variable is correlated to oxygen content via an evolution function. As stated previously, in continuum mechanics theory the spatial heterogeneity of a material is not considered explicitly. Instead, the effects of heterogeneity on the macroscopic response is usually captured through development of proper constitutive relationships of state variables. State variables are used to describe the mathematical state of a transient system. The rate of the aging state variable is derived by its conjugate variable, oxygen content. In other words, the aging state variable is responsible to account for the hardening effects due to oxidation and associate those effects to mechanical properties of asphalt mixtures on a continuum scale. It should be noted that this subsection will not aim to model the oxidation kinetics and chemical reactions that occur due to oxidation. In fact, the purpose is to propose and present a constitutive modeling framework of aging effects, which is consistent with oxidation kinetics, on mechanical response of asphalt mixtures.

As briefly discussed before, asphalt concrete, when subjected to traffic loading, exhibits time-dependent recoverable and irrecoverable strain response. In this study the former is called viscoelastic and the latter is termed viscoplastic strains. Additionally, in certain conditions, such as repetitive loads and lower temperatures, asphalt concrete may show time-dependent damage (viscodamage) response. Moreover, it is known that the bituminous materials have the potential to heal with time and recover part of their strengths and stiffness under specific circumstances. This phenomenon is called micro-damage healing in this study. PANDA is a finite element package that has been developed by researchers at Texas A&M University which includes the above-mentioned constitutive relationships (i.e., nonlinear viscoelastic, viscoplastic, viscodamage, and micro-damage healing) to account for mechanical behavior of asphalt concrete under different loading conditions (Abu Al-Rub et al., 2013; Abu Al-Rub et al., 2011; Darabi et al., 2011, 2012b; Darabi et al., 2012c, 2013; Huang et al., 2011; Shakiba et al., 2013). Consequently, in order to associate the hardening effects of aging on mechanical properties of asphalt concrete, the developed aging constitutive relationship is implemented in PANDA model.

1.3.2 Calibration and Validation of the Framework

The application of the developed framework to analyze the asphalt concrete performance requires identification of material parameters associated with the constitutive relationships. Therefore, the second goal of this research is to design and analyze appropriate experiments that will enable determination of each of the material parameters of the constitutive relationships in a decoupled way. The identification

procedure is implemented in MATLAB® software. Moreover, the coupled aging-mechanical constitutive relationship is validated against several sets of experimental data. These experiments are conducted on unaged and aged specimens at different stress levels, strain rates, and temperatures. In this instance, the predictions of the constitutive relationship are compared with experimental measurements.

1.3.3 Application of the Model in Macroscopic and Microscopic Simulations

The application of the proposed framework is investigated in both macroscopic and microscopic scales. The former is focused on applying the developed oxidative aging constitutive framework on the pavement structures in macro-scale to predict distresses of the aged asphalt structure. In this case, the pavement structure is subjected to repetitive loadings with different aging times. It should be noted that even with the current power in computational analysis, the complex nature of the loading conditions, large number of loading cycles, and complicated constitutive behavior of asphalt concrete make the accurate prediction of distresses in pavement structures a difficult task.

In addition, microstructural analysis is performed on asphalt concrete to obtain insight into the behavior of the material when subjected to oxidative aging. In this case, finite element microstructural models of asphalt concrete are constructed in two and three dimensions, including asphalt matrix, aggregates, and air voids. Such microstructures are subjected to various aging and loading conditions, first to investigate the oxygen diffusion problem into the asphalt layer and, second, to analyze how the diffused oxygen affects the mechanical response of the material. The microstructures

used in this study do not include interconnected air voids. Hence, the only mechanism for oxygen transport into pavement is by diffusion, which is assumed to occur only from the top surface into the asphalt concrete. Furthermore, the consumption of oxygen throughout the pavement by reaction with asphalt is not included. These are important areas that require attention for future development of the modeling approach presented in this dissertation.

2. A CONTINUUM COUPLED OXIDATIVE AGING-MECHANICAL CONSTITUTIVE FRAMEWORK

2.1 Overview

This section presents a framework to model and simulate oxidative aging effects on mechanical behavior of asphalt concrete by introducing the evolution rate of the aging state variable. The proposed continuum-based constitutive relationship is applicable to simulate asphalt concrete behavior in both microscopic and macroscopic scales. The rate of evolution of the aging state variable is formulated to be a function of temperature, oxygen content, and aging history.

In order to relate the degrading effects of oxidation to the mechanical behavior of asphalt concrete, the aging state variable is linked to mechanical constitutive relationships (PANDA) including thermo-viscoelastic, viscoplastic, viscodamage, and micro-damage healing relationships. The presented framework is implemented in Abaqus, the well-known finite element analysis (FEA) software, through the user material (UMAT) subroutine to verify the model over the experimental data.

2.2 Oxidative Aging Constitutive Relationship

The oxidative aging constitutive relationship accounts for the degradation of the material properties within the oxidation period. As discussed in the introduction, when oxygen reaches asphalt and diffuses into the depth of the pavement, the oxidation procedure begins. As oxidation proceeds, more asphaltene fractions are produced, along

with the original asphaltenes, which mainly contribute to forming carbonyl functional groups. These oxygen-containing groups have more polarity and, therefore, increase the molecular association within the material. As mentioned in the literature review, as asphalt oxidizes, the maltene phase, which governs the rubber-like behavior, is consumed and transformed to more insoluble fractions. The result is the increase in viscosity of the asphalt. Moreover, the formation of hard phases (i.e., carbonyl groups) contributes to growing stiffness of the material (Lau et al., 1992). It has been shown that temperature and oxygen pressure are two major factors affecting the rate of asphalt oxidation. As temperature increases, the mobility of reacting molecules increases, leading to faster oxidation rate. Also, availability of more oxygen molecules results in production of more oxygen-containing groups (Domke et al., 2000; Kliewer et al., 1996).

The production of carbonyl groups during the oxidation process is of great importance. Most studies have shown that carbonyl functional groups are the major oxidation products affecting the physical-chemical properties. Moreover, it has been proven that the increase in oxygen content is linearly correlated with the increase in formation of carbonyl area. The kinetics of carbonyl formation was studied by Liu et al. (1996). They showed that after an initial rapid growth, the carbonyl formation continues with a lengthy slower rate stage. Thus, the carbonyl formation rate is expressed to be a function of a power law equation for oxygen pressure dependency and an Arrhenius-type relation for temperature variation, such that:

$$\frac{dCA}{dt} = r_{CA} = \beta P^{\alpha} \exp\left[\frac{-E}{RT}\right] \tag{2.1}$$

where CA is carbonyl area (the measured area under the carbonyl absorption band in the infrared spectrometer), r_{CA} is the rate of carbonyl formation, β is the frequency factor, and α is the reaction order with respect to oxygen pressure, F. The term E is the activation energy, R is the gas constant, and T is the absolute temperature. Eq. (2.1) expresses the dependency of the oxidation rate on the oxygen pressure and the temperature in which the reaction occurs.

In general, Eq. (2.1) defines the oxidative aging phenomenon and the rate at which it evolves at the molecular level. It actually relates the influence of environmental actions like oxygen pressure and temperature to the formation of molecular bonds (i.e., C=O). However, in order to translate such a relationship in the continuum scale, where the oxidation effects on physical and rheological properties are dealt with, it is necessary to define a state to which the material is aged and the physical properties are changed. In this work, such state is expressed by the aging state variable. In particular, the aging state variable, A is a surrogate to measure the changes in physical and rheological properties of asphalt mixture due to age-hardening. Although in our particular problem asphalt concrete is essentially a multicomponent composite, the concept of a continuum representation of such a heterogeneous medium is theoretically accepted. In other words, the continuum mechanics theory ignores the spatial heterogeneity of the material, treating it in terms of macroscopically homogeneous observables or "state variables." In a general sense, state variables are used to describe the mathematical state of a transient system. When asphalt is being subjected to oxidative aging, there is a thermodynamic process between the reactive molecules of asphalt and oxygen. The repercussion of such

a progressive process on a macroscopic scale is a change in mechanical material properties or change in state that the material has reached due to oxidation. In this study, this phenomenon is accounted for via an aging state variable.

The phenomenological mechanistic-based constitutive relationship of oxidative aging that is conceptually similar to the carbonyl formation relation in Eq. (2.1) is a function of oxygen content and temperature variation as follows:

$$\dot{A} = \frac{dA}{dt} = \Gamma^{a}\theta^{\alpha_1}\left(1-A\right)^{\alpha_2} f\left(T\right) \tag{2.2}$$

where $\dot{A}$ is the time rate of the aging state variable, A. In Eq. (2.2) and subsequent equations, the superimposed dot indicates derivatives with respect to time. In fact, the aging state variable measures changes in material properties as a result of oxidation. The aging state variable is the parameter that couples the oxidative aging effects with the mechanical behavior and lies between 0 and 1. In this case, $A=0$ implies no aging has occurred, whereas $A=1$ indicates a completely aged material and that there is no property change to any further extent due to formation of oxygen-containing functional groups. However, it is noted that it is not viable to have a completely aged material in practice, as it takes a substantially long time to fully age an asphalt concrete.

2.2.1 Aging Fluidity Parameter, Γ^{a}

The term Γ^{a} is the aging fluidity parameter, and it can be a counterpart of the frequency factor in Eq. (2.1). The aging fluidity parameter is the inverse of the viscosity parameter controlling the growth rate of the aging state variable having the unit of $1/time$. The fluidity parameter can also be used to rank order the different types of

asphalt mixtures and asphalt binders for their susceptibility to oxidative aging. In this case, when Γ^a is greater for a particular material, then based on this constitutive modeling framework, it is more susceptible to oxidative aging. In other words, it controls how fast aging occurs. At the mixture level, the mixture characteristics such as air void distribution, volume fraction of components, and shape of the aggregates can influence the aging vulnerability. However, the aging fluidity parameter, once properly identified from experiments, describes the combined effects of binder and mixture variables on the aging susceptibility. In fact, at mixture level, Γ^a provides the average behavior of the asphalt concrete against oxidative aging. Figure 2.1 shows the effect of the aging fluidity parameter on the evolution of the aging variable. The time is normalized in this figure since the aging time can be varied widely for different combination of material parameters. Figure 2.1 shows that the aging state variable, A evolves faster with time as Γ^a increases. Therefore, in the physical sense, the aging fluidity parameter is a material property that describes the relative rate that reactive components will react with oxygen. This corresponds phenomenologically to the molecular scale in that a greater value of the aging fluidity parameter increases the rate at which oxygen will react with the asphalt.

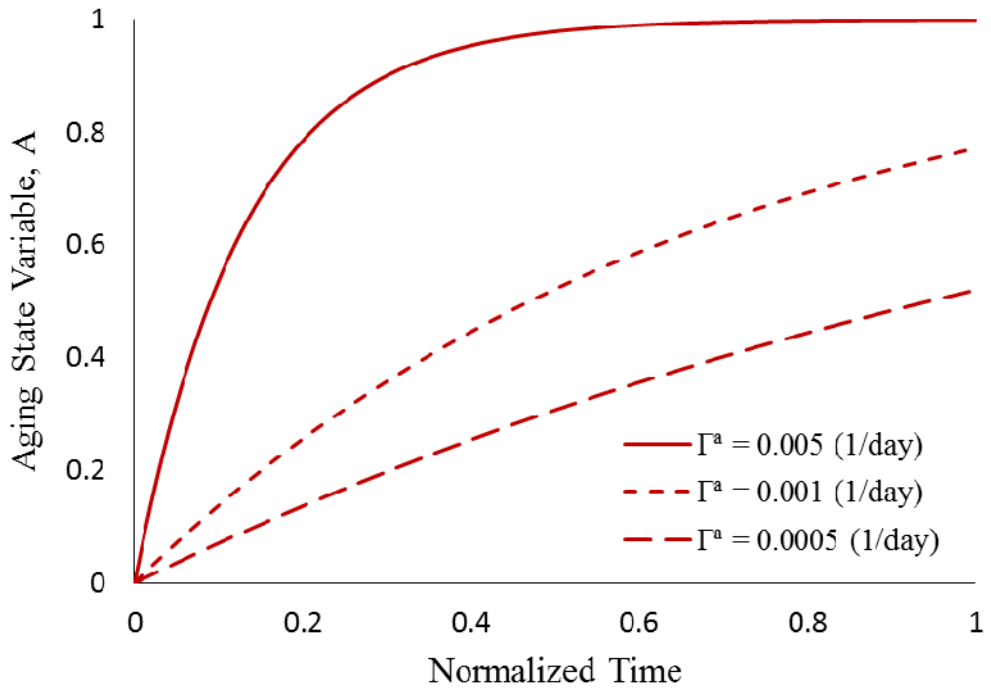

Figure 2.1. The effect of the aging fluidity parameter, Γ^a on the evolution of the aging state variable. The oxygen content is assumed to be constant for all cases.

2.2.2 Oxygen-Related Parameters, θ and α_1

In this study, the aging constitutive equation is formulated based on continuum theory such that the aging state variable, A is correlated to oxygen content, θ via an evolution function. In the aging constitutive equation, the rate of change of the aging state variable and oxygen content are formulated as conjugate variables. In this case, oxygen content is deemed as the driving force for the rate of change of the aging variable. In Eq. (2.2) θ is normalized oxygen content to account for effects of oxygen on aging rate that varies as $0 \le \theta \le 1$. The value $\theta = 0$ indicates there is no oxygen available for reaction, whereas $\theta = 1$ describes the state when the maximum amount of oxygen is

diffused and present for reaction to happen. The model parameter, α_1 controls the effect of oxygen content on the aging rate. In fact, the roles of the oxygen content parameter, θ, and the oxygen controlling parameter, α_1, in Eq. (2.2) are very similar to the roles of oxygen pressure, P, and the reaction order, α, in Eq. (2.1), and Figure 2.2(a) and Figure 2.2(b) represent the effects of these two parameter on the evolution rate of the aging state variable where the other parameters are kept constant.

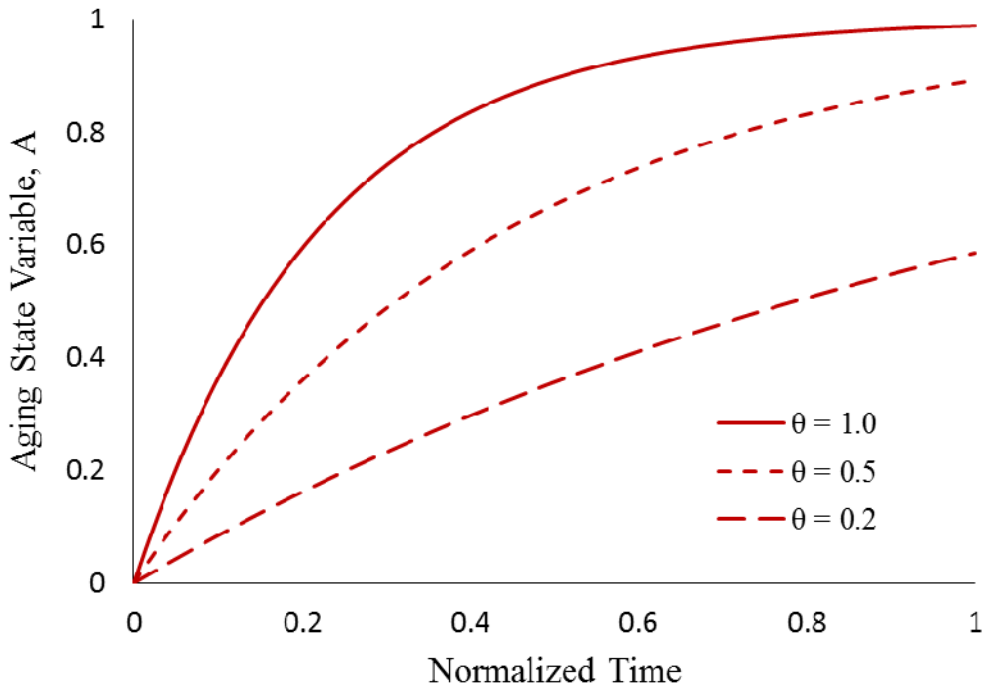

(a)

Figure 2.2. The effect of oxygen-related parameters on the aging state variable evolution: (a) effect of oxygen content, θ and (b) effect of oxygen content controlling parameter, α_1.

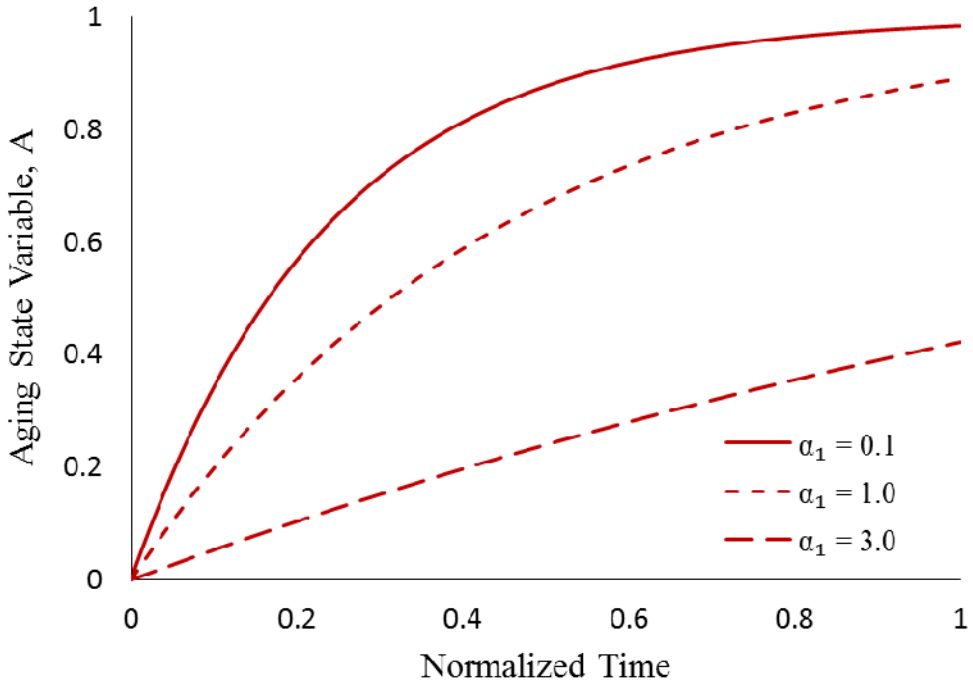

(b)

Figure 2.2. Continued.

2.2.3 Aging History Terms

In Eq. (2.2), the term $(1 - A)$ is called the aging history term and controls the decreasing rate of the aging state variable during the aging time. In fact, the aging history term captures two important mechanisms during oxidation in an implicit manner. First, the amount of the reactive component to form oxygen-containing groups decreases with age, and second, the rate of oxygen diffusion into the asphalt pavement is reduced as material undergoes more aging. In other words, the presence of $(1 - A)$ in Eq. (2.2) assures the fast aging rate at early stages and the slower rate reactions at later ages. Also, the material parameter, α_2 controls the effect of the aging history term. Figure 2.3 shows

the effect of this parameter on the rate of the aging state variable when the other parameters are kept constant. When the aging history term, $(1 - A)$ is not considered (i.e., $\alpha_2 = 0.0$), the aging state variable evolves until it reaches the fully aged state without a decrease in the aging rate. But, when the aging history term is included (i.e., $\alpha_2 \neq 0.0$), the aging rate decreases such that it requires relatively longer time for the material to reach the fully aged state. It is noteworthy to mention, as it is seen in Figure 2.3, the aging history term does not affect the evolution of the aging state variable at low aging levels. However, as material is subjected to more aging, the effect of the aging history term becomes more profound.

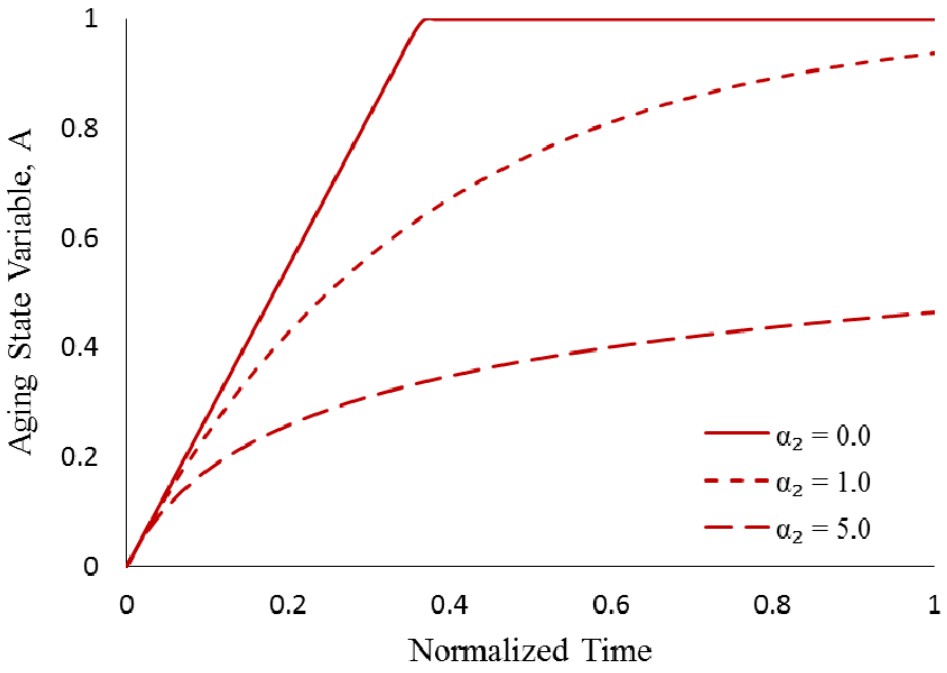

Figure 2.3. The effect of the aging history term on the evolution rate of the aging state variable.

2.2.4 Temperature Coupling Parameters

As mentioned previously, oxidation temperature has an important effect on the oxidation reaction and the resultant oxidation products. Consequently, the oxidation temperature influences the properties of the aged asphalt. In order to include the temperature effect on the oxidative aging rate, a temperature-dependent function, $f(T)$, is implemented in the oxidative aging constitutive relationship, Eq. (2.2). The thermal coupling term reads:

$$f(T) = \exp\left[-\alpha_3\left(1 - T/T_0\right)\right] \tag{2.3}$$

where T is the temperature at which the oxidation occurs, and T_0 is the reference temperature. The parameter, α_3, represents the temperature-dependency of the evolution of the aging state variable. This parameter is interpreted as the counterpart of the thermal term, $\exp\left(-E/RT\right)$, in Eq. (2.1); therefore, it is related to the chemical composition of the asphalt and the activation energy. In this regard, Figure 2.4 examines the effect of temperature coupling function parameters, α_3 and T/T_0, on the evolution rate of the aging state variable. Figure 2.4(a) shows that greater value of α_3 intensifies the evolution of the aging variable, particularly at the early stages. Similarly, Figure 2.4(b) represents that as the aging temperature increases with respect to the reference temperature, the rate of aging variable significantly increases.

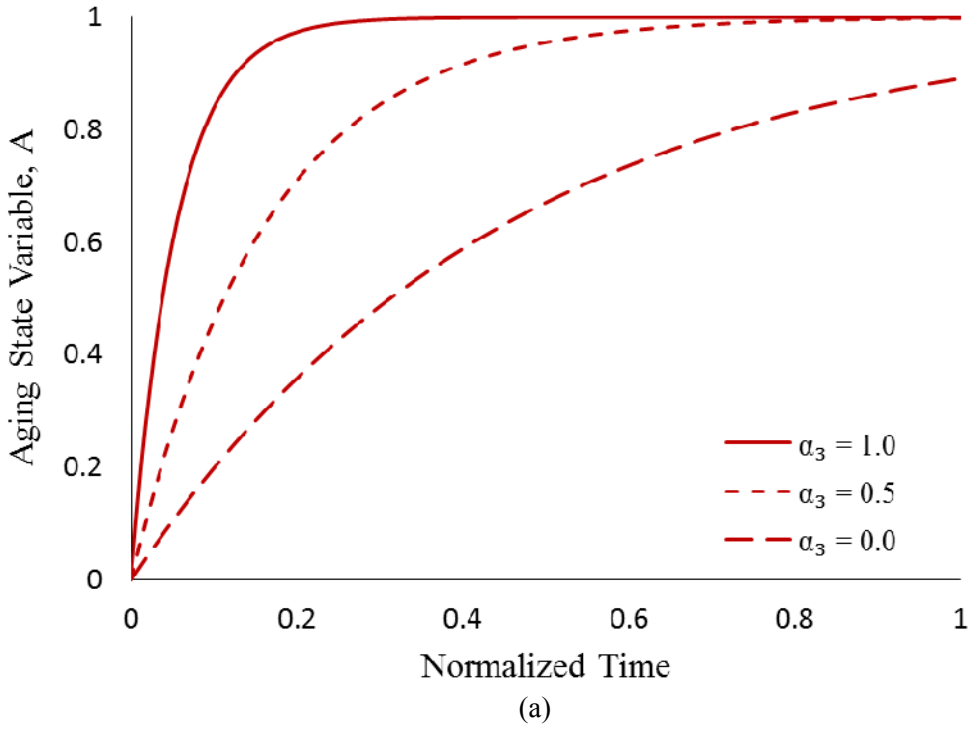

(a)

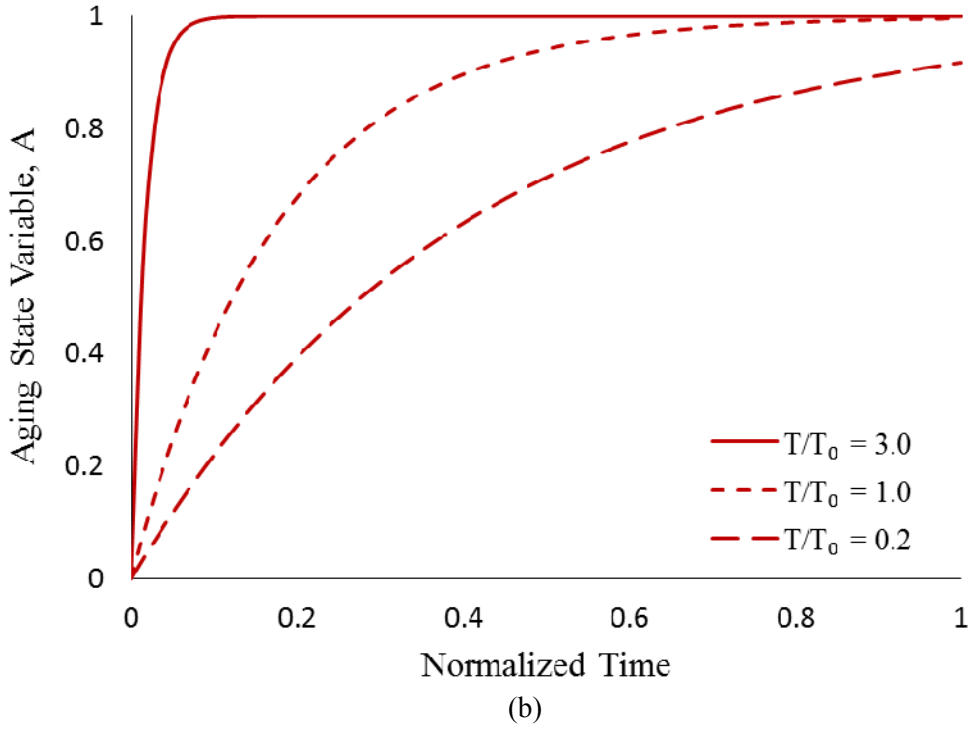

(b)

Figure 2.4. The effect of thermal coupling parameters on the evolution rate of the aging state variable: (a) effect of α_3 and (b) effect of T/T_0.

2.3 Constitutive Relationships to Account for Mechanical Response of Unaged Asphalt Concrete

This subsection presents the constitutive equations required to account for the response of asphalt concrete under mechanical loading. As discussed previously, the viscoelastic, viscoplastic, and viscodamage constitutive relationships are used to address the mechanical behavior of asphalt concrete. PANDA, as briefly introduced in Section 1, is a package that includes all these mechanical constitutive relationships. However, to include the aging effects on the mechanical response, the aging state variable will be coupled to the mechanical constitutive relationships. Hence, in this subsection, first the mechanical constitutive modeling are presented, then the incorporation of the aging state variable to these constitutive models is discussed.

2.3.1 Classical Continuum Damage Mechanics: The Effective Stress Concept

The concept of continuum damage mechanics was first introduced by Kachanov (1958) through a scalar measure of continuity, ζ. In continuum damage mechanics framework, two configurations can be defined for a damaged material:

(a) Nominal or damaged configuration

(b) Effective or undamaged configuration

Based on these definitions, Rabotnov (1969) was able to physically define the continuity parameter as:

$$\zeta = \frac{\bar{A}_r}{A_r} \tag{2.4}$$

where A_r is the damaged or apparent area, and $\bar{A}_r$ is the real or undamaged area carrying the load. In other words, as Figure 2.5 shows, $\bar{A}_r$ is the resulting effective area after micro-damages and micro-cracks are removed from the damaged area, A_r.

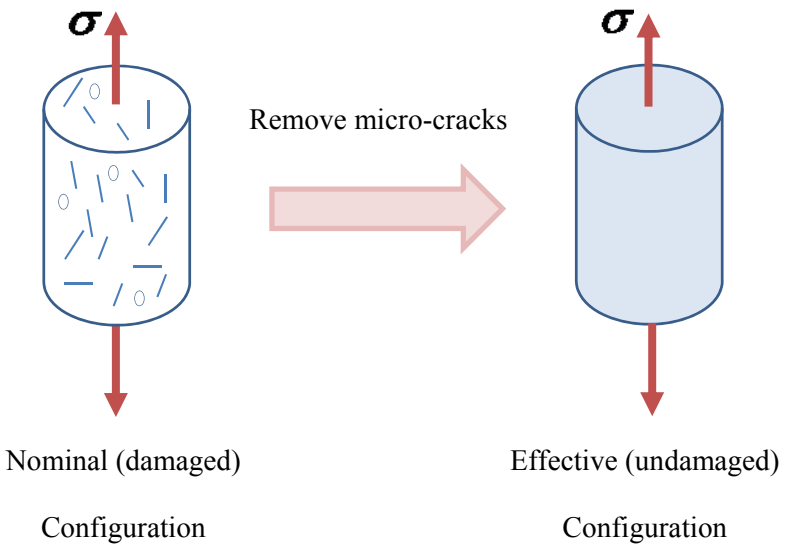

Figure 2.5. Schematic representation of the material configuration in continuum damage mechanics, nominal and effective configuration.

Odqvist and Hult (1961) introduced another variable that defines the reduction of area because of the micro-damages:

$$\phi = 1 - \zeta = \frac{A_r - \bar{A}_r}{A_r} = \frac{A_r^D}{A_r} \tag{2.5}$$

where A_r^D is the area of micro-damages. The parameter, ϕ, is the damage variable or damage density, which is interpreted as the density of micro-damages with values ranging from 0 (undamaged) to 1 (fully damaged). In this study, isotropic damage is assumed such that the stress tensor components are degraded equally in different directions. Once the material undergoes degradation due to mechanical loads, the undamaged portion of the material sustains further loading. Assuming that the applied forces in undamaged and damaged configurations are equal, the relationship between stresses in the undamaged (effective) material and the damaged (nominal) material is defined as:

$$\bar{\sigma}_{ij} = \frac{\sigma_{ij}}{1-\phi} \tag{2.6}$$

where $\bar{\sigma}_{ij}$ is the effective stress tensor in the effective configuration, and σ_{ij} is the nominal Cauchy stress tensor in the nominal configuration. A detailed review of effective stress concept can be found in Chaboche (2003).

It should be noted that the effective stress, $\bar{\sigma}_{ij}$, is the stress driving the material deformation under the mechanical loading. Additionally, it is argued that once the material is damaged, further loading can only affect the undamaged material skeleton. As a result, the viscoelastic, viscoplastic, and viscodamage constitutive relationships in this work are defined as a function of variables in the effective (undamaged) configuration. The superimposed "$\bar{}$" designates the effective configuration.

2.3.2 Nonlinear Thermo-Viscoelastic Constitutive Relationship

Under the assumption of small deformations, the total deformation of asphalt concrete subjected to an applied load can be additively decomposed into viscoelastic (recoverable) and viscoplastic (irrecoverable) components. Since the asphalt concrete is a time-temperature dependent material, viscoelastic and viscoplastic strain responses are significantly influenced by time, temperature, and loading rate. As a result, the total strain response can be written as follows:

$$\bar{\varepsilon}_{ij} = \bar{\varepsilon}_{ij}^{ve} + \bar{\varepsilon}_{ij}^{vp} \tag{2.7}$$

where $\bar{\varepsilon}_{ij}$, $\bar{\varepsilon}_{ij}^{ve}$, and $\bar{\varepsilon}_{ij}^{vp}$ are the total, viscoelastic, and viscoplastic strain tensors, respectively. In this work, Schapery's nonlinear viscoelastic theory (Schapery, 1966) is used to model the viscoelastic response of asphalt concrete.

Schapery's one-dimensional single integral constitutive relation expressed in the effective configuration is as follows:

$$\bar{\varepsilon}^{ve,t} = g_0 \bar{D}_0 \bar{\sigma}^t + g_1 \int_0^t \Delta\bar{D}\left(\psi^t - \psi^\tau\right) \frac{d\left(g_2 \bar{\sigma}^t\right)}{d\tau} d\tau \tag{2.8}$$

where $\bar{\varepsilon}^{ve,t}$ and $\bar{\sigma}^t$ are the viscoelastic strain and effective stress; $\bar{D}_0$ is the instantaneous compliance; $\Delta\bar{D}$ is the transient compliance; and g_0, g_1, and g_2 are the stress-dependent nonlinear parameters. The parameter ψ^t is the reduced time and is given by:

$$\psi^t = \int_0^t \frac{d\zeta}{a_T} \tag{2.9}$$

where a_T is the time-temperature shift factor. It can be interpreted from Eq. (2.8) that when the nonlinear stress-dependent parameters (g_0, g_1, and g_2) are equal to unity, the Schapery nonlinear viscoelastic relationship is simplified to the Boltzmann superposition integral for linear viscoelasticity. For numerical convenience, the transient compliance is represented by the Prony series as follows:

$$\Delta\bar{D} = \sum_{n=1}^{N} D_n \left[1 - \exp\left(-\lambda_n \psi^t\right)\right] \tag{2.10}$$

where D_n is the *n*th compliance associated with the *n*th retardation time, λ_n, and N is the number of Prony series coefficients. In the above and subsequent equations, the superimposed t and τ define the associated parameter at a specific time.

The aforementioned Schapery model is defined in the one-dimensional case and needs to be generalized into the three-dimensional (3D) case. Lai and Bakker (1996) generalized the Schapery single integral model to a 3D problem by decomposing the nonlinear viscoelastic strain into its deviatoric and volumetric components as follows:

$$\bar{\varepsilon}_{ij}^{ve} = \bar{e}_{ij}^{ve} + \frac{1}{3}\bar{\varepsilon}_{kk}^{ve}\delta_{ij} \tag{2.11}$$

where $\bar{e}_{ij}^{ve}$ and $\bar{\varepsilon}_{kk}^{ve}$ are the deviatoric strain tensor and the volumetric component of the strain tensor, respectively, and δ_{ij} is the Kronecker delta. Consequently, the

decomposed deviatoric and volumetric viscoelastic strains can be derived using Eq. (2.8) such that:

$$\bar{e}_{ij}^{ve,t} = \frac{1}{2} g_0 \bar{J}_0 \bar{S}_{ij}^t + \frac{1}{2} g_1 \int_0^t \Delta \bar{J} \left(\psi^t - \psi^\tau \right) \frac{d\left(g_2 \bar{S}_{ij}^\tau \right)}{d\tau} d\tau \tag{2.12}$$

$$\bar{\varepsilon}_{kk}^{ve,t} = \frac{1}{3} g_0 \bar{B}_0 \bar{\sigma}_{kk}^t + \frac{1}{3} g_1 \int_0^t \Delta \bar{B} \left(\psi^t - \psi^\tau \right) \frac{d\left(g_2 \bar{\sigma}_{kk}^\tau \right)}{d\tau} d\tau \tag{2.13}$$

where $\bar{S}_{ij}$ and $\bar{\sigma}_{kk}$ are the deviatoric stress tensor and the volumetric stress in the effective configuration. The relationship between instantaneous and transient shear and bulk compliances with instantaneous and transient compliance is as follows:

$$\bar{J}_0 = 2\left(1+\bar{\nu}\right)\bar{D}_0 \ , \ \Delta \bar{J}\left(\psi\right) = 2\left(1+\bar{\nu}\right)\Delta \bar{D}\left(\psi\right) \tag{2.14}$$

$$\bar{B}_0 = 3\left(1-2\bar{\nu}\right)\bar{D}_0 \ , \ \Delta \bar{B}\left(\psi\right) = 3\left(1-2\bar{\nu}\right)\Delta \bar{D}\left(\psi\right) \tag{2.15}$$

It is noted that the Poisson's ratio in the above equations is assumed to be time-independent. This is a fairly reasonable assumption for a range of temperatures and stress rates in bituminous materials (Di Benedetto et al., 2007).

2.3.3 Thermo-Viscoplastic Constitutive Relationship

In order to account for the permanent or irrecoverable deformation (viscoplastic) in asphalt concrete, Perzyna-type viscoplasticity is used (Perzyna, 1971). The viscoplastic constitutive formulation is outlined in Huang et al. (2011), Masad et al. (2005), and Tashman et al. (2005) based on the nominal configuration, and later is modified in terms of the effective configuration and expressed with the effective stress

tensor by Darabi et al. (2011). The derivations and formulations of the viscoplastic constitutive relationship is presented as follows.

Taking the time derivative of Eq. (2.7) in the effective configuration yields:

$$\dot{\bar{\varepsilon}}_{ij} = \dot{\bar{\varepsilon}}_{ij}^{ve} + \dot{\bar{\varepsilon}}_{ij}^{vp} \tag{2.16}$$

where $\dot{\bar{\varepsilon}}_{ij}^{ve}$ and $\dot{\bar{\varepsilon}}_{ij}^{vp}$ are the viscoelastic and the viscoplastic strain rate tensors in the effective configuration, respectively. The viscoplastic strain rate is defined by the following classical flow rule:

$$\dot{\bar{\varepsilon}}_{ij}^{vp} = \dot{\bar{\gamma}}^{vp} \frac{\partial g}{\partial \bar{\sigma}_{ij}} \tag{2.17}$$

where $\dot{\bar{\gamma}}^{vp}$ and g are the viscoplastic multiplier and the viscoplastic potential function in the effective configuration, respectively. In fact, the viscoplastic multiplier is a positive scalar that determines the magnitude of the viscoplastic strain rate, $\dot{\bar{\varepsilon}}_{ij}^{vp}$, and $\partial g / \partial \bar{\sigma}$ determines the direction of $\dot{\bar{\varepsilon}}_{ij}^{vp}$. The viscoplastic multiplier is defined in terms of a viscosity parameter and an overstress function that relates the viscoplastic strain rate to the effective stress. In this case, the viscoplastic multiplier can be expressed as:

$$\dot{\bar{\gamma}}^{vp} = \Gamma^{vp} \left\langle \Phi\left(f\right) \right\rangle^{N} \tag{2.18}$$

where Γ^{vp} is called the viscoplastic fluidity parameter such that $1/\Gamma^{vp}$ represents the viscoplastic relaxation time. The term N is the viscoplastic rate sensitivity exponent, and Φ is the overstress function expressed in terms of the yield function, f. The symbol

$\langle\ \rangle$ is the MacAulay bracket defined by $\langle\Phi\rangle = \left(\Phi + |\Phi|\right)/2$. The overstress function can be expressed as follows:

$$\Phi(f) = \frac{f}{\sigma_y^0} \tag{2.19}$$

where σ_y^0 is a yield stress quantity used to normalize the overstress function and can be assumed to be unity. It can be interpreted from Eq. (2.18) that viscoplasticity occurs only when the overstress function has a positive value. This work utilizes the modified Drucker-Prager yield function. The modified Drucker-Prager yield surface takes into account the pressure sensitivity and distinguishes the distinct behavior of asphalt concrete in tension and compression (Masad et al., 2007). The modified Drucker-Prager yield function can be expressed in the effective configuration such that:

$$f = \bar{\tau} - \alpha \bar{I}_1 - \kappa\left(\varepsilon_e^{vp}\right) \tag{2.20}$$

where α is a material parameter related to the internal friction of the material, and $\kappa\left(\varepsilon_e^{vp}\right)$ is the isotropic hardening function associated with the cohesive characteristic of the material and depends on the effective viscoplastic strain, ε_e^{vp}. The term $\bar{I}_1 = \bar{\sigma}_{kk}$ is the first stress invariant, and $\bar{\tau}$ is the deviatoric effective shear stress modified to distinguish the asphalt concrete behavior under compressive and extensive loads, and is expressed as:

$$\bar{\tau} = \frac{\sqrt{3\bar{J}_2}}{2}\left[1 + \frac{1}{d} + \left(1 - \frac{1}{d}\right)\frac{3\bar{J}_3}{\sqrt{3\bar{J}_2^3}}\right] \tag{2.21}$$

where $\bar{J}_2 = \frac{3}{2}\bar{S}_{ij}\bar{S}_{ij}$ and $\bar{J}_3 = \frac{9}{2}\bar{S}_{ij}\bar{S}_{jk}\bar{S}_{ki}$ are the second and third deviatoric stress invariants of the effective stress tensor, and d is a material parameter being interpreted as the ratio of the yield stress in uniaxial tension to that in uniaxial compression. Therefore, d gives the distinction of asphalt concrete behavior in compression and tension. It is noted that the magnitude of d should be in the range of $0.778 \le d \le 1.0$ to ensure that the yield surface convexity is maintained (Masad et al., 2007).

The isotropic hardening function, $\kappa\left(\varepsilon_e^{vp}\right)$ is expressed as an exponential function of the effective viscoplastic strain, such that:

$$\kappa\left(\varepsilon_e^{vp}\right) = \kappa_0 + \kappa_1\left\{1 - \exp\left[-\kappa_2\left(\varepsilon_e^{vp}\right)\right]\right\} \tag{2.22}$$

where κ_0, κ_1, and κ_2 are material parameters defining the initial yield stress, the saturated yield stress, and the strain hardening rate, respectively. The asphalt concrete has been proven to follow a non-associative viscoplasticity (i.e., $g \neq f$). Therefore, in order to obtain the viscoplastic potential function, g, the parameter α is replaced by another parameter, β, such that:

$$g = \bar{\tau} - \beta\bar{I}_1 \tag{2.23}$$

where β is a material parameter that describes the dilation or contraction behavior of the material. In addition, the effective viscoplastic strain rate, $\dot{\varepsilon}_e^{vp}$, is expressed as follows:

$$\dot{\varepsilon}_e^{vp} = \frac{1}{\sqrt{1+2\left(\frac{0.5+\beta}{1-\beta}\right)^2}} \sqrt{\dot{\bar{\varepsilon}}_{ij}^{vp} \dot{\bar{\varepsilon}}_{ij}^{vp}} \tag{2.24}$$

2.3.4 Thermo-Viscodamage Constitutive Relationship

This subsection provides the formulation to calculate the evolution of the damage density parameter within the continuum damage mechanics framework described in Subsection 2.3.1. The time-, rate-, and temperature-dependent damage density evolution used in this study is from the work of Darabi et al. (2011) and Darabi et al. (2013). Moreover, the thermodynamic consistency of their constitutive relationship is validated in Abu Al-Rub and Darabi (2012) and Darabi et al. (2012c).

The viscodamage constitutive relationship expresses the evolution of the damage density parameter and is a function of damage driving force, $\overline{Y}$, and effective total strain, $\overline{\varepsilon}_{eff}$, such that:

$$\dot{\phi} = \Gamma^{vd} \left(\frac{\overline{Y}}{Y_0}\right)^q (\overline{\varepsilon}_{eff})^k \tag{2.25}$$

where Γ^{vd} is the viscodamage fluidity parameter, and Y_0 is the reference damage force to normalize the damage force, which can be assumed to be unity. The terms q and k are the stress and strain dependency parameters, respectively. The effective total strain is expressed as:

$$\overline{\varepsilon}_{eff} = \sqrt{\overline{\varepsilon}_{ij} \overline{\varepsilon}_{ij}} \tag{2.26}$$

where $\bar{\varepsilon}_{ij}$ is the total strain including both viscoelastic and viscoplastic components. It is noteworthy that the dependence of the damage density on the total strain implicitly couples the viscodamage constitutive relationship to the viscoelasticity and viscoplasticity. Therefore, any change in loading time, rate, and temperature implicitly affects the damage density parameter through changes in the viscoelastic and viscoplastic components. On the other hand, it is known that the time of rapture in creep tests and the peak points in stress-strain diagrams for constant strain rate tests are highly stress dependent. As a result, the presence of the stress dependency term, $\left(\bar{Y}/Y_0\right)$, in Eq. (2.25) is inevitable. The damage driving force, $\bar{Y}$, is assumed to have a Drucker-Prager type form, such that:

$$\bar{Y} = \bar{\tau} - \alpha \bar{I}_1 \tag{2.27}$$

where $\bar{I}_1$ is the first stress invariant in the effective configuration, and $\bar{\tau}$ and α have definitions identical to that provided in the viscoplastic constitutive relationship. This states that viscodamage and viscoplastic constitutive relationships have similar driving forces with different evolution functions. Moreover, presence of the deviatoric effective shear stress, $\bar{\tau}$, in Eq. (2.27) ensures that the damage response in extension and contraction loading conditions is different by including the parameter, d. Furthermore, the viscodamage driving force confirms the sensitivity to the hydrostatic pressure.

2.4 Thermo-Chemo-Mechanical Coupling

In the previous subsection, the constitutive modeling framework was presented to calculate the mechanical response of the unaged asphalt concrete. In order to incorporate the oxidative aging effects on the mechanical behavior of the material, the aging constitutive relationship must be coupled to the viscoelastic-viscoplastic-viscodamage constitutive relationship. The effects of oxidation on the physical and rheological properties was thoroughly discussed in the introduction subsection. Time-dependent increase in stiffness and viscosity is the primary consequence of asphalt oxidation, which is an on-going process within the course of a pavement life. It was discussed that the aging state variable is a time-dependent parameter that measures the property change of asphalt concrete due to oxidation, and its evolution rate is based on oxygen content and temperature. Therefore, the degrading effects of oxidative aging are integrated to the mechanical response through coupling the aging state variable with the fundamental properties of the viscoelastic asphalt concrete.

This study proposes a phenomenological relationship for aged transient compliance of a viscoelastic material. In this case, the aged transient compliance is expressed to be a function of the aging state variable and unaged transient compliance, such that:

$$\Delta\bar{D}^{A} = f(\Delta\bar{D}, A) \tag{2.28}$$

where $\Delta\bar{D}^{A}$ and $\Delta\bar{D}$ are the transient compliance of the aged and unaged material in the effective configuration, respectively. Eq. (2.28) allows for the viscoelastic properties of

the aged material to be expressed in two different time scales: loading time and aging time. In other words, $\Delta\overline{D}$ is a function that is defined in a time scale when the mechanical loading is applied and the aging state variable, A, is expressed in terms of a time when oxidative aging happens.

In order to capture the influence of the oxidation on the viscoelastic behavior of the aged asphalt concrete, the following relationships are proposed for parameters of the aged transient compliance:

$$D_n^A = \left(1 - A\right)^{k_1} D_n \tag{2.29}$$

$$\lambda_n^A = \left(1 - A\right)^{k_2} \lambda_n \tag{2.30}$$

where D_n^A and λ_n^A are compliance terms and retardation times of the aged material, and k_1 and k_2 are material properties. It is noted that the compliance terms are measures of the stiffness, whereas the retardation times are the characteristic properties of viscoelastic materials being inversely related to viscosity of the matter. Moreover, the mechanistic-based relationships in Eq. (2.29) and Eq. (2.30) imply that the compliance terms and the retardation times decrease with age. Therefore, it is interpreted that the proposed relationship for the aged viscoelasticity ensures that the stiffness and viscosity of the aged material increases by decreasing the compliance terms and the retardation times. Finally, by substituting Eq. (2.29) and Eq. (2.30) in Eq. (2.28), the aged transient compliance of asphalt concrete can be defined, such that:

$$\Delta\bar{D}^{A} = \sum_{n=1}^{N} (1-A)^{k_1} D_n \left[1 - \exp\left(-(1-A)^{k_2} \lambda_n \psi^{t}\right)\right] \tag{2.31}$$

Figure 2.6 shows the effect of the aging state variable on the transient compliance of the aged material presented in Eq. (2.31). As seen in this figure, $\Delta D(t)$ is significantly influenced by the aging state variable as aging time increases. In fact, at higher levels of aging, for instance $A = 0.8$, the corresponding transient compliance tends to be a constant value. In a constitutive modeling point of view, this implies that as the aging level increases with increase in A, the viscoelastic material tends to drop the time-dependent response and behave more elastically.

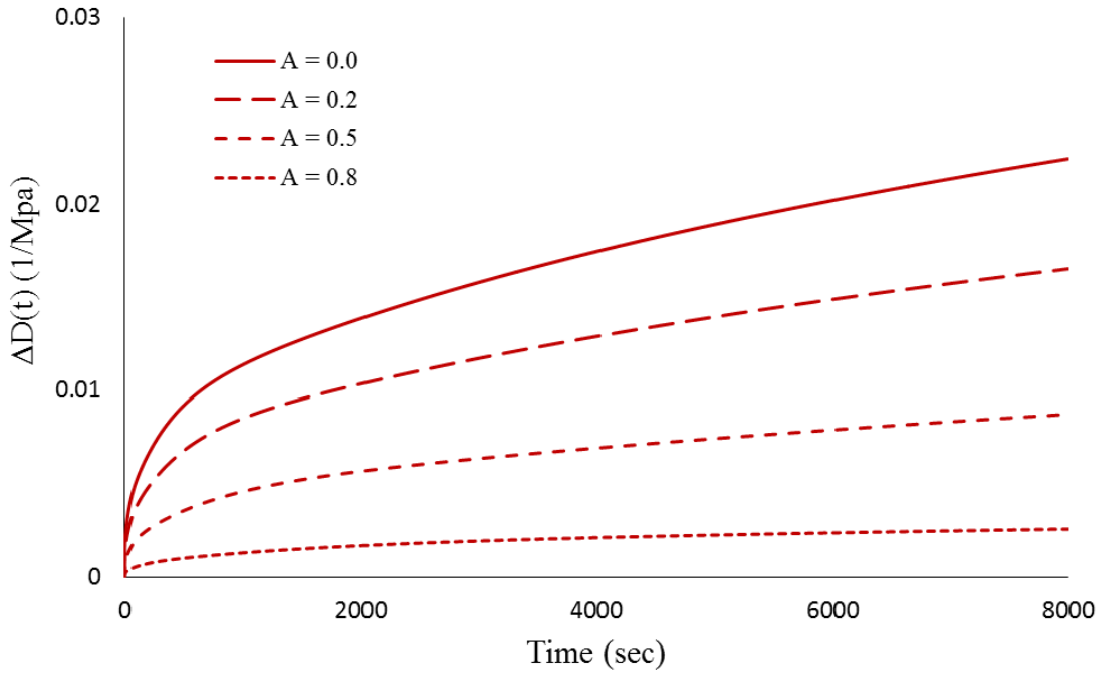

Figure 2.6. The effect of the aging state variable on transient compliance of asphalt concrete.

It is also interesting to see that the proposed relationships in Eq. (2.29) and Eq. (2.30) are supported by experimental data. In this case, an unaged, a 3-month aged, and a 6-month aged asphalt concrete are considered. The experiments and the descriptions of the asphalt mixtures are explained in the following section. Seven data points are considered to represent the Prony series of the transient compliance of the asphalt concrete. The data shown in this subsection correspond to asphalt concrete with 7% air void content. In the first case, as Figure 2.7(a) shows, the aged compliance terms, D_n^A, are presented with respect to the unaged compliance terms, D_n, in log scale along with power law functions being fitted. In the other case, as shown in Figure 2.7(b), the aged retardation times, λ_n^A, are depicted against the unaged retardation times, λ_n, with corresponding fits. Two important facts can be interpreted out of these figures. First, the aged Prony series coefficients make a perfect power-type fit with the unaged ones, suggesting the linear relationship between them as described in Eq. (2.29) and Eq. (2.30) . Second, the fitted lines for both cases fall under the line y=x (the Prony series coefficients of the unaged specimen) implying that the Prony series coefficients (D_n and λ_n) decrease with aging time.

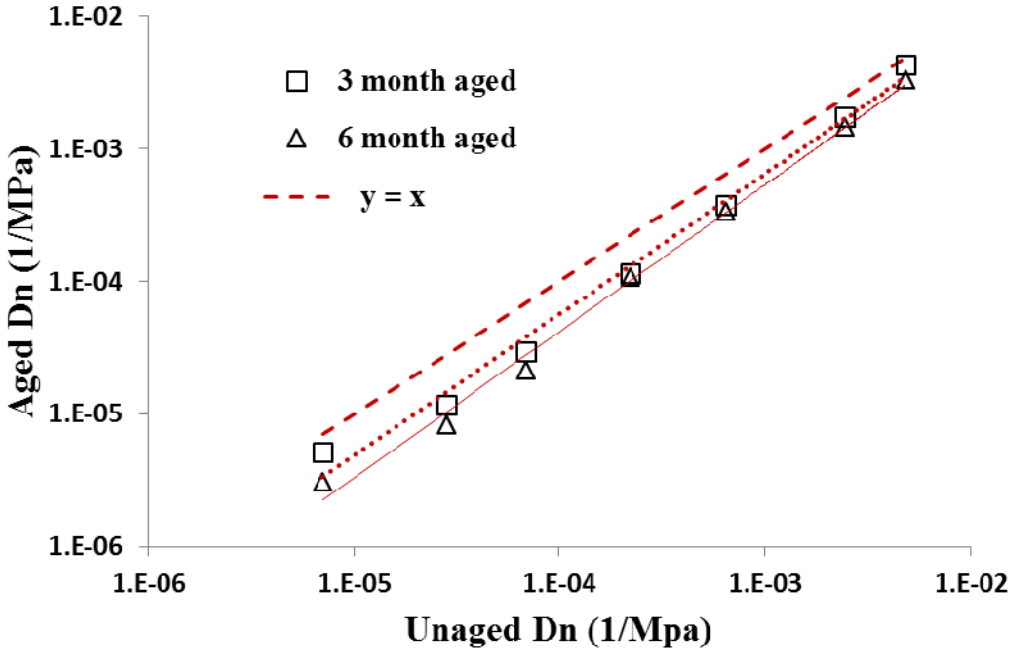

(a)

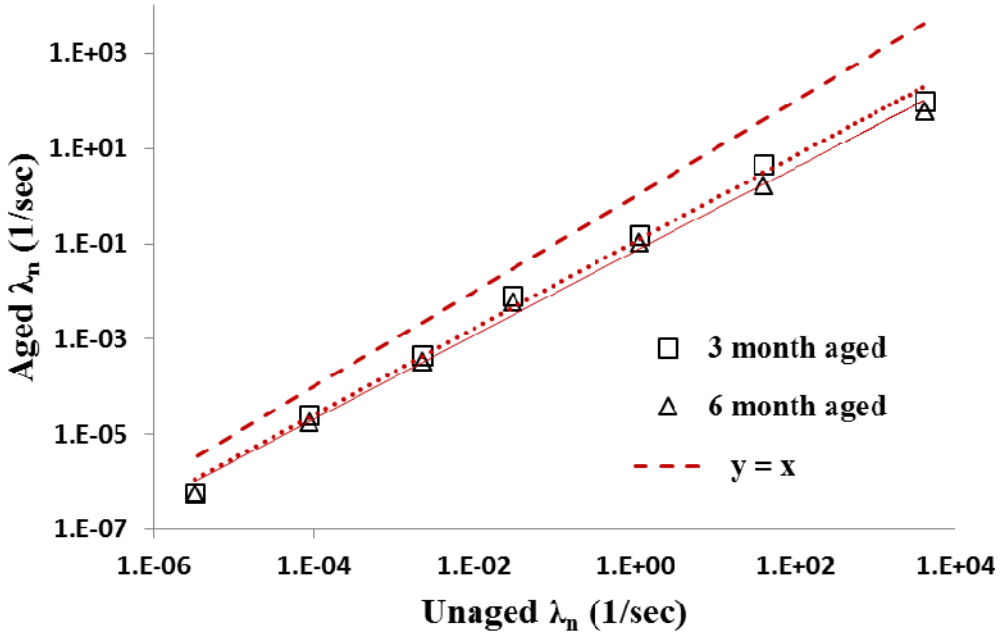

(b)

Figure 2.7. Relationship between aged and unaged Prony series coefficients: (a) relationships for compliance terms and (b) retardation times (figures are shown in logarithmic scales). Figures indicate a linear relationship between aged and unaged viscoelastic properties.

In the case of the unaged material, the viscoplastic fluidity parameter, Γ^{vp}, is constant and represents the material's viscosity through $1/\Gamma^{vp}$. In order to include the aging effect in the viscoplastic formulation, it should be noted that as the material ages it gets stiffer and its viscoplastic potential decreases, such that the resistance of the material to undergo viscoplastic deformation increases. Such increase in the resistance can be phenomenologically explained by the changes in the viscoplastic fluidity parameter. In this case, the viscoplastic fluidity parameter of the aged material, $\Gamma^{vp,A}$ is expressed in terms of the aging state variable, A, and the fluidity parameter at unaged state, such that:

$$\Gamma^{vp,A} = (1-A)^{k_3}\Gamma^{vp} \tag{2.32}$$

where k_3 is a material parameter that controls the aging effect on the viscoplastic response.

Likewise, the effect of oxidative aging on the viscodamage behavior of asphalt concrete is incorporated through the viscodamage fluidity parameter, Γ^{vd}. Oxidative aging increases the stiffness of the material. However, the increase in the stiffness is associated with the decrease in the toughness of the material. In other words, oxidative aging alters the material behavior from ductile-type to brittle-type response. Therefore, it is expected that the damage density evolves faster in the aged material. It is noted that Eq. (2.29) and Eq. (2.30) ensure the rapid evolution of damage density evolves for aged cases. However, for the longer aging times (i.e., larger aging state variables) the rate of damage density dramatically increases such that the model predicts unreasonable

responses. As a result, to control the increasing rate of the damage density variable the following equation is proposed for the aged viscodamage fluidity parameter, $\Gamma^{vd,A}$:

$$\Gamma^{vd,A} = (1-A)^{k_4}\Gamma^{vd} \tag{2.33}$$

where $k_4 > 0$ is a material parameter controlling the aging effect on the damage density evolution. In order to explain the functionality of Eq. (2.33), a simple uniaxial strain rate test is studied. Three different cases are considered: (1) an unaged state (i.e., $A = 0$), (2) an aged state without including Eq. (2.33) (i.e., $A = 0.6, k_4 = 0$), and (3) an aged state including Eq. (2.33) (i.e., $A = 0.6, k_4 = 1$). In all these cases the stress responses under uniaxial strain load are calculated using viscoelastic and viscodamage constitutive relationships. Figure 2.8(a) shows the stress-strain diagram, and Figure 2.8(b) represents the evolution of damage density corresponding to each of the three cases. As seen in these figures, in the third case the damage density evolves with a rapid rate such that the material reaches the ultimate strength that is lower than the ultimate strength of the unaged case. However, when subjected to the uniaxial strain load, the aged asphalt concrete is expected to exhibit higher ultimate strength with more brittle-like performance. Such a behavior can be seen in the second case, where the aged viscodamage fluidity parameter is modified by the aging state variable.

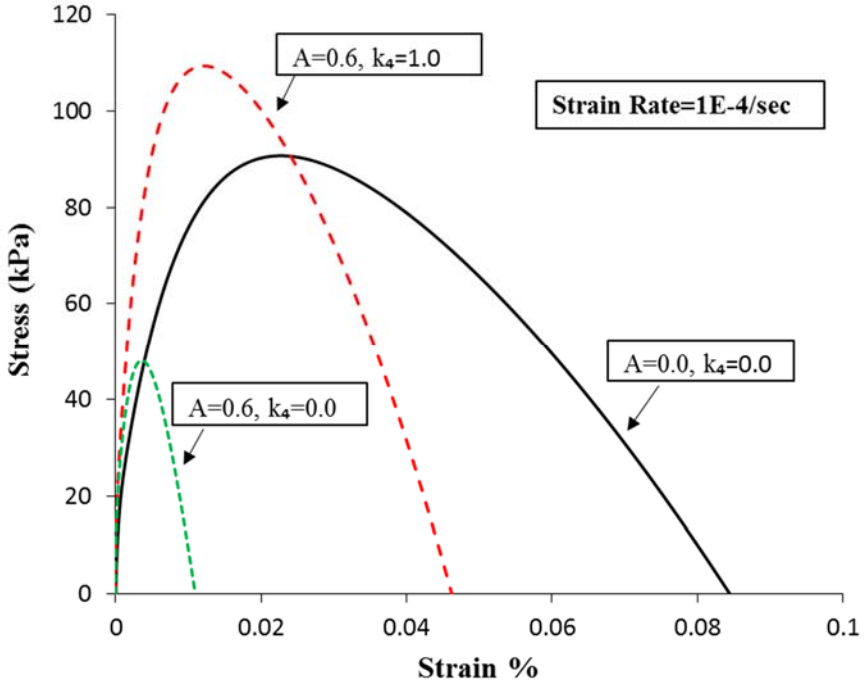

(a)

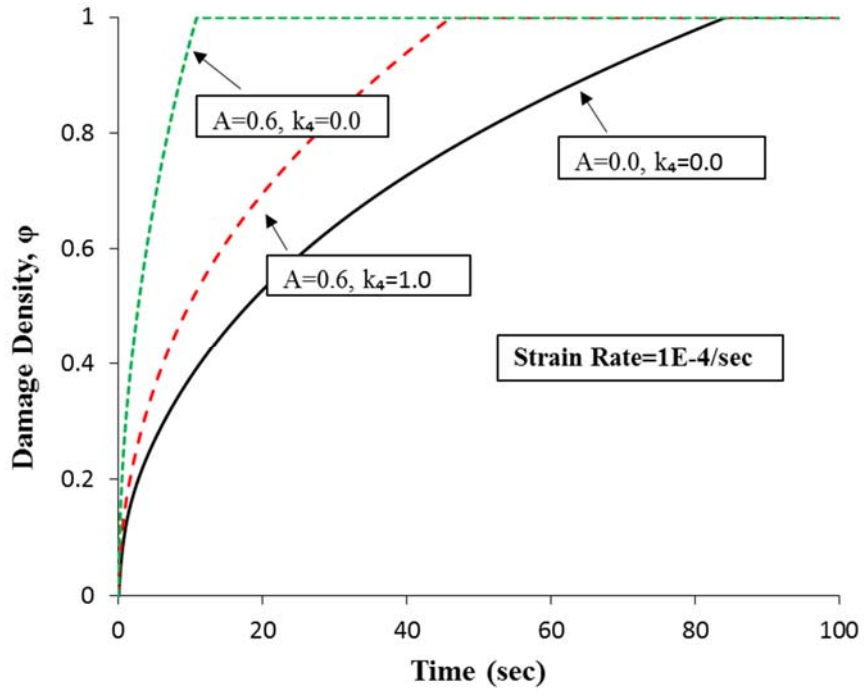

(b)

Figure 2.8. The comparison of viscodamage behavior of different cases to investigate the model parameters proposed in Eq. (2.33): (a) stress-strain diagrams and (b) evolution of damage density.

2.5 Conclusions

This section presented a framework for constitutive modeling of aged asphalt concrete. The oxidative aging constitutive relationship is based on the evolution of the aging state variable, which is a function of oxygen content and temperature. The effect of different material parameters on the rate of the aging state variable and the importance of each were outlined. In order to relate the oxidative aging effects to the mechanical response of asphalt concrete, the viscoelastic, viscoplastic, and viscodamage constitutive relationships were presented based on the continuum damage mechanics framework. Finally, the aging state variable is coupled to the fundamental viscoelastic properties of asphalt concrete, compliance terms, and retardation times. Relationships were proposed to express the aged transient compliance that is influenced by the degrading effects of oxidative aging, increased stiffness and viscosity. Some experimental observations were provided in this section to support the proposed phenomenological relationships.

The constitutive modeling framework and the flowchart of the tasks needed to be done in order to predict an aged asphalt concrete response is schematically illustrated in Figure 2.9.

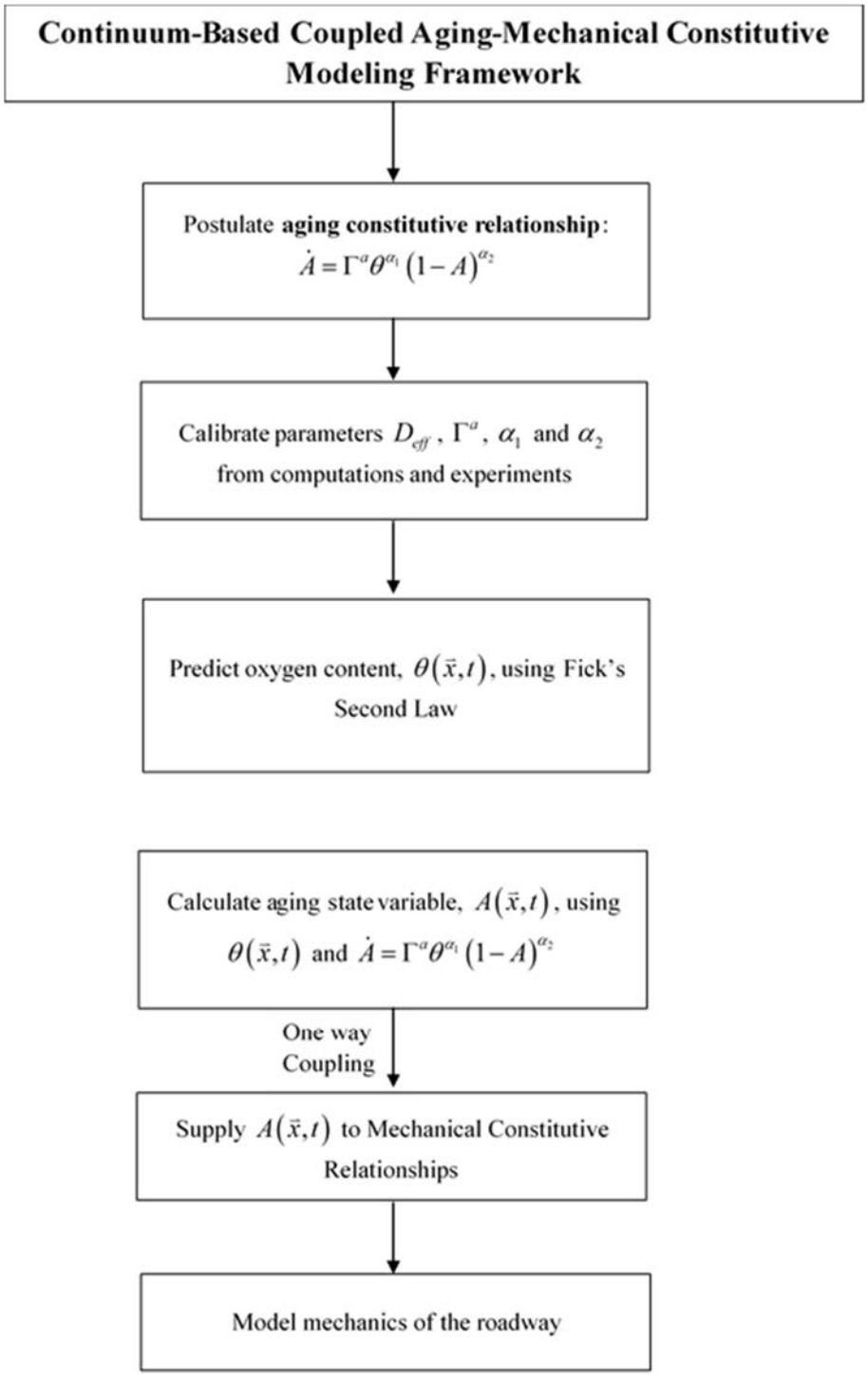

Figure 2.9. The flowchart of the framework of constitutive modeling of coupled aging-mechanical response of asphalt concrete.

3. MATERIALS AND EXPERIMENTS

3.1 Overview

This section covers the specification and properties of the material used to prepare asphalt mixture samples and laboratory testing methods. The results of the experimental test are used, first, to identify the material properties associated with the constitutive relationships presented in Section 2, and second, to validate the capability of the proposed framework to predict the coupled aging-mechanical response of the aged asphalt concrete. The laboratory experiments presented in this work are of mixture No.1 of the Asphalt Research Consortium (ARC) (http://www.arc.unr.edu/outreach.html). The procedures to identify the model parameters and model validations are described in Section 4.

3.2 Test Specimens

Cylindrical specimens were prepared in the laboratory using a Superpave Gyratory Compactor (SGC). The SGC was used to compact specimens that were 15.2 cm diameter by 17.8 cm height. These specimens were cored and cut to 10 cm diameter by 15.2 cm height. Specimens were compacted to have different percentages of air voids: 4.0 ±0.5%, 7.0 ±0.5%, and 10.0 ±0.5%. Limestone aggregate and binder PG 67-22 were used to prepare the test specimens. The aggregate blend includes 30% Type C rock, 36% Type F rock, 24% washed screening, and 10% manufactured sand. The nominal maximum aggregate size was 19.0 mm. Table 3.1 and Figure 3.1

summarize the sieve analysis and mixture gradation. Two replicates were tested for each condition. The hot-mix asphalt specimens in this study were prepared following AASHTO TP4/T312 (2007) procedures, and mixtures were subjected to short-term aging in the oven for two hours prior to compaction.

Table 3.1. Limestone mixture gradation.

Aggregate Type	Limestone Type C	Limestone Type F	Limestone Washed Screening	Manufactured Sand	Combined Gradation
Individual Percent	30%	36%	24%	10%	
Sieve Size: (mm)	Cumulative Percent Passing	Cumulative Percent Passing	Cumulative Percent Passing	Cumulative Percent Passing	Cumulative Percent Passing
25	100	100	100	100	100
19	98.7	100	100	100	99.6
9.5	21.5	93	100	100	74
4.75	3.4	65.3	99.4	97.4	58.1
2.36	1.4	29	74.8	85.3	37.3
0.6	1.3	8.9	40	64.5	19.7
0.3	1.3	3.8	20	15	8.1
0.075	1	3.6	3.6	2.5	2.8

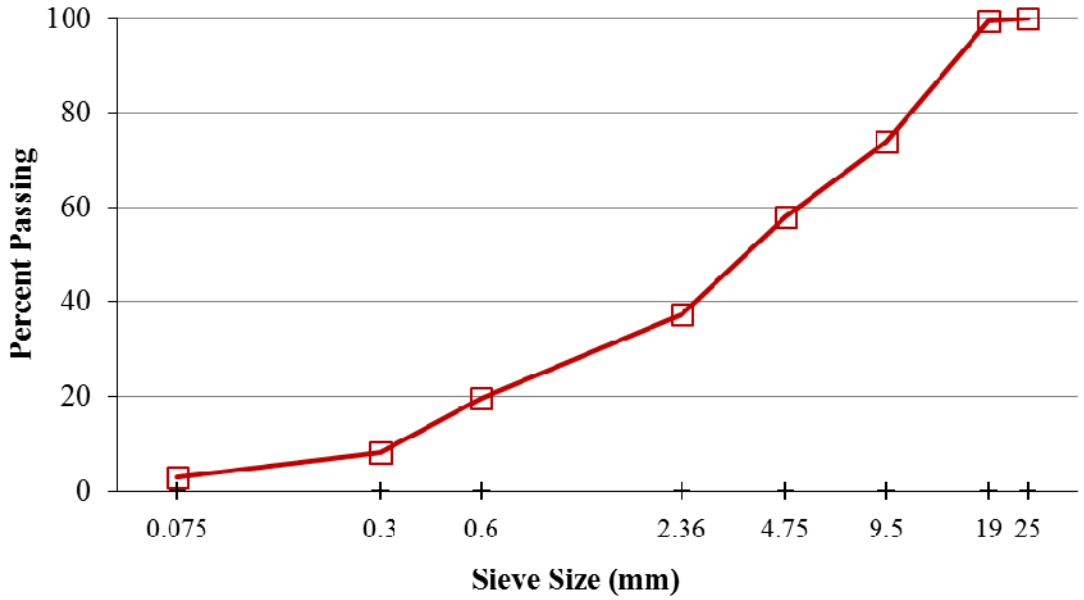

Figure 3.1. Sieve analysis of limestone aggregate used in the asphalt mixture.

3.3 Aging Conditioning

In order to simulate the long-term aging that occurs in asphalt pavement's service life, some asphalt mixture specimens were aged in a storage room at a temperature of $60^{\circ}C$ and atmospheric pressure. These specimens were aged for 3 months and 6 months. Other samples were stored at regular room temperature to represent unaged conditions. Figure 3.2 shows examples of unaged, 3-month aged, and 6-month aged specimens. Walubita et al. (2006a) have shown that 6-month laboratory aging conditioning at $60^{\circ}C$ simulates approximately up to 12 years of Texas field aging at a critical pavement service temperature.

No aging **3-month aging** **6-month aging**

Figure 3.2. Different aging conditionings on asphalt mixture samples to investigate the long-term aging effects on asphalt concrete.

3.4 Mechanical Tests

3.4.1 Dynamic Modulus Test

The dynamic modulus test results are used primarily to identify the linear viscoelastic parameters, including the Prony series coefficients and time-temperature shift factors. This test is conducted in accordance with the AASHTO TP-62 (2007). Based on that, the dynamic modulus test is conducted at five different temperatures (−10°C, 4.4°C, 21.1°C, 37.8°C, and 54.4°C), and six loading frequencies (0.1, 0.5, 1.0, 5.0, 10.0, and 25.0 Hz) at each temperature. A sinusoidal loading is applied and adjusted to obtain axial strain between 80 to 110 microstrain to ensure that the material does not get damaged and the response remains within the linear region. Testing starts from the

lowest to highest temperature and from highest to lowest frequency. The applied stress and recorded strain are used to calculate the dynamic modulus and phase angle. The secondary usage of the dynamic modulus test results is to obtain the aging state variable out of the recorded data for the aged specimens.

3.4.2 Repeated Creep-Recovery Test at Variable Stress Levels

The repeated creep-recovery test at variable stress levels (RCRT-VS) is used first to identify the nonlinear viscoelastic parameters and viscoplastic parameters of unaged asphalt concrete, and second to validate the predictive capabilities of the aging constitutive relationship. The test consists of several loading blocks depending on the test temperature. Each loading block includes eight creep-recovery cycles with increasing applied stress levels. The loading and unloading times of each loading cycle remain constant through the entire test. The loading time is 0.4 sec followed by the unloading time of 30 sec. The applied stress of the first loading cycle of the first loading block is 140 kPa, and it increases by a factor of 1.2^{n-1}, where n is the number of loading cycles in a specific loading block, for the next loading cycles until the eighth loading cycle. The first stress level of the subsequent loading block equals the third stress level in the previous loading block, and it increases by the same factor for the next loading cycles until the eighth loading cycle of that loading block. A constant confinement pressure can be applied during the RCRT-VS. Figure 3.3 shows an example of the first three loading blocks of the RCRT-VS.

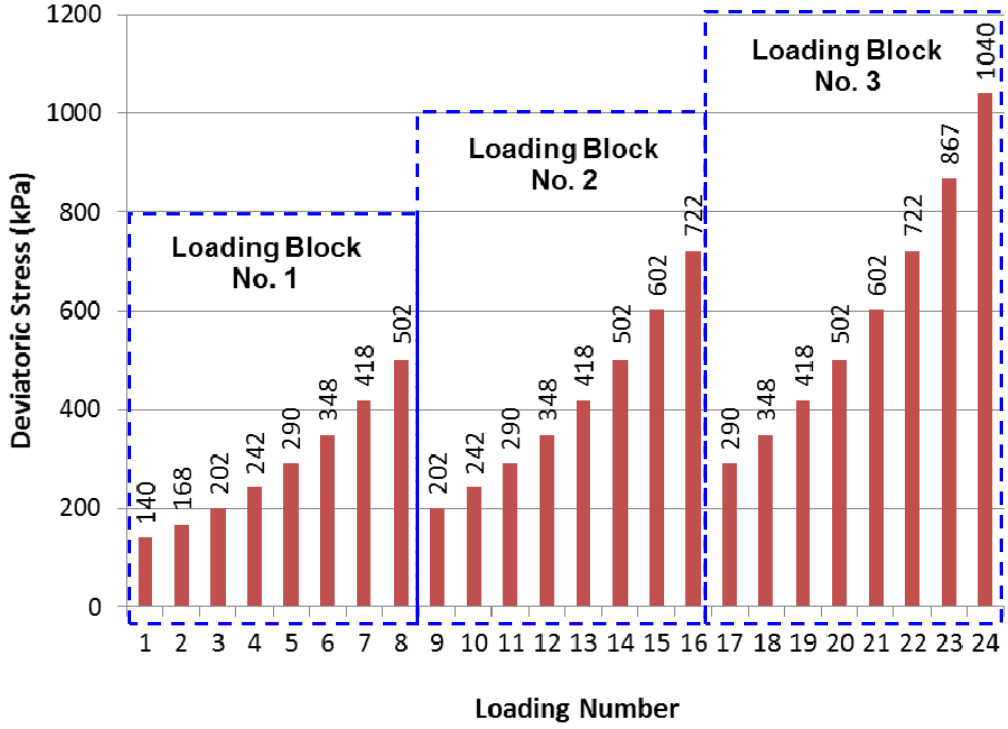

Figure 3.3. Applied axial stresses in the first three loading blocks during repeated creep-recovery test with variable stress levels.

In this test, three axial and three radial linear variable differential transformers (LVDTs) are spaced at 120° from each other to record the axial and radial strain responses. Figure 3.4 represents the experimental testing setup.

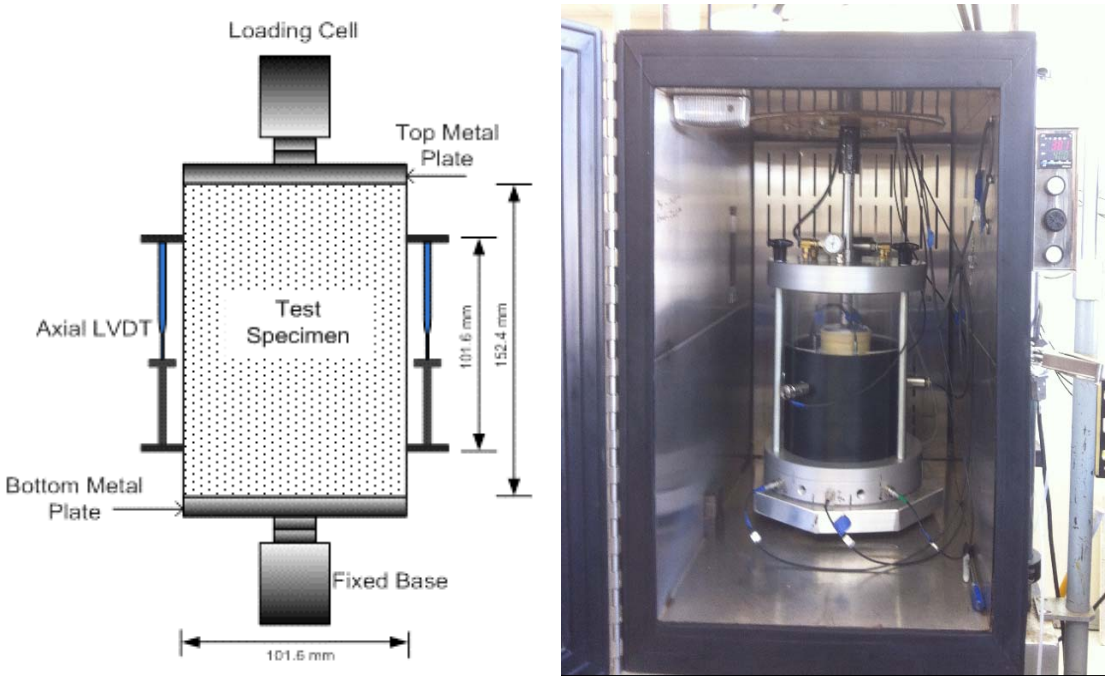

(a) (b)

Figure 3.4. Experimental testing setup for the RCRT-VS, including (a) schematic view of the test specimen with mounted axial LVDTs and (b) triaxial cell equipped with radial LVDTs inside the environmental chamber (Rahmani et al., 2013).

3.4.3 Repeated Creep-Recovery Test with Variable Resting Time

The repeated creep-recovery test with variable resting time (RCRT-VRT) is used to identify the parameters associated with the micro-damage healing constitutive relationship. This test is conducted at a temperature of 19°C. Similar to the RCRT-VS, this test also includes several loading blocks. The applied stress level and the loading time remain constant during the entire test; however, the resting time varies. The resting time starts with 0.9 sec at the first loading cycle and increases by a factor of 1.2^{n-1}, where n is the number of the loading cycle. When the rest period becomes too long

(i.e., longer that 30 sec), the rest period is reset to 0.9 sec and the block of the repeated creep-recovery is repeated. The schematic of the applied stress history is shown in Figure 3.5.

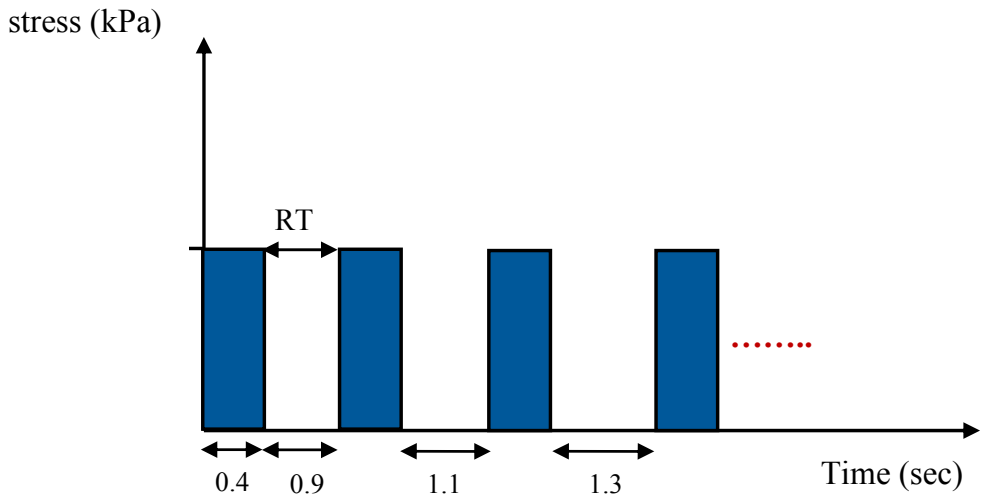

Figure 3.5. Schematic representation of the stress input for the RCRT-VRT. The loading time remains constant through the entire test, whereas the resting time (RT) changes for each loading cycle.

3.4.4 Uniaxial Constant Strain Rate Test

The uniaxial constant strain rate (UCSR) test is conducted primarily for calibration of the viscodamage constitutive relationship, and to validate the presented chemo-mechanical constitutive modeling framework. In this test, a constant uniaxial strain rate is applied to test specimens in tension or compression until failure. In order to

fully calibrate the viscodamage parameters, the UCSR test should be done at different strain rates. In this study, 5×10^{-6}, 1×10^{-5}, and $5\times10^{-5}/\sec$ are used.

3.4.5 Cyclic Displacement-Controlled Test

The cyclic displacement-controlled (CDC) test is used to validate the capabilities of the coupled aging-mechanical constitutive relationship in predicting the fatigue performance of the aged asphalt concrete specimens. In the CDC test a cyclic sinusoidal displacement is applied to the end plates that are glued to the specimen. The application of the loading cycles continues until the specimen fails. There are three LVDTs mounted on the on-specimen strain. Although the amplitude of the cyclic applied displacement at the end plates is constant, the strain response recorded in the middle of the specimen does not have a constant amplitude. Figure 3.6 shows the schematic representation of the CDC test.

3.5 Summary

The material description and the experimental tests required for calibration and validation of the coupled aging-mechanical constitutive relationship were outlined in this section. Dynamic modulus test, repeated creep-recovery test at variable stress levels at 55°C, uniaxial strain rate test, and repeated creep-recovery test with variable resting time are used for calibration; and repeated creep-recovery test at variable stress level at 19 and 40°C and cyclic displacement-controlled test at 5°C and 19°C are used for validation purposes. The calibration and validation procedures are covered in the next two sections.

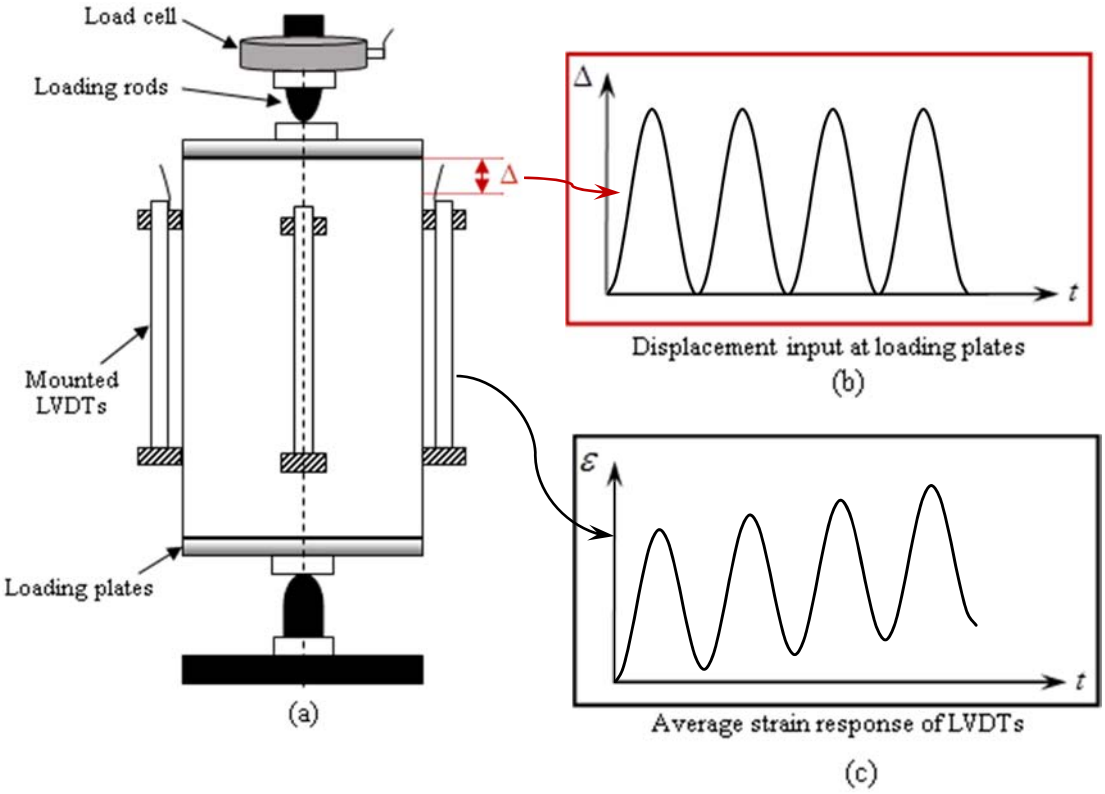

Figure 3.6. Schematic representation of the cyclic displacement-controlled test, including (a) the testing machine apparatus, (b) cyclic displacement input at the end plates at a given frequency and fixed amplitude, and (c) averaged strain response measured at the LVDTs. The frequency of the strain response is almost the same as the frequency of the applied cyclic displacement. However, the strain amplitude changes during each loading cycle.

4. CALIBRATION OF THE COUPLED AGING-MECHANICAL CONSTITUTIVE RELATIONSHIP*

4.1 Overview

This section covers the procedure and methods to identify the material properties using a set of laboratory tests conducted on asphalt mixtures that were described in the previous section. First, the process to obtain the material parameters associated with the oxidative aging constitutive relationship is described. Second, the nonlinear viscoelastic, viscoplastic, viscodamage, and micro-damage healing constitutive relationships are characterized. Table 4.1 lists the summary of the tests for calibration of the framework.

4.2 Calibration of the Oxidative Aging Constitutive Relationship

The principal material parameters that are required to calibrate the oxidative aging constitutive relationship are the aging fluidity parameter, Γ^a, and the temperature dependency parameter, α_3. It is noted that in order to obtain the temperature-dependency parameter, the aging conditioning discussed in Subsection 3.3 has to be conducted at least at two different temperatures. However, in this work, the asphalt concrete samples are aged only at 60°C; therefore, the investigation on the thermal

* Part of this section is reprinted with permission from "Effect of confinement pressure on the nonlinear-viscoelastic response of asphalt concrete at high temperatures" by Rahmani, E., Darabi, M.K., Abu Al-Rub, R.K., Kassem, E., Masad, E.A., Little, D.N., Construction and Building Materials, Volume 47, October 2013, Pages 779–788, Copyright 2013 Elsevier.

coupling term is a subject for future study. On the other hand, two steps have to be taken to identify the aging fluidity parameter, Γ^a. At the first step, the oxygen content at different ages should be calculated, and at the second step the aging state variable, A, at least at two different ages must be characterized. In order to estimate the oxygen content at different ages, the effective oxygen diffusivity of the material should be calculated. Below, these two steps to identify the aging fluidity parameter are discussed.

Table 4.1. The summary of the tests used to calibrate the material parameters.

	Procedure	***Loading Mode***	***Temperature (°C)***	***Aging Condition***	***Loading Level***
Oxidative Aging					
	Dynamic Module Test	Tension/ Compression	Varies	0, 3, 6 months	Varies
	Finite Element Method	Diffusion	Varies	Varies	-
Linear Viscoelasticity					
	Dynamic Modulus Test	Compression	Varies	Unaged	Varies
Nonlinear Viscoelasticity					
	Repeated Creep-Recovery (RCRT-VS)	Compression	19, 40, 55	Unaged	138 to 2500 (kPa)
Viscoplasticity					
	Repeated Creep-Recovery (RCRT-VS)	Compression	55	Unaged	138 to 2500 (kPa)
Viscodamage					
	Uniaxial Constant Strain Rate Test	Tension	5	Unaged	1E-5, 5E-5, 5E-6 (1/sec)
Micro-damage Healing					
	Repeated Creep-Recovery (RCRT-VRT)	Tension	19	Unaged	620 (kPa)

4.2.1 Calculation of the Effective Oxygen Diffusivity of Asphalt Concrete

In order to identify an effective property of a composite material (such as asphalt concrete, being composed of asphalt binder, aggregates, and air voids), a homogenization problem needs to be solved. In fact, the objective of the homogenization is to predict an effective property equivalent to a hypothetical simple homogeneous material with a single phase that at the same condition responds the same way as the composite material. The solution of a homogenization problem can take different forms. Analytical measures, divided into direct approaches and rigorous bounds, computational methods, and laboratory tests are the ways to calculate effective properties of a composite material.

Most of the analytical models are based on the basic models. Parallel and Series models are the simplest ones to consider two-phase composite systems with known volume fractions of components (Guild, 1990; Wong and Bollampally, 1999). In more general cases of randomly distributed particles in a medium, several other models have been proposed (Beran, 1965; Hashin and Shtrikman, 1962; Jeffrey, 1973; McCoy, 1976). Another common practice to estimate effective properties of composites, especially when dealing with complex microstructures, is to find upper and lower bounds or the range of solutions. One of the basic models was developed by Hashin and Shtrikman (1962) based on a variational approach; researchers then contributed to improve and develop new models to cover more general cases (Gibiansky and Milton, 1993; Lado and Torquato, 1986; Miller and Torquato, 1990; Weissberg, 1963).

Although these analytical models are low-cost and easy-to-use methods, they are inherently limited. Most of these models are based on simplified physical assumptions that restrict their application. Moreover, they mostly deal with simple structural models, so that their performances are questionable when dealing with more complicated structures. Furthermore, in a composite structure with high contrast of components' properties, the capability of the rigorous bounds significantly reduces.

On the other hand, numerical methods and computational approaches have been able to overcome some of these limitations associated with the analytical models. Generally in computational methods, first the microstructure of the composite material is constructed and then related governing equations are solved using computer-aided algorithms. To name a few, Adams and Crane (1984), Povirk (1995), and Zhang and Evans (1988) used unit cell models, and Sun and Vaidya (1996), Kanit et al. (2003), and Gusev (1997) used representative volume element to identify different effective properties of various composite structures.

In this work, the effective diffusivity of asphalt concrete is calculated by solving a diffusion problem using finite element simulations on the realistic microstructures constructed by X-ray computed tomography images. Asphalt concrete is viewed as a composite structure containing asphalt binder, aggregates, and air voids. In the case of oxygen diffusion, constituents of asphalt concrete exhibit either super diffusible (air voids) or indiffusible (aggregates) behavior. The microstructural models adopted for this work do not include connected air void pores. Thus, the only mechanism for oxygen transport into the pavement is by diffusion from the outside boundaries to the interior. In

most of the simulations, it is assumed that the diffusion occurs only from the top surface of the pavement. In this regard, a single diffusion coefficient, an effective or average diffusion coefficient, needs to be calculated and used uniformly throughout the asphalt concrete. Furthermore, this model does not include the consumption of oxygen throughout the pavement by reaction with asphalt. Therefore, these model calculations provide a starkly different representation of oxygen content in the pavement, as a function of time and depth, from that which is obtained from models of oxygen transport and reaction in pavements previously presented by Prapaitrakul et al. (2009), Jin et al. (2013), and Glover et al. (2014).

The procedure to construct the realistic microstructures is discussed in Section 6. In order to calculate the effective oxygen diffusivity of asphalt concrete, both two-dimensional (2D) and three-dimensional microstructures are considered for analysis. Figure 4.1 and Figure 4.2 represent the 2D and 3D RVEs of microstructures along with their components, respectively.

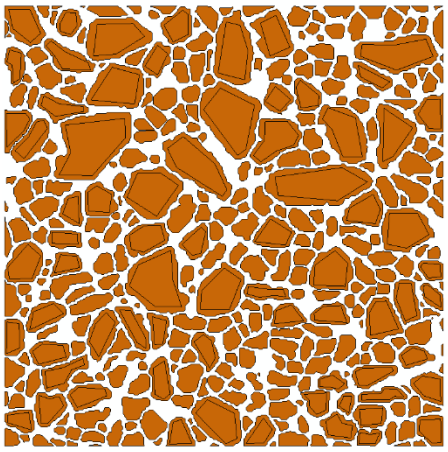

Aggregates

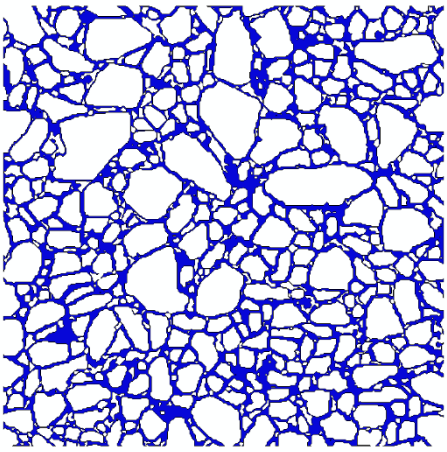

Matrix

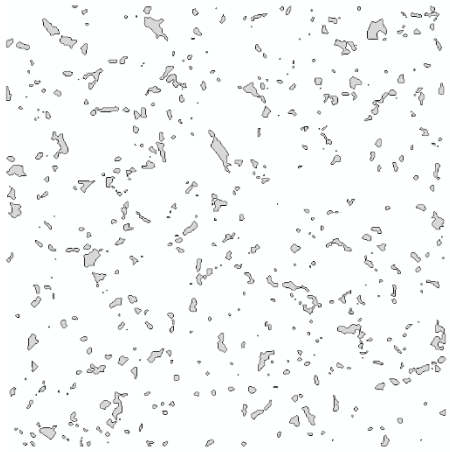

Air voids

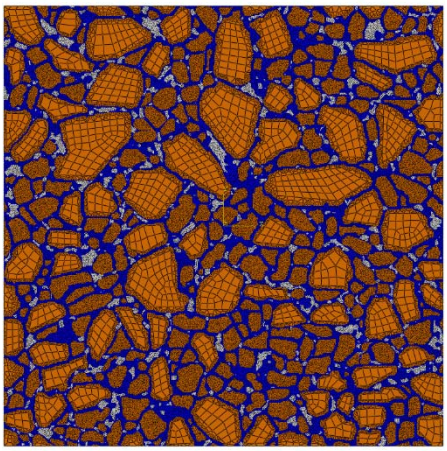

Finite element mesh

Figure 4.1. Two-dimensional asphalt concrete microstructure created by an X-ray image for diffusion analysis to calculate the effective oxygen diffusion coefficient. The microstructure includes the air void, aggregate, and matrix phases.

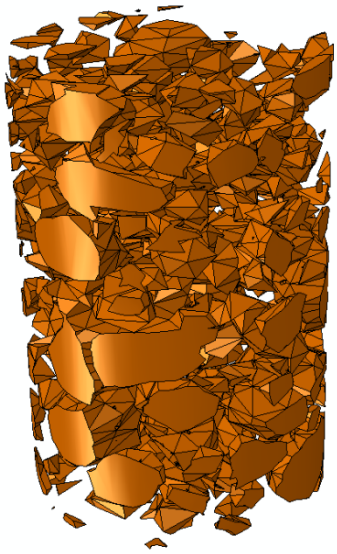

Aggregates

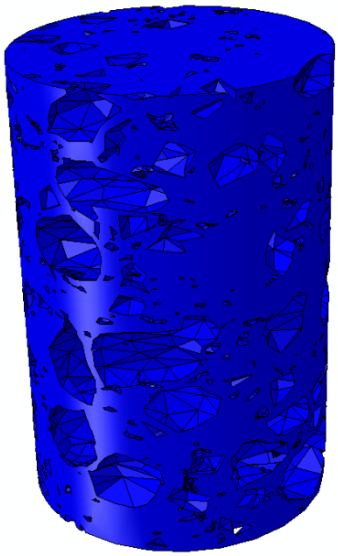

Matrix

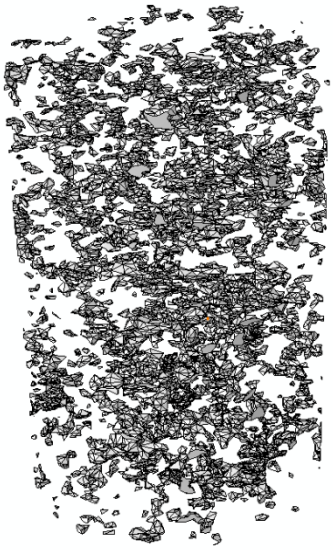

Air voids

Finite element mesh

Figure 4.2. Three-dimensional asphalt concrete microstructure created by the sliced X-ray images for diffusion analysis to calculate the effective oxygen diffusion coefficient. The microstructure includes the air void, aggregate, and matrix phases.

The determination of the effective oxygen diffusivity of asphalt concrete requires the knowledge of the oxygen content at every structural local point. The governing equation of the one-dimensional non-steady diffusion is described by partial differential equation of Fick's second law as:

$$\frac{\partial \theta}{\partial t} = D_{eff} \frac{\partial^2 \theta}{\partial x^2} \tag{4.1}$$

where θ is oxygen content, and D_{eff} is the effective oxygen diffusivity of the composite microstructure assumed to be independent of the spatial coordinates. It is understood that using Fick's second law to calculate oxygen content is an approximation in that it does not account for the reaction term, which is the case in the oxygen transport phenomenon. Such an approximation could be improved by employing more accurate transport models that take into account both diffusion and reaction terms in the oxygen transport problem. However, this has not been done in this study because the focus of the current research is on predicting the effect of aging on mechanical properties. Oxygen in the ambient air and in the interconnected air voids diffuses into the asphalt matrix and therefore reacts with binder. As oxygen diffuses into the binder, the rate of diffusion decreases due to the hardening induced by chemical reactions and consumption of oxygen. The reduction in diffusion rate results in decreasing of the rate of age hardening. Despite the assumption of constant oxygen diffusivity in this study, the decreasing rate of age hardening is indirectly described by introducing the aging history term in the aging constitutive relationship as described in subsection 2.2.3.

The equivalent weak form of Eq. (4.1) can be written as follows:

$$\int_V \delta\phi\left(\frac{d\theta}{dt}+\frac{\partial}{\partial x}.\mathrm{J}\right)dV=0 \tag{4.2}$$

where $\delta\phi$ is an arbitrary scalar field, $\mathbf{J}$ is the flux of oxygen concentration that is given by $\mathbf{J}=-D_{eff}\,\partial\theta/\partial x$, and V is any volume whose surface is S. Using the divergence theorem, Eq. (4.2) is rewritten such that:

$$\int_V\left[\delta\phi\left(\frac{d\theta}{dt}\right)-\frac{\partial\delta\phi}{\partial x}.\mathbf{J}\right]dV+\int_S\delta\phi\,\mathbf{n}.\mathbf{J}\,dS=0 \tag{4.3}$$

where $\mathbf{n}$ is the outward normal to S. To obtain the oxygen content profile at any local point of the microstructure, Eq. (4.3) is solved using the commercial finite element software, Abaqus FEA, utilizing the backward Euler method. The proper boundary conditions should be applied to the microstructure to solve the above equation. A unit oxygen content is introduced only on the top boundary and oxygen transport is assumed to be derived by concentration gradient. As previously mentioned, the only mechanism accounted for in these simulations for oxygen transport into the asphalt concrete microstructure is diffusion from the top surface. Therefore, a single diffusion coefficient, an effective or average diffusion coefficient, is assumed and used uniformly throughout the microstructure. As discussed earlier, the consumption of oxygen throughout the asphalt concrete by reaction with asphalt is not included. Following these assumptions, the initial oxygen content within the RVE is zero, and no concentration flux at the opposite surface is assumed, such that:

$$\theta(0,x)=0,\quad \theta(t,l)=1,\quad \frac{d\theta}{dx}(t,0)=0 \tag{4.4}$$

where l is the vertical length of the microstructure, and x is measured from the bottom surface opposite side of the oxygen source. Given these boundary conditions, oxygen flow is introduced to the top surface of the asphalt concrete microstructure. However, the model can be easily used to conduct simulations using oxygen flow from different and multiple sides.

Once the appropriate initial and boundary conditions are applied, the diffusivity of each component of asphalt concrete microstructure should be assigned. As previously stated, the aggregates can be assumed to be the indiffusible matters, whereas the air voids are super diffusible. The appropriate oxygen diffusion coefficient of the asphalt binder can be achieved by either direct experiments or available empirical relationships. In this study, due to unavailability of such experimental data for the specific asphalt binder used in this work, the oxygen diffusivity of binder is estimated using the following equation that relates the viscosity and temperature to the diffusion coefficient (Herrington, 2012), such that:

$$\log D = -12.3083 - 0.3351\left(\log \eta\right) + \log(RT) \tag{4.5}$$

where D is oxygen diffusivity $\left(m^2 s^{-1}\right)$, η is the binder viscosity $(Pa\ s)$, R is the ideal gas constant $\left(8.3143 JK^{-1}mol^{-1}\right)$, and T is the temperature in Kelvin. Consequently, the proper viscosity of the asphalt binder can be estimated using "A-VTS relationship" described by ASTM D 2493-01 (2009):

$$\log\log(\eta) = \begin{cases} A + VTS\log\left(T_R\right) & T_R > T_c \\ 2.7\times10^{12} & T_R \le T_c \end{cases} \tag{4.6}$$

where η is the viscosity (cP); A and VTS are the intercept and slope of the temperature susceptibility relationship, respectively; T_R is the temperature in Rankine; and T_c is the temperature in Rankine at which the viscosity is equal to $2.7\times10^{12}\,cP$. It is noted that Eq. (4.5) simply expresses the binder diffusivity in terms of binder viscosity and temperature. However, to better estimate the binder diffusion coefficient that takes into account the reaction terms, more accurate relationships can be used (Han et al., 2013).

Figure 4.3 and Figure 4.4 demonstrate the results of the diffusion analysis showing the normalized oxygen content distribution at different ages at 5°C, at which oxidative aging occurs at relatively smaller rates. Hence, it is rational for oxygen to require a significantly long time to reach the very bottom surface of the RVE. The vertical length of the 2D and 3D RVEs are 71 mm and 75 mm, respectively.

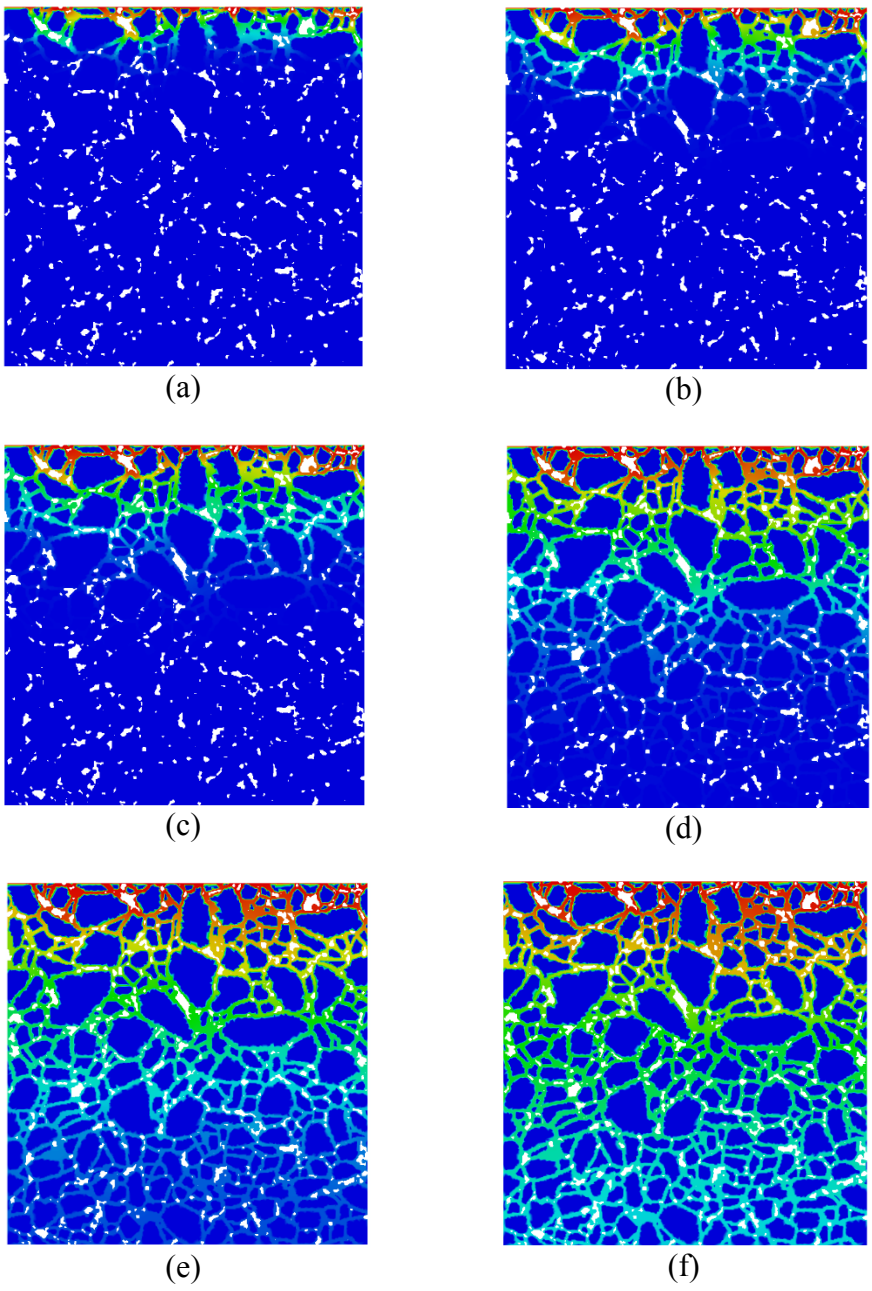

Figure 4.3. Two-dimensional oxygen diffusion analysis of asphalt concrete, showing the normalized oxygen concentration inside the asphalt concrete RVE for (a) 6 months, (b) 2 years, (c) 8 years, (d) 16 years, (e) 32 years, and (f) 55 years. Red color corresponds to the concentration equal to unity, and blue color is zero concentration. These simulations are based on several assumption: unit oxygen content on the top surface only, no oxygen transport by convection through air voids, and no oxygen consumption by reaction throughout the specimen; more information about these assumptions are given in subsection 4.2.1.

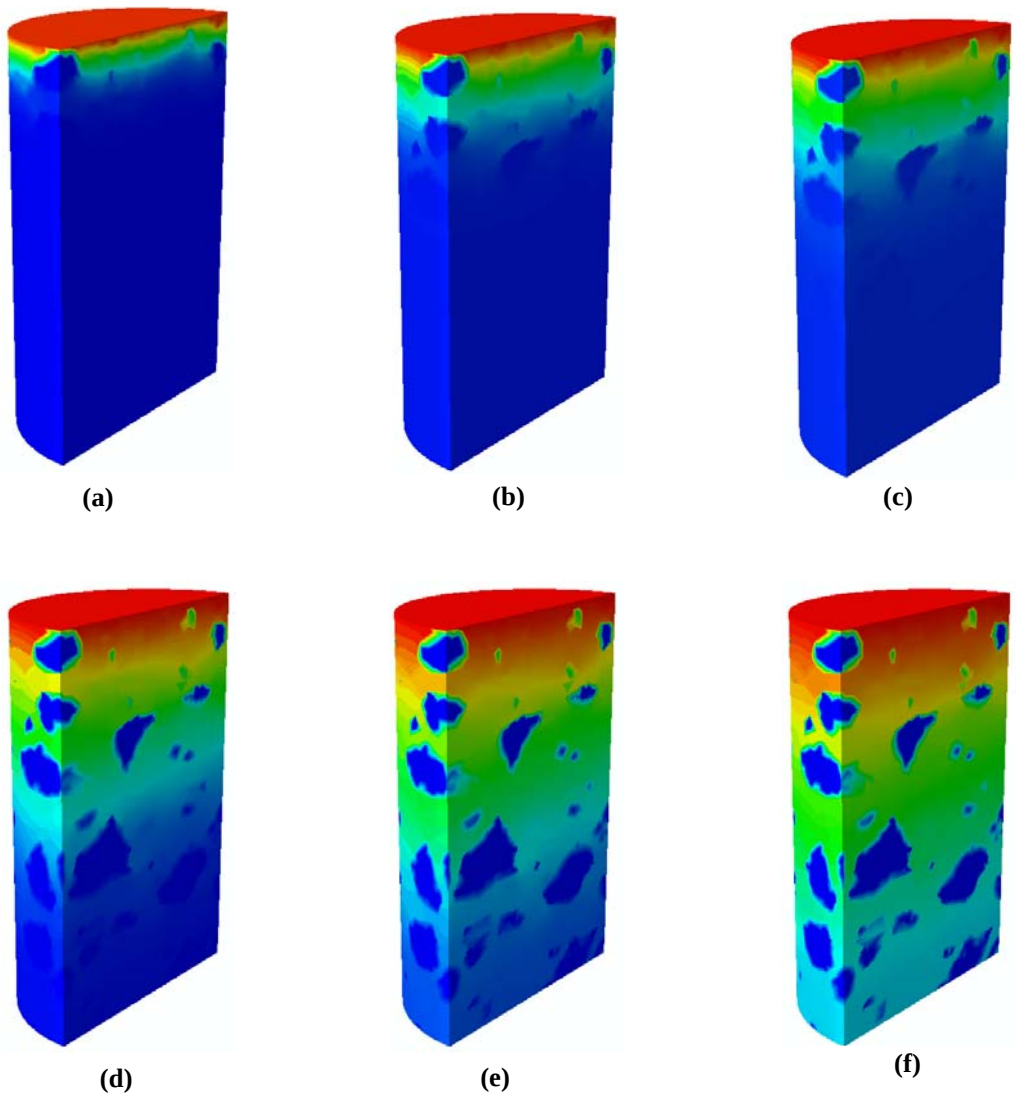

Figure 4.4. Three-dimensional oxygen diffusion analysis of asphalt concrete, showing the normalized oxygen concentration inside the asphalt concrete RVE for (a) 6 months, (b) 2 years, (c) 8 years, (d) 16 years, (e) 32 years, and (f) 55 years. Red color corresponds to the concentration equal to unity, and blue color is zero concentration. These simulations are based on several assumption: unit oxygen content on the top surface only, no oxygen transport by convection through air voids, and no oxygen consumption by reaction throughout the specimen; more information about these assumptions are given in subsection 4.2.1.

The effective oxygen diffusivity of the RVEs can now be calculated by fitting the simulation results to the closed-form solution of Eq. (4.1) with the boundary conditions expressed in Eq. (4.4). The analytical solution in this case reads (Carslaw, 1959):

$$\theta(t,x) = \sum_{n=0}^{\infty} (-1)^n \, erfc \frac{(2n+1)l - x}{2\sqrt{D_{eff} t}} + \sum_{n=0}^{\infty} (-1)^n \, erfc \frac{(2n+1)l + x}{2\sqrt{D_{eff} t}} \tag{4.7}$$

where t is the elapsed time since diffusion starts, n is the number of terms, and $erfc(Y)$ is the complementary Gaussian error function expressed as:

$$erfc(Y) = \frac{1}{\sqrt{\pi}} \int_0^Y \exp\left(-v^2\right) dv \tag{4.8}$$

Eq. (4.7) expresses the oxygen content at any specific time and location within the RVE. In fact, by fitting the simulation results to this equation, one can obtain the effective oxygen diffusivity at any x. Then, the effective diffusivity of the material is the average of the values obtained at different surface layers of the RVE. Figure 4.5 shows the normalized oxygen content obtained by finite element simulations of the 3D RVE and the analytical solution for different x, and with respect to aging time. The value of the effective diffusivity used in the analytical solution is the average diffusivity within the whole structure.

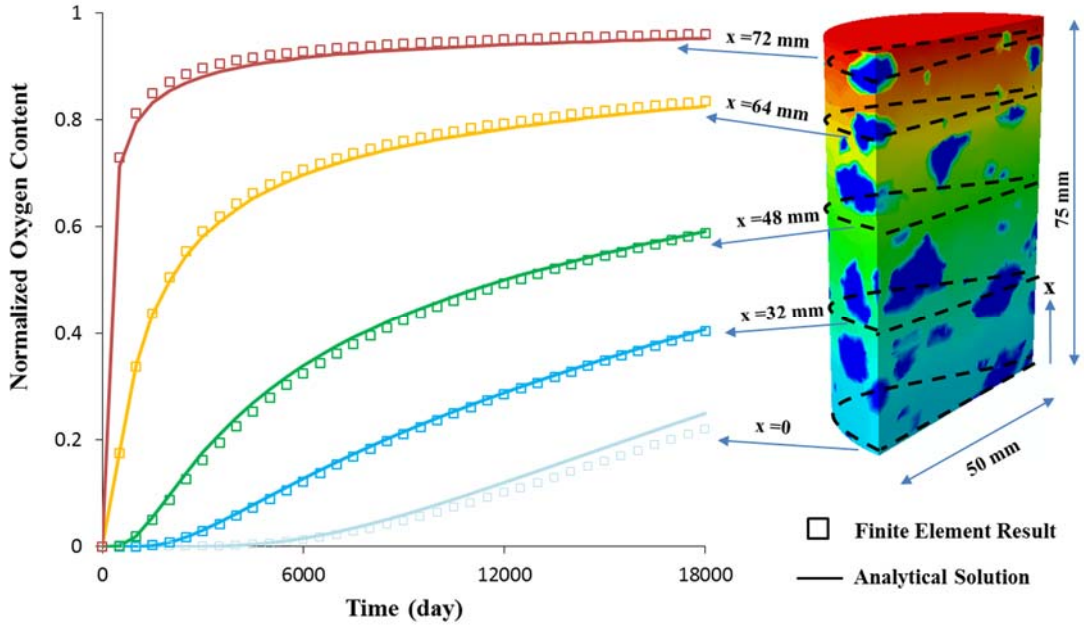

Figure 4.5. The average normalized oxygen content at different microstructural surfaces compared to the analytical solution. The effective oxygen diffusivity of the RVE is calculated by averaging the diffusivities obtained at each layer within the RVE. These simulations are based on several assumption: unit oxygen content on the top surface only, no oxygen transport by convection through air voids, and no oxygen consumption by reaction throughout the specimen; more information about these assumptions are given in subsection 4.2.1.

Table 4.2 summarizes the oxygen diffusivities of asphalt mixture and its components used in this study at 5°C. The comparison of the 2D and 3D RVEs indicates that the asphalt concrete in the 3D microstructure is 20% more diffusible than the asphalt concrete in the 2D case. In fact, this observation is quite valid, since the diffusing phase (oxygen) can freely pace the path length from the oxygen source to the bottom, whereas, in the 2D RVE the diffusing phase is restricted to only two dimensions. In other words, the 2D asphalt concrete microstructure is more tortuous than results in smaller effective diffusivity.

Table 4.2. Oxygen diffusivities for different phases of asphalt concrete and the effective diffusivity resulted by finite element simulations of 2D and 3D asphalt concrete microstructures.

	Oxygen diffusivity (mm^2/day) at 5°C		
Component	2D	3D	Volume fraction (%)
Asphalt binder	0.1218	0.1218	10.5
Aggregate	10^{-10}	10^{-10}	82
Air void	10^{5}	10^{5}	7.5
Asphalt mixture	0.0527	0.0630	-

4.2.2 Identification of the Aging State Variable

It was previously stated that to obtain the aging fluidity parameter, the aging state variable has to be known at least at two different ages. In order to achieve this, dynamic modulus test results are used. The procedure to perform the dynamic modulus test was described in Subsection 3.4.1. In the case of the air void percentage, three asphalt concretes were considered: 4%, 7%, and 10%. In the case of aging time, unaged, 3-month aged, and 6-month aged asphalt concretes were used. First, the master curves of dynamic modulus of these asphalt concrete samples are constructed. A sigmoidal-type fitting function is used in this work to create the master curves. Figure 4.6 represents the constructed master curves corresponding to the specified asphalt concrete specimens.

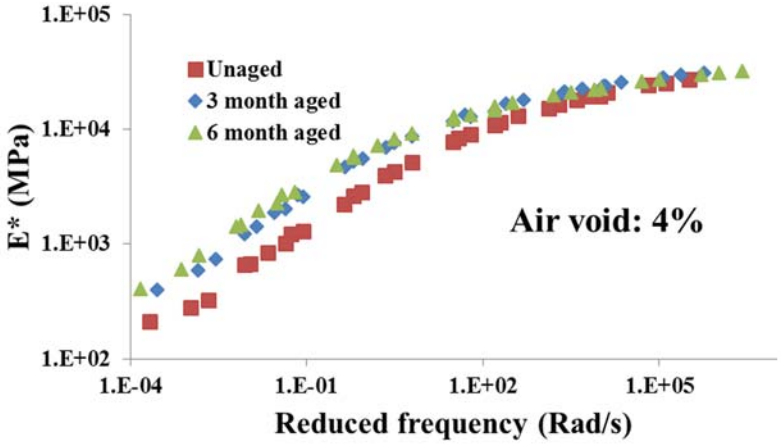

(a)

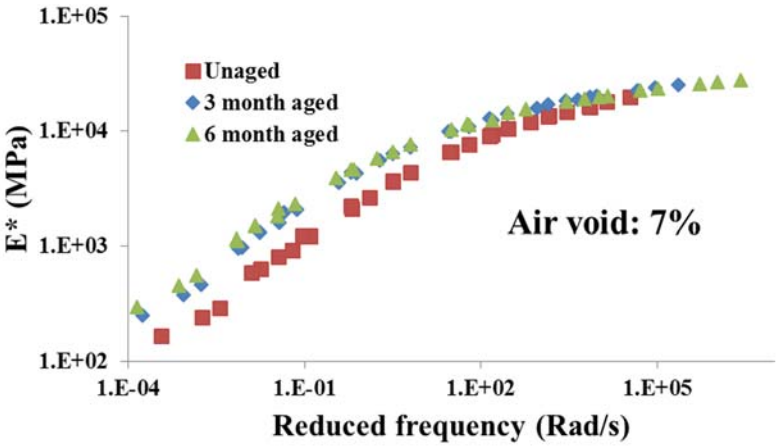

(b)

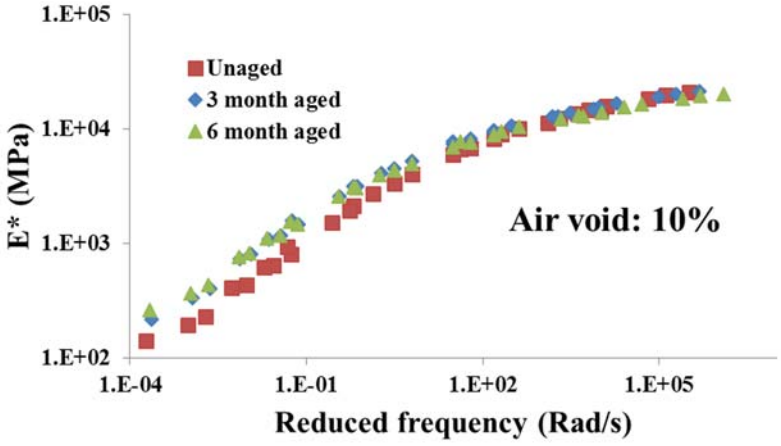

(c)

Figure 4.6. The dynamic modulus master curves for unaged, 3-month aged, and 6-month aged asphalt concrete samples with (a) 4%, (b) 7%, and (c) 10% air void content. Oxidative aging increases the dynamic modulus specifically at lower frequencies and higher temperatures.

In general, it is observed that the dynamic modulus increases with aging for asphalt concretes with different air void contents. In particular, this increase is more significant at higher temperatures and lower frequencies.. Asphalt concrete shows more transient behavior at lower loading frequencies and higher temperatures. This suggests that oxidative aging mainly affects the viscous or transient behavior of asphalt concrete. In fact, this can be justified by the previous discussion of this work; at higher temperatures, the mobility of asphalt molecules increases, making it easier for oxygen to react with reactive components. On the other hand, the increase in dynamic modulus from unaged to 3-month aged samples is more significant than from 3-month aged to 6-month aged ones, thereby suggesting that the rate of change in dynamic modulus is faster at early ages and becomes slower with age.

Using the constructed master curves and phase angle data, the storage and loss compliances can be calculated as follows:

$$D'(\omega) = D^* \cos(\delta), \quad D''(\omega) = D^* \sin(\delta) \tag{4.9}$$

where D' and D'' are storage and loss compliances with respect to angular frequency, ω, and D^* is complex compliance, where $D^* = E^{*-1}$. The term δ is the phase angle. The storage and loss compliances are related to the Prony series coefficients as follows (Park and Schapery, 1999):

$$D'(\omega) = D_0 + \sum_{1}^{N} \frac{D_n}{(\omega / \lambda_n)^2 + 1} \tag{4.10}$$

$$D''(\omega) = \sum_{1}^{N} \frac{(D_n)(\omega/\lambda_n)}{(\omega/\lambda_n)^2 + 1} \tag{4.11}$$

Eq. (4.10) and Eq. (4.11) represent the properties of unaged materials. In order to rewrite them in terms of aged properties, the storage and loss compliances, as well as the Prony series coefficients, should be replaced by the unaged ones (i.e., $D'^{A}, D''^{A}, D_n^A,$ and λ_n^A). Then, using Eq. (2.29) and (2.30) one can write:

$$D'^{A}(\omega) = D_0 + \sum_{1}^{N} \frac{(1-A)^k D_n}{[\omega/(1-A)^k \lambda_n]^2 + 1} \tag{4.12}$$

$$D''^{A}(\omega) = \sum_{1}^{N} \frac{(1-A)^k D_n [\omega/(1-A)^k \lambda_n]}{[\omega/(1-A)^k \lambda_n]^2 + 1} \tag{4.13}$$

The above equations, in fact, relate the aged storage and loss compliances to the unaged Prony series coefficients using the aging state variable, A. The dynamic modulus test data provide all the parameters in Eq. (4.12) and Eq. (4.13), except the aging state variable and k_1 . For simplicity, k_1 is assumed to be equal to unity. The aging state variable can now be identified by minimizing the error between two sides of these equations using optimization techniques. On another case, when the aging state variable is known, these equations can be used to predict the dynamic modulus of the aged material using the unaged viscoelastic properties. Table 4.3 lists the identified aging state variable out of the dynamic modulus test results. It should be noted that Eq. (4.12) assumes the instantaneous compliance term, D_0, does not change with aging. In fact, the dynamic modulus test results verify the assumption, as shown in Figure 4.7.

Table 4.3. The identified aging state variable for asphalt concrete specimens with different air void contents using dynamic modulus test results.

Aging Time (month)	Air Void Percentage		
	4%	7%	10%
	Aging State Variable, *A*		
0	0.00	0.00	0.00
3	0.37	0.16	0.216
6	0.40	0.26	0.284

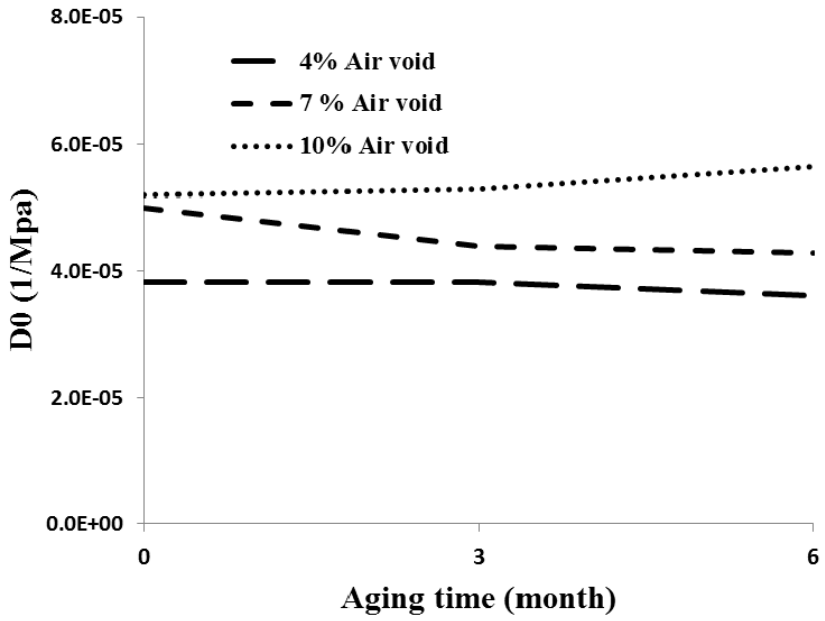

Figure 4.7. Variation of the instantaneous compliance with respect to aging time.

4.2.3 Identification of the Aging Fluidity Parameter, Γ^a

Once the aging state variable and the average oxygen content for 3-month and 6-month aged specimens are determined, the aging fluidity parameter can be estimated. For simplicity, the controlling parameters, α_1 and α_2, are assumed to be unity. By taking the integral of Eq. (2.2) and rearranging, one can write:

$$\int \frac{1}{(1-A)} dA = \Gamma^a \int \theta dt \tag{4.14}$$

In Eq. (4.14), the aging state variable and oxygen content are determined at two ages; therefore, the only unknown parameter is the aging fluidity parameter. Utilizing this approach, the aging fluidity parameter is estimated to equal 0.002375 1/day at 60°C.

4.3 Calibration of the Linear Viscoelastic Parameters

The objective of this subsection is to identify the Prony series coefficients and time-temperature shift factors. It was previously stated that the loading level in the dynamic modulus test is kept low, such that the material behaves in a linear viscoelastic range. Therefore, the dynamic modulus test data are used to calibrate the appropriate linear viscoelastic parameters. The master curve is constructed using a sigmoidal-type fitting function as (Pellinen et al., 2004):

$$Log\left|E^*\right| = \delta' + \frac{\alpha'}{1+\exp\left(\beta' + \gamma' \log \xi\right)} \tag{4.15}$$

where E^* is the dynamic modulus, δ' is the minimum value of E^*, $\delta' + \alpha'$ is the maximum value of E^*, β' and γ' are parameters describing the shape of the sigmoidal function, and ξ is the reduced frequency defined as:

$$\log \zeta = \log \omega + \log a_T \tag{4.16}$$

where a_T is the time-temperature shift factor. Time-temperature shift factor is calculated by shifting the dynamic modulus curves at each temperature horizontally with respect to a reference temperature, such that the resultant curve forms the sigmoidal function in Eq. (4.15). The identified values of time-temperature shift factor at each temperature are listed in Table 4.4.

Table 4.4. Values of time-temperature shift factor for the unaged asphalt concrete test specimens with different air void contents.

	Air Void Percentage		
	4%	7%	10%
Temperature (°C)	Log (Time-Temperature Shift Factor)		
−10	3.32	2.35	3.31
4	1.79	1.67	1.82
21	0.00	0.00	0.00
37	−1.85	−1.70	−2.06
54	−3.46	−3.24	−3.52

Once the time-temperature shift factors are identified, the Prony series coefficients can be obtained. Using the dynamic modulus test data of storage and loss compliances, combined with Eq. (4.10) and Eq.(4.11), an error function is defined as follows:

$$ERR = \frac{1}{m}\left\{\sum_{i=1}^{m}\left(\frac{D'_{fit}}{D'_{\exp}}-1\right)^2+\left(\frac{D''_{fit}}{D''_{\exp}}-1\right)^2\right\} \tag{4.17}$$

where *m* is the number of data points, subscript "*fit*" is used for calculations of Eq. (4.10) and Eq. (4.11), and subscript "*exp"* refers to the experimental measurements. The Prony series coefficients can be obtained by minimizing the error described above. The identified compliance terms and retardation times are listed in Table 4.5.

4.4 Calibration of the Nonlinear Viscoelastic Parameters

Recall the Schapery uniaxial nonlinear viscoelastic theory:

$$\bar{\varepsilon}^{ve,t} = g_0\bar{D}_0\bar{\sigma}^t + g_1\int_0^t \Delta\bar{D}\left(\psi^t-\psi^\tau\right)\frac{d\left(g_2\bar{\sigma}^t\right)}{d\tau}d\tau \tag{4.18}$$

The identification of the stress-dependent nonlinear parameters, g_0, g_1, and g_2, is the objective of this subsection. The nonlinear parameter, g_0, governs the effect of stress level on the instantaneous compliance; g_1 operates on the transient compliance and identifies the effect of stress level on the transient response of the material; and g_2 is the parameter that controls the effect of loading rate on the strain response.

Table 4.5. The Prony series coefficients identified using dynamic modulus test data for asphalt concrete specimens with different air void contents. The reference temperature is 21°C.

	Air Void Percentage					
	4%		7%		10%	
n	$\lambda_n\,(1/\sec)$	$D_n(1/\mathrm{MPa})$	$\lambda_n\,(1/\sec)$	$D_n(1/\mathrm{MPa})$	$\lambda_n\,(1/\sec)$	$D_n(1/\mathrm{MPa})$
0		3.871×10^{-5}		5.272×10^{-5}		5.182×10^{-5}
1	5.193×10^{4}	9.899×10^{-6}	5.549×10^{3}	1.773×10^{-5}	5.119×10^{4}	1.301×10^{-5}
2	1.534×10^{3}	2.601×10^{-5}	2.596×10^{2}	4.709×10^{-5}	1.481×10^{3}	3.455×10^{-5}
3	4.532×10^{1}	7.235×10^{-5}	1.214×10^{1}	1.259×10^{-4}	4.286×10^{1}	9.347×10^{-5}
4	1.339×10^{0}	2.601×10^{-4}	5.681×10^{-1}	4.051×10^{-4}	1.240×10^{0}	3.302×10^{-4}
5	3.955×10^{-2}	2.799×10^{-4}	2.658×10^{-2}	8.553×10^{-4}	3.589×10^{-2}	1.028×10^{-3}
6	1.168×10^{-3}	2.905×10^{-3}	1.243×10^{-3}	3.668×10^{-3}	1.039×10^{-3}	3.767×10^{-3}
7	3.451×10^{-5}	6.749×10^{-3}	5.817×10^{-5}	6.776×10^{-3}	3.005×10^{-5}	9.219×10^{-3}

The creep-recovery test at variable stress levels with confinement pressure is used to characterize the nonlinear viscoelastic parameters. The confinement stress is included in this test to capture the effect of the triaxial stress on the nonlinear viscoelastic behavior of asphalt concrete. In a creep-recovery test with confinement pressure, the stress tensor is:

$$\sigma_{ij} = \begin{bmatrix} \Delta\sigma + \sigma_c & 0 & 0 \\ 0 & \sigma_c & 0 \\ 0 & 0 & \sigma_c \end{bmatrix} \tag{4.19}$$

where σ_c is the confinement stress, and $\Delta\sigma$ is the additional axial stress that is applied at each loading cycle in the *1−1* direction. The deviatoric stress tensor, S_{ij}, and volumetric stress, σ_{kk}, during the RCRT-VS can be written as follows:

$$S_{ij} = \begin{bmatrix} \frac{2}{3}\Delta\sigma & 0 & 0 \\ 0 & -\frac{1}{3}\Delta\sigma & 0 \\ 0 & 0 & -\frac{1}{3}\Delta\sigma \end{bmatrix} \tag{4.20}$$

$$\sigma_{kk}\delta_{ij} = \begin{bmatrix} 3\sigma_c + \Delta\sigma & 0 & 0 \\ 0 & 3\sigma_c + \Delta\sigma & 0 \\ 0 & 0 & 3\sigma_c + \Delta\sigma \end{bmatrix} \tag{4.21}$$

The effect of the nonlinear viscoelastic parameters on the mechanical response of asphalt concrete is comprehensively covered by Masad et al. (2009). Parameters g_1 and g_2 govern the nonlinearity of the transient portion of the strain response (or equivalently the time-dependent portion of the viscoelastic strain response). During a creep cycle (loading stage), the viscoelastic nonlinearity is stemmed through the combined effect of g_1 and g_2. However, g_2 is the one controlling the nonlinear response during the recovery (unloading stage). The instantaneous nonlinear parameter, g_0, only has influence on the instantaneous response. It is noted that the instantaneous strain response at high temperature is very small compared to the total viscoelastic response. Additionally, measuring such small values during the cyclic creep-recovery test is very

difficult and depends on several other factors, such as rate of the data collection, loading time, and rest period. Even if measured, the measured value of the instantaneous strain will have a high level of variability, which makes it difficult to assign a unique value to it. Thus, in this study g_0 is assumed to be unity and the viscoelastic nonlinearity is captured through the parameters g_1 and g_2. It is noteworthy that, assuming $g_0 = 1$ does not exclude the instantaneous (i.e., elastic) strain response. Instead, it implies that the instantaneous creep compliance is independent of the stress level.

As mentioned previously, the total strain response of asphalt concrete during the creep-recovery test includes both viscoelastic and viscoplastic strains. In order to characterize the nonlinear viscoelastic response, the permanent strain or viscoplastic strain should be removed from the strain response. During a creep cycle, both viscoelastic and viscoplastic strains evolve; however, during the recovery cycle, viscoplastic strain remains constant and only viscoelastic strain recovers. A data reduction method (Masad et al., 2009) is used in this work to identify the nonlinear viscoelastic parameters using the RCRT-VS. Figure 4.8 demonstrates the schematic stress and the corresponding strain response during a single creep-recovery cycle.

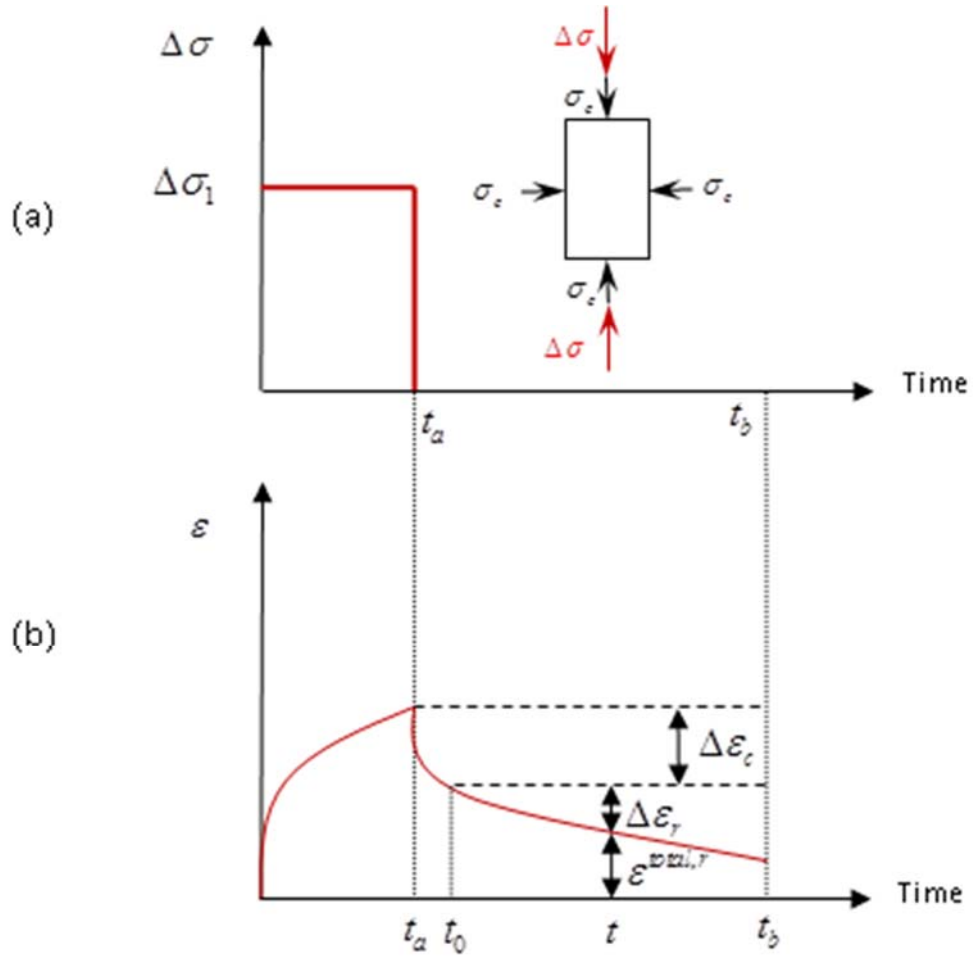

Figure 4.8. The schematic diagram of the (a) stress and (b) strain response during a single creep and recovery test that is used to identify the nonlinear viscoelastic parameters.

Eq. (2.12) can be simplified and the deviatoric strain in the *1–1* direction during the creep cycle, $\overline{e}_{11}^{c}$, is obtained by:

$$\overline{e}_{11}^{c} = \frac{1}{2}\left(g_0^a \overline{J}_0 + g_1^a g_2^a \Delta\overline{J}\left(\psi^t\right)\right)\frac{2}{3}\Delta\sigma_1, \quad 0 < t < t_a \tag{4.22}$$

where $g_0^a, g_1^a,$ and g_2^a are the nonlinear parameters corresponding to the stress level, $\Delta\sigma_1$, during the first loading cycle, and t_a is the loading time. Similarly, the volumetric strain in Eq. (2.13), $\bar{\varepsilon}_{vol}^c$ during the creep is obtained, such that:

$$\bar{\varepsilon}_{vol}^c = \frac{1}{3}\left(g_0^a \bar{B}_0 + g_1^a g_2^b \Delta\bar{B}(\psi^t)\right)3\sigma_c + \frac{1}{3}\left(g_0^a \bar{B}_0 + g_1^a g_2^a \Delta\bar{B}(\psi^t)\right)\Delta\sigma_1, \quad 0 < t < t_a \tag{4.23}$$

where $g_0^b, g_1^b,$ and g_2^b are the nonlinear parameters corresponding to the confinement level, σ_c. Therefore, the total strain during the creep is the summation of Eq. (4.22) and Eq. (4.23) plus the amount of accumulated viscoplastic strain, such that:

$$\bar{\varepsilon}_{11}^{total,c}(t) = \bar{e}_{11}^c(t) + \frac{1}{3}\bar{\varepsilon}_{vol}^c(t) + \bar{\varepsilon}^{vp}(t), \quad 0 < t < t_a \tag{4.24}$$

where $\bar{\varepsilon}^{vp}$ is the viscoplastic strain. Next, the strain components during the recovery can be written as:

$$\bar{e}_{11}^r = \frac{1}{2} g_1^b g_2^a \left(\Delta\bar{J}\left(\psi^t\right) - \Delta\bar{J}\left(\psi^t - \psi^{t_a}\right)\right)\frac{2}{3}\Delta\sigma_1, \quad t_a < t < t_b \tag{4.25}$$

$$\bar{\varepsilon}_{vol}^r = \frac{1}{3} g_1^b g_2^a \left(\Delta\bar{B}\left(\psi^t\right) - \Delta\bar{B}\left(\psi^t - \psi^{t_a}\right)\right)\Delta\sigma_1 + \frac{1}{3}\left(g_0^b \bar{B}_0 + g_1^b g_2^b \Delta\bar{B}\left(\psi^t\right)\right)(3\sigma_c), \quad t_a < t < t_b \tag{4.26}$$

where $\bar{e}_{11}^r$ and $\bar{\varepsilon}_{vol}^r$ are the deviatoric and volumetric strains during the recovery cycle, respectively, and t_b is the time at the end of the recovery. Therefore, the total strain

during the recovery cycle is calculated by the summation of Eq. (4.25), Eq. (4.26), and the accumulated viscoplastic strain at the end of the loading cycle, such that:

$$\bar{\varepsilon}_{11}^{total,r}(t) = \bar{e}_{11}^{r}(t) + \frac{1}{3}\bar{\varepsilon}_{vol}^{r}(t) + \bar{\varepsilon}^{vp}(t_a), \quad t_a < t < t_b \tag{4.27}$$

It is emphasized that the amount of the viscoplastic strain remains constant during the recovery cycle.

It is noted that the material response under pure confinement stress is assumed to be linear in this study, as presented in Figure 4.9. This figure shows the isochrones of the material response at different confinement stresses when the material is only subjected to the confinement pressure. Figure 4.9 suggests that the viscoelastic response varies linearly with the increase in confinement stress over the range of the assumed confinement levels in this study. As a result, the values of nonlinear parameters corresponding to the confinement stress are equal to unity ($g_0^b = g_1^b = g_2^b = 1.0$). By assigning these values to Eq. (4.27), the only unknown parameters in this equation are g_2^a and the viscoplastic strain.

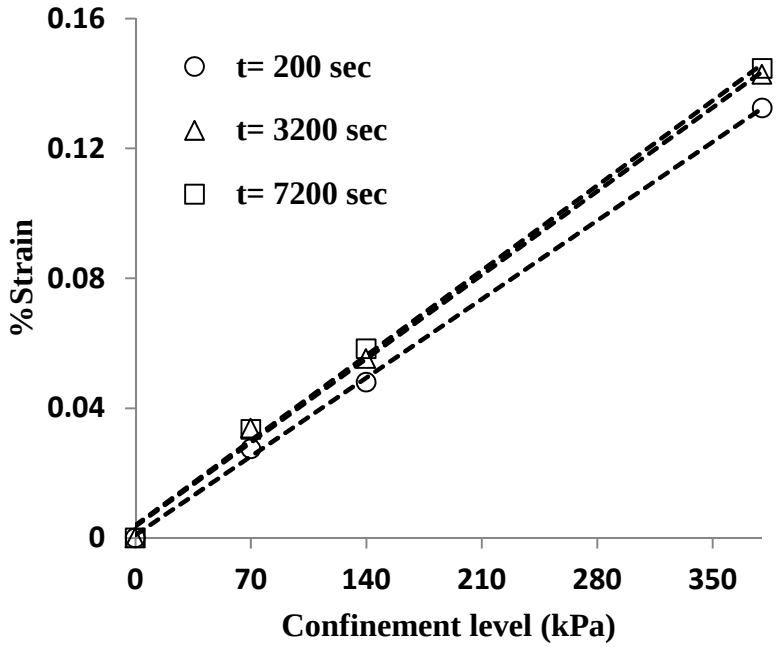

Figure 4.9. The isochrones of the strain response of asphalt concrete subjected to the confinement pressure only. This implies that the material response over the range of applied confinement stresses is linear viscoelastic.

In order to exclude the viscoplastic strain, a recoverable strain of $\Delta\varepsilon_r$ is considered, as presented in Figure 4.8(b). In fact, $\Delta\varepsilon_r$ is expressed as follows:

$$\Delta\varepsilon_r = \bar{\varepsilon}^{total,r}\left(t_0\right) - \bar{\varepsilon}^{total,r}\left(t\right), \quad t_0 < t < t_b \tag{4.28}$$

In this case, the value of $\Delta\varepsilon_r$ is a function of the unknown nonlinear parameter, g_2^a. Therefore, g_2^a can be identified by minimizing the error between the measured value of $\Delta\varepsilon_r$ and the calculations using Eq. (4.28).

To identify g_1^a, the term $\Delta\varepsilon_c$ is introduced, which is the difference between the creep strain at the end of the loading cycle and the strain at an arbitrary point after the load is removed:

$$\Delta\varepsilon_c = \bar{\varepsilon}^{total,c}\left(t_a\right) - \bar{\varepsilon}^{total,r}\left(t\right) \tag{4.29}$$

Likewise, the nonlinear parameter g_1^a can be obtained by minimizing the error between the measured value of $\Delta\varepsilon_c$ and the calculation using Eq. (4.29).

After identifying the nonlinear viscoelastic parameters for different stress levels during the RCRT-VS, the nonlinear viscoelastic behavior of the asphalt concrete is characterized. Once both the linear and nonlinear viscoelastic model parameters are known, the viscoplastic strain response can be obtained by subtracting the viscoelastic behavior from the total measured strain response. The viscoplastic strain is then used to calibrate the viscoplastic constitutive relationship, which is the subject of the next subsection. Therefore, characterizing the nonlinear viscoelastic response of asphalt concrete allows for more accurate estimation of the viscoplastic or even damage responses. Figure 4.10 presents the identified values of the nonlinear parameters in each loading cycle for different confinement levels. These figures indicate that the parameter, g_1, increases as the confinement level increases, while g_2 decreases as the confinement level increases.

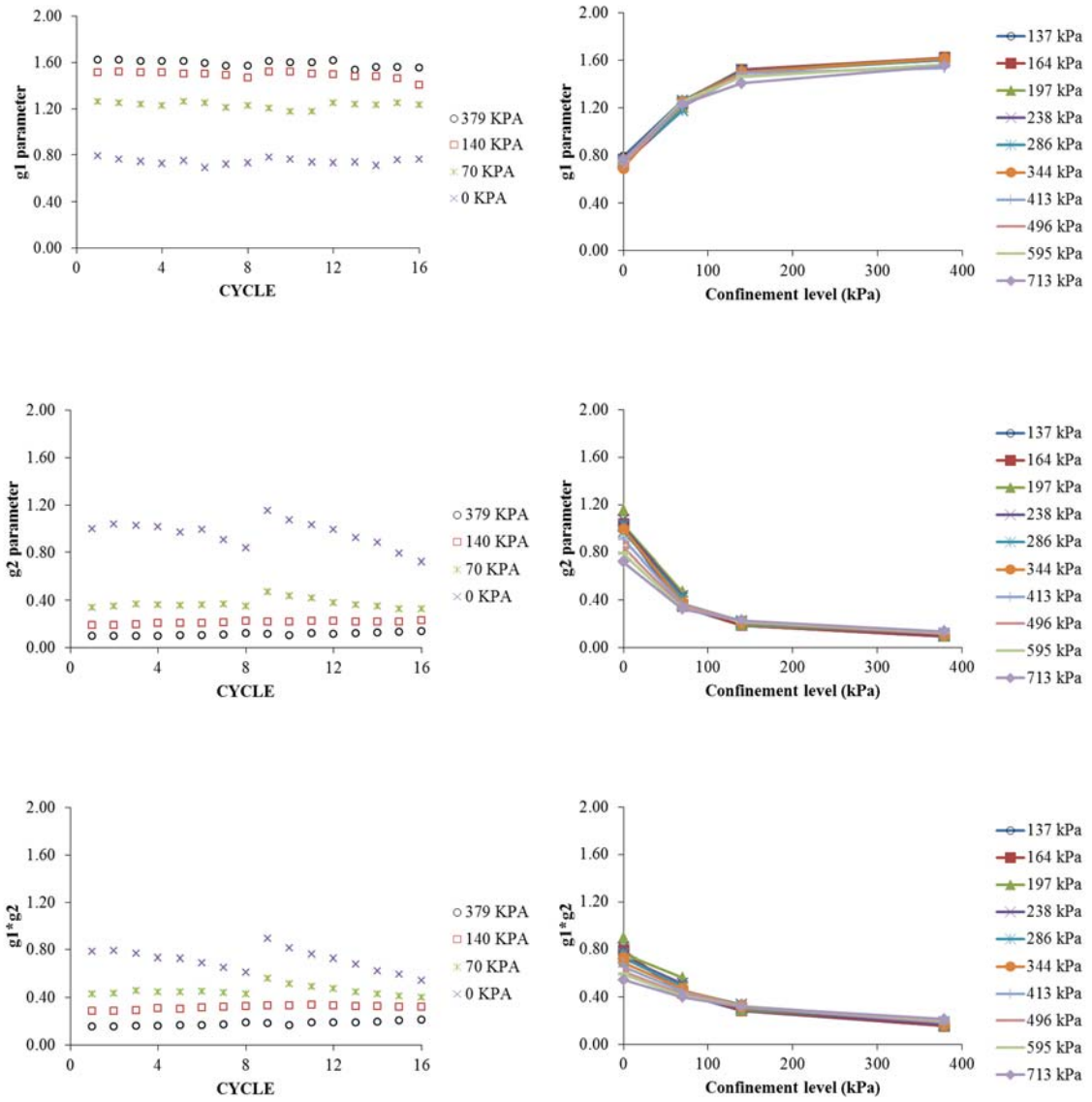

Figure 4.10. Variation of the nonlinear parameters with respect to the loading cycle (left-side figures), and variation of the nonlinear parameters with respect to confinement level for different axial stresses (right-side figures). As the confinement level increases, then *g1g2*, which expresses the transient response, decreases. It means the confinement pressure makes the material stiffer and less time-dependent.

It should be noted that the multiplication of g_1 and g_2 (i.e., $g_1 g_2$) is controlling the nonlinear effect during the creep loading stages. On the other hand, g_2 governs the level of nonlinearity in the strain response during the recovery. As shown in Figure 4.10, both $g_1 g_2$ and g_2 values decrease as the confinement level increases. This observation is physically sound since the increase in the confinement level reduces the mobility of the aggregates and the binder in between during the deformation. As this mobility decreases, material shows a less time-dependent response. Figure 4.10 also shows that $g_1 g_2$ and g_2 asymptote to a small value as the confinement level increases. It should be noted that while strain history affects the viscoelastic nonlinearity, the reduction in values of g_2 and $g_1 g_2$ is not believed to be due to the strain hardening effect. Strain hardening is physically related to the mechanism where resistance of the material continuously increases due to permanent rearrangement of materials microstructure. In asphalt concrete these permanent rearrangements are mostly because of the friction between the aggregates and the breakage of the interlocking bonds. This mechanism is mostly responsible for permanent deformation of asphalt concrete materials rather than the recoverable part of the deformation. However, the extracted strain response analyzed in this study, although nonlinear in behavior, is completely recoverable when long enough rest periods are applied. Moreover, strain hardening in asphalt concrete takes place when the applied load is sufficiently high to overcome the friction and interlocking of the aggregates. High stress levels cause permanent rotation and sliding of the aggregates to

form a stiffer microstructure in order to resist more to the applied load. However, reduction in values of $g_1 g_2$ is observed even from the initial loading cycles when the stress level is relatively low, such that the strain hardening is not expected to be significant. Moreover, the decrease in the value of $g_1 g_2$ results in the decrease in the effective transient compliance as suggested by Eq. (4.18) (i.e., $g_1 g_2 \Delta \bar{D}$). Therefore, as the confinement level increases, the effective transient modulus increases (or equivalently, the effective transient compliance decreases).

Figure 4.11 presents the comparison of the experimental measurements and the model predictions for the recovered strain at different confinement levels (i.e., 0, 70, 140, and 379 kPa) for the first two loading blocks of the RCRT-VS (or equivalently 16 loading cycles). Figure 4.11 shows that the identified nonlinear viscoelastic model parameters well predict the recovered strain. Figure 4.11(e–f) shows that the value of the strain at each loading cycle (at similar axial stress levels) decreases with the increase in the confinement level, since the confinement pressure stiffens the material and makes it more resistant to the axial deformation.

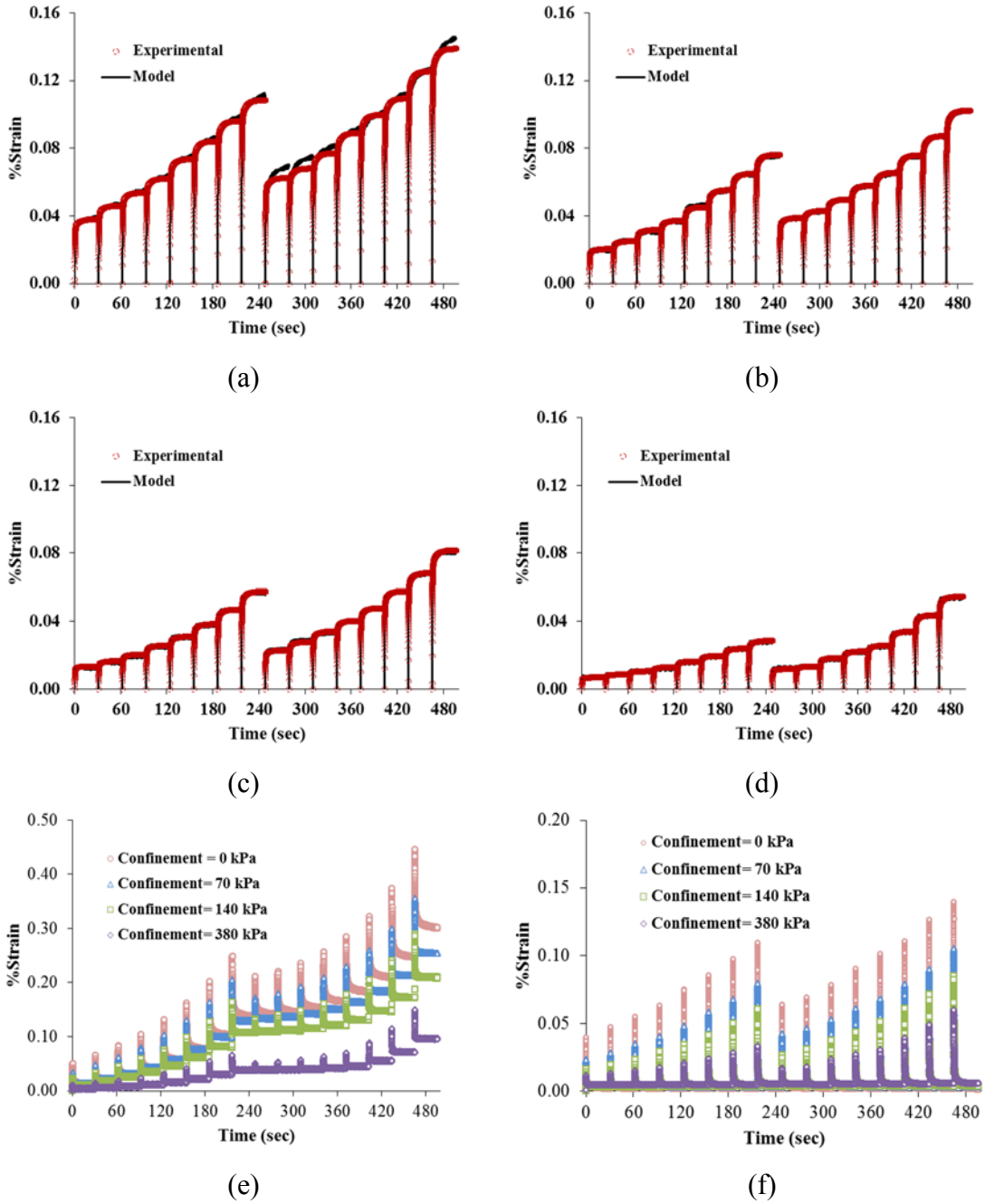

Figure 4.11. Comparison of experimental measurements and model predictions for recovered strain, when confinement levels are (a) zero (i.e., unconfined); (b) 70 kPa; (c) 140 kPa; and (d) 379 kPa. The values of strain responses at the same uniaxial deviatoric stress levels at different confinement pressures are shown for (e) experimental measurements and (f) model predictions. The more the confinement pressure, the less the strain magnitude, meaning that due to the effect of the confinement pressure the material has become more resistible to the applied axial stress.

The triaxiality ratio is defined as the measure of the first stress invariant over the second deviatoric stress invariant. This ratio is termed by the hydrostatic pressure, or mean stress, over the von Mises equivalent stress, such that:

$$\eta = \frac{\bar{I}_1 / 3}{\sqrt{3\bar{J}_2}} \tag{4.30}$$

where η is the triaxiality ratio, $\bar{I}_1$ is the first stress invariant, and $\bar{J}_2$ is the second deviatoric stress invariant. The triaxiality ratio is known to strongly affect the level of permanent strain of ductile materials. The triaxiality ratio is positive when the material is under the contraction mode of loading and is negative when the material is under the extension mode of loading. This ratio increases as the confinement level dominates the von Mises equivalent stress. Therefore, higher values of η correspond to either high confinement levels or low values of the von Mises equivalent stress. The triaxiality ratio η in the creep-recovery test is the confinement pressure over the deviatoric applied stress, such that:

$$\eta = \frac{\sigma_c + \Delta\sigma / 3}{\Delta\sigma} = \frac{\sigma_c}{\Delta\sigma} + \frac{1}{3} \tag{4.31}$$

The variations of the nonlinear parameters with respect to the triaxiality ratio are plotted in Figure 4.12. Accordingly, the trend of these variations matches a power low type function, such that:

$$g_i(\eta) = a_i \eta^{b_i} + c_i;\ i = 1,2 \tag{4.32}$$

where a_i, b_i, and c_i are material properties. Table 4.6 lists the identified values for these parameters. Figure 4.12 shows that as the triaxiality ratio increases, the variations of the nonlinear parameters decrease. As shown in Figure 4.12, the nonlinear model parameters are almost constant when η is larger than unity. According to Eq. (4.31) for a fixed axial stress (i.e., $\Delta\sigma$), the triaxiality ratio η increases as the confinement level σ_c increases. Moreover, for a constant confinement level, σ_c, the triaxiality ratio η can still have large values when the axial stress $\Delta\sigma$ is low. The direct implications of Eq. (4.31) and Eq. (4.32) and the results shown in Figure 4.12 are that the nonlinear response of material at low confinement levels is significantly affected by the level of the axial stress. However, the level of axial stress might have negligible effect on the nonlinear response of asphalt concrete materials if the confinement level is higher compared to the axial stress level. As shown in Figure 4.12, the values of g_2 and $g_1 g_2$ decrease as the triaxiality ratio increases, confirming that asphalt concrete materials show less time-dependent response at high confinement levels.

Table 4.6. Fitting parameters for the power law introduced in Eq. (4.32).

	a_i	b_i	c_i
i=1 (corresponds to g_1)	−0.1023	−1.9460	1.6200
i=2 (corresponds to g_2)	0.0298	−3.0030	0.1432

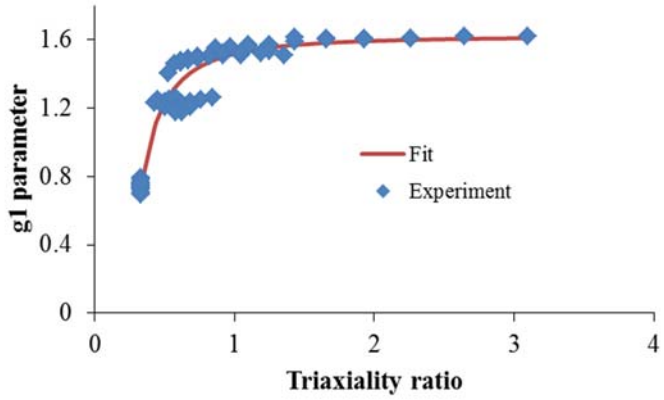

(a)

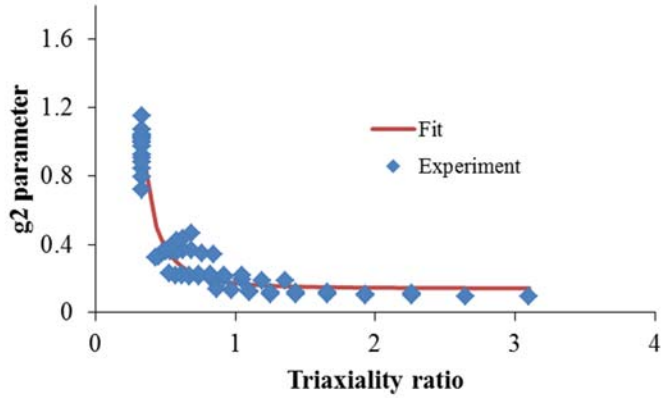

(b)

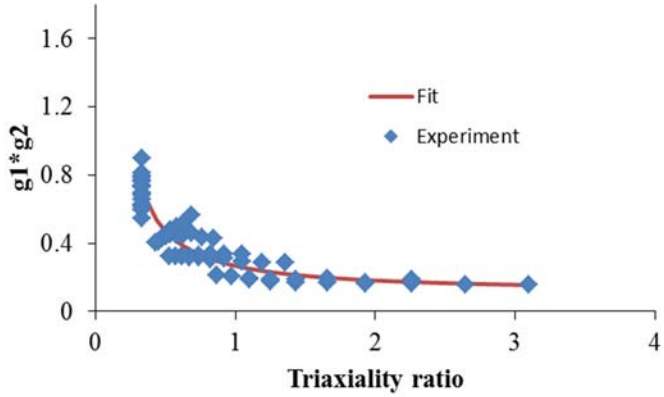

(c)

Figure 4.12. Variation with respect to the triaxiality ratio for the nonlinear viscoelastic parameters, (a) g_1, (b) g_2, and (c) $g_1{*}g_2$. The nonlinear parameters are sensitive to the lower values of the triaxiality ratio. The nonlinear response of material at low confinement levels is significantly affected by the level of the axial stress. However, the level of axial stress might have negligible effect on the nonlinear response of asphalt concrete materials if the confinement level is higher compared to the axial stress level.

It is interesting to see that the results obtained in this subsection agree with the conclusions drawn by Pellinen and Witczak (2002). They showed that the stress-dependent dynamic modulus of asphalt concrete can be expressed using a sigmoidal function modified by an equilibrium modulus, δ. Based on their studies, the equilibrium modulus is explained in terms of the first stress invariant and second deviatoric stress invariant, or in mathematical form:

$$\delta = f\left(p_a\right) I_1^{k_2} J_2^{k_3} \tag{4.33}$$

where p_a is atmospheric pressure, I_1 and J_2 are the first and second deviatoric stress invariants, and k_2 and k_3 are model coefficients. In their proposed relationship, as the ratio of J_2 / I_1 increased, the stiffness of the material decreased, which is in agreement with the results of the current work. It should be emphasized that this study presents both variables (i.e., the first stress invariant and the second deviatoric stress invariant) in terms of a single common parameter (i.e., triaxiality ratio), which is more convenient and advantageous. Moreover, expressing the nonlinear viscoelastic behavior of the material using g_1 and g_2 through the expression of the triaxiality ratio will considerably simplify the implementation of the model.

Consequently, the results shown in this subsection can be used to enhance the Schapery nonlinear viscoelastic model to consider the nonlinearity of asphalt concrete materials subjected to the multi-axial state of stresses. The common practice for implementing the nonlinear Schapery model is to express and implement the nonlinear

parameters as a function of the effective von Mises stress. However, these implementations can be modified to include the effect of mode of loading and confinement level under multi-axial stress states. This enhancement is imperative for pressure-sensitive materials such as asphalt concrete, geo-materials, and polymer composites.

4.5 Identification of the Viscoplastic Material Properties

In the RCRT-VS, once the viscoelastic strain response is calculated using the linear and nonlinear viscoelastic parameters, the viscoplastic strain can be simply obtained by subtracting the calculated viscoelastic strain from the measured total strain. Figure 4.13 shows the separated viscoplastic strain for the first cycle during the RCRT-VS. The separated viscoplastic strain is used to identify the parameters associated with the viscoplastic constitutive relationship described in Subsection 2.3.3. It is noted that several of the viscoplastic parameters are assumed, because they do not vary significantly from one asphalt mixture to another, and they can be assumed constant with reasonable accuracy. Based on the previous works in this regard (Darabi et al., 2011; Huang et al., 2011), values of parameters such as α, d^{vp}, and κ_1 are assumed in this study.

4.5.1 Identification of the Parameter, β

Using Eq. (2.17), the ratio of axial viscoplastic strain, $\overline{\varepsilon}_{11}^{vp}$, to the radial viscoplastic strain, $\overline{\varepsilon}_{22}^{vp}$, can be written as follows:

$$\frac{\bar{\varepsilon}_{22}^{vp}}{\bar{\varepsilon}_{11}^{vp}} = \frac{-\partial g / \partial \bar{\sigma}_{22}}{\partial g / \partial \bar{\sigma}_{11}} \tag{4.34}$$

where $\bar{\sigma}_{22}$ and $\bar{\sigma}_{11}$ are the stresses on axial and radial directions. The derivatives in Eq. (4.34) can be calculated using Eq. (2.23), such that:

$$\frac{\partial g}{\partial \bar{\sigma}_{ij}} = \frac{\partial \bar{\tau}}{\partial \bar{\sigma}_{ij}} - \beta \frac{\partial \bar{I}_1}{\partial \bar{\sigma}_{ij}} \tag{4.35}$$

where the differential of $\bar{I}_1$ and $\bar{\tau}$ is calculated as follows:

$$\frac{\partial \bar{I}_1}{\partial \bar{\sigma}_{ij}} = \delta_{ij} \tag{4.36}$$

$$\frac{\partial \bar{\tau}}{\partial \bar{\sigma}_{ij}} = \frac{1}{2}\left[\frac{\frac{\partial \bar{J}_2}{\partial \bar{\sigma}_{ij}}}{2\sqrt{\bar{J}_2}}\left(1+\frac{1}{d}\right)+\left(\frac{\frac{\partial \bar{J}_3}{\partial \bar{\sigma}_{ij}}\bar{J}_2 - \frac{\partial \bar{J}_2}{\partial \bar{\sigma}_{ij}}\bar{J}_3}{\bar{J}_2^2}\right)\left(1-\frac{1}{d}\right)\right] \tag{4.37}$$

Consequently, the differentials of the second and third deviatoric stress invariants can be calculated as:

$$\frac{\partial \bar{J}_2}{\partial \bar{\sigma}_{ij}} = 3\bar{S}_{ij},\ \frac{\partial \bar{J}_3}{\partial \bar{\sigma}_{ij}} = \frac{27}{2}\bar{S}_{ik}\bar{S}_{kj} - 3\bar{J}_2\delta_{ij} \tag{4.38}$$

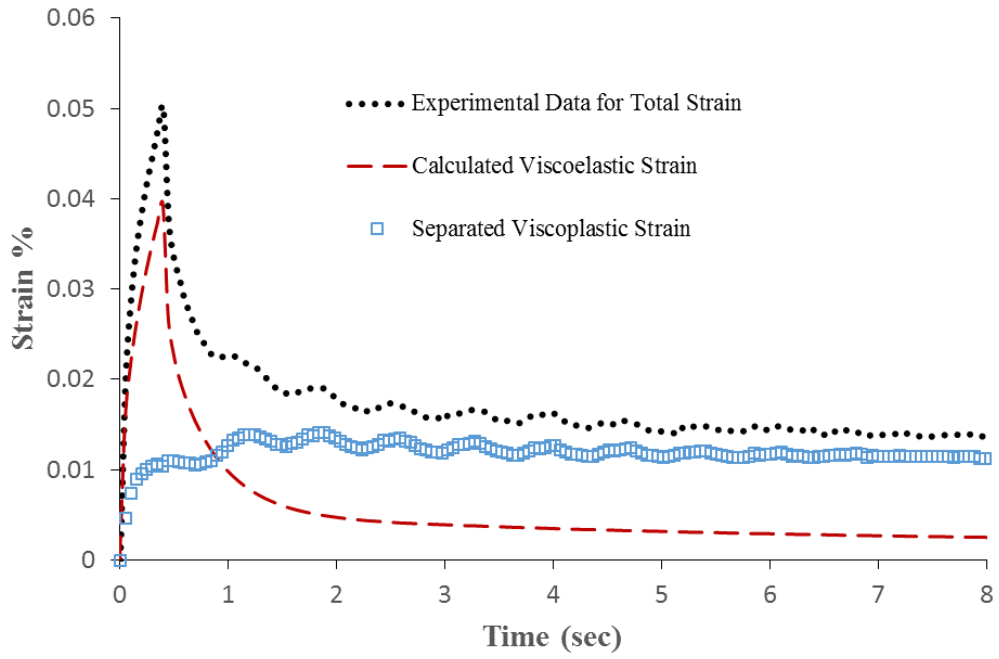

Figure 4.13. The separated viscoplastic strain from the total strain response during the first cycle of the RCRT-VS.

By substituting Eq. (4.36), Eq. (4.37), and Eq. (4.38) into Eq. (4.35), the differential of the viscoplastic potential function yields:

$$\frac{\partial g}{\partial \bar{\sigma}_{ij}} = \frac{1}{2}\left[\frac{3\bar{S}_{ij}}{2\sqrt{\bar{J}_2}}\left(1+\frac{1}{d}\right)+\left(\frac{\left(\frac{27}{2}\bar{S}_{ik}\bar{S}_{kj}-3\bar{J}_2\delta_{ij}\right)\bar{J}_2-3\bar{S}_{ij}\bar{J}_3}{\bar{J}_2^2}\right)\left(1-\frac{1}{d}\right)-2\beta\delta_{ij}\right] \quad (4.39)$$

Therefore, Eq. (4.34) can be rewritten, such that:

$$\frac{\bar{\varepsilon}_{22}^{vp}}{\bar{\varepsilon}_{11}^{vp}} = \frac{-\left(-1/2-\beta\right)}{1-\beta} \quad (4.40)$$

The parameter, β, can now be determined using Eq. (4.40), provided that the radial and axial viscoplastic strains are known from the experimental data. In other words, β is identified such that the ratio $\bar{\varepsilon}_{22}^{vp} / \bar{\varepsilon}_{11}^{vp}$ remains constant, as shown by Figure 4.14.

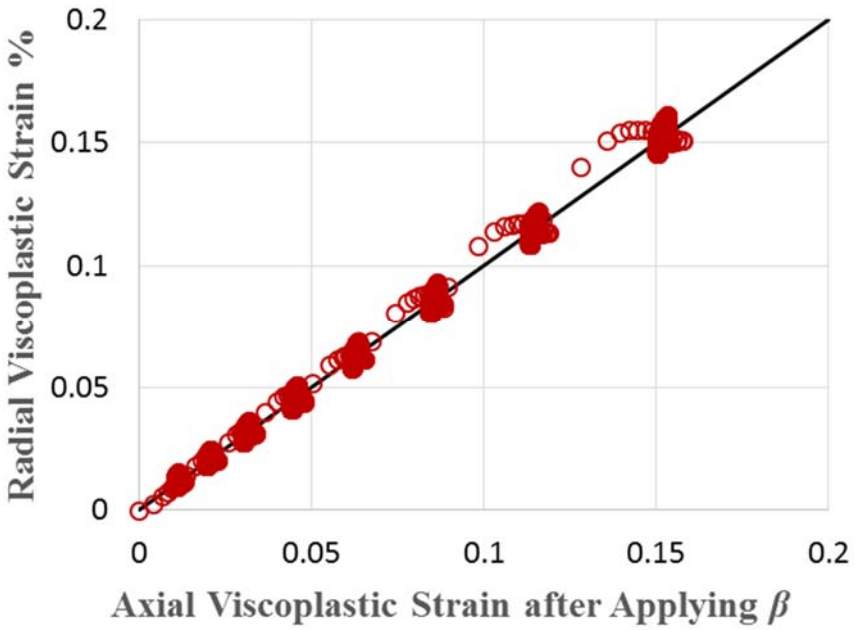

Figure 4.14. The ratio of the radial viscoplastic strain to the axial viscoplastic strain remains constant after applying β.

4.5.2 Identification of the Hardening Parameter, κ_2

Using Eq. (2.19), Eq. (2.20), and Eq. (2.22), one can rearrange Eq. (2.18), such that:

$$\frac{\Delta\bar{\gamma}^{vp}}{\Delta t}=\Gamma\left[\frac{\left\{\bar{\tau}-\alpha\bar{I}_1-\left[\kappa_0+\kappa_1\left(1-\exp\left(-\kappa_2\varepsilon_e^{vp}\right)\right)\right]\right\}}{\sigma_y^0}\right]^N \tag{4.41}$$

Using Eq. (4.39) and Eq. (2.17), $\Delta\bar{\gamma}^{vp}$ can be calculated using the separated axial viscoplastic strain, $\Delta\bar{\varepsilon}_{11}^{vp}$, as follows:

$$\Delta\bar{\gamma}^{vp}=\Delta\bar{\varepsilon}_{11}^{vp}/\left(1-\beta\right) \tag{4.42}$$

The effective viscoplastic strain, ε_e^{vp}, is calculated using the radial and axial viscoplastic strains and Eq. (2.24), such that:

$$\varepsilon_e^{vp}=\left[1+2\left(\frac{0.5+\beta}{1-\beta}\right)\right]^{-0.5}\sqrt{\left(\bar{\varepsilon}_{11}^{vp}\right)^2+2\left(\bar{\varepsilon}_{22}^{vp}\right)^2} \tag{4.43}$$

Next, Eq. (4.41) is rearranged as:

$$\bar{\tau}-\alpha\bar{I}_1-\kappa_1\left(1-Exp\left(-\kappa_2\varepsilon_e^{vp}\right)\right)=M \tag{4.44}$$

where $M=\sigma_y^0\left(\frac{\Delta\bar{\gamma}^{vp}}{\Gamma^{vp}\Delta t}\right)^{1/N}+\kappa_0$, and it has a constant value when constant values are picked for $\Delta\bar{\gamma}^{vp}$ at different stress levels during the RCRT-VS. As a result, the hardening parameter, κ_2, is captured in such a way that the left side of Eq. (4.44) also becomes constant at each stress level. As previously mentioned, the hardening parameter, κ_1, and the parameter, α, are assumed.

4.5.3 Identification of the Parameters, κ_0 and N

After the hardening parameters, κ_2 and κ_1, are known, then using Eq. (4.41), one can write:

$$\frac{\Delta\bar{\gamma}^{vp}}{\Delta\bar{\gamma}^{vp,t_0}}=\left[\frac{\bar{\tau}-\alpha\bar{I}_1-\left[\kappa_0+\kappa_1\left(1-Exp\left(-\kappa_2\varepsilon_e^{vp}\right)\right)\right]}{\bar{\tau}-\alpha\bar{I}_1-\left[\kappa_0+\kappa_1\left(1-Exp\left(-\kappa_2\varepsilon_e^{vp,t_0}\right)\right)\right]}\right]^N \tag{4.45}$$

where t_0 is an arbitrary time for which $\Delta\bar{\gamma}^{vp}$ and ε_e^{vp} are calculated. In this case, the only two unknown parameters in Eq. (4.45) are κ_0 and N. By minimizing the error between two sides of the above equation, these two parameters can be identified.

4.5.4 Identification of the Parameter, Γ^{vp}

Once all other viscoplastic material parameters are obtained or assumed, the viscoplastic fluidity parameter, Γ^{vp}, can be identified using Eq. (4.41). The final calibrated values of the viscoplastic material properties are listed in Table 4.7, and the calculated viscoplastic strain using these parameters is compared to the experimentally extracted viscoplastic strain in Figure 4.15. Moreover, the total strain response during the RCRT-VS can be achieved by summation of the calculated viscoelastic and viscoplastic strains. Figure 4.16 shows the comparison of the calculated total strain and experimentally measured total strain,

Table 4.7. The identified viscoplastic material parameters using the RCRT-VS at 55°C.

α	β	$\Gamma^{vp}\left(1/\text{sec}\right)$	N	$\kappa_0\left(kPa\right)$	$\kappa_1\left(kPa\right)$	κ_2	$\sigma_y^0\left(kPa\right)$
0.3	0.28	0.1836	1.24	89.73	1752.15	162.65	1000

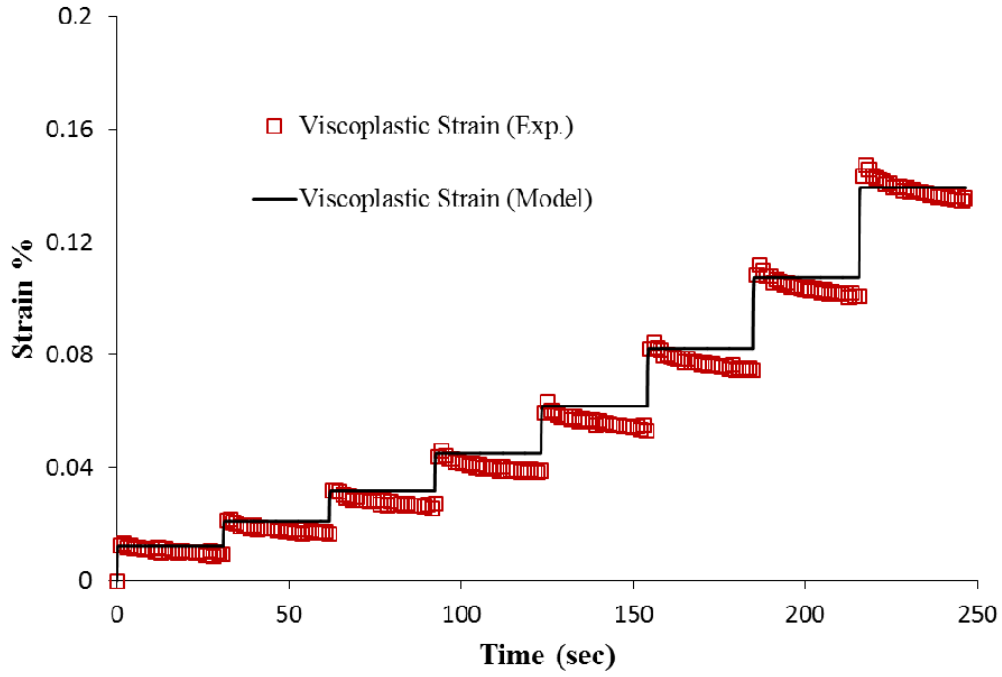

Figure 4.15. The comparison of the calculated viscoplastic strain with the experimentally extracted viscoplastic strain in the RCRT-VS at 55°C.

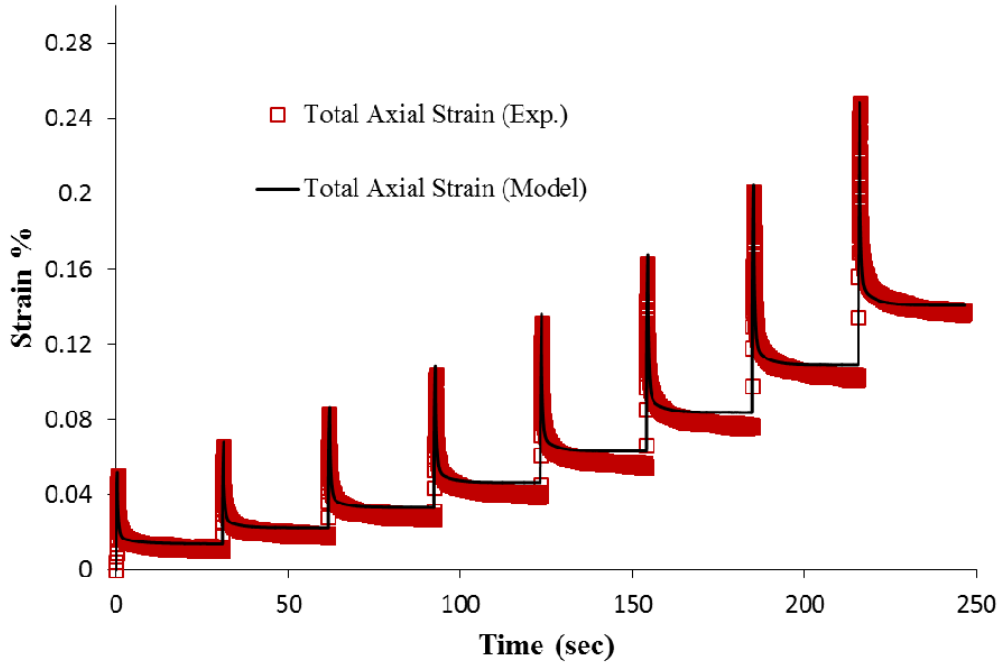

Figure 4.16. The comparison of the calculated total axial strain with measured axial strain during the RCRT-VS at 55°C.

4.6 Identification of the Viscodamage Parameters

The procedure to identify the viscodamage material parameters is briefly described in Darabi et al. (2013). The uniaxial constant strain rate test at various strain rates (Subsection 3.4.4) is used to identify the material parameters for the viscodamage constitutive relationship. The first step is to calculate the damage density variable during this test at different rates. This test is conducted at low temperature (5°C) to ensure that the major failure mechanism governs by damage evolution and the viscoplastic strain is neglected. In this study, three different strain rates are considered for calibration

purposes. In the uniaxial constant strain rate test, the strain input in the effective configuration can be expressed as:

$$\bar{\varepsilon}(t) = Ct \tag{4.46}$$

where C is the constant strain rate. The induced stress in the effective or undamaged configuration is analytically calculated by:

$$\bar{\sigma}(t) = C\int_0^t \bar{E}(\tau)d\tau \tag{4.47}$$

where $\bar{E}(t)$ is the relaxation modulus in the effective configuration. The relaxation function can be obtained using dynamic modulus test data with the same procedure that was previously explained to calculate the Prony series coefficients. Once the effective stress is calculated using Eq. (4.47), the damage density can be calculated using the obtained effective stress, $\bar{\sigma}(t)$ and experimentally measured stress, $\sigma(t)$, such that:

$$\phi(t) = 1 - \frac{\sigma(t)}{\bar{\sigma}(t)} \tag{4.48}$$

Next, the rate of the damage density is simply calculated as:

$$\dot{\phi} = \frac{\Delta\phi}{\Delta t} = \frac{\phi(t+\Delta t) - \phi(t)}{\Delta t} \tag{4.49}$$

4.6.1 Identification of the Parameter, q

The effective damage force is calculated using Eq. (2.27) and Eq. (2.21). Taking the logarithm of both sides of Eq. (2.25) yields:

$$\log\left(\dot{\phi}\right) = \log\left(\Gamma^{vd}\right) + q\log\left(\frac{\bar{Y}}{Y_0}\right) + k\log\left(\bar{\varepsilon}_{eff}\right) \tag{4.50}$$

As shown in Figure 4.17(a), once the damage density rate, $\dot{\phi}$, is calculated using Eq. (4.48), it can be plotted versus the effective total strain, $\bar{\varepsilon}_{eff}$. It is noted that the first and the third terms in the right side of Eq. (4.50) are constants at a fixed effective strain level. To identify the parameter, q, the values of normalized effective damage force, $\bar{Y}/Y_0$, at several arbitrary strain levels, within the range of the experiment, are plotted against the damage density rate for different strain rate tests. In this case, q is the average slope of the lines shown in Figure 4.17(b).

4.6.2 Characterizing the Parameter, k

Similarly, the damage density rate, $\dot{\phi}$, can be plotted against the normalized damage force, $\bar{Y}/Y_0$, and the plot is shown in Figure 4.18(a). In this case, several arbitrary values of $\bar{Y}/Y_0$ are selected. Therefore, the first and the second terms on the right side of Eq. (4.50) remain constant at the fixed normalized damage force. As illustrated in Figure 4.18(b), in order to calibrate k, this time $\dot{\phi}$ is plotted versus the effective total strain, $\bar{\varepsilon}_{eff}$, at the fixed $\bar{Y}/Y_0$. The average of the slopes of the fitted lines in Figure 4.18(b) defines the strain-dependent parameter.

4.6.3 Identification of the Damage Fluidity Parameter, Γ^{vd}

Once the stress- and strain-dependent parameters (q and k) are obtained, the damage fluidity parameter can be identified. In this step, by simply selecting several data points within the experiments at different strain rates, all the terms in Eq. (4.50) are known except the first term on the right side. The damage fluidity parameter, Γ^{vd}, is characterized by averaging the calculated Γ^{vd} at different data points and strain rates.

The finalized viscodamage parameters are listed in Table 4.8. The calculated damage density parameter using this set of parameters and Eq. (2.25) is compared to the experimentally calculated damage density for different strain rate tests in Figure 4.19. And in Figure 4.20, the stress in the nominal configuration calculated using the computed damage density variable is compared to the experimentally measured stresses at different strain rate inputs. These comparisons show that the identified parameters can fairly well predict the experimental measurements.

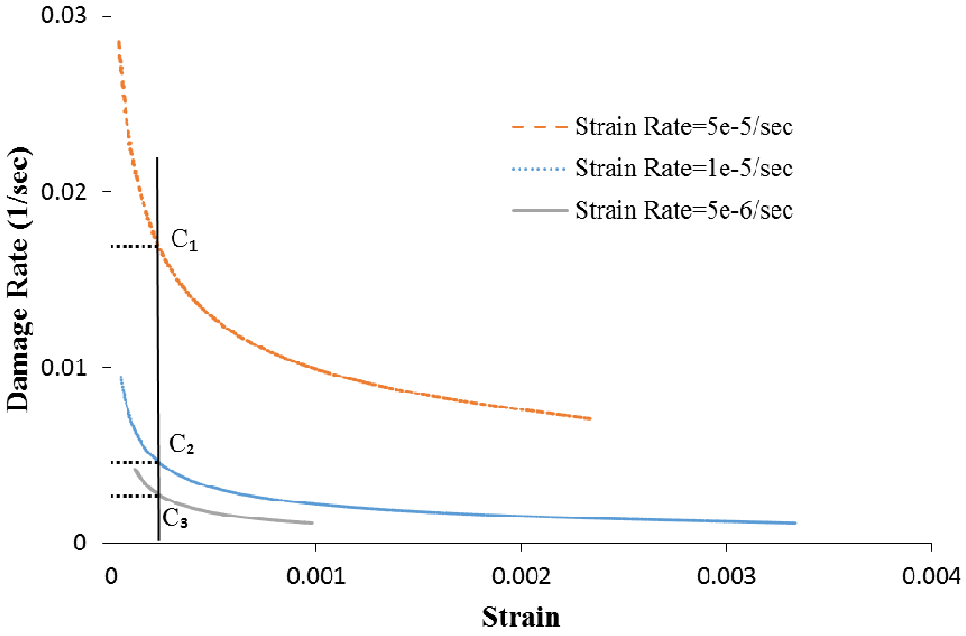

(a)

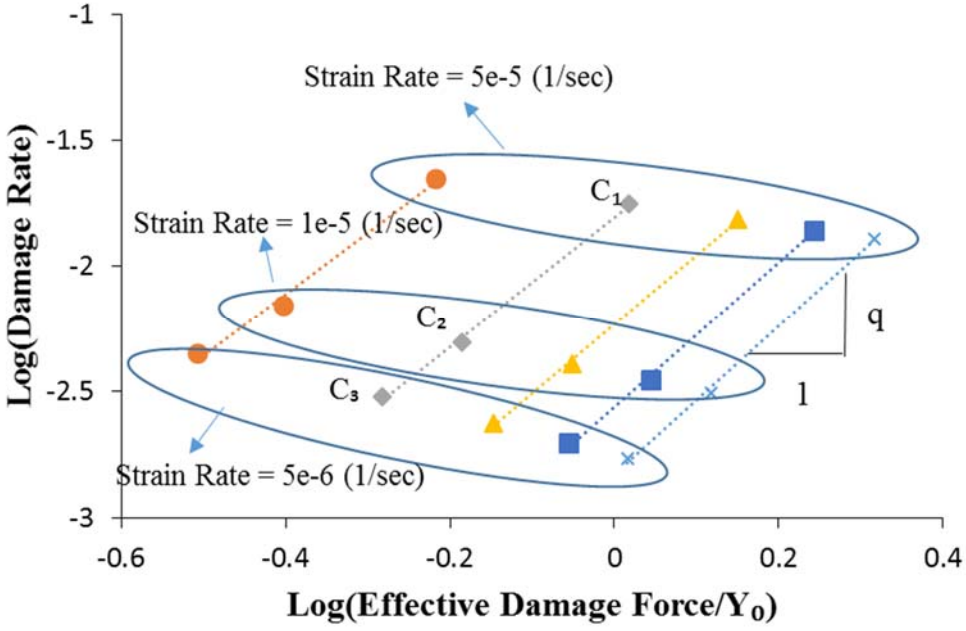

(b)

Figure 4.17. (a) Rate of the damage density versus the effective strain plotted at different strain rates for the uniaxial constant strain rate test; (b) Plot of the damage density rate against the normalized effective damage force to identify the parameter, q.

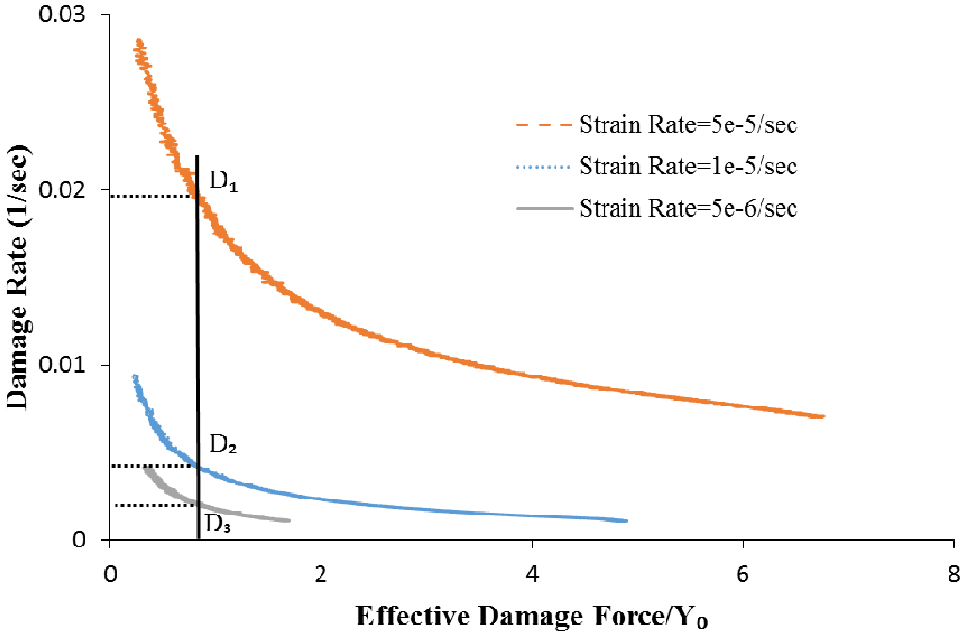

(a)

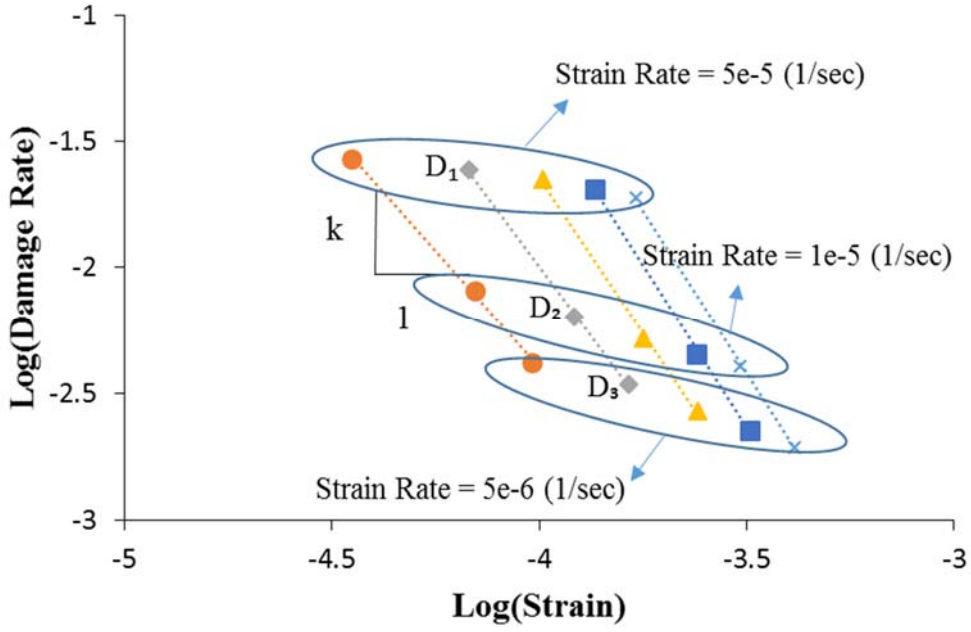

(b)

Figure 4.18. (a) Rate of the damage density versus the normalized effective damage force plotted at different strain rates for the uniaxial constant strain rate test; (b) Plot of the damage density rate against the effective total strain to identify the parameter, *k*.

Table 4.8. The identified viscodamage material parameters using the uniaxial constant strain rate test at 5°C.

α	d	$\Gamma^{vd}\left(1/\text{sec}\right)$	$Y_0(kPa)$	q	k
0.3	0.778	5.78×10^{-12}	1000	2.83	−2.55

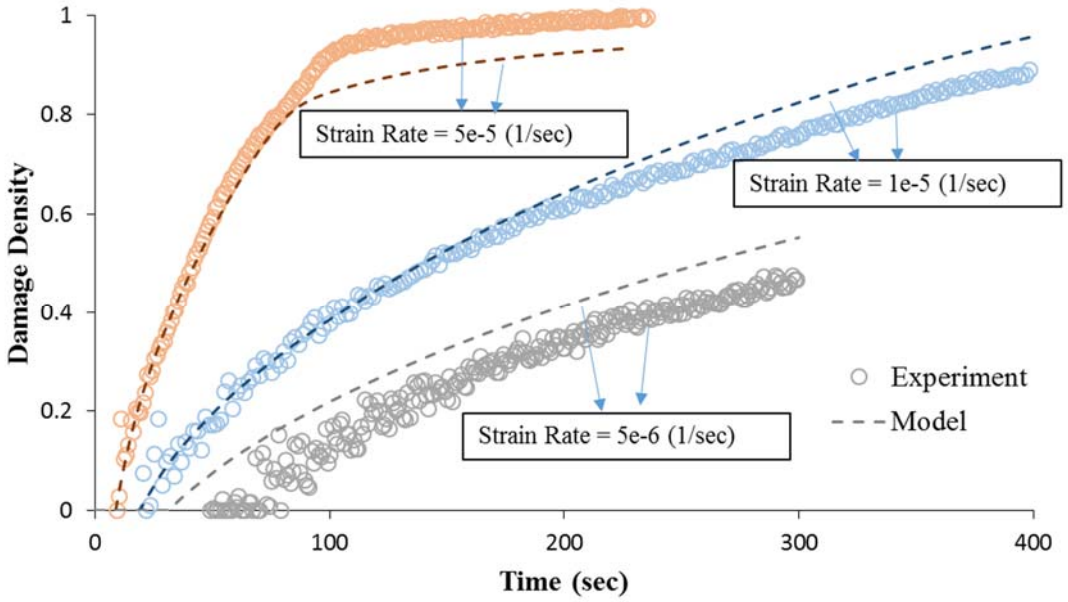

Figure 4.19. The comparison of the calculated damage density using the viscodamage constitutive relationship to the damage density calculated using the experimental data in the uniaxial constant strain rate test.

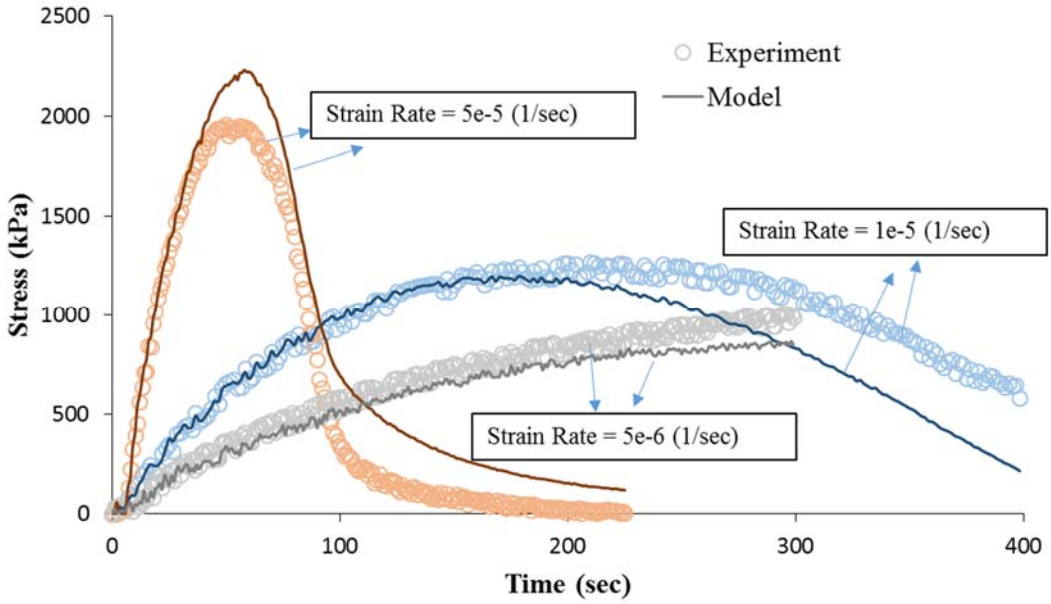

Figure 4.20. The comparison of the calculated nominal stress using the viscodamage constitutive relationship to the experimentally measured stress in the uniaxial constant strain rate test.

4.7 Calibration of the Micro-Damage Healing Constitutive Relationship

Micro-damage healing is another important factor that needs to be accounted for when simulating asphalt concrete response that shows the ability of self-healing (Bhasin et al., 2011). When subjected to cyclic loading, asphalt concrete undergoes the coupled mechanisms of damage and healing. During the rest period between the loading cycles, some of the induced micro-damages during the loading cycle will tend to heal and recover the material strength. This study utilizes the work of Abu Al-Rub et al. (2010) and Darabi et al. (2012a) to incorporate the healing effects on the mechanical response of asphalt concrete.

Similar to what was discussed in Subsection 2.3.1 regarding the continuum damage mechanics, Darabi et al. (2012a) extended the framework to the continuum damage-healing mechanics to enhance the ability of the theory to simulate the micro-damage healing phenomenon in asphalt concrete. They introduced the healing natural configuration as the extension of the effective (undamaged) configuration by incorporating the contribution of the healed damaged areas in bearing and transferring the load. In this case, the stress tensor in the nominal (damaged) and healing configuration is expressed as a function of the damage density, ϕ, and a physically defined healing state variable, h, as:

$$\sigma_{ij} = \left[1-\phi\left(1-h\right)\right]\tilde{\sigma}_{ij}; \quad \phi = \frac{A_r^D}{A_r}; \; h = \frac{A_r^h}{A_r^D} \tag{4.51}$$

where the superimposed " ˜ " designates the healing configuration, and A_r^h is the area of the healed micro-damage. The term, h, represents the healed fraction of the total damaged area that ranges from 0 to 1, for which $h = 0$ indicates no healing and $h = 1$ means that all damage is healed. The constitutive relationship for micro-damage healing is expressed as follows (Abu Al-Rub et al., 2010):

$$\dot{h} = \Gamma^h \left(1-\phi\right)^{b_1} \left(1-h\right)^{b_2} \tag{4.52}$$

where Γ^h is the micro-damage healing fluidity parameter that controls the rate of healing, and b_1 and b_2 are the parameters that control the effect of damage and healing

history, respectively. In order to reduce the number of material parameters, in the above equation it is assumed that $b_1 = b_2 = b$.

The material parameters associated with the micro-damage healing constitutive relationship are identified using repeated creep-recovery test in tension with variable rest periods in between the loading cycles, as described in Subsection 3.4.3. This test is conducted at an intermediate temperature (19°C) to ensure that the healing mechanism occurs. The stress level during the loading cycles of this test is constant. Based on the theory, the micro-damage healing happens when the load is removed and the material is in the rest period. Therefore, it is expected that as the rest period increases the effect of micro-damage healing considerably increases. As a result, the micro-damage healing relationship is calibrated against the RCRT-VRT, where the material is subjected to rest periods in variable times.

The stress level applied in this test is 620 kPa. Figure 4.21 represents the measured strain and the calculated strain response when only viscoelastic and viscodamage constitutive relationships are used without including the micro-damage healing effect ($h = 0$). Then the micro-damage healing material parameters can be characterized using the difference between the measured and calculated strain responses when no healing is considered. Figure 4.22 represents the case when the micro-damage healing effect is considered in the calculation of the strain response. Table 4.9 lists the material parameters that are identified for the micro-damage healing constitutive relationship.

Table 4.9. The identified micro-damage healing material parameters using the RCRT-VRT at 19°C.

$\Gamma^h \left(1/\text{sec}\right)$	b
0.03	3.0

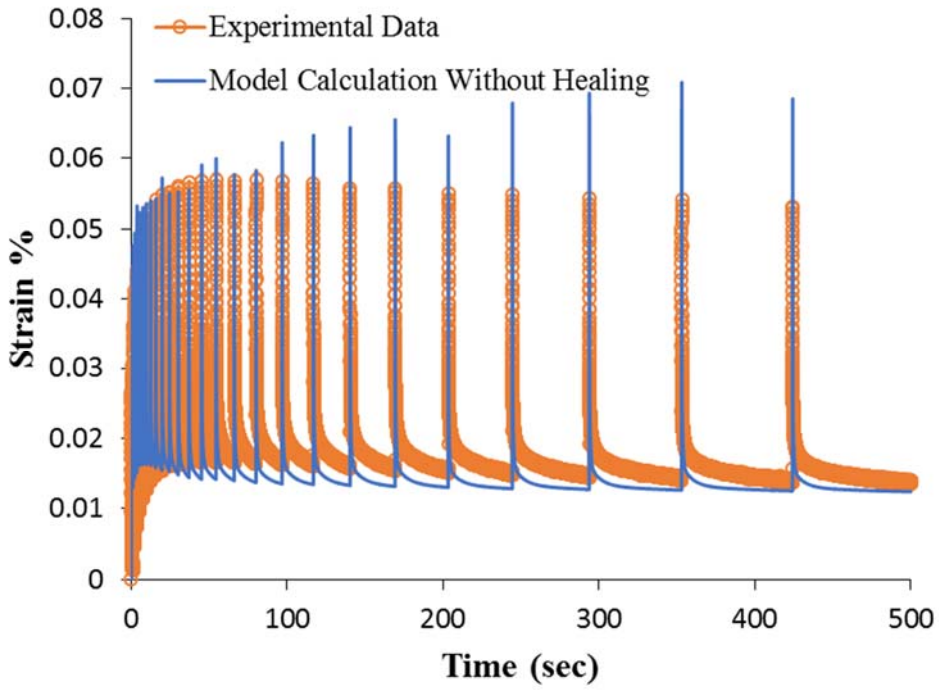

Figure 4.21. The measured and calculated strain responses during the repeated creep-recovery test with variable resting periods. The calculated strain response is for the case when the micro-damage healing is not included. The amount of calculated strain that deviates from the measured strain is used to characterize the micro-damage healing material parameters.

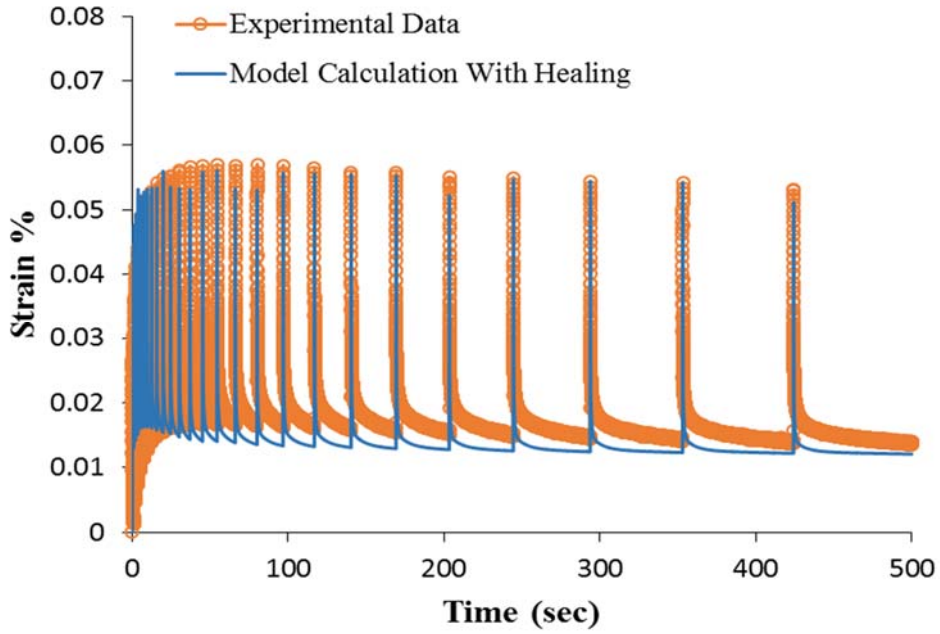

(a)

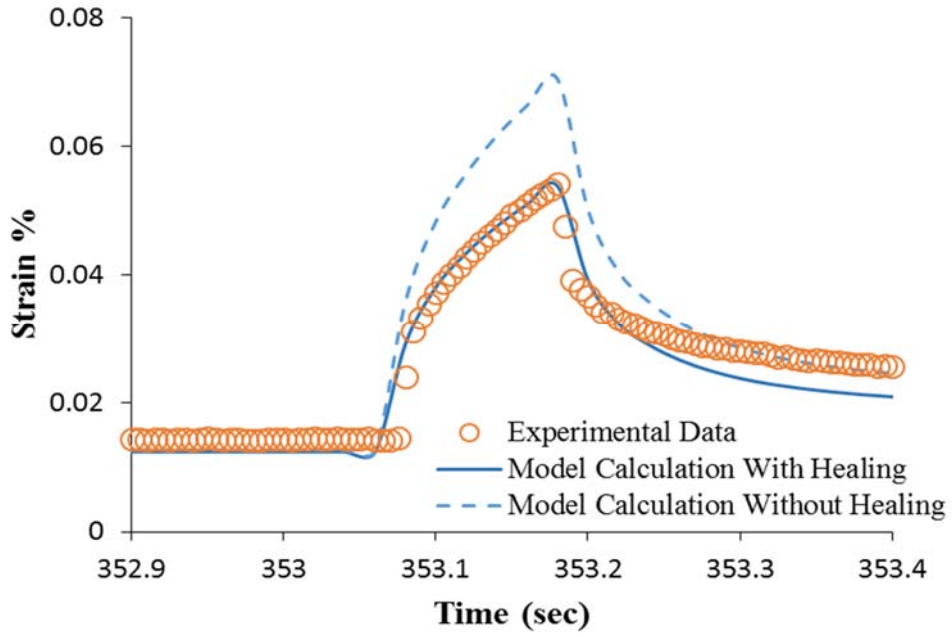

(b)

Figure 4.22. (a) The measured and calculated strain responses during the RCRT-VRT at 19°C. The calculated strain response is for the case when the micro-damage healing is included. (b) The comparison of the two cases with and without consideration of the micro-damage healing effect for one loading cycle.

4.8 Summary

This section covered the systematic procedure to identify all the material parameters associated with the oxidative aging-mechanical constitutive relationship. The microstructures presented herein did not include interconnected air voids. Therefore, the oxygen transport model did not account for convection flow; and the only mechanism for oxygen transport into asphalt concrete was by diffusion, which was assumed to occur only from the top boundary of the microstructure. The effective oxygen diffusivity of the asphalt concrete was calculated using the computational approach. Then, 2D and 3D microstructural RVEs were used to simulate the oxygen diffusion problem within the asphalt microstructure. Consequently, the aging state variable was identified using the experimental data of the dynamic modulus test. This test was performed on unaged, 3-month aged, and 6-month aged specimens to characterize the aging state variable at different ages.

The linear viscoelastic properties (Prony series coefficients and time-temperature shift factors) were characterized using dynamic modulus test results. The nonlinear viscoelastic parameters (or stress-dependent parameters) were calibrated using the RCRT-VS with confinement pressure at high temperature. The relationship of the nonlinear parameters with triaxiality ratio was discussed. The calculated viscoelastic strain response in the RCRT-VS was used to extract the irrecoverable or viscoplastic strain out of the total measured strain response. The extracted viscoplastic response was then used to identify the viscoplastic material parameters. The uniaxial constant strain rate test, conducted at different strain rates and at low temperature, was used to

characterize the viscodamage material parameters. Finally, to incorporate the micro-damage healing effect into the constitutive modeling, healing material parameters were characterized using the RCRT-VRT at the intermediate temperature.

5. VALIDATION OF THE COUPLED OXIDATIVE AGING-MECHANICAL CONSTITUTIVE RELATIONSHIP

5.1 Overview

The previous section explained and illustrated a systematic procedure to identify all the material parameters related to the oxidative aging-mechanical constitutive relationship. Once the aged and unaged material properties are obtained, the response of the asphalt concrete against a variety of laboratory tests can be predicted. Hence, the objective of this section is to use the material parameters, which were identified using the specified laboratory tests in the last section, to predict the response of asphalt concrete against additional tests that have not been used in the calibration process. All the experimental tests used in this work were performed on mixture 1 of the Federal Highway Administration through ARC. The tests in compression were conducted at Texas A&M University, and the tests in tension were performed at North Carolina State University. Table 5.1 lists the experiments used to validate the aging-mechanical constitutive relationship.

Table 5.1. List of tests to validate the coupled oxidative aging-mechanical constitutive relationship.

Procedure	*Loading Mode*	*Temperature (°C)*	*Aging Condition*	*Loading Level*
Repeated Creep-Recovery (RCRT-VS)	Compression	40, 55	3, 6 months	Varies
Purpose:	Validation of Aging-Viscoelastic-Viscoplastic Constitutive Relationship			
Repeated Creep-Recovery (RCRT-VRT)	Tension	19	3, 6 months	825 kPa
Purpose:	Validation of Aging-Viscoelastic-Viscodamage-Healing Constitutive Relationship			
Cyclic Displacement-Controlled Test	Tension	5, 19	3, 6 months	Varies
Purpose:	Validation of Aging-Viscoelastic-Viscodamage-Healing Constitutive Relationship			

5.2 Validation against the Repeated Creep-Recovery Test at Variable Stress Level

The ultimate goal of this study is to develop a unified continuum model to predict the behavior of asphalt concrete when subjected to oxidative aging. Pavements are normally subjected to repeated traffic loading during their service life. Therefore, simulating repeated creep-recovery tests of aged asphalt concrete in the laboratory is important. The description of the repeated creep-recovery test at variable stress level and the material characterization were discussed in Subsection 3.4.2. In this test, the loading time and unloading time is constant. This test was conducted at high temperatures, 40 and 55°C, to ensure that the material response is governed by viscoelasticity and viscoplasticity, and the micro-damage effect is negligible. A constant confinement stress of 140 kPa is applied during this test. The applied axial stress history was described in Subsection 3.4.2. Three different asphalt mixtures with 4%, 7%, and 10% air void

content are validated in this subsection. In order to predict the strain response of the material during the RCRT-VS, the nonlinear viscoelastic-viscoplastic constitutive relationship is used. When calculating the aged material response, the oxidative aging constitutive relationship is also included in the computation.

Figure 5.1(a) to (c) represent the comparison of the experimental data and model calculation at 55°C. In these figures, the results and calculations for asphalt concretes with 4%, 7%, and 10% air void content are presented, respectively. In each of these figures, the experimental results and model predictions for aged asphalt specimens are shown. Figure 5.1(a) to (c) show that the strain response calculated with the proposed aging-mechanical constitutive relationship compares very well with the experimental measurements. It should be emphasized that the material parameters to calculate the strain response of the aged asphalt samples are identified from different tests as discussed in Section 4. The strain responses presented in Figure 5.1(a) to (c), which correspond to the first two loading blocks of the RCRT-VS, verify that the proposed aging-mechanical constitutive relationship is capable of predicting the material response at 55°C, when only viscoelastic and viscoplastic behavior is concerned. The effect of aging on the strain response of the asphalt concrete is clear in these figures. As the material ages, the amount of creep strain during each loading cycle decreases. Moreover, the effect of aging on the strain response is not significant at the first loading block (the first eight loading cycles). However, when the loading time increases, the influence of aging becomes noteworthy, as it decreases the accumulated permanent strain substantially. The reason is stiffening of the asphalt due to oxidation. Therefore, the

modulus of the aged asphalt concrete increases. As a result, it exhibits less strain when subjected to the same amount of stress level.

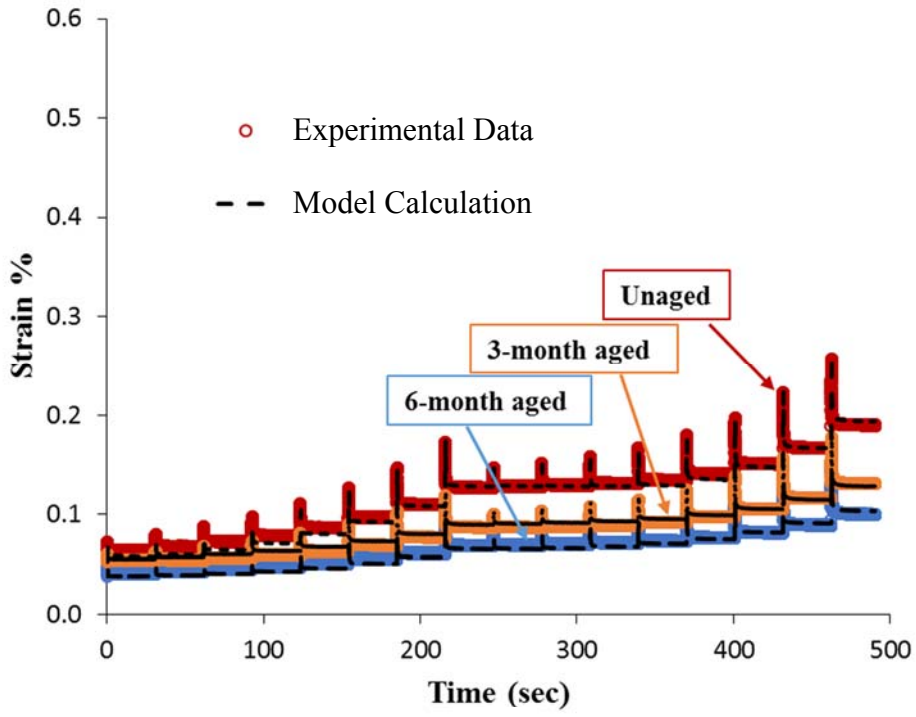

(a)

Figure 5.1. The comparison of the experimental measurements and model predictions of strain response of aged and unaged asphalt concrete at 55°C during the RCRT-VS after two loading blocks. The strain responses are presented for asphalt mixtures with (a) 4% air void, (b) 7% air void, and (c) 10% air void content.

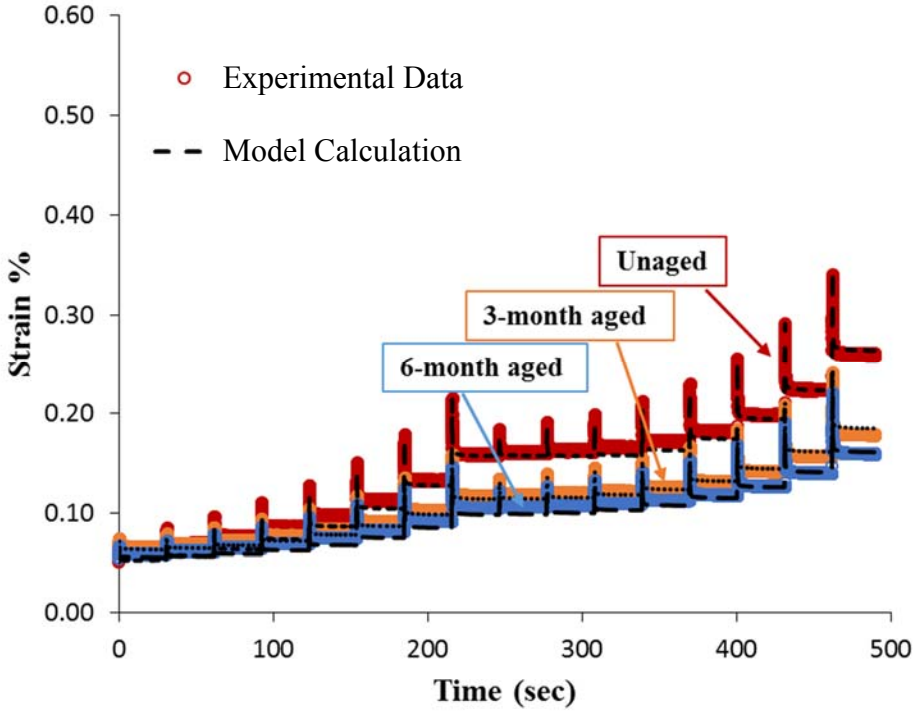

(b)

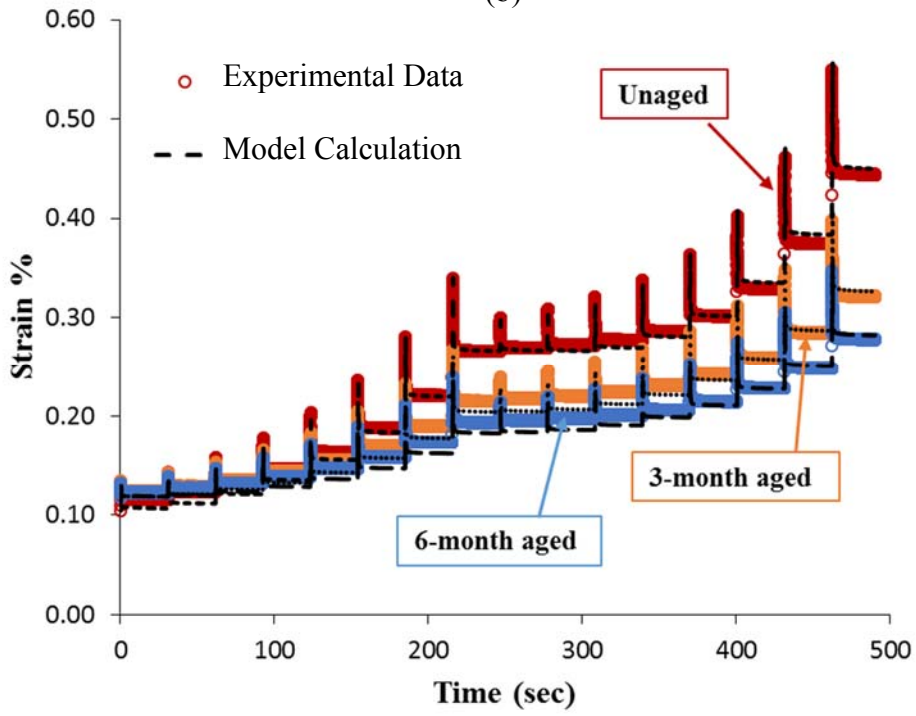

(c)

Figure 5.1. Continued.

Another interesting remark regarding the counteracting effects of oxidative aging and air void contents on the strain response can be seen in Figure 5.2(a) to (c). These figures compare the air void content effect on the strain response of asphalt concrete during the RCRT-VS with the same aging time. Oxidative aging reduces the amount of accumulated strain, while an increase in air void content increases the magnitude of strain response. Such trends can be easily seen from Figure 5.2(a) to (c). In Figure 5.2(a), where unaged asphalt concrete is presented, the asphalt mixture with the higher air void content exhibits the highest magnitude of strain response. Subsequently, the effect of oxidation can be observed in Figure 5.2(b) and Figure 5.2(c). As material undergoes longer aging time, the difference between strain responses of asphalt mixes with different air void contents significantly reduces. Higher air void contents represent the upper layers of asphalt concrete in a pavement structure, and the lower air void content corresponds to the bottom layers. Therefore, the asphalt concrete specimen with 10% air void can be regarded as the surface asphalt layer of pavements. The trend in Figure 5.2(a) to (c) suggests that oxidative aging has the most influence on the asphalt sample with 10% air void content. This observation is quite valid with the actual phenomenon happening in the field, since upper layers of pavements significantly oxidize and gain more stiffness. Despite this increase in the stiffness of oxidized asphalt mixture, the asphalt oxidation should not be considered as a positive action. This is because, while the stiffness of the material increases, the strain response decreases with the same stress level; therefore, its fracture toughness also decreases. As a result, the oxidized asphalt mixture is prone to undergo damage fracture faster than the unaged one.

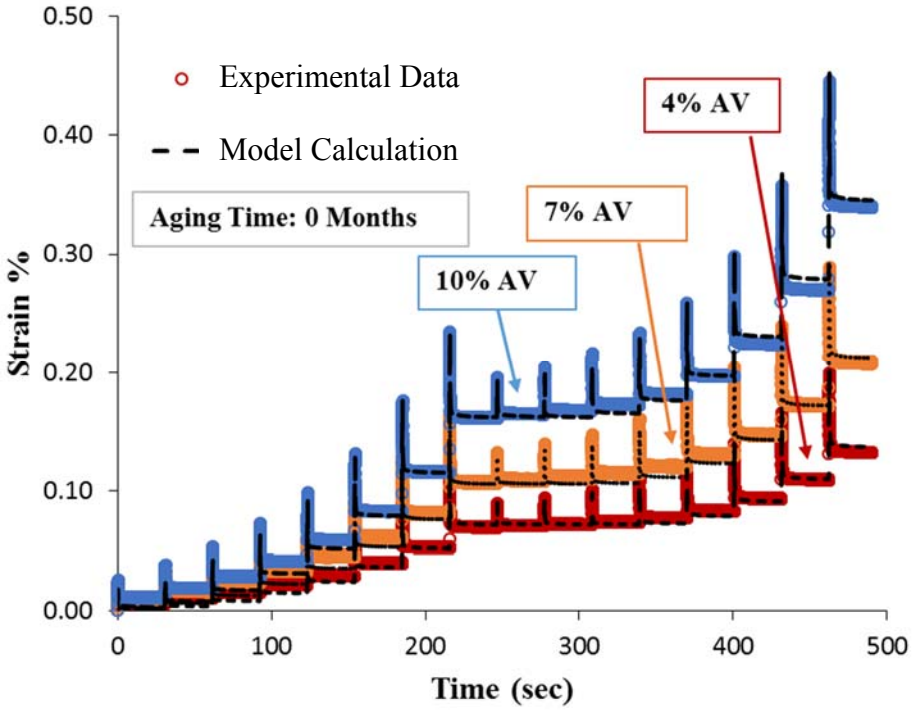

(a)

Figure 5.2. The comparison of the experimental measurements and model predictions of strain response of aged and unaged asphalt concrete at 55°C during the RCRT-VS after two loading blocks. The objective of these figures is to observe the effect of oxidative aging on asphalt mixtures with different air void contents. The strain responses are presented for (a) unaged, (b) 3-month aged, and (c) 6-month aged asphalt mixtures.

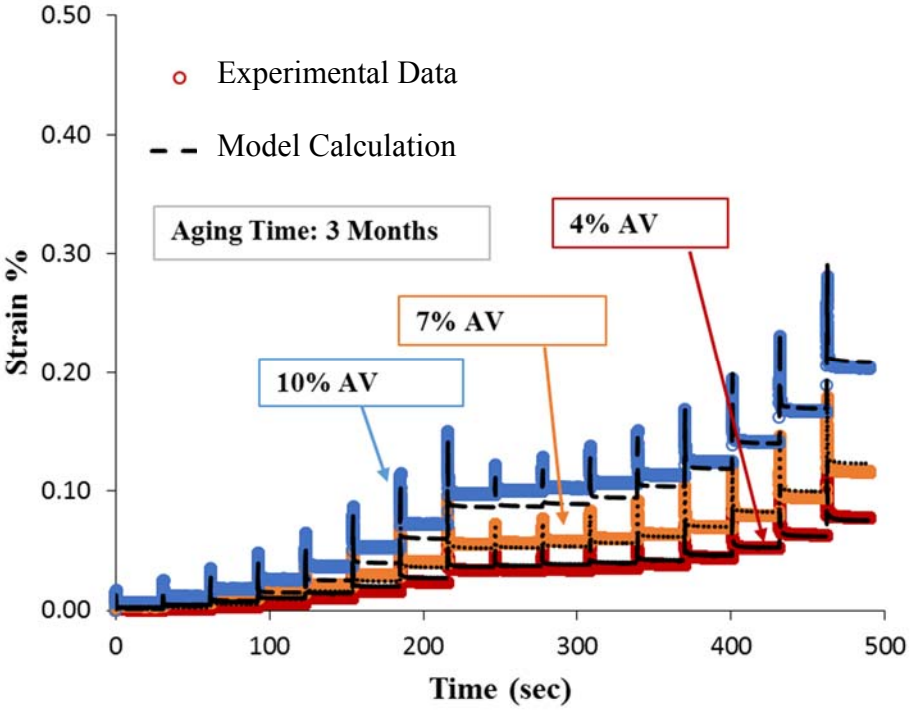

(b)

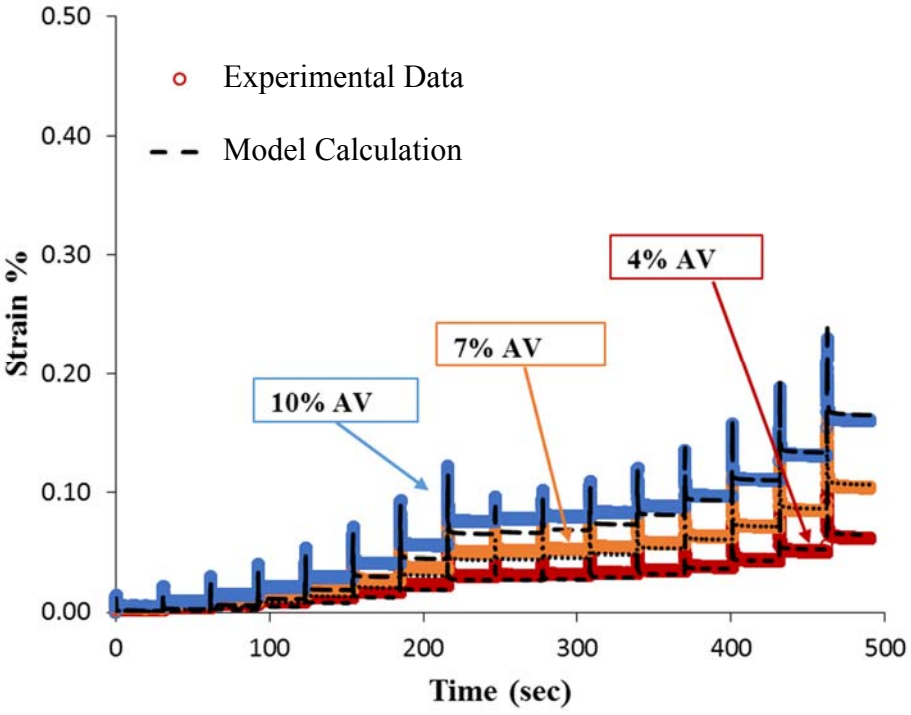

(c)

Figure 5.2. Continued.

Similar to the RCRT-VS results at 55°C, the capabilities of the aging-mechanical constitutive relationship are investigated in predicting the strain response at a lower temperature (40°C). Figure 5.3(a) to (c) show the comparison of the measured strain and the calculated strain response during the first two blocks of the RCRT-VS at 40°C. These figures verify that the proposed modeling framework can predict the material response of the aged material subjected to creep-recovery cycles with variable stress levels.

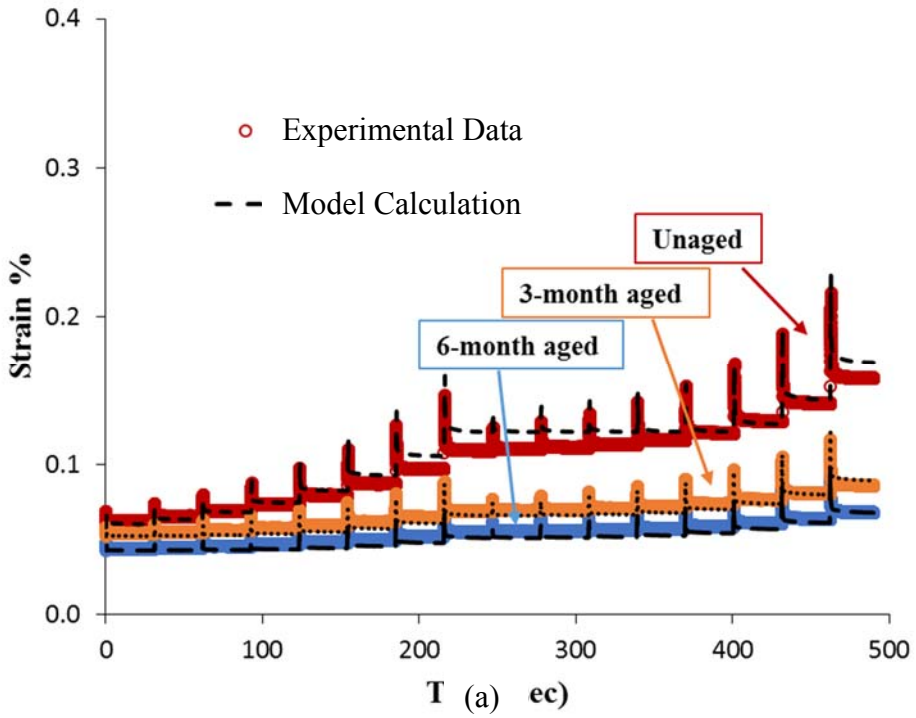

Figure 5.3. The comparison of the experimental measurements and model predictions of strain response of aged and unaged asphalt concrete at 40°C during the RCRT-VS after two loading blocks. The strain responses are presented for asphalt mixtures with (a) 4% air void, (b) 7% air void, and (c) 10% air void content.

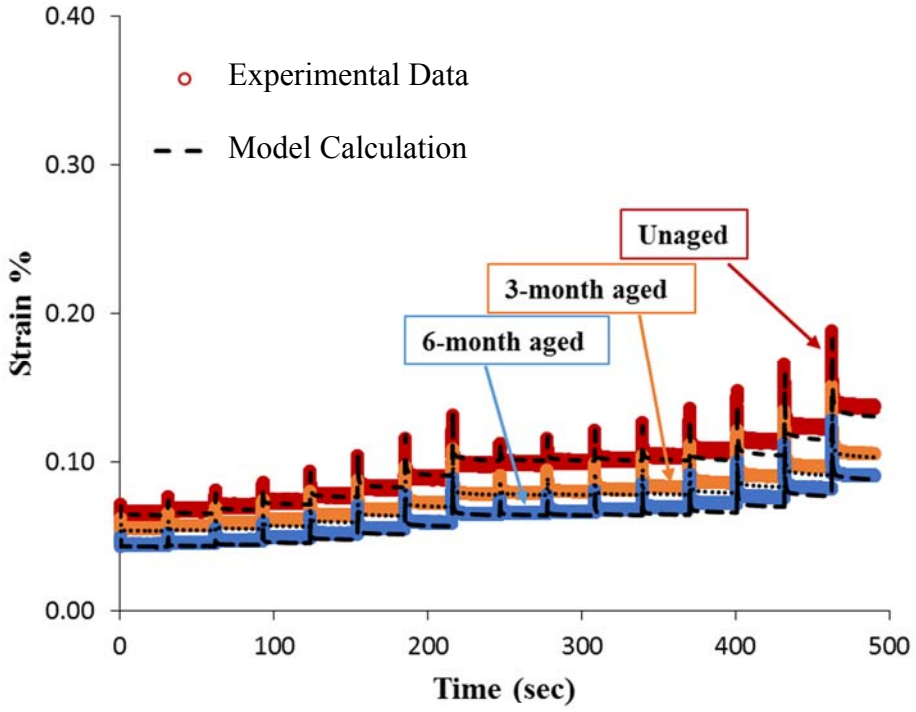

(b)

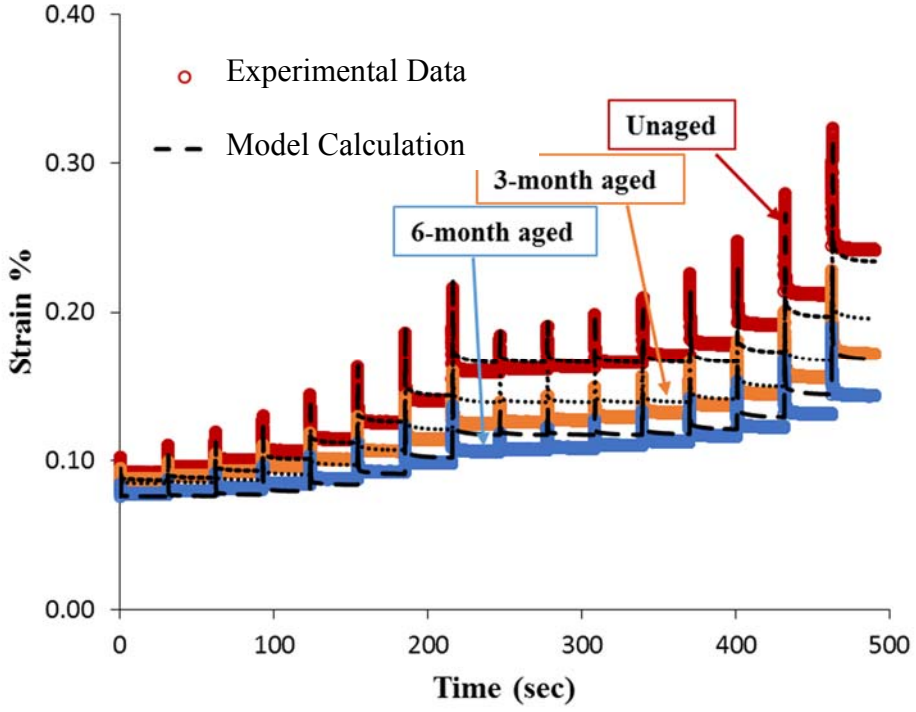

(c)

Figure 5.3. Continued.

5.3 Validation against the Repeated Creep-Recovery Test with Variable Resting Time

The description of the RCRT-VRT and the material characterization were provided in Subsection 3.4.3. Since this experiment was conducted at an intermediate temperature (19°C), the mechanism of the induced distress is captured by viscodamage and micro-damage healing coupled with the nonlinear viscoelastic constitutive relationship. Multiple creep and recovery cycles are applied in this test with constant stress level. However, the period of the recovery at each cycle changes. It was previously discussed in subsection 4.7 that the micro-damage healing happens when the load is removed and the material is in the rest period. Therefore, it is expected that as the rest period increases, the effect of micro-damage healing considerably increases. As a result, the objective of this test is to investigate the capabilities of the proposed aging-mechanical constitutive modeling framework in predicting the strain response, focusing on viscodamage and micro-damage healing behavior of the aged asphalt concrete specimens.

The magnitude of the constant applied stress in the RCRT-VRT is 825 kPa for aged and 620 kPa for unaged samples. Figure 5.4 shows the comparison of the experimentally measured strain response and the strain calculated using the coupled aging-viscoelastic-viscodamage-healing constitutive relationship. In Figure 5.4(a), the strain response of the 3-month aged asphalt mixture is compared with the model predictions, and Figure 5.4(b) represents the model calculation and experimental data for 6-month aged asphalt concrete.

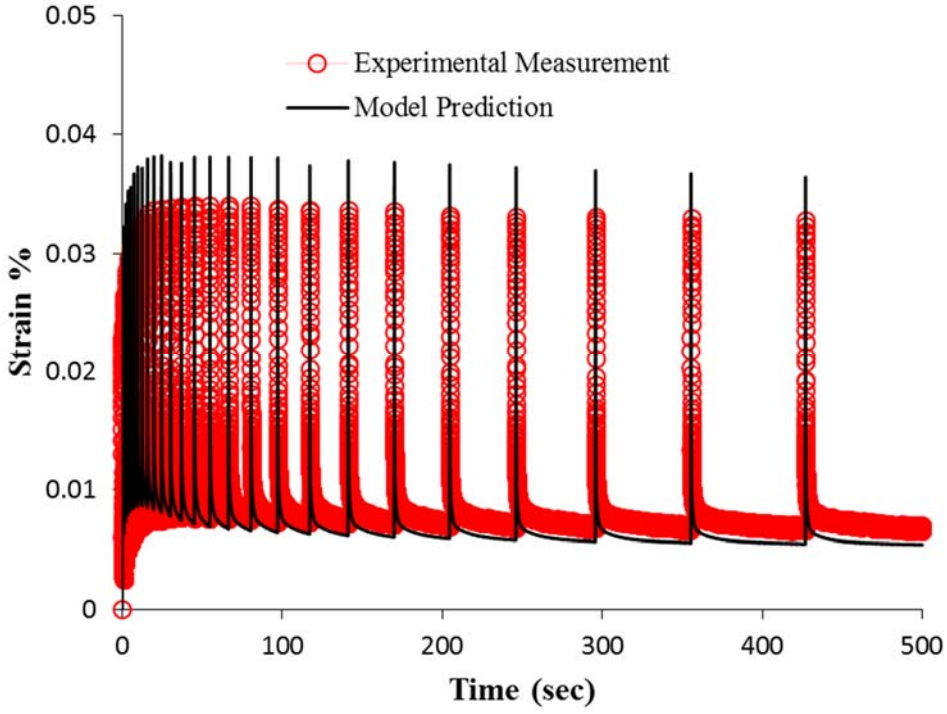

(a)

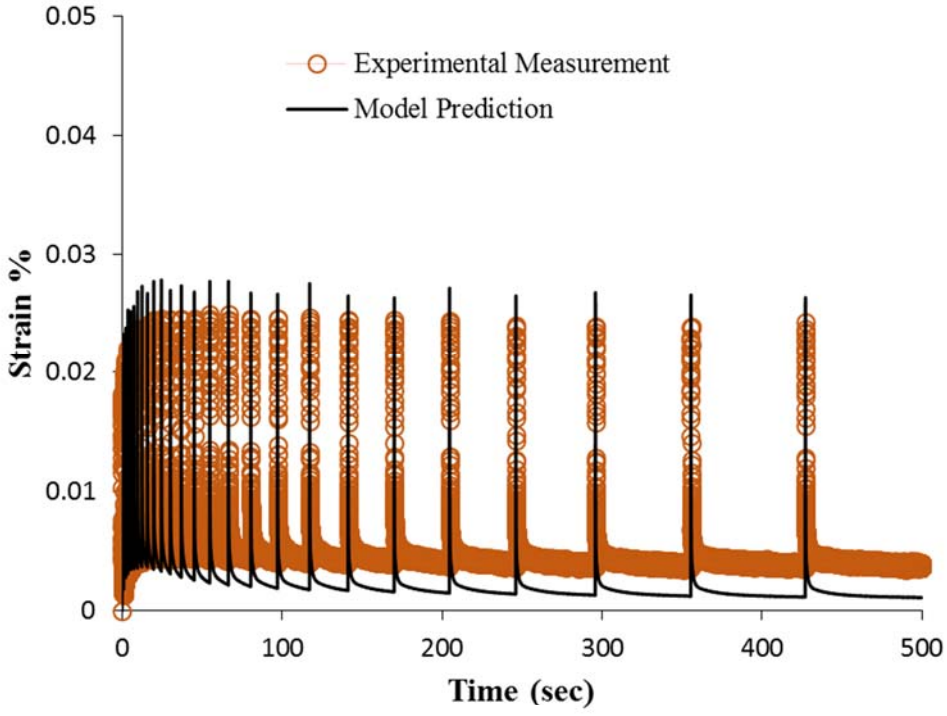

(b)

Figure 5.4. The comparison of the model calculations and experimental data of strain response in the RCRT-VRT at 19°C for (a) 3-month aged and (b) 6-month aged asphalt mixtures.

Figure 5.5 illustrates the strain response comparison of the aged and unaged asphalt mixtures in the RCRT-VRT. It is noted that the stress input for the unaged asphalt mixture is smaller than the applied stress on the aged mixtures. Even with the higher applied stress level, the aged asphalt concrete exhibits lower strain response, and as the aging time increases, the strain amplitude decreases. As also previously discussed, this is because the stiffness of the material significantly increases due to oxidative aging. Moreover, the trend of the irrecoverable or viscoplastic strain in this figure shows that after an initial jump, the viscoelastic strain remains constant and does not accumulate in the subsequent loading cycles. This verifies the initial assumption that at an intermediate temperature (i.e., 19°C in this test), the viscoplastic strain is negligible and all the behavior can be captured by only viscoelastic and viscodamage constitutive relations.

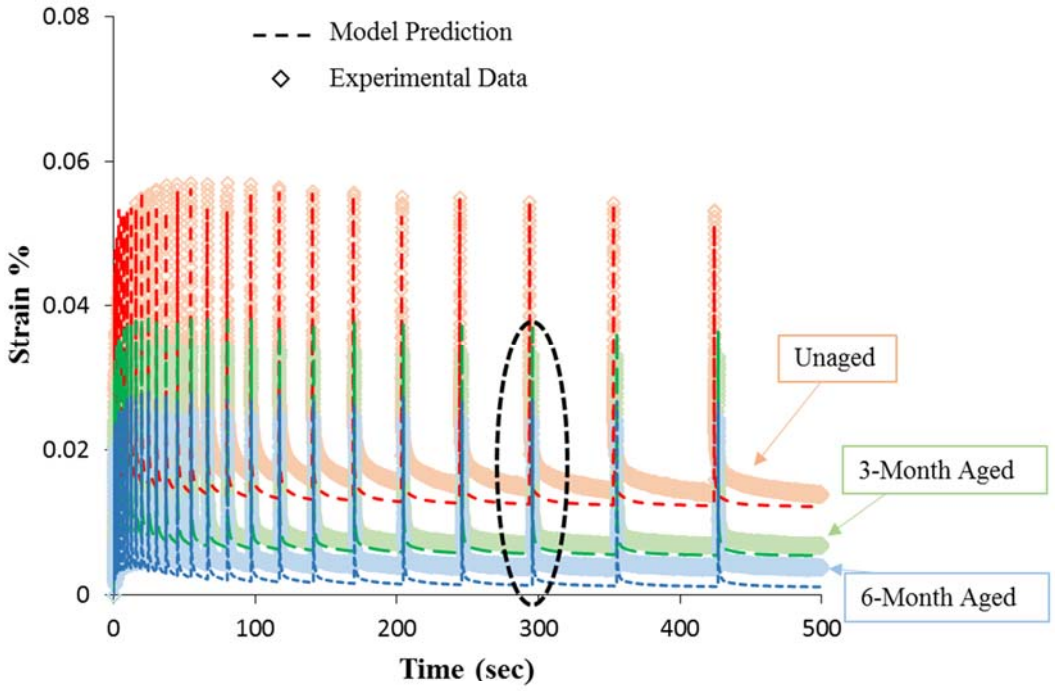

(a)

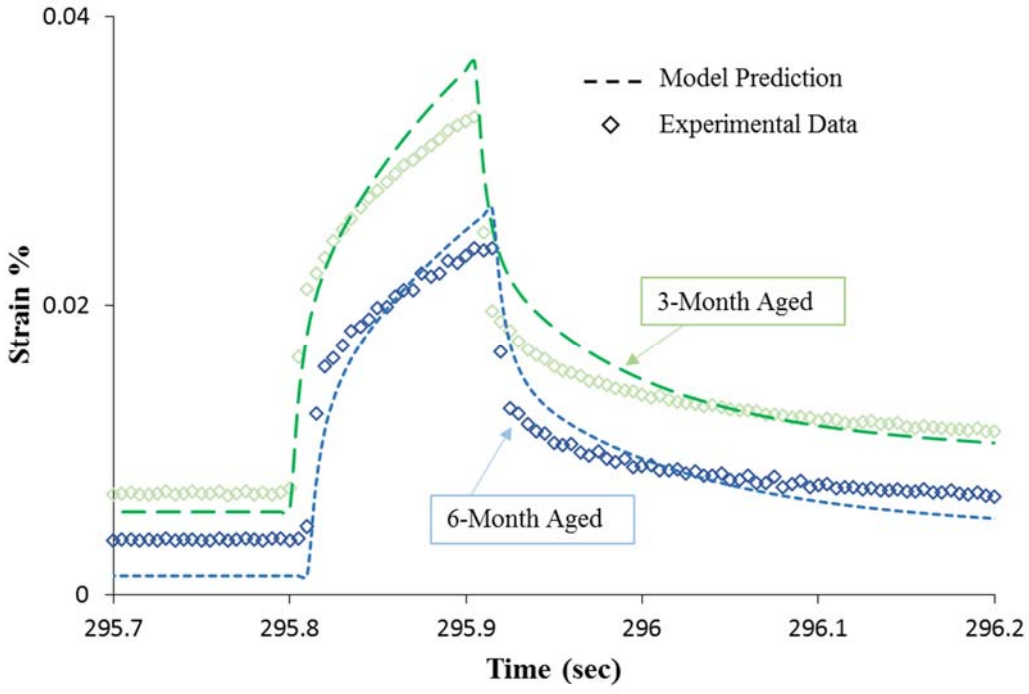

(b)

Figure 5.5. The comparison of the model prediction and experimental measurements in the RCRT-VRT at 19°C for (a) different aging times and (b) different aging times shown for one loading cycle.

5.4 Validation against the Cyclic Displacement-Controlled Test

The procedure and characteristics of this test were described in Subsection 3.4.5. In this test, a cyclic displacement is applied at the end plate of the specimen. The average strain measured at the LVDTs is recorded as the strain input. Although the amplitude of the cyclic applied displacement at the end plates is constant, the recorded strain on the specimen does not have a constant amplitude and increases with time. The CDC test was conducted at 5°C and 19°C on the unaged, 3-month aged, and 6-month aged specimens with two different displacement amplitudes for each aging time. The CDC test is normally used to investigate the fatigue behavior of asphalt mixture under several hundred loading cycles. Table 5.2 summarizes the specifications of the CDC test.

Since this test is conducted at low and intermediate temperatures, it is anticipated that the material response can be predicted by using only viscoelastic, viscodamage, and micro-damage healing constitutive behavior. In the CDC test the applied displacement, Δ, can be written as:

$$\Delta = \frac{\Delta_{max}}{2}\left[\cos\left(2\pi ft\right) - 1\right] \tag{5.1}$$

where f is the loading frequency, which is 10 cycle/sec in this study. The term, Δ_{max}, is the maximum displacement amplitude applied at the end plates. If l is the specimen height, then Δ_{max}/l is the amplitude of the average strain applied to the specimen. However, to minimize the edge effect in the calculations, the average measured on-specimen strain of the LVDTs is considered as the strain input. In fact, the term

"measured initial on-specimen strain" in Table 5.2 refers to the average recorded strain of the LVDTs in the first 50 cycles of the test.

Table 5.2. The summary of the specifications of the CDC test to validate the fatigue behavior of aged asphalt concrete specimens.

Test No.	Aging condition	Temperature (°C)	Measured initial on-specimen strain (microstrain)	Loading frequency (cycle/sec)
1	Unaged	5	122	10
2			75	10
3	3 Months	5	114	10
4			106	10
5	6 Months	5	105	10
6			103	10
7	Unaged	19	340	10
8			260	10
9	3 Months	19	290	10
10			200	10
11	6 Months	19	180	10
12			155	10

5.4.1 CDC Test at 5°C

It is noted that only the upper and lower strain/stress bands are presented in the figures hereafter. Figure 5.6(a) and Figure 5.7(a) represent the measured upper and lower strain bands and the strain amplitude for the unaged material of Tests No.1 and No.2, respectively. Subsequently, Figure 5.6(b) and Figure 5.7(b) show the comparison of the recorded upper and lower stress bands and the stress amplitude with the model calculations. The constitutive modeling framework appears to predict the stress response of the material fairly well for both cases of the unaged asphalt concrete. In Figure 5.6(a) and Figure 5.7(a), the cycle that the strain amplitude begins to dramatically increase is considered to be the failure cycle. In fact, at this point the material cannot tolerate the applied load such that the stress amplitude undergoes a sudden decrease. In other words, at this failure point, the asphalt specimen has lost a great deal of stiffness due to initiation of micro-damages. In the model calculations shown in Figure 5.6(b) and Figure 5.7(b), the stress amplitudes also start to significantly decrease about the failure point. This verifies that the presented viscoelastic-viscodamage constitutive relationship can reasonably predict the laboratory fatigue performance of the asphalt concrete.

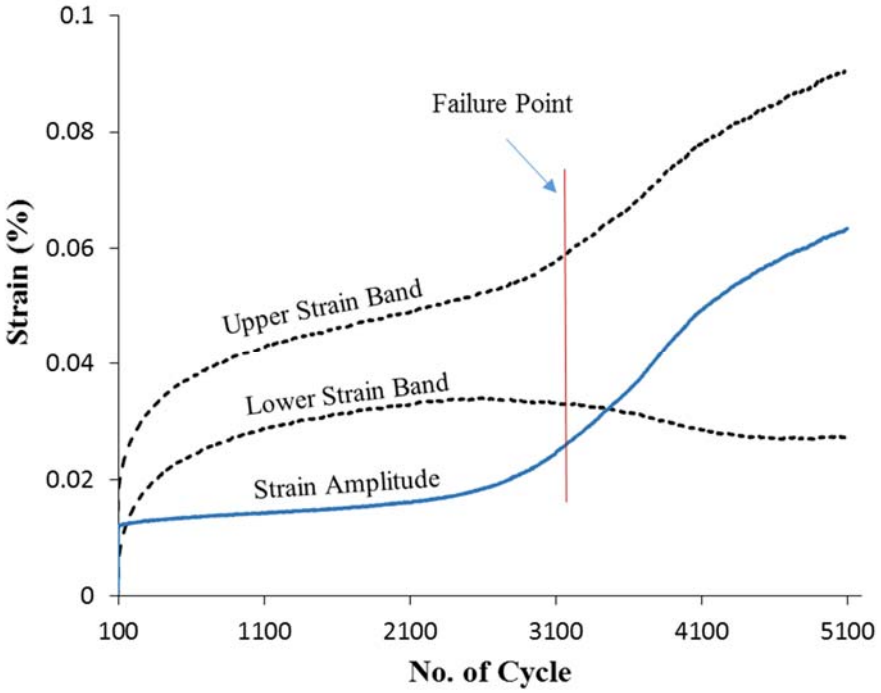

(a)

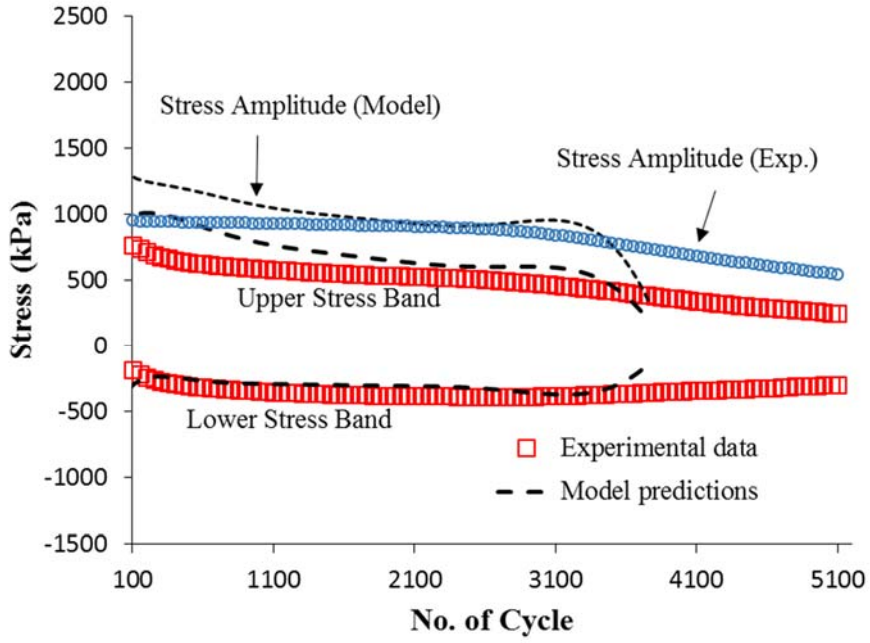

(b)

Figure 5.6. Cyclic displacement-controlled test results at 5°C for unaged asphalt concrete corresponding to Test No.1 in Table 5.2. (a) Measured upper and lower strain bands and the strain amplitude; (b) The comparison of the recorded upper and lower stress bands and the stress amplitude with model predictions.

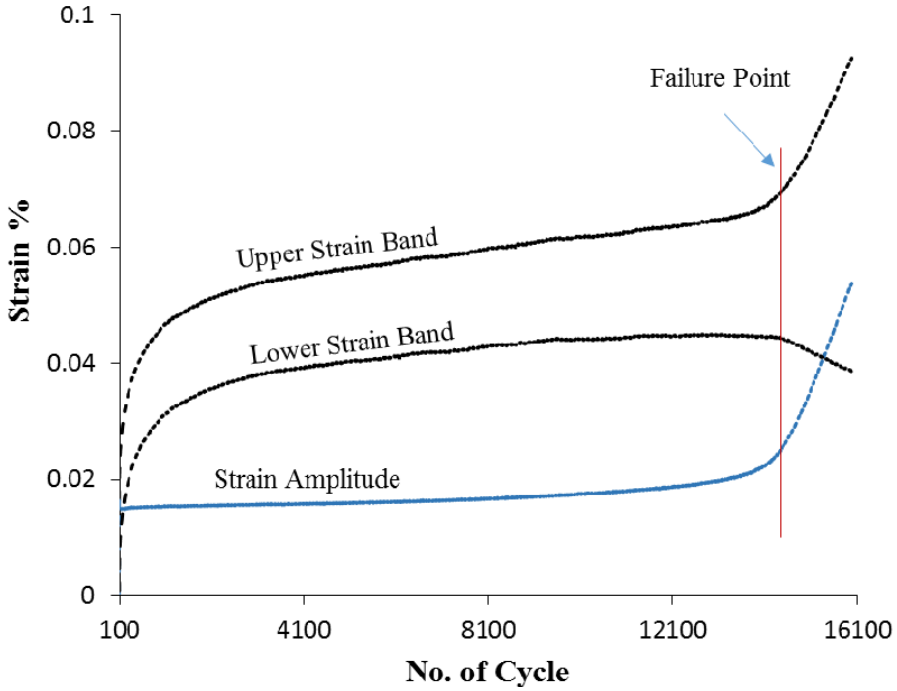

(a)

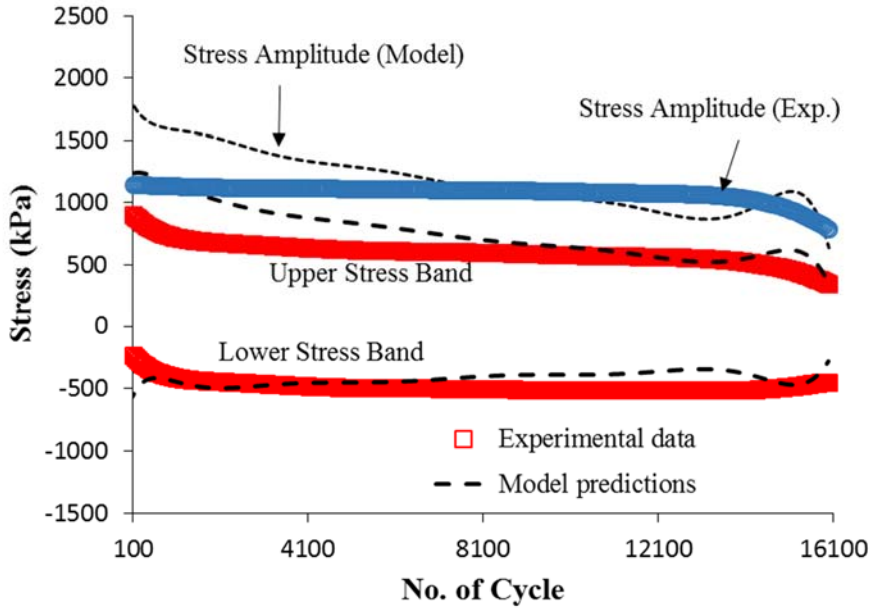

(b)

Figure 5.7. Cyclic displacement-controlled test results at 5°C for unaged asphalt concrete corresponding to Test No.2 in Table 5.2. (a) Measured upper and lower strain band and the strain amplitude; (b) The comparison of the recorded upper and lower stress bands and the stress amplitude with model predictions.

Likewise, the CDC test results of 3-month aged asphalt mixtures are presented in Figure 5.8 and Figure 5.9 corresponding to Tests No.3 and 4, respectively. Figure 5.8(a) and Figure 5.9(a) illustrate the measured upper and lower strain bands and the strain amplitude for 3-month aged material. Subsequently, Figure 5.8(b) and Figure 5.9(b) show the comparison of the recorded upper and lower stress bands and the stress amplitude with the model calculations. The coupled aging-viscoelastic-viscodamage framework predicts the stress response of the material fairly well. Similarly, as shown in Figure 5.8(a) and Figure 5.9(a), the cycle that the strain amplitude begins to intensely increase is considered to be the failure point. Also, in the model calculations shown in Figure 5.8(b) and Figure 5.9(b), stress amplitudes start to significantly decrease at the failure point. This confirms the capability of the proposed aging-mechanical constitutive model in predicting the laboratory fatigue performance of the aged asphalt concrete.

The CDC test results for 6-month aged asphalt concrete corresponding to Tests No.5 and 6 are shown in Figure 5.10 and Figure 5.11. In Figure 5.10(a) and Figure 5.11(a) the measured upper and lower strain bands and the strain amplitude for the 6-month aged material is presented. Then, Figure 5.10(b) and Figure 5.11(b) compares the recorded upper and lower stress bands and stress amplitude with the model predictions. The model calculations indicate that the coupled aging-mechanical constitutive relationship is capable of capturing, first, the degradation of the material due to mechanical loading (i.e., loss of stiffness with increase in loading cycle) and, second, the degrading effects of oxidative aging.

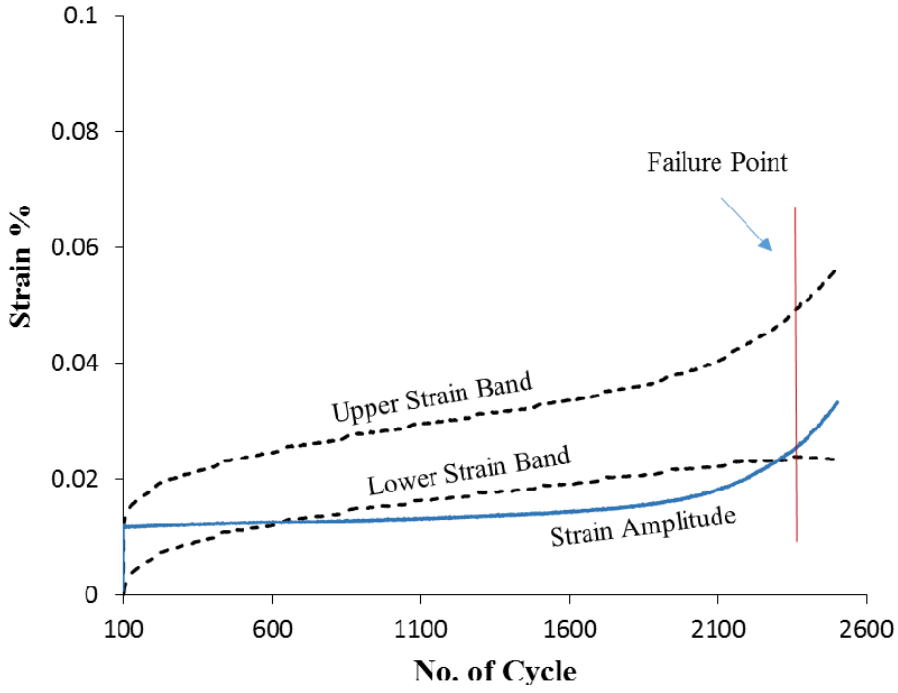

(a)

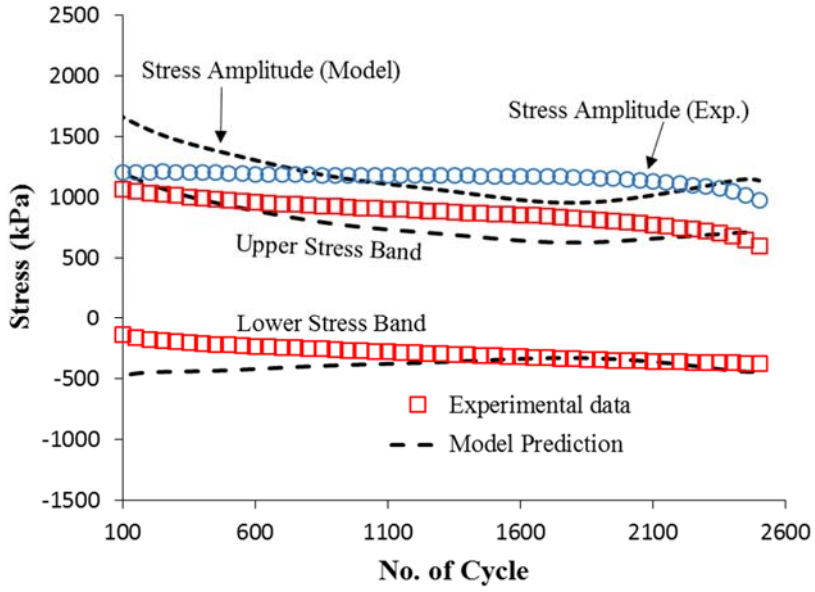

(b)

Figure 5.8. Cyclic displacement-controlled test results at 5°C for 3-month aged asphalt concrete corresponding to Test No.3 in Table 5.2. (a) Measured upper and lower strain bands and the strain amplitude; (b) The comparison of the recorded upper and lower stress bands and the stress amplitude with model predictions.

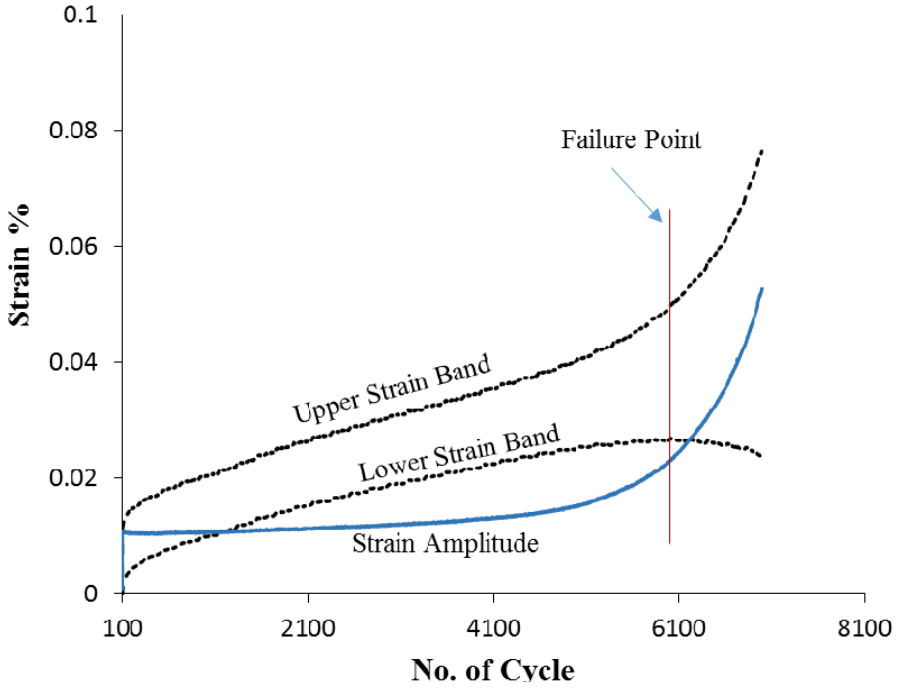

(a)

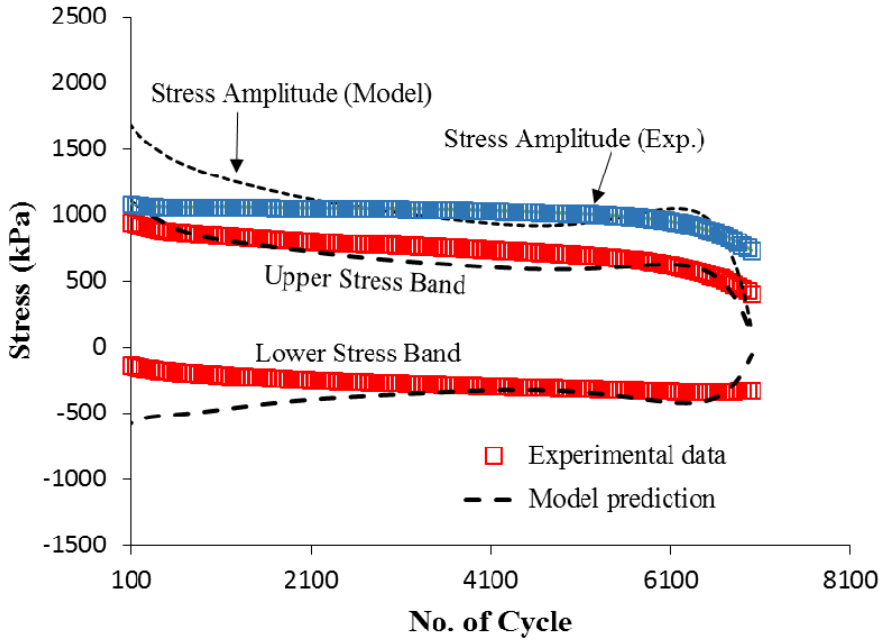

(b)

Figure 5.9. Cyclic displacement-controlled test results at 5°C for 3-month aged asphalt concrete corresponding to Test No.4 in Table 5.2. (a) Measured upper and lower strain bands and the strain amplitude; (b) The comparison of the recorded upper and lower stress bands and the stress amplitude with model predictions.

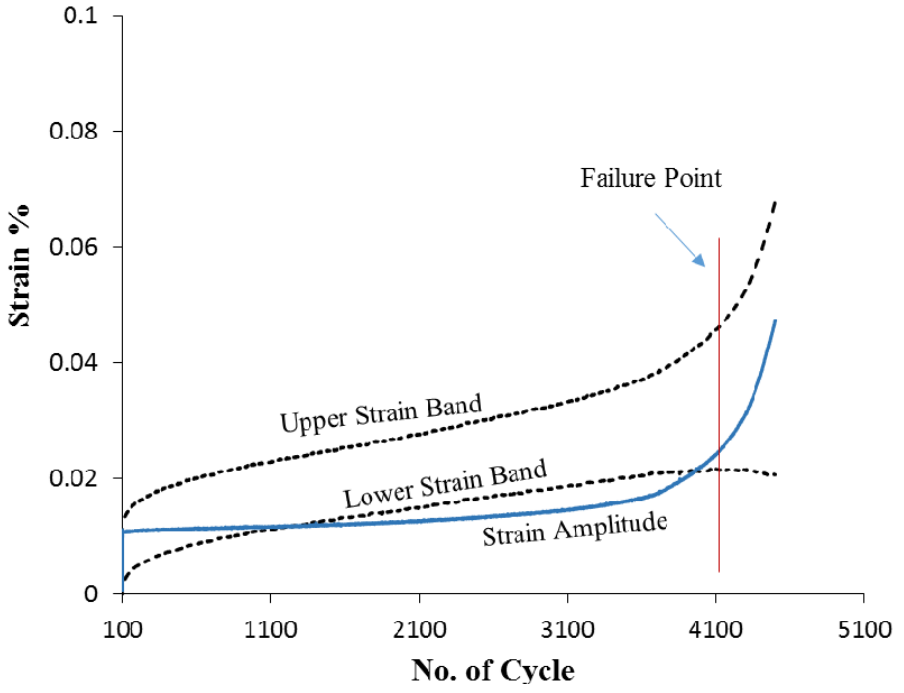

(a)

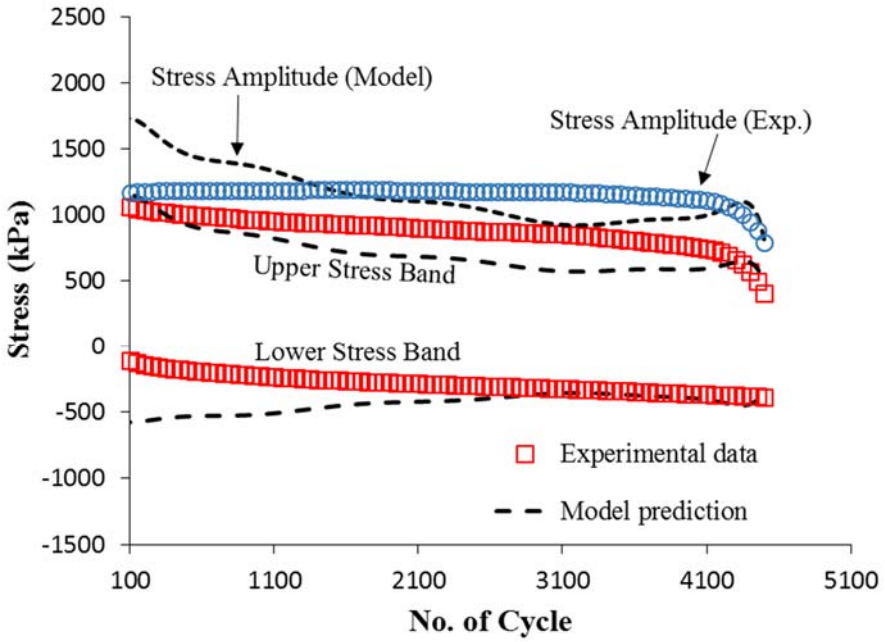

(b)

Figure 5.10. Cyclic displacement-controlled test results at 5°C for 6-month aged asphalt concrete corresponding to Test No.5 in Table 5.2. (a) Measured upper and lower strain bands and the strain amplitude; (b) The comparison of the recorded upper and lower stress bands and the stress amplitude with model predictions.

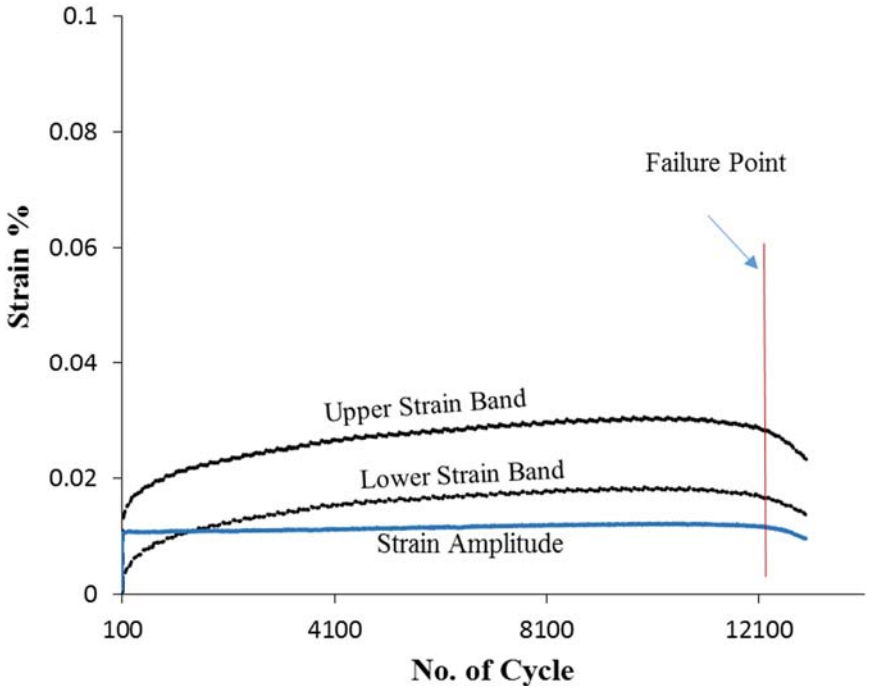

(a)

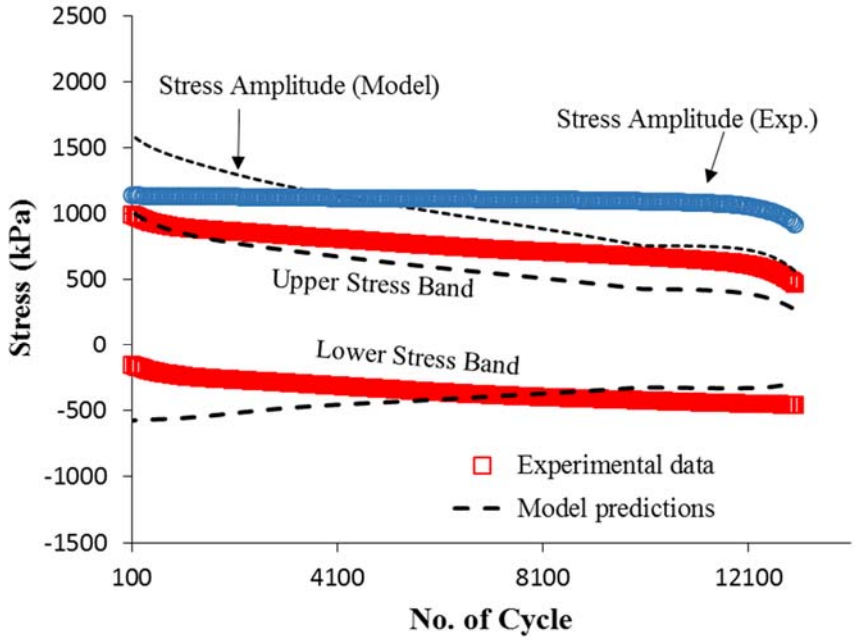

(b)

Figure 5.11. Cyclic displacement-controlled test results at 5°C for 6-month aged asphalt concrete corresponding to Test No.6 in Table 5.2. (a) Measured upper and lower strain bands and the strain amplitude; (b) The comparison of the recorded upper and lower stress bands and the stress amplitude with model predictions.

5.4.2 CDC Test at 19°C

Similar to the comparisons in the previous subsection, the experimental measurements of the cyclic displacement-controlled test at 19°C are compared to the model predictions for unaged and aged asphalt mixtures. When the test is conducted at higher temperature, the general trend is that the transient compliance of the material increases. Therefore, in order for the material to fail after about the same loading cycles compared to the temperature of 5°C, higher strain amplitudes should be applied.

In the case of the unaged asphalt concrete, Figure 5.12(a) and Figure 5.13(a) represent the measured upper and lower strain bands and the strain amplitude corresponding to Tests No.7 and No.8 in Table 5.2, respectively. The loading cycle at which the strain amplitude starts to abruptly increase is considered the failure point. Figure 5.12(b) and Figure 5.13(b) show the comparison of the recorded upper and lower stress bands and the stress amplitude with the model predictions using the viscoelastic-viscodamage-healing constitutive relationship.

Subsequently, Figure 5.14(a), Figure 5.15(a), Figure 5.16(a), and Figure 5.17(a) represent the measured upper and lower strain bands and the strain amplitude of the 3-month and 6-month aged specimens corresponding to Tests No.9, 10, 11, and 12, respectively. Then, the corresponding measured stress responses and the model calculations are shown in Figure 5.14(b), Figure 5.15(b), Figure 5.16(b), and Figure 5.17(b). Comparing the model calculations and the recorded stress responses suggests the proposed aging-mechanical framework is capable of predicting the fatigue performance of the aged asphalt concrete subjected to cyclic displacement loading.

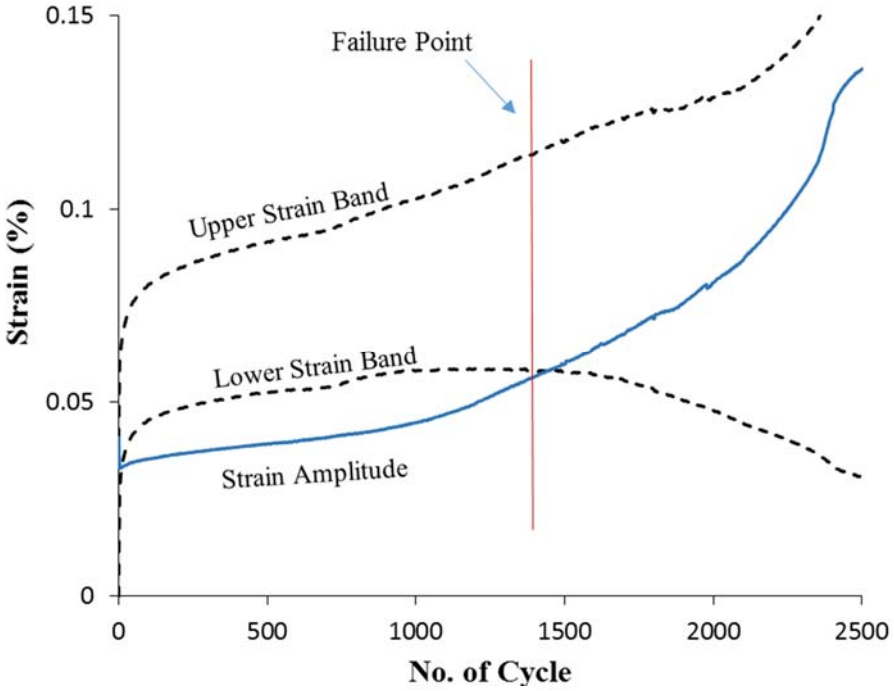

(a)

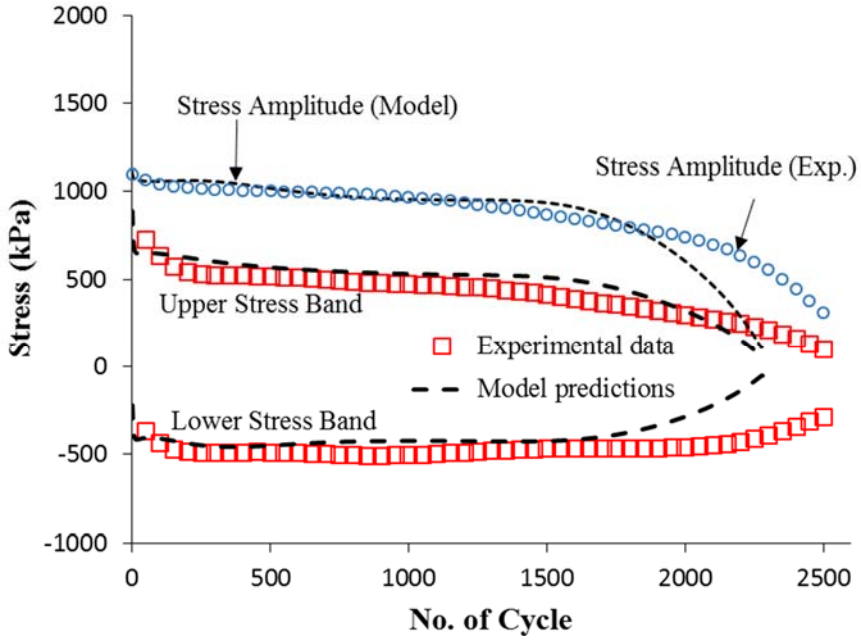

(b)

Figure 5.12. Cyclic displacement-controlled test results at 19°C for unaged asphalt concrete corresponding to Test No.7 in Table 5.2. (a) Measured upper and lower strain bands and the strain amplitude; (b) The comparison of the recorded upper and lower stress bands and the stress amplitude with model predictions.

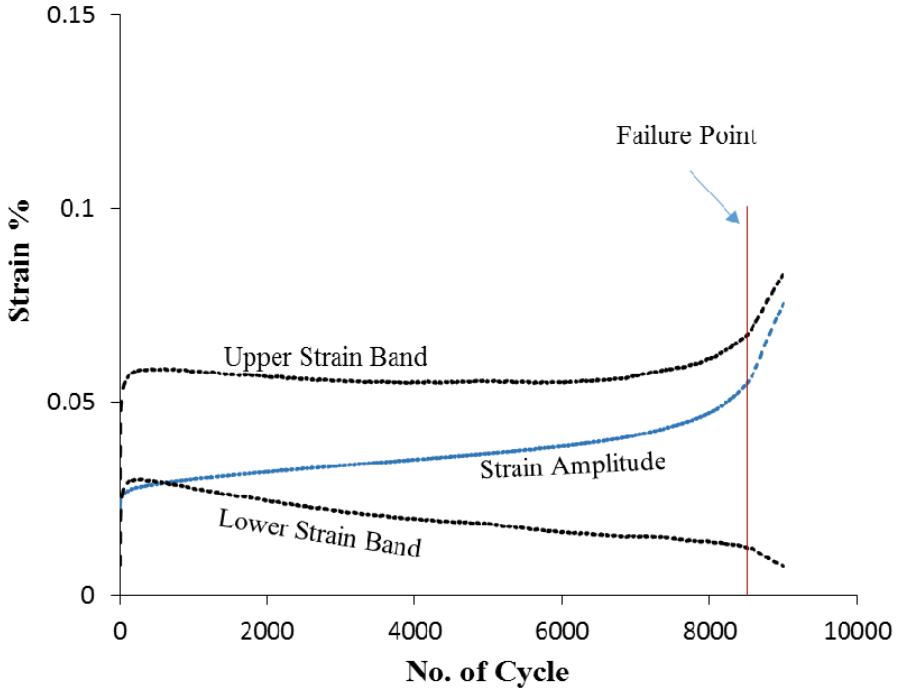

(a)

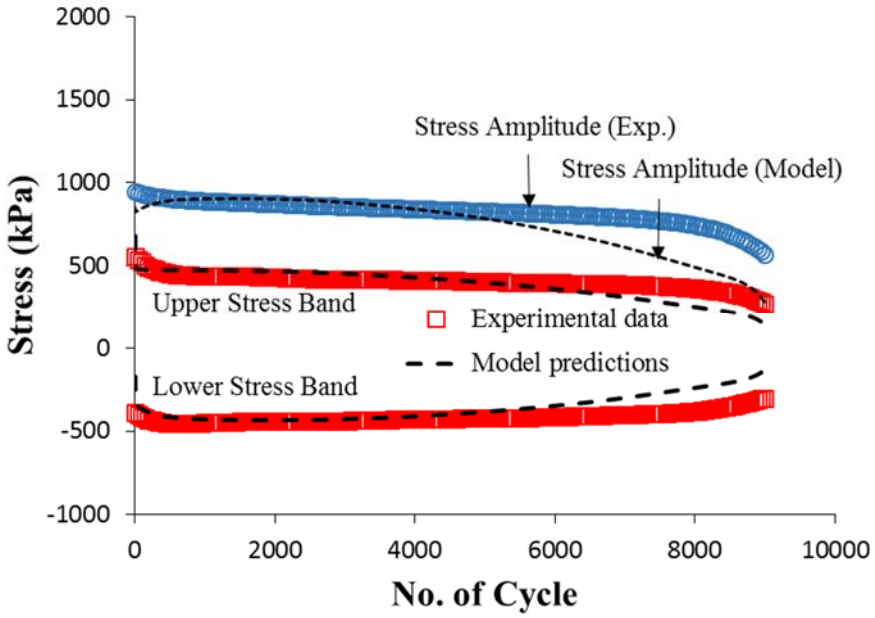

(b)

Figure 5.13. Cyclic displacement-controlled test results at 19°C for unaged asphalt concrete corresponding to Test No.8 in Table 5.2. (a) Measured upper and lower strain bands and the strain amplitude; (b) The comparison of the recorded upper and lower stress bands and the stress amplitude with model predictions.

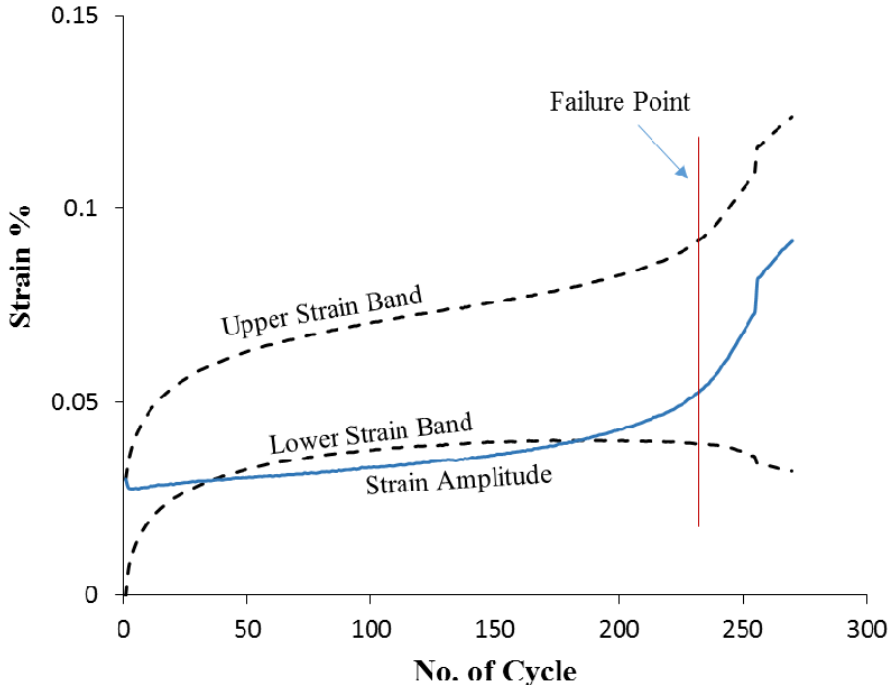

(a)

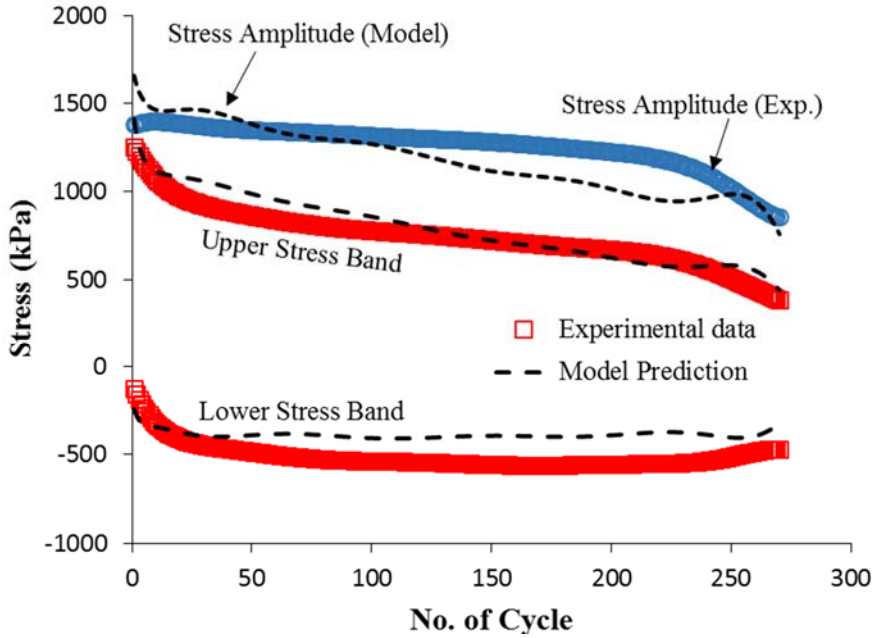

(b)

Figure 5.14. Cyclic displacement-controlled test results at 19°C for 3-month aged asphalt concrete corresponding to Test No.9 in Table 5.2. (a) Measured upper and lower strain bands and the strain amplitude; (b) The comparison of the recorded upper and lower stress bands and the stress amplitude with model predictions.

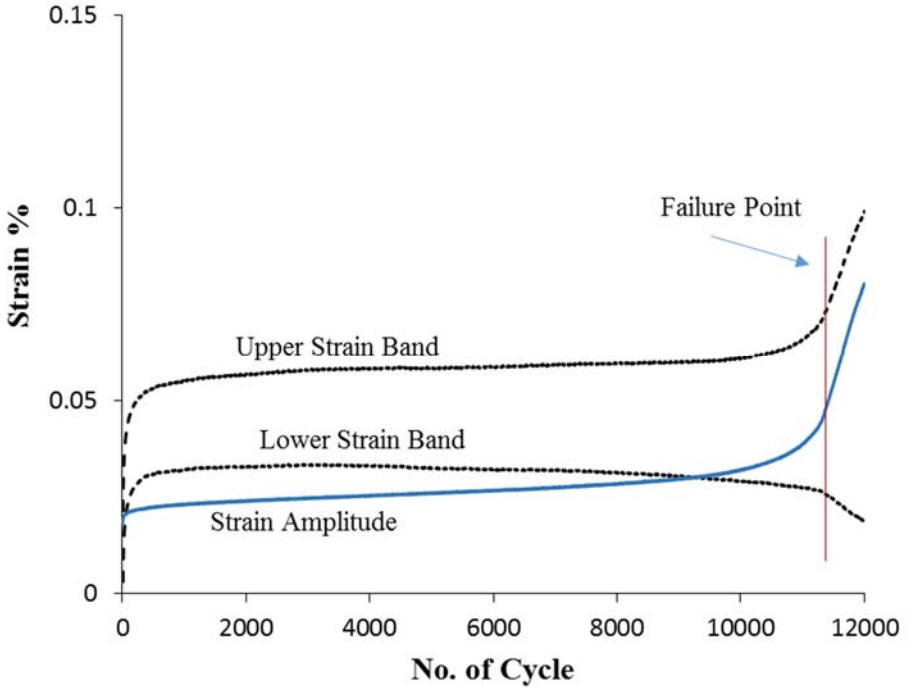

(a)

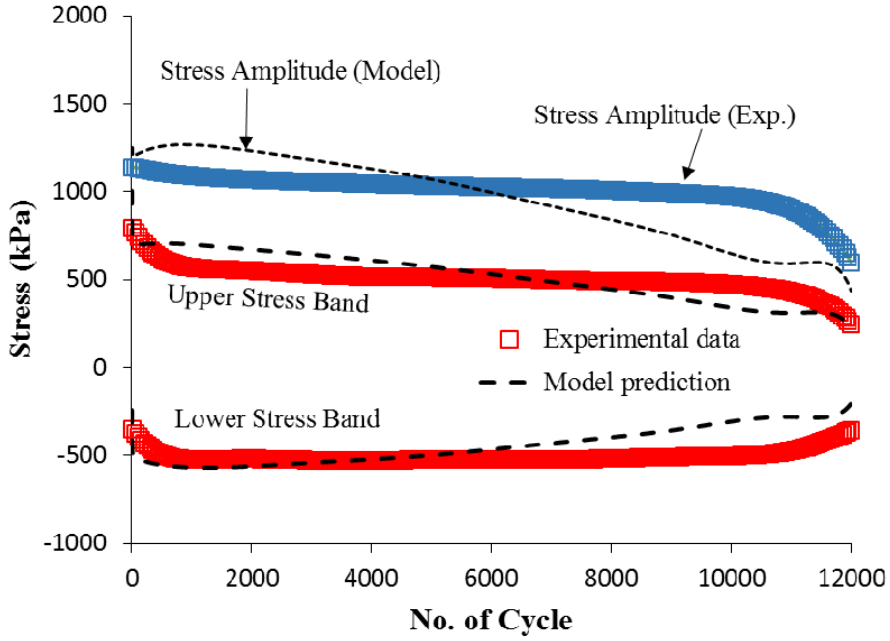

(b)

Figure 5.15. Cyclic displacement-controlled test results at 19°C for 3-month aged asphalt concrete corresponding to Test No.10 in Table 5.2. (a) Measured upper and lower strain bands and the strain amplitude; (b) The comparison of the recorded upper and lower stress bands and the stress amplitude with model predictions.

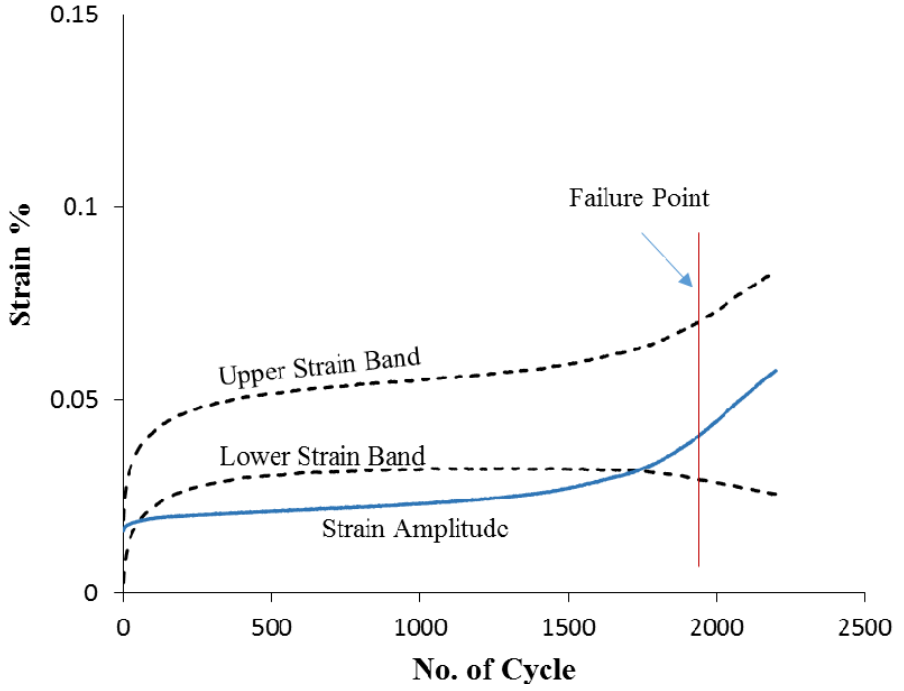

(a)

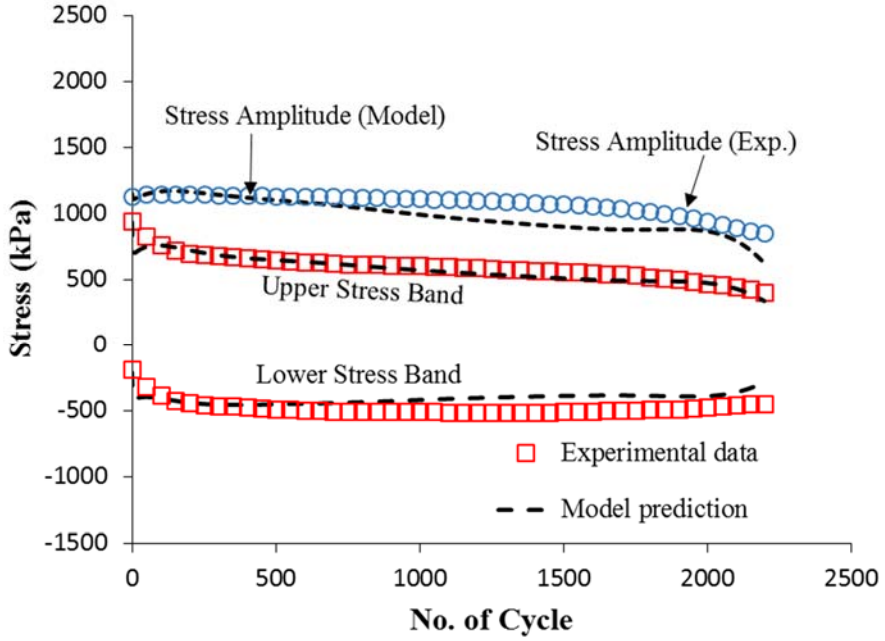

(b)

Figure 5.16. Cyclic displacement-controlled test results at 19°C for 6-month aged asphalt concrete corresponding to Test No.11 in Table 5.2. (a) Measured upper and lower strain bands and the strain amplitude; (b) The comparison of the recorded upper and lower stress bands and the stress amplitude with model predictions.

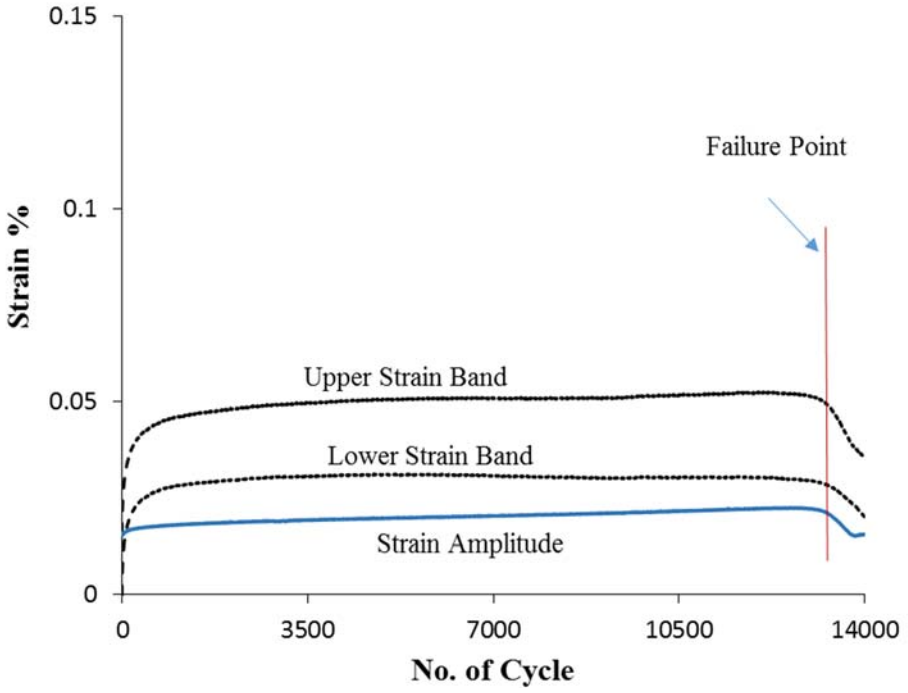

(a)

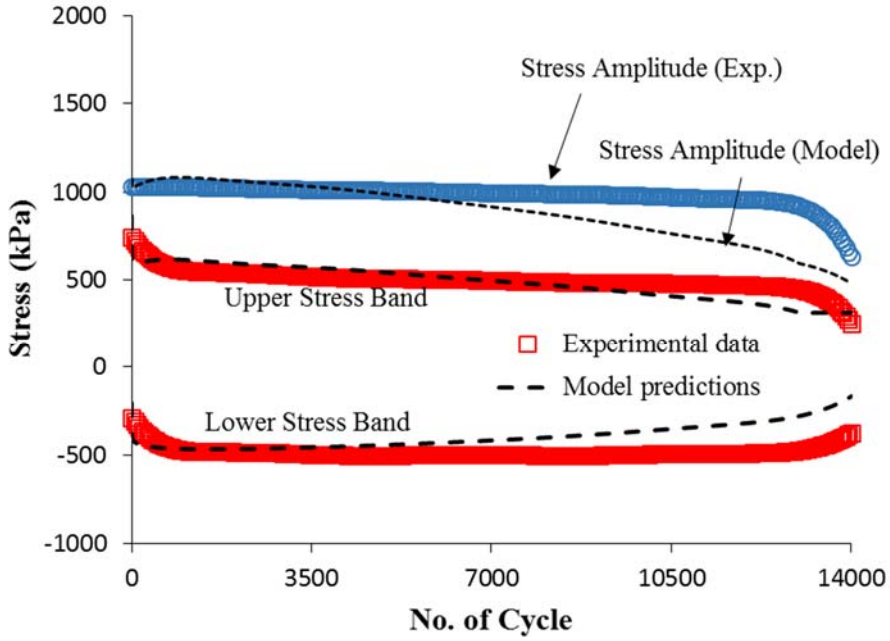

(b)

Figure 5.17. Cyclic displacement-controlled test results at 19°C for 6-month aged asphalt concrete corresponding to Test No.12 in Table 5.2. (a) Measured upper and lower strain bands and the strain amplitude. (b) The comparison of the recorded upper and lower stress bands and the stress amplitude with model predictions.

It is noted that, in the performed CDC tests in this subsection, the average strain amplitude that asphalt concrete specimens at different aging time experience is not identical; thus, a conclusion about the effect of aging on the number of cycles to failure and overall fatigue performance seems challenging. However, the results of the tests at which the applied strain amplitude is in a close range can be compared.

The overall trend is that when the initial applied strain amplitude increases, the asphalt specimen fails faster. This is visible in all tests conducted in this subsection at both temperatures. Additionally, the effect of oxidative aging on the fatigue performance of the material is apparently negative. At 5°C, the unaged asphalt concrete with the applied strain of 75 microstrain failed after about 15,000 loading cycles, whereas, the 3-month and 6-month aged specimens with strain amplitudes of 106 and 105 microstrain failed at 6100 and 4100 loading cycles, respectively (Tests No. 2, 4, and 5). Likewise, the failure of the unaged asphalt mixture with a strain amplitude of 122 microstrain occurred after 3100 cycles, while the 3-month aged sample with 114 microstrain failed at 2400 loading cycles (Tests No. 1 and 3).

Similarly, the same trend appeared at a temperature of 19°C. The unaged asphalt concrete with applied strain amplitude of 340 microstrain failed after 1400 loading cycles; however, the 3-month aged specimen with 290 microstrain strain amplitude failed at 240 cycles (Tests No.7 and 9). Furthermore, the number of cycles at which the 3-month aged asphalt mixture failed with applied strain amplitude of 200 microstrain was 11,500, whereas, the 6-month aged specimen with 180 microstrain failed at a significantly lower loading cycle at 1900.

It is interesting to observe how the proposed coupled aging-mechanical constitutive relationship evaluates the fatigue performance of asphalt concrete when subjected to an equal strain amplitude. For this reason, three cases with different aging times are considered, and the cyclic strain with the frequency of 10 cycles per second and amplitude of 340 microstrain is applied and the resultant stress is calculated using the model. Figure 5.18(a) illustrates the resultant stress amplitude for the unaged, 3-month aged, and 6-month aged materials. Figure 5.18(a) shows that as aging time increases, the initial stress amplitude also increases; however, with increasing number of loading cycles, the number of loading cycles to failure decreases for the case with larger aging time. Oxidative aging increases the stiffness of the aged material, which causes an increase in stress amplitude when strain amplitude is constant. On the other hand, the aged asphalt concrete is also more brittle, and therefore, undergoes failure faster than unaged material. Figure 5.18(b) also shows the evolution of the damage density in three different aging times. The damage density of 6-month aged asphalt concrete evolves faster, such that it reaches the failure point more rapidly.

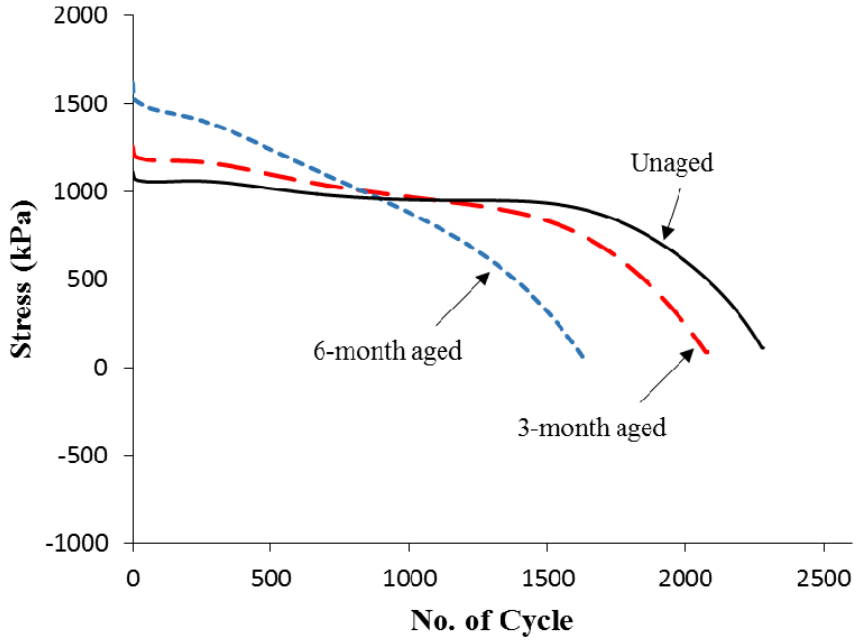

(a)

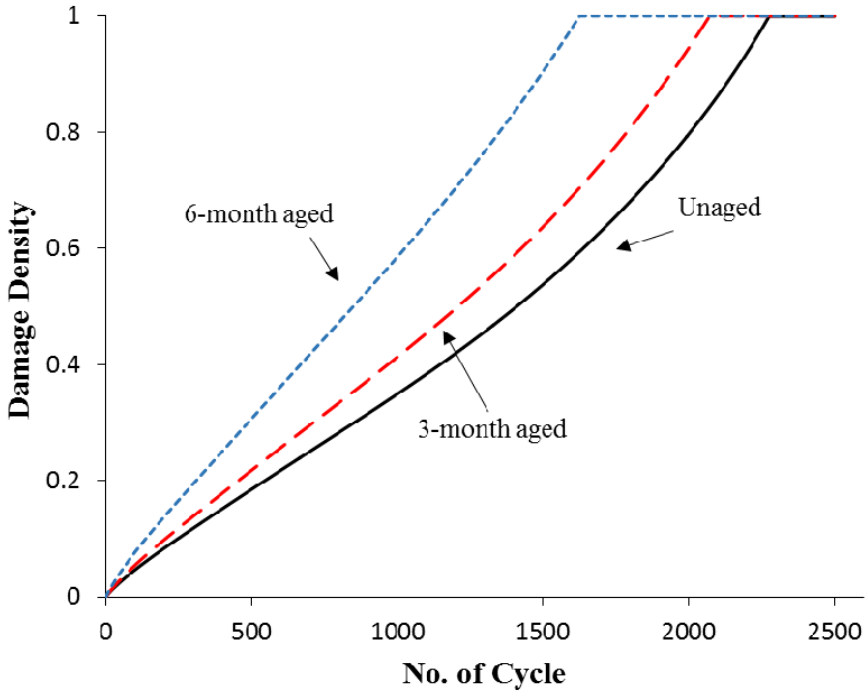

(b)

Figure 5.18. The comparison of model calculation of the response of asphalt concrete with different aging times subjected to cyclic strain with amplitude of 340 microstrain, including (a) the resultant stress amplitude, and (b) the evolution of damage density.

5.5 Summary

In this section the capabilities of the proposed oxidative aging-mechanical constitutive modeling framework were investigated in predicting the behavior of aged asphalt concrete subjected to different loading scenarios. Several experimental tests were used to validate the constitutive modeling capabilities. The repeated creep-recovery test at variable stress levels and high temperatures were used to validate the aging-nonlinear-viscoelastic-viscoplastic constitutive relationship. Model predictions were shown to capture very well the strain response of the material at different air void contents and aging times.

In addition, the repeated creep-recovery test at variable resting time and at the intermediate temperature was used to assess the proficiency of the model in predicting the strain response of asphalt concrete when subjected to the constant stress level and variable unloading times. It was shown that the aging-viscodamage-healing constitutive relationship appropriately predicted the response of the material at different ages. In this case, aging significantly decreased the viscoelastic strain response of the material.

Furthermore, the cyclic displacement-controlled test at low and intermediate temperatures was utilized to verify the ability of the model to predict the damage behavior and fatigue performance of the material. Several experiments at various strain amplitudes were conducted to compare the model predictions with the measured stress responses. The model calculations showed a good proficiency in predicting the behavior of aged asphalt concrete when subjected to hundreds of thousands of loading cycles.

6. FINITE ELEMENT SIMULATIONS OF ASPHALT CONCRETE STRUCTURES AT MULTIPLE SCALES

6.1 Overview

This section focuses on finite element simulations of asphalt concrete at the micro- and macro-scale. Two- and three-dimensional microstructural representations of asphalt concrete were constructed using X-ray images. Then, they were used to investigate the effect of constituents on the overall performance of the asphalt concrete subjected to various loading scenarios and aging times. Such simulations provide proper insights on the effects of oxidative aging by simulating oxygen diffusion inside the asphalt microstructure and investigating the degrading effects of oxygen presence on the overall mechanical behavior of asphalt concrete. As discussed in subsection 4.2.1, it is assumed that the only mechanism for oxygen transport is through diffusion only from the top surface of the asphalt concrete microstructure. Since the air void interconnectivity is not included, the oxygen transport from the surrounding to the pavement internal structure because of convection flow is not considered.

In the final subsection of this section, 2D finite element simulations are presented for a pavement structure in order to explore the capabilities of the proposed aging-mechanical constitutive relationship in evaluating the performance of the aged asphalt pavement subjected to repeated loading.

6.2 Simulation of 2D Finite Element Asphalt Concrete Microstructural Representation

In order to create the realistic 2D finite element model of asphalt concrete, X-ray computed tomography (CT) in the Advanced Characterization of Infrastructure Materials (ACIM) laboratory at Texas A&M University was used to scan asphalt concrete specimens. Details of the procedure to construct the finite element models of asphalt concrete can be found in You (2013). The scanned CT image of asphalt concrete has different grayscale intensities, as shown in Figure 6.1(a). The 2D CT image has three phases: aggregates that have higher intensities, air voids, and matrix (binder with fine aggregates). The grayscale image was then processed to clearly show the three phases, as represented in Figure 6.1(b). Next, the processed image was converted to a binary image, where each pixel represents 0 or 1 (black or white as shown in Figure 6.1(c)). Finally, the binary images were processed using specific thresholds to smoothly identify the three phases, as pictured in Figure 6.1(d). Once the X-ray CT image was processed, it was imported to the commercial finite element software, Abaqus, to produce the finite element model. The 2D asphalt concrete microstructure is used to perform finite element simulations under different loads and aging times.

The different asphalt concrete components (phases) and the finalized finite element model are shown in Figure 6.2. It is noted that, for simplicity and limited computational cost, very fine aggregates and asphalt binder are considered to be one single phase, the matrix phase. The volume fractions of aggregate, matrix, and air void in the 2D asphalt concrete microstructure are 67%, 26%, and 7%, respectively. In this

study, the aggregates are assumed to be isotropic-linear elastic with elastic modulus and Poisson's ratio of 25 GPa and 0.25, respectively. The matrix phase is assumed to have nonlinear viscoelastic, viscoplastic, and viscodamage behavior, and the material parameters identified in Section 4 are used in the simulations in the current section. Although these parameters were identified using experimental data conducted on asphalt mixture, they are compatible to be applied to the asphalt matrix that exhibits time-, rate- and temperature-dependent behavior.

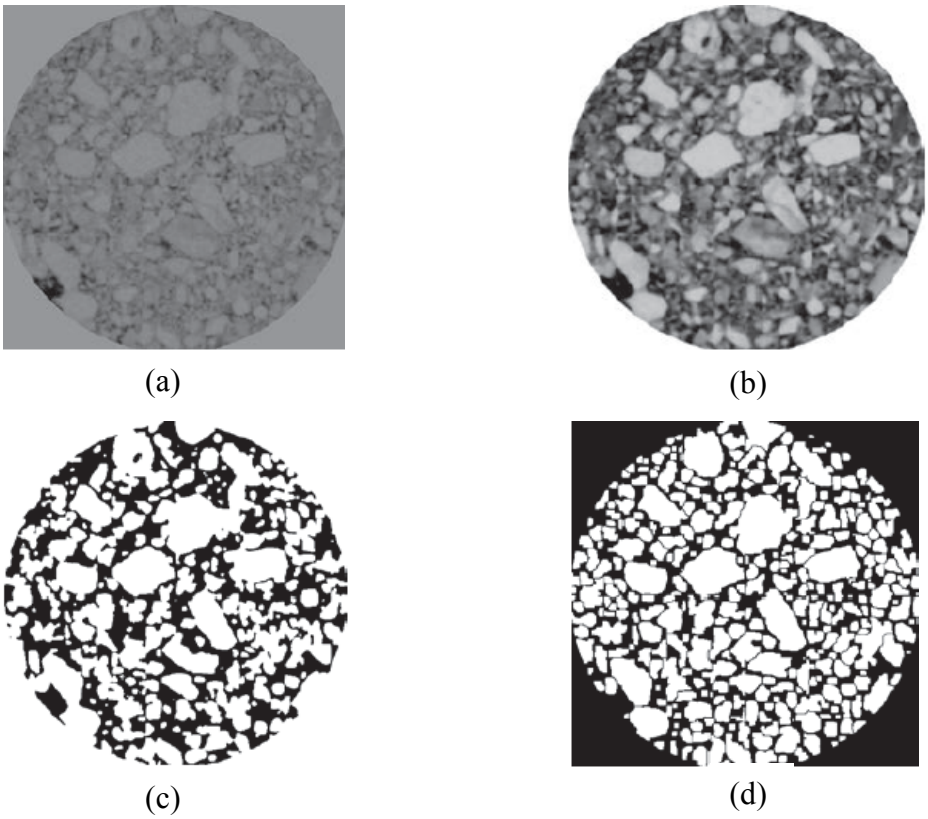

Figure 6.1. Constructing asphalt concrete microstructure; shown as (a) original X-ray CT grayscale image, (b) processed grayscale image, (c) converted binary image, and (d) processed binary image. Figure adapted from You (2013).

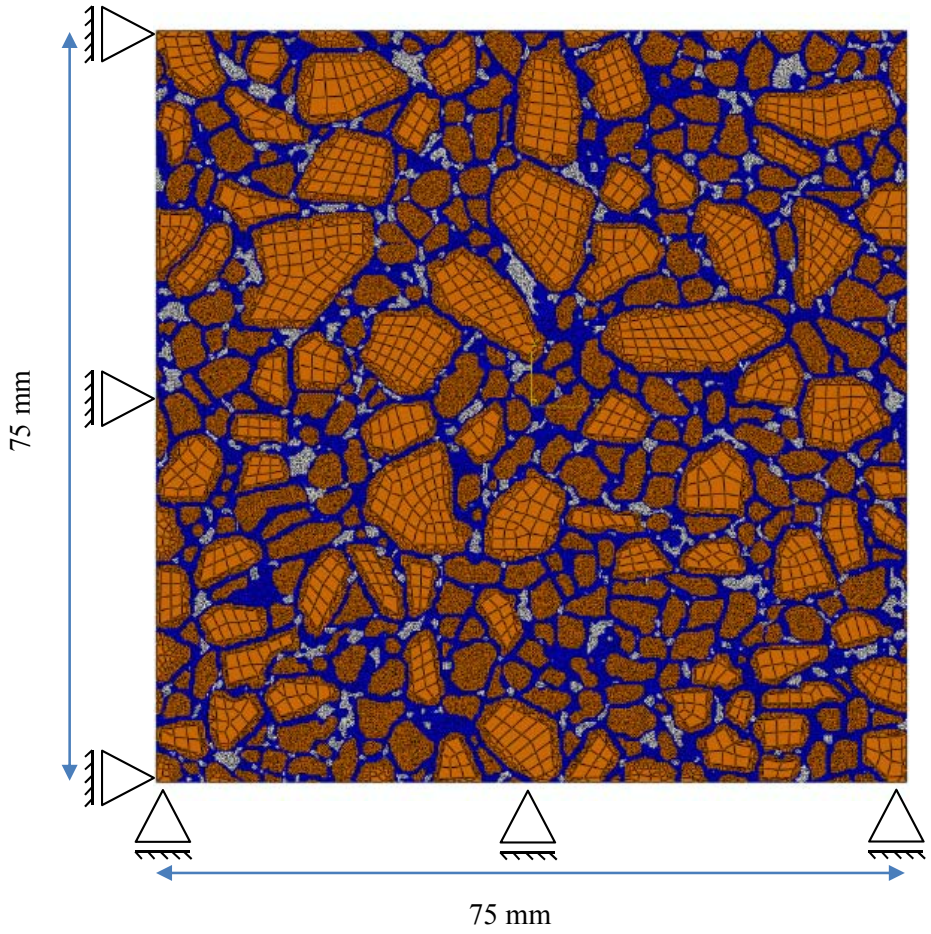

Figure 6.2. Two-dimensional asphalt concrete microstructural model created by an X-ray image. The microstructure includes the air void, aggregate, and matrix phases.

6.2.1 Oxygen Diffusion Analysis

Prior to performing simulations involving the mechanical loading, the oxygen diffusion analysis needs to be conducted. Three different aging times are considered for microstructural simulations of asphalt concrete: zero aging, 5-year aging, and 15-year aging. The steps for diffusion analysis were previously explained in Subsection 4.2.1. The simulations are performed at two temperatures: 5°C and 19°C. The same oxygen

diffusivities for asphalt concrete phases that were listed in Subsection 4.2.1 are considered herein. It is noted that, the aging-mechanical analysis in this work is conducted in a sequential manner. In the first step, the oxygen diffusion analysis is performed and the aging state variable is obtained based on the calculated oxygen content at each material point. Then, mechanical loads are applied to the microstructure, whose material properties are altered by the aging state variable.

Table 6.1 lists the material parameters related to the oxidative aging constitutive relationship required for oxygen diffusion analysis. The contours of the calculated aging state variable at different aging times are illustrated in Figure 6.3.

Table 6.1. Material parameters related to oxygen diffusion analysis and calculating the aging state variable within asphalt concrete microstructure.

	Oxygen Diffusivity (mm^2/day)		Aging Fluidity Parameter, Γ^a (1/day)	
Component	5°C	19°C	5°C	19°C
Asphalt Matrix	0.1218	0.3523	6.37×10^{-4}	1.37×10^{-3}
Aggregate	10^{-10}	10^{-10}	-	-
Air Void	10^{5}	10^{5}	-	-

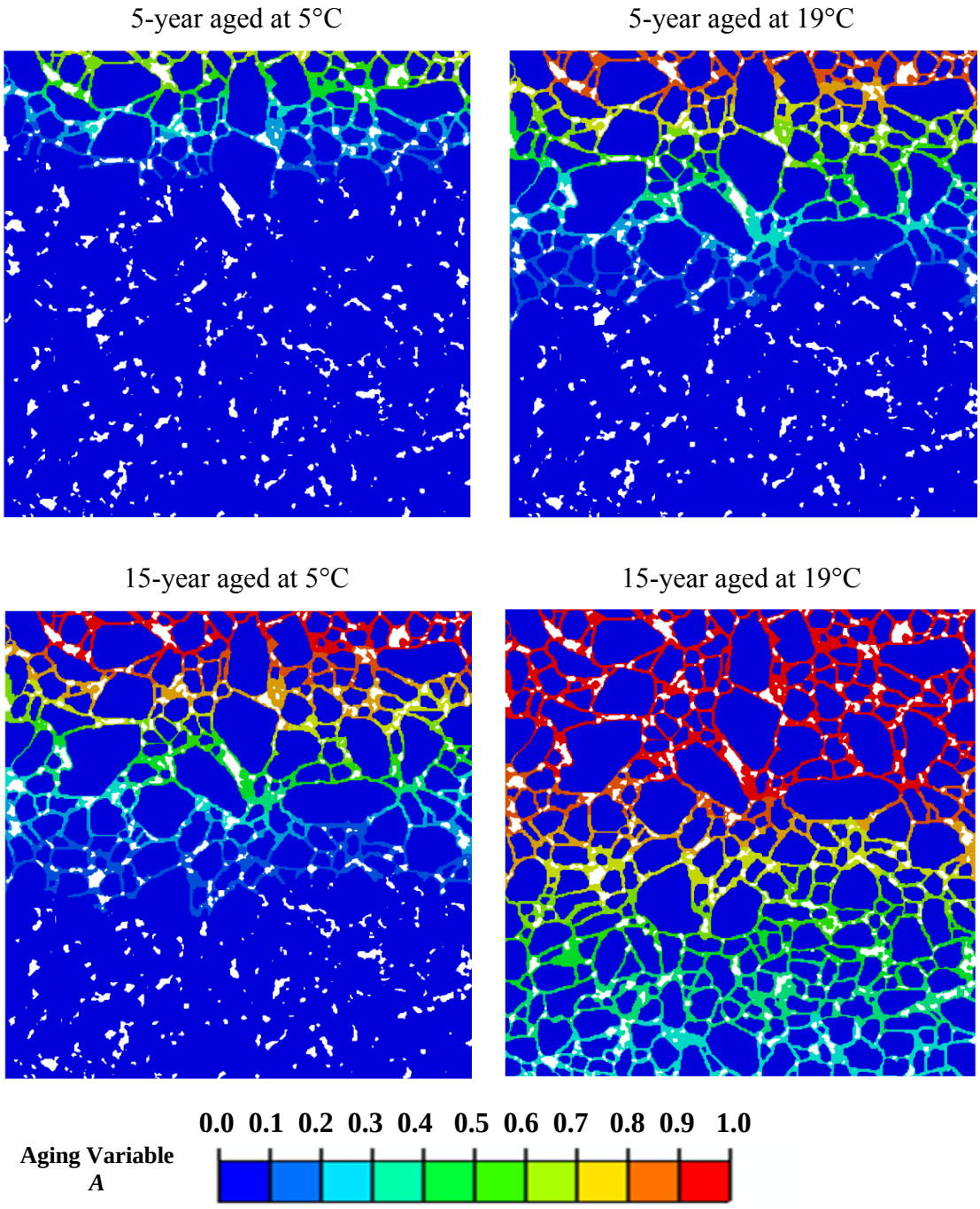

Figure 6.3. The contours of the aging state variable calculated at different aging times and temperatures. These simulations are based on several assumption: unit oxygen content on the top surface only, no oxygen transport by convection through air voids, and no oxygen consumption by reaction throughout the specimen; more information about these assumptions are given in subsection 4.2.1.

Once the aging state variable is calculated within the RVE, the mechanical load can be applied. Constant tensile strain rate at two different rates and compressive creep-recovery test at constant stress level are utilized to perform the mechanical finite element simulations.

6.2.2 Effect of Oxidation Time

The goal of this subsection is to investigate the response of the 2D asphalt concrete RVE that is subjected to different aging times with constant strain rate and constant temperature. The constant displacement is applied to the top boundary of the microstructure for a specific amount of time until the material reaches the highest tensile strength and undergoes the post-peak region. These simulations are conducted at 5°C, and two different strain rates are considered. As discussed earlier, three different aging times are investigated in this subsection.

Figure 6.4(a) and Figure 6.4(b) represent the average stress-strain diagram for the uniaxial strain rate test at $1\times10^{-4}/\sec$ and $5\times10^{-5}/\sec$, respectively, at different aging times. As can be seen in these figures, the initial modulus of the material increases with aging time. This phenomenon has been thoroughly discussed in the previous subsections. The ultimate strength of the material also increases by aging. However, it is noted that the material is transformed from the ductile-type to the brittle-type behavior.

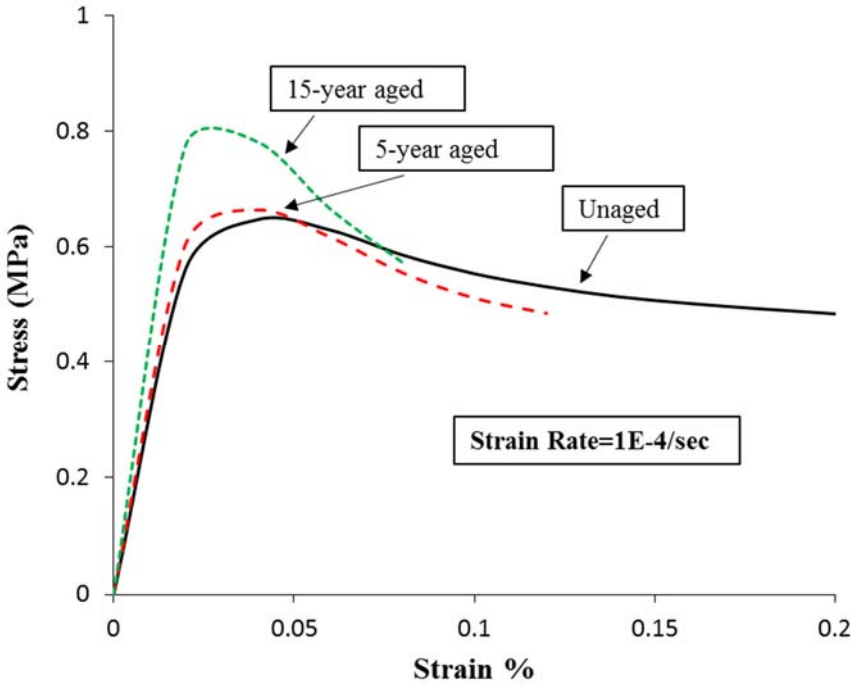

(a)

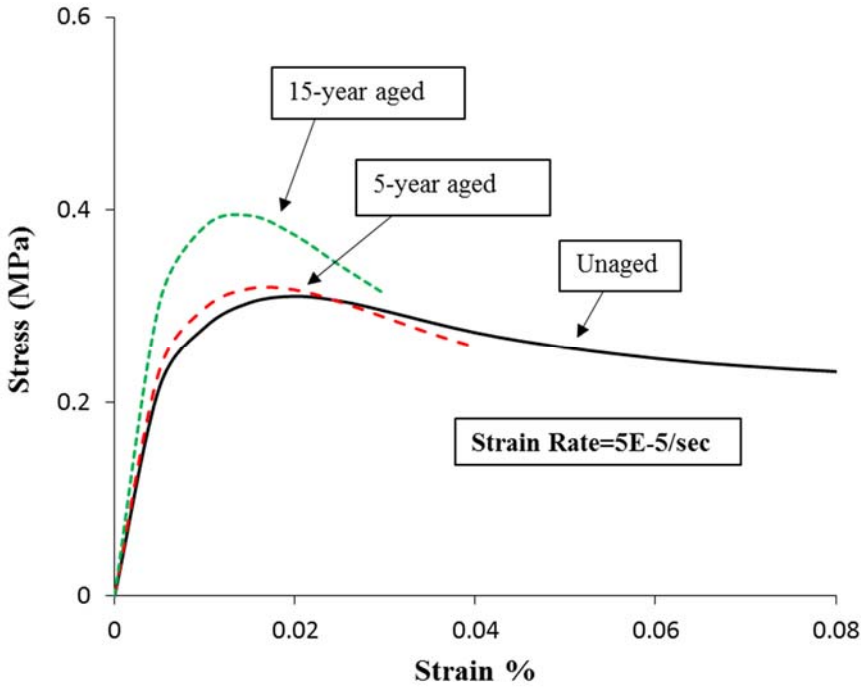

(b)

Figure 6.4. The resultant average stress-strain diagram of 2D asphalt concrete at different aging times and temperature 5°C corresponding to applied strain rate of (a) 1E-4/sec and (b) 5E-5/sec.

Figure 6.5 and Figure 6.6 illustrate the corresponding induced damage contours for different aging times at strain rates of $1\times10^{-4}/\sec$ and $5\times10^{-5}/\sec$, respectively. The damage contours are shown at the strain level at which the material reaches the ultimate strength, and at the strain level in the post-peak region. In the case of the zero-aging material, the damage density variable is evenly distributed within the microstructure. It is noted that damage density in the unaged material mainly propagates horizontally at the interface of the aggregate and the matrix phases, perpendicular to the loading direction. However, the mode of damage density distribution changes when the material is subjected to aging. As can be seen from Figure 6.5 and Figure 6.6, in the aged microstructure, the damage density variable initiates and nucleates mostly in the upper surface where the RVE was subjected to the oxygen source. In fact, this phenomenon can be explained with the actual damage mechanism in the field, where the top–bottom cracks are normally observed in aged pavement structures.

The reason for this is that the diffused oxygen from the top boundary significantly degrades the mechanical properties of the matrix phase that is in contact with oxygen, whereas the properties of the matrix at the bottom sections remain the same. Therefore, the aged matrix phase becomes more prone to initiate the damage density. It is noted that the propagation of the damage density variable is intensified when the aging time is increased.

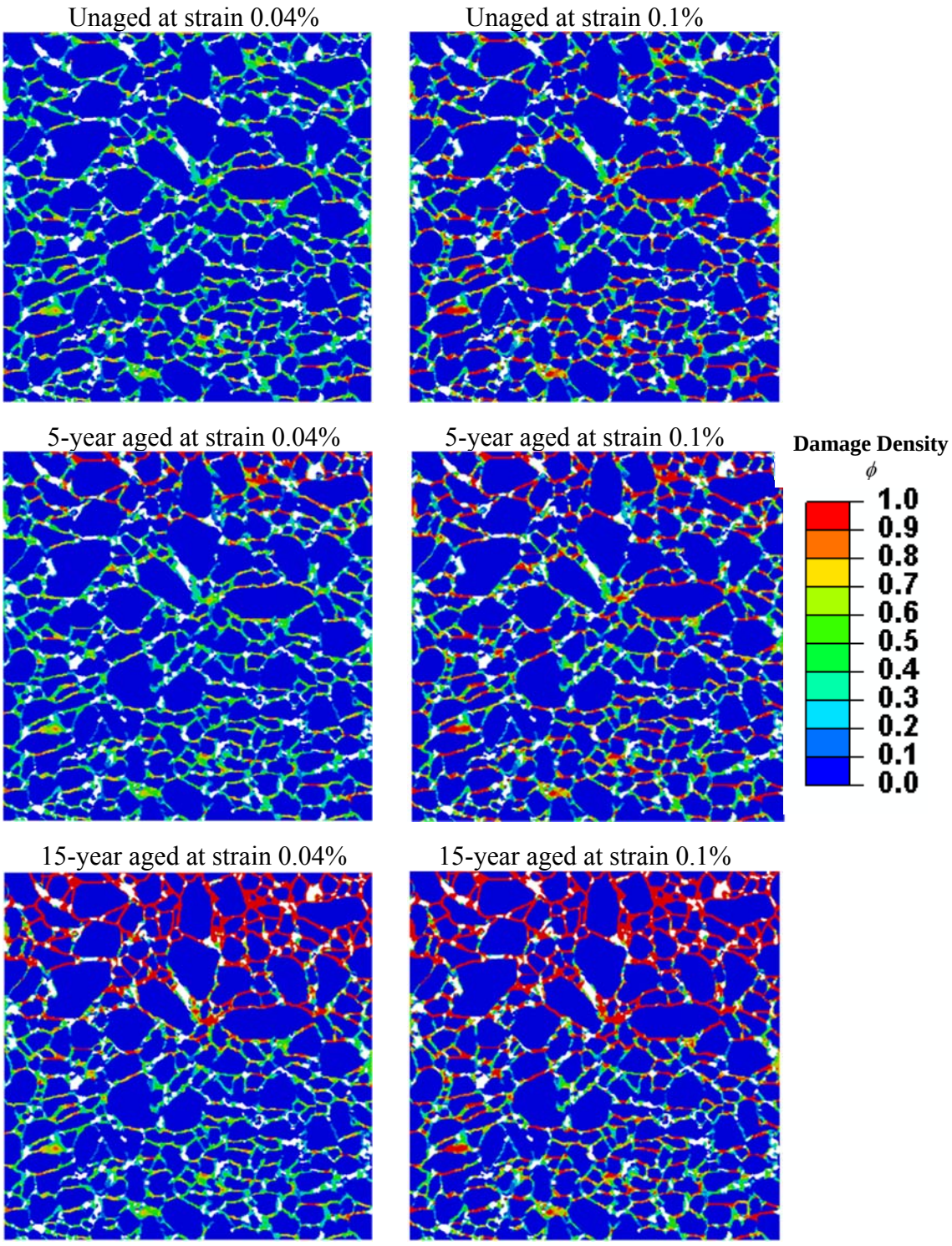

Figure 6.5. The damage density distribution at different aging times shown at two strain levels. The results correspond to the simulation with applied strain rate 1E-4/sec at 5°C.

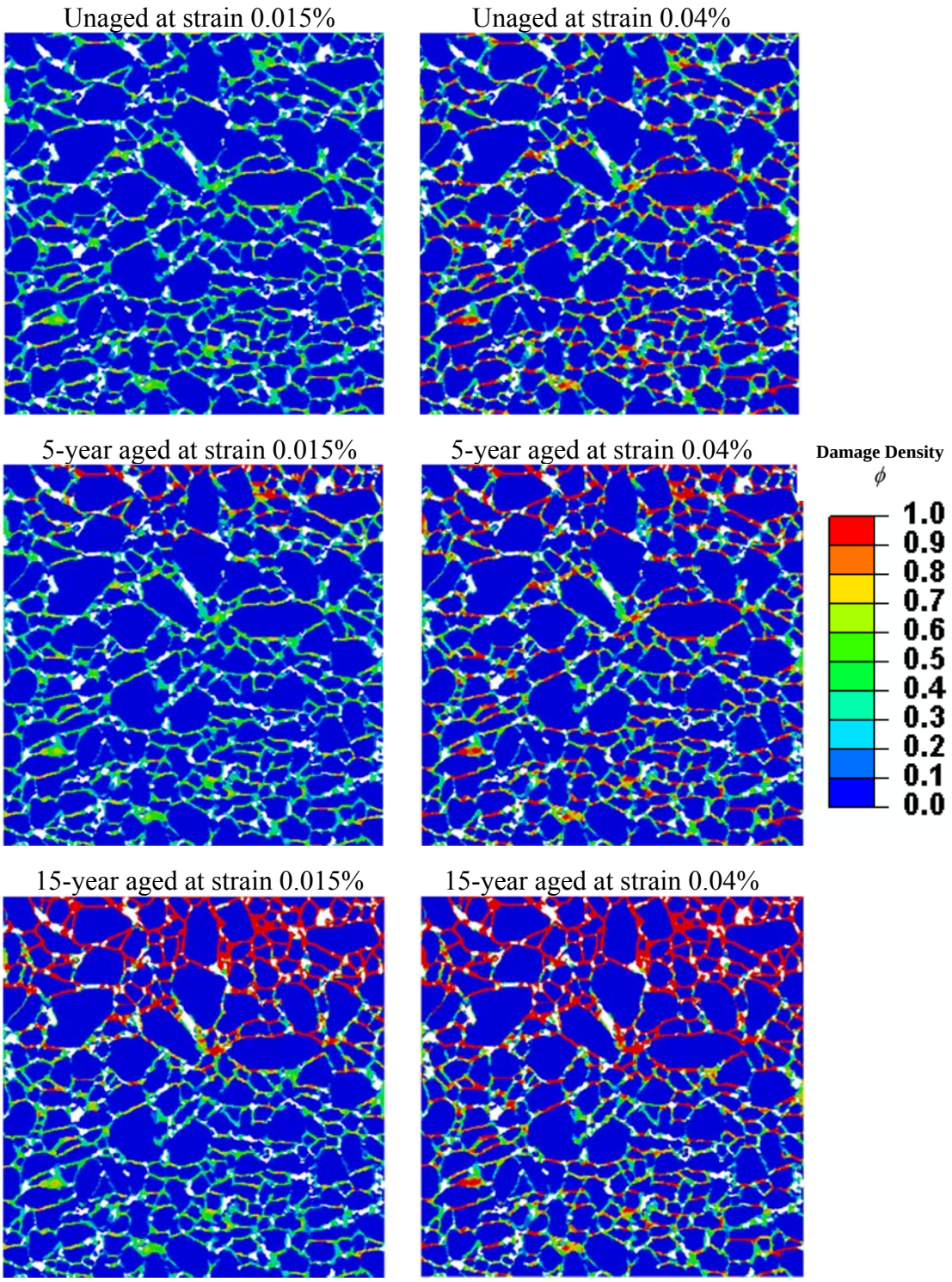

Figure 6.6. The damage density distribution at different aging times shown at two strain levels. The results correspond to the simulation with applied strain rate 5E-5/sec at 5°C.

6.2.3 Effect of Temperature

Asphalt concrete is a temperature-dependent material, and oxidative aging occurs faster at higher temperatures. Therefore, to study the temperature effect on the mechanical behavior of the asphalt concrete microstructure, subjected to different aging times, simulations are conducted at 5°C and 19°C. In this case, the tensile strain load is applied at two different rates. The model parameters associated with different temperatures were previously described in Section 4. Figure 6.7(a) and Figure 6.7(b) represent the average stress-strain diagrams corresponding to strain rates $1\times10^{-4}/\sec$ and $5\times10^{-5}/\sec$, respectively. These figures clearly show the dependency of the asphalt concrete response on the temperature changes, even for the aged materials. The overall trend is that by increasing the temperature from 5°C and 19°C, the ultimate strength considerably decreases. Moreover, comparing the 15-year aged material responses at two temperatures shows that as the material ages, the dependency on the temperature decreases.

The damage density distributions are illustrated in Figure 6.8 and Figure 6.9, corresponding to different strain rate tests. These figures are plotted at the point where the material reached the ultimate strength. As seen in Figure 6.8 and Figure 6.9, oxidative aging at the higher temperature has significant impact on the damage density evolution. The aging state variable evolves more rapidly at the higher temperature, making the mechanical material properties more prone to damage.

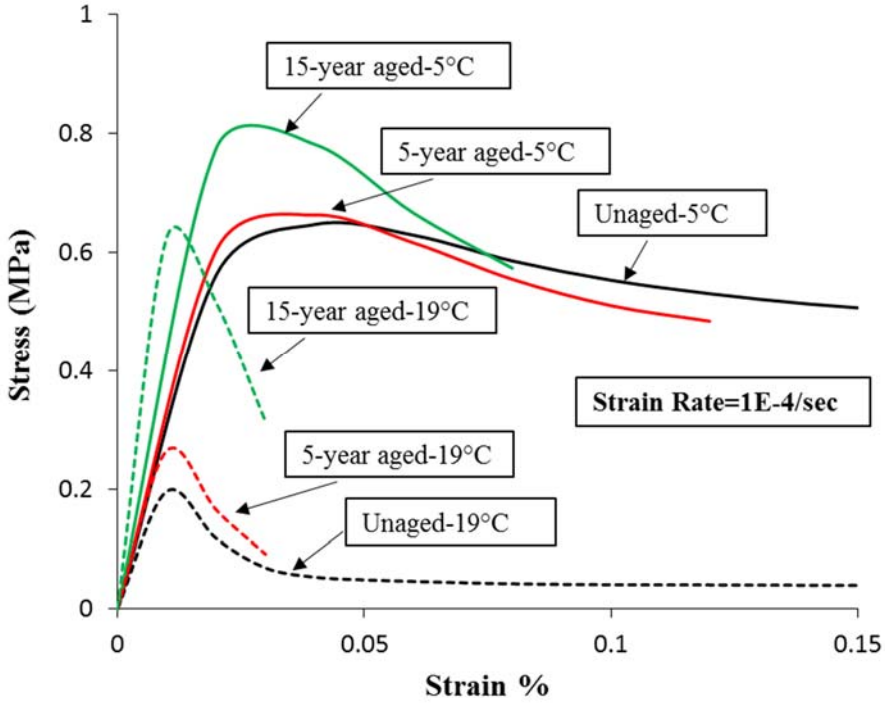

(a)

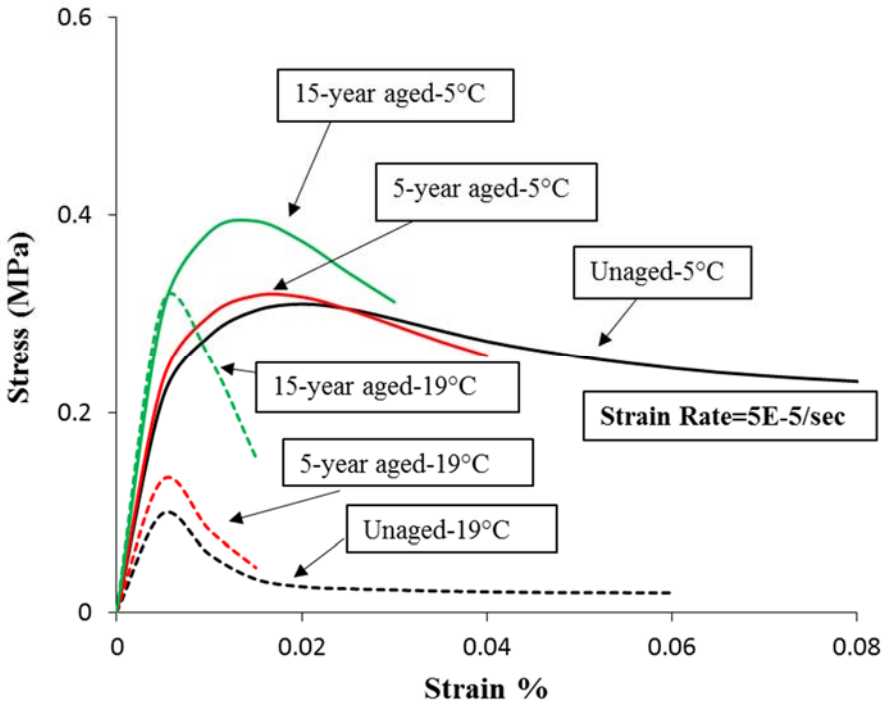

(b)

Figure 6.7. Comparing the temperature dependency of asphalt concrete response at tensile strain rates of (a) 1E-4/sec and (b) 5E-5/sec, and at different aging times.

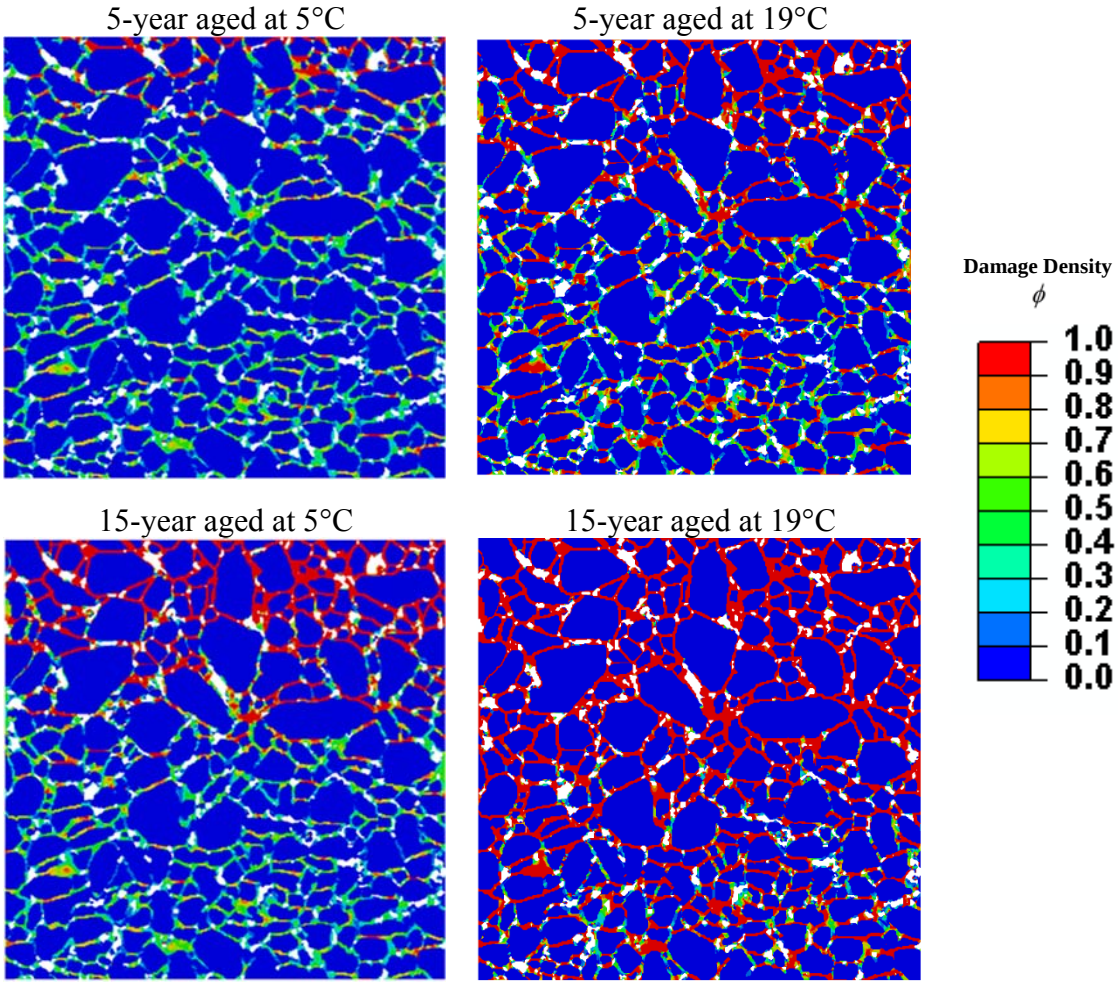

Figure 6.8. The damage density distribution at different aging times shown at the ultimate strength. The results correspond to the simulation with applied strain rate of 1E-4/sec.

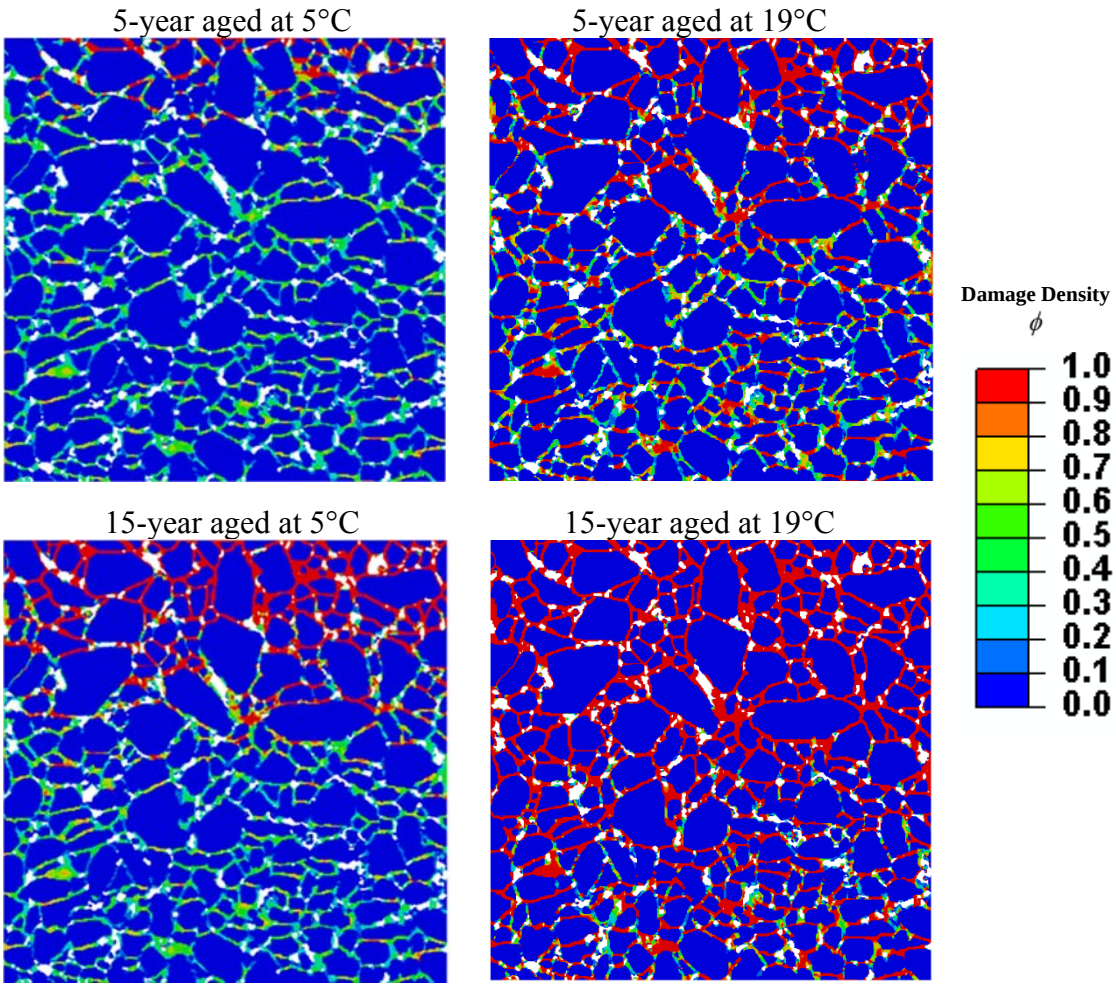

Figure 6.9. The damage density distribution at different aging times shown at the ultimate strength. The results correspond to the simulation with applied strain rate of 5E-5/sec.

6.2.4 Repeated Creep-Recovery Response

In order to investigate the capabilities of the proposed model in simulating the cyclic loading, the repeated creep-recovery test at a constant compressive stress level is performed on the 2D RVE at 5°C. The loading time is 0.7 sec followed by a 1.1 sec unloading period. The simulations are conducted on unaged and aged conditions.

Figure 6.10(a) shows the stress history that is applied on the top boundary of the RVE, and Figure 6.10(b) represents the resultant strain response. It is expected that due to oxidative aging, the amount of strain response due to cyclic creep-recovery loading reduces, as this was previously verified by experimental data in Section 5. As shown in Figure 6.10(b), the finite element simulations on the asphalt microstructure and using the coupled aging-viscoelastic-viscodamage constitutive relationship on the aged and unaged cases is able to predict the anticipated behavior. The amount of accumulated strain during loading time and the recovered strain during unloading time decrease as aging time increases.

Correspondingly, the distribution of the damage density variable is illustrated in Figure 6.11 at different loading times and aging conditions. At unaged condition, the damage density variable initiates and propagates equally at different material points within the RVE. However, when oxygen diffusion from the top boundary is included in the simulations, the mode of distribution of the damage density significantly changes. The top layers of the RVE, which are mostly affected and degraded by oxygen diffusion, absorb a great deal of damage.

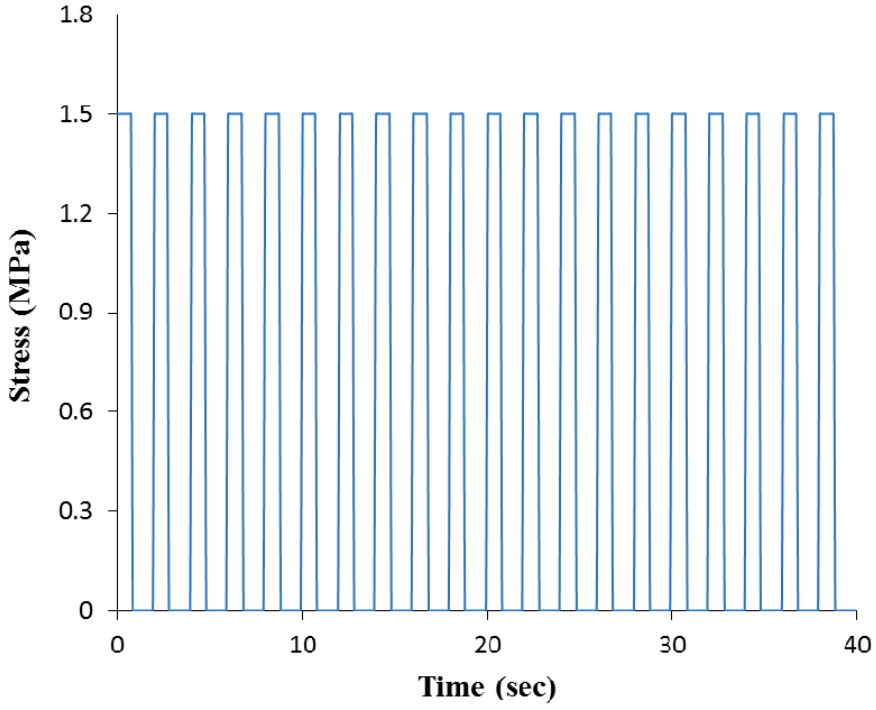

(a)

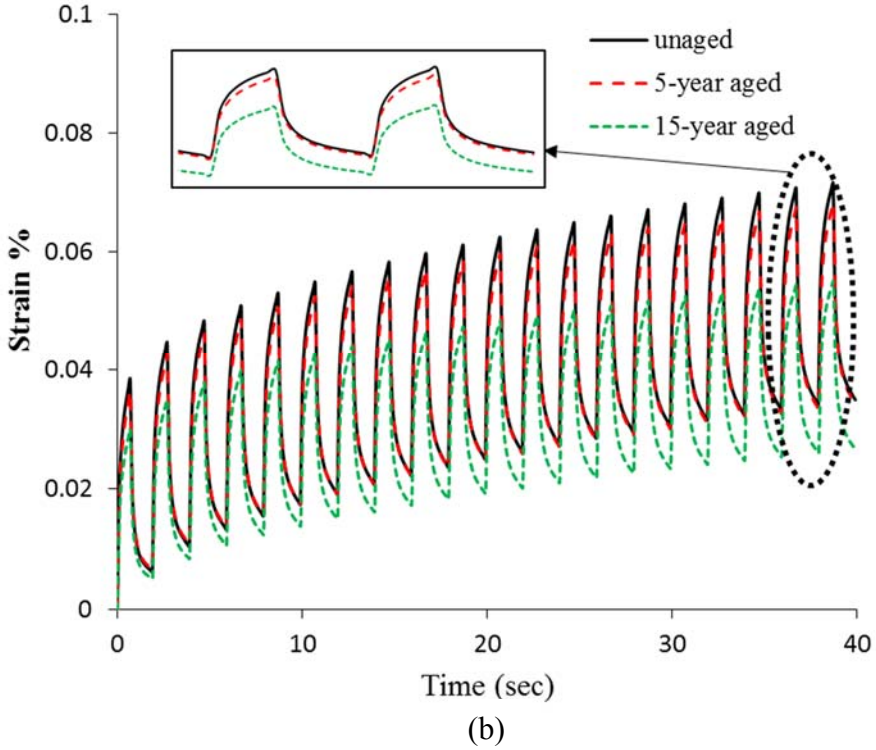

(b)

Figure 6.10. The repeated creep-recovery test simulated at 5°C and different aging times, shown by (a) the compressive stress-time diagram and (b) the strain-time response.

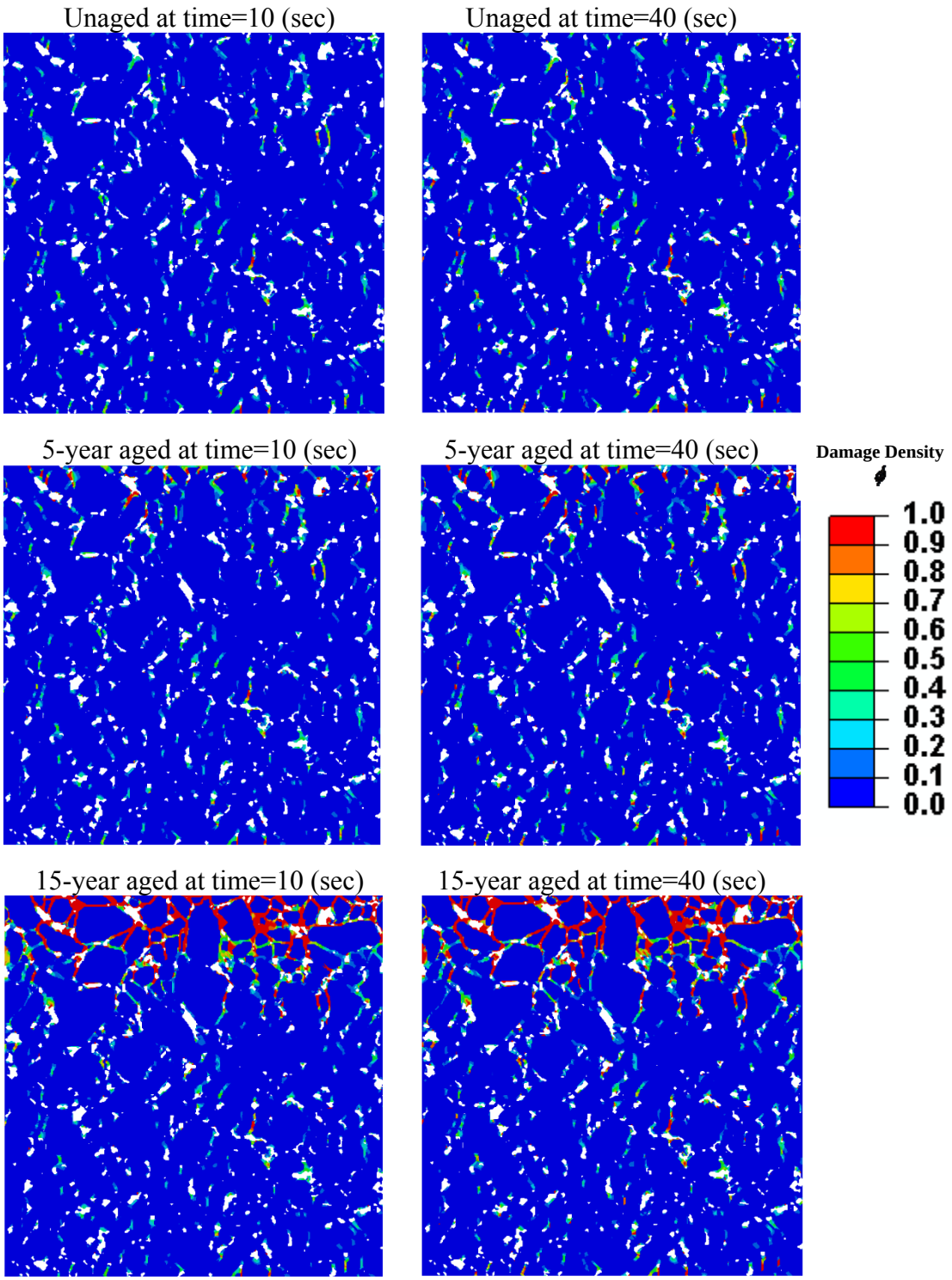

Figure 6.11. The damage density distribution during the repeated creep-recovery test at 5°C and different aging times shown after 10 sec and 40 sec of loading. The constant compressive stress level of 1.5 MPa is applied during the loading intervals.

6.2.5 Effect of Boundary Condition of Oxygen Source

In previous subsections the oxygen source was assumed to be placed on the top boundary of the RVE. In this case, the air voids within the microstructure have the transitional role, such that they contribute to diffuse the oxygen in a faster pace. However, it is probable in the actual asphalt pavement that air voids are interconnected such that they act like oxygen sources. In this subsection, the objective is to investigate and compare the two cases with finite element simulations. Therefore, the first case (Case-1) is when the oxygen source is placed only on the top boundary. In the second case (Case-2) the air voids act as oxygen sources in addition to diffusion from the top surface. Then, the uniaxial constant tensile strain loading is applied to the top boundary at the rate of $5 \times 10^{-5} / \sec$.

Figure 6.12 compares the calculated aging state variable for the two cases. As seen in this figure, when the air voids are oxygen sources, the whole RVE is affected by oxygen diffusion, and it is anticipated that the material properties at all material points of the microstructure are altered and degraded. The damage density distribution of the two cases is depicted in Figure 6.13. These figures are plotted at the strain where the material has reached its ultimate strength. Apparently, the case when the air voids are assumed to be oxygen sources (Case-2) shows more damage as compared to the case when the oxygen source is on the top boundary. This phenomenon is particularly important when asphalt pavements have cracks that extend to the bottom layers of the structure. In this case, the air oxygen can freely reach the lower layers, which could lead to a great deal of extra damage when associated with traffic loading.

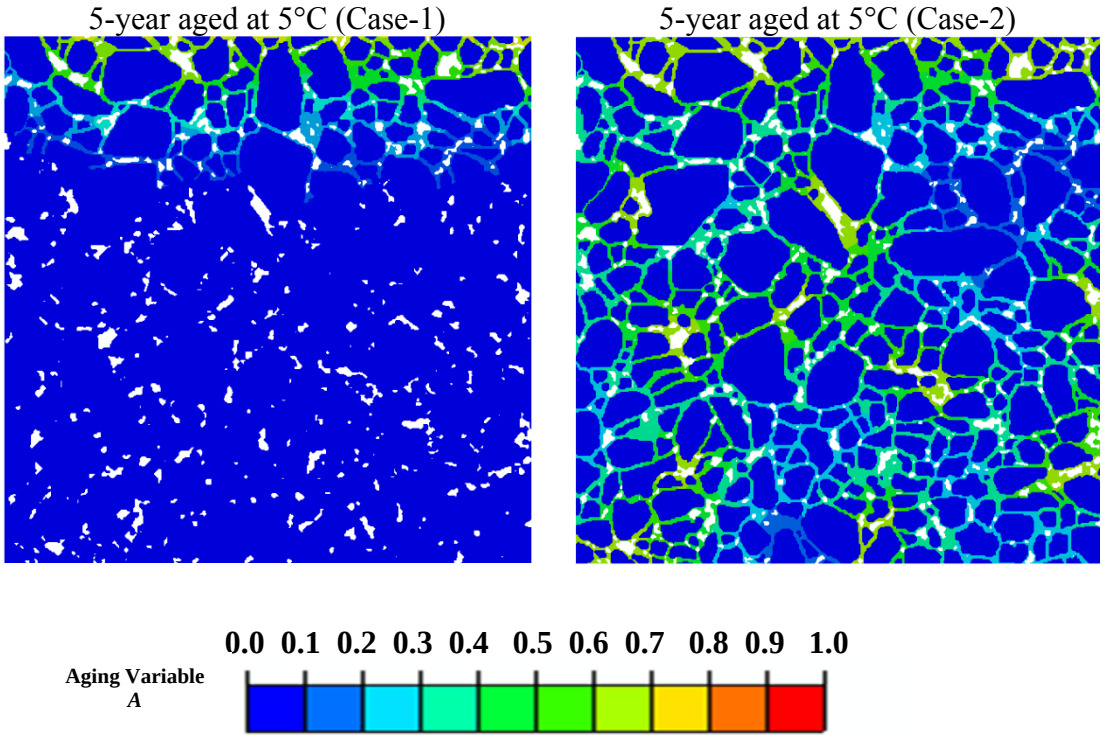

Figure 6.12. The comparison of the calculated aging state variable for two cases. Case-1 is when the oxygen source is placed only on the top boundary, and Case-2 is when the air voids are also sources of oxygen. These simulations are based on several assumption: no oxygen transport by convection through air voids and no oxygen consumption by reaction throughout the specimen; more information about these assumptions are given in subsection 4.2.1.

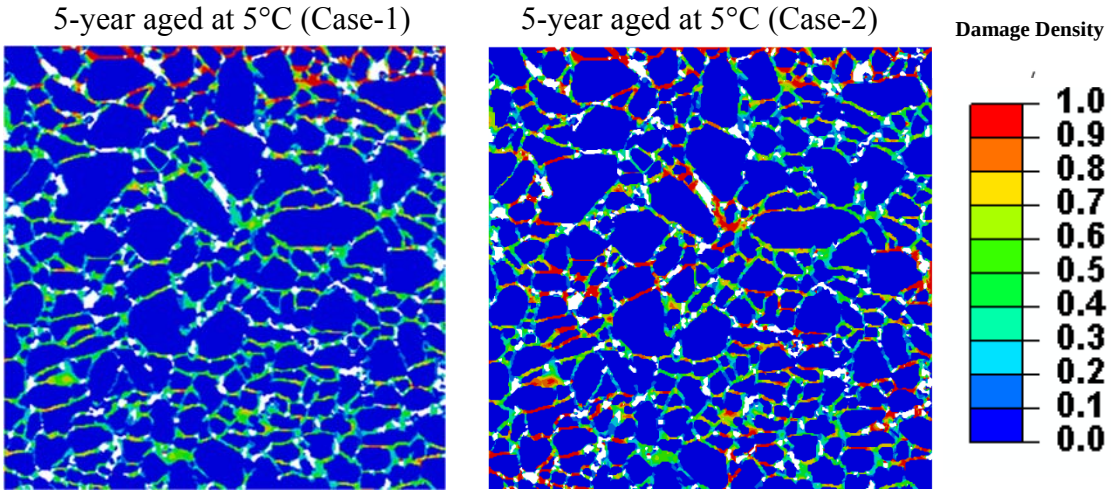

Figure 6.13. The comparison of the damage density distribution for two cases with different aging boundary conditions. The applied load is a constant strain rate of 5E-5/sec.

6.3 Simulation of 3D Finite Element Asphalt Concrete Microstructural Representation

In order to perform more realistic microstructural simulations, the 3D microstructural representation of asphalt concrete is constructed, such that the finite element simulations are conducted in the three-dimensional state of stress. To create the 3D microstructure (You, 2013), several planar images obtained by an X-ray CT system were used. After these images were processed in the way described in the previous subsection for the 2D case, the 3D microstructure was constructed by connecting the several image slices of the asphalt specimen along the vertical direction with equivalent 1 mm spacing. Figure 6.14 illustrates the final processed 2D images to construct the 3D asphalt microstructure. It is noted that the very fine aggregates (smaller than 2.32 mm) are neglected in the final 3D microstructure, as they are assumed to be part of the matrix

phase to reduce the computational cost. Moreover, the direct aggregate to aggregate contact is also neglected in this study. The geometry and the finite element mesh of the final constructed cylindrical RVE that consists of the aggregate, matrix, and air void phases is represented in Figure 6.15.

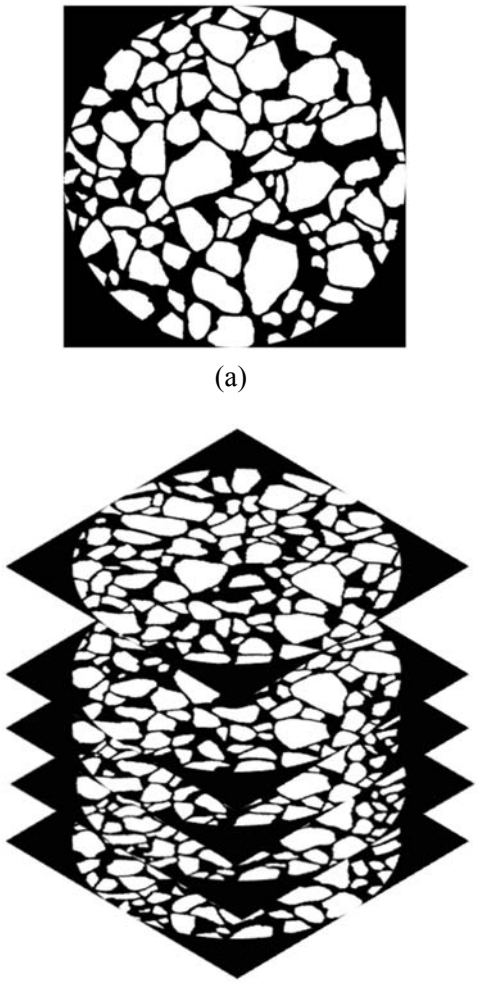

(a)

(b)

Figure 6.14. The X-ray CT images showing (a) the processed single 2-D image and (b) the slices of the 2-D processed image to construct the 3D microstructure. Pictures taken from You et al. (2012).

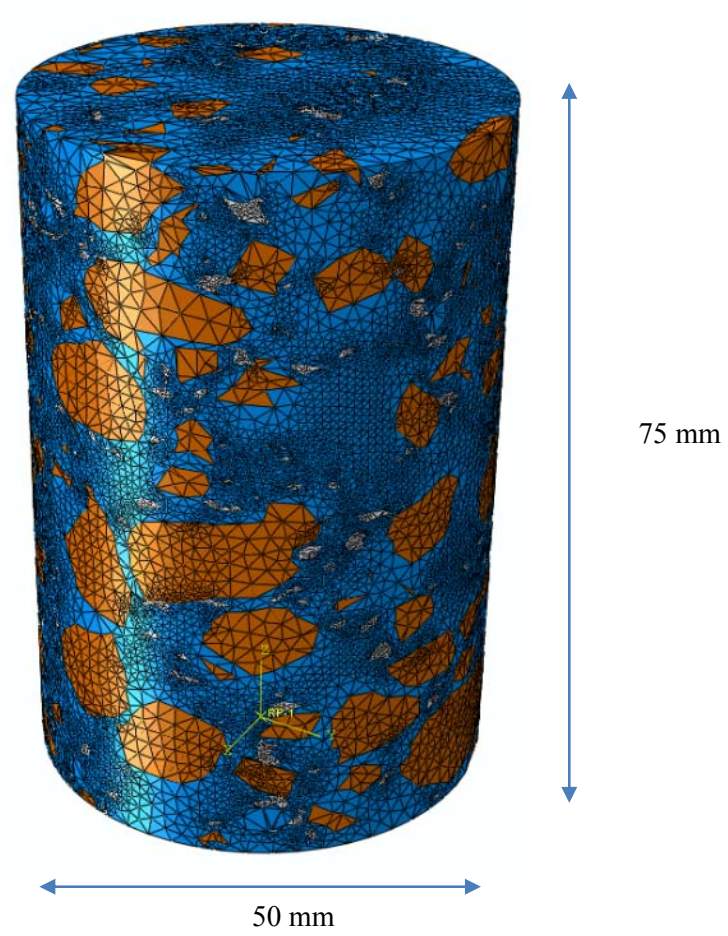

Figure 6.15. The geometry and finite element model of the three-dimensional asphalt concrete microstructure created by the sliced X-ray images. The microstructure includes the air void, aggregate, and matrix phases.

6.3.1 Oxygen Diffusion Analysis

In order to investigate the capabilities of the constitutive modeling framework for predicting the mechanical behavior of the aged asphalt concrete, the oxygen diffusion analysis is performed similar to the presented framework for the 2D microstructural case. Three different aging times are considered: zero aging, 5-year aging, and 15-year

aging. The steps for diffusion analysis were previously explained in Subsection 4.2.1. The simulations are performed at two different temperatures: 5°C and 19°C. The oxygen diffusivities for asphalt concrete phases were previously listed in Subsection 4.2.1 for the 3D case.

The aging-mechanical analysis in this study is performed in a sequential mode. In the first step, the oxygen diffusion analysis is performed and the aging state variable is calculated based on the obtained oxygen content at material points at different aging times. Then, various mechanical loads are applied to the microstructure, whose material properties are altered by the aging state variable. The oxygen source is placed on the top surface of the RVE and the resultant aging state variable at different aging times is presented in Figure 6.16. These figures show that as the aging time and temperature increases, the aging state variable is increased. The calculated aging state variable close to the oxygen source in the upper portions of the microstructure is higher. This indicates that the material properties where the aging state variable is high have significantly degraded, making these material points more susceptible to damage initiation and propagation.

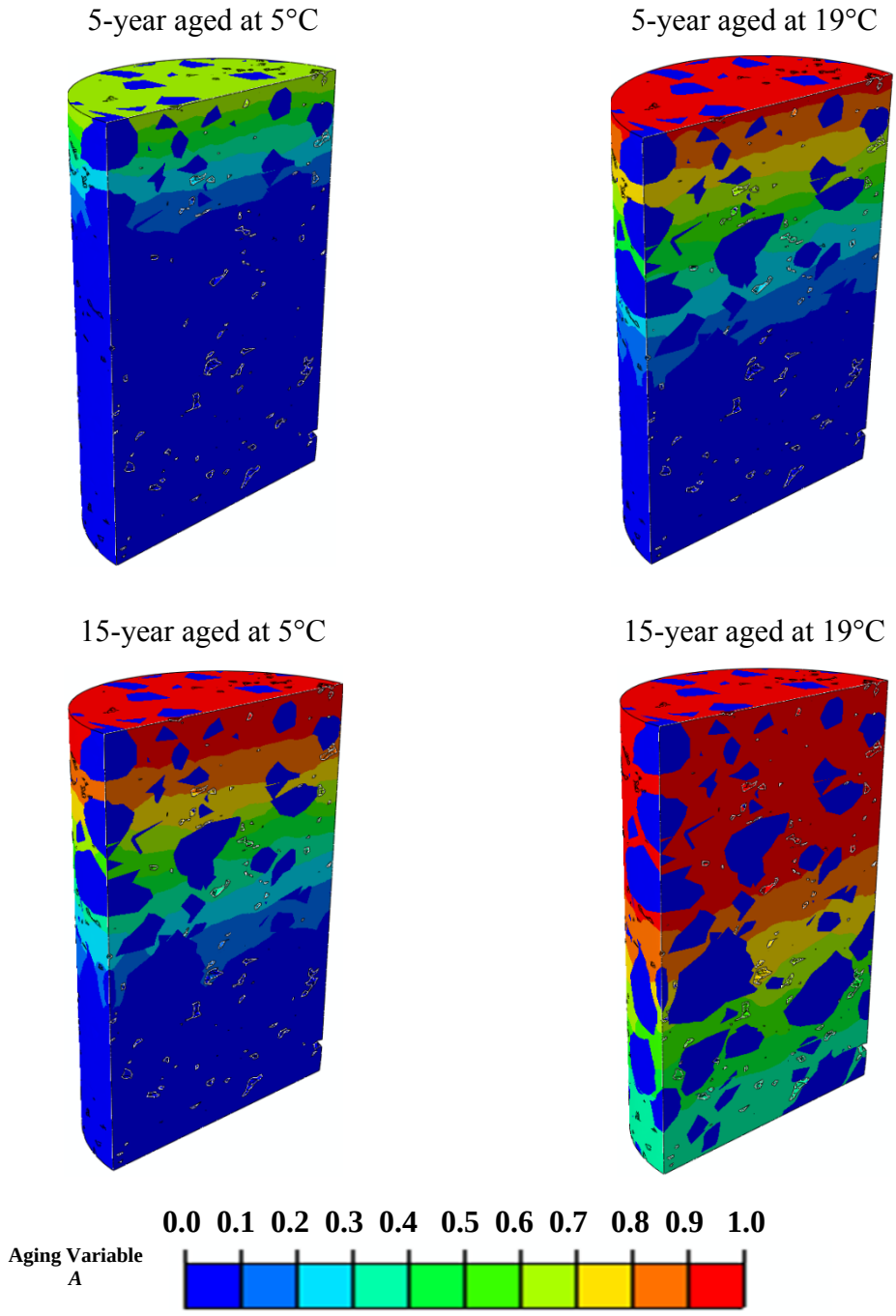

Figure 6.16. The contours of the aging state variable calculated at different aging times and temperatures, shown on the half cut of the 3D microstructure. These simulations are based on several assumption: unit oxygen content on the top surface only, no oxygen transport by convection through air voids, and no oxygen consumption by reaction throughout the specimen; more information about these assumptions are given in subsection 4.2.1.

6.3.2 Effect of Oxidation Time

The objective is to investigate the behavior of the different aged 3D asphalt concrete RVE subjected to constant tensile strain rate at a constant temperature. The constant strain rate is applied to the top surface of the microstructure for a specific amount of time until the material reaches the highest tensile strength and undergoes the post-peak region. These simulations are conducted at 5°C, and two different strain rates are considered.

Figure 6.17(a) and Figure 6.17(b) represent the average stress-strain diagram for the uniaxial strain rate test at $1\times10^{-4}/\sec$ and $5\times10^{-5}/\sec$, respectively, at different aging times. As seen in these figures, the initial modulus of the material increases with aging time, and the ultimate strength of the material also increases with aging. However, it is seen that the aged material reaches the ultimate strength earlier than the unaged one, suggesting that due to aging, the material has been transformed from ductile to brittle behavior.

Furthermore, the corresponding induced damage density contours for different aging times at strain rates $1\times10^{-4}/\sec$ and $5\times10^{-5}/\sec$, respectively, are depicted in Figure 6.18 and Figure 6.19. These damage density contours are shown at two strain levels: the strain level at which the material reaches the ultimate strength level and at the strain level in the post-peak region. It is observed that in the zero-aged material, the damage density variable is evenly distributed within the microstructure. However, the mode of damage density distribution changes when the material is subjected to oxidative aging. As can be seen from Figure 6.18 and Figure 6.19, in the aged asphalt concrete

microstructure, the damage density variable initiates and nucleates mostly in the upper parts where the oxygen source was applied. The diffused oxygen from the top surface degrades the mechanical properties of the matrix phase that is in contact with oxygen, whereas the properties of the matrix at the bottom parts of the RVE remain the same. Therefore, the aged matrix becomes more prone to initiate and propagate the damage density. It is noted that the propagation of the damage density variable is intensified when the aging time is increased.

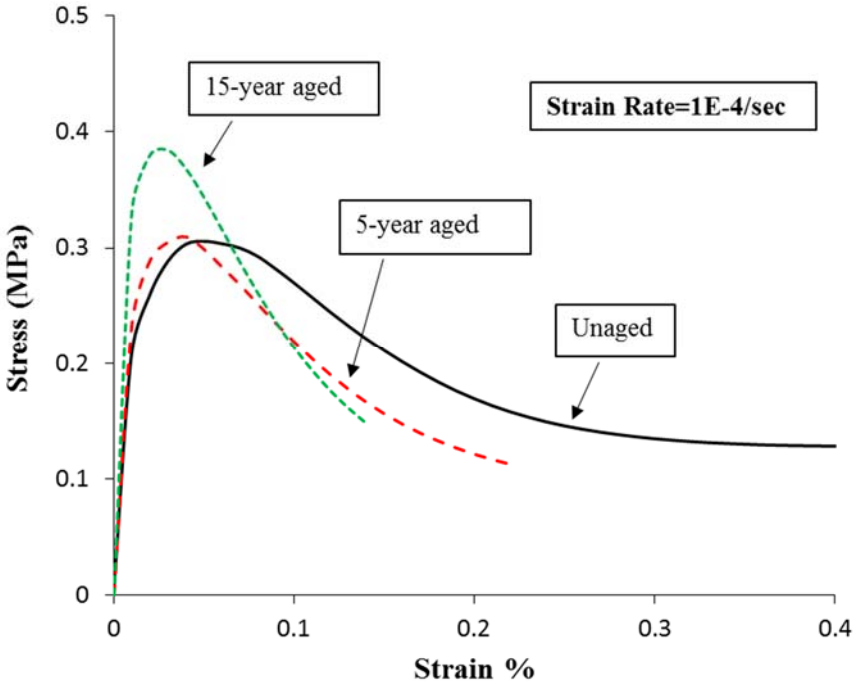

(a)

Figure 6.17. The resultant average stress-strain diagram of 3D asphalt concrete at different aging times and temperature 5°C corresponding to an applied strain rate of (a) 1E-4/sec and (b) 5E-5/sec.

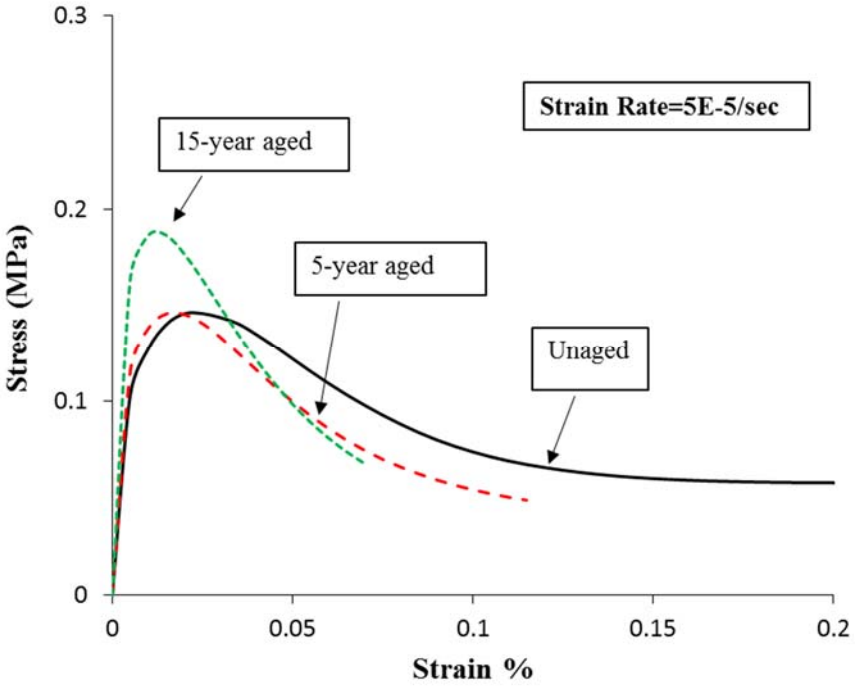

(b)

Figure 6.17. Continued.

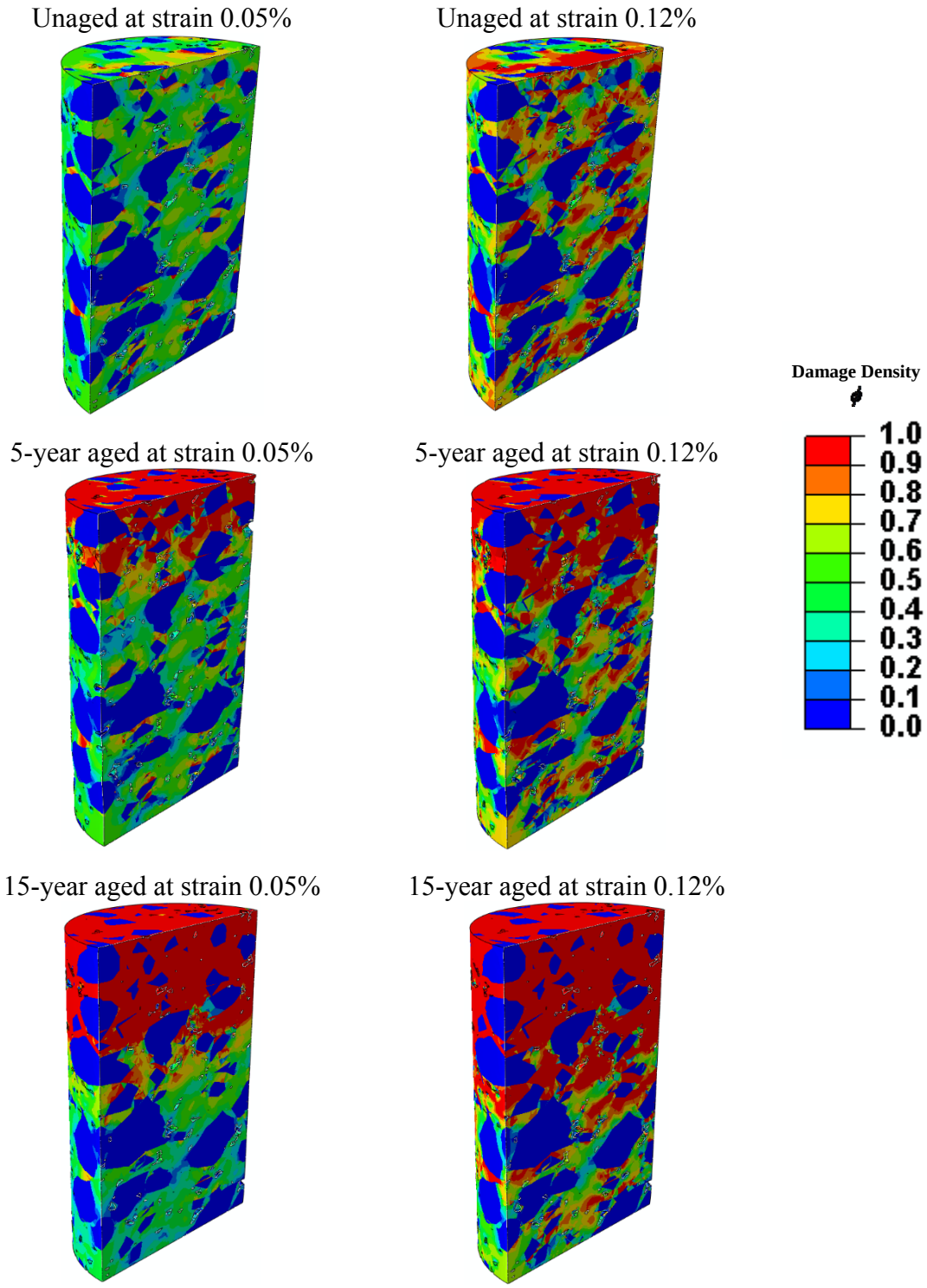

Figure 6.18. The damage density distribution at different aging times shown at two strain levels. The results correspond to the simulation with applied strain rate 1E-4/sec at 5°C.

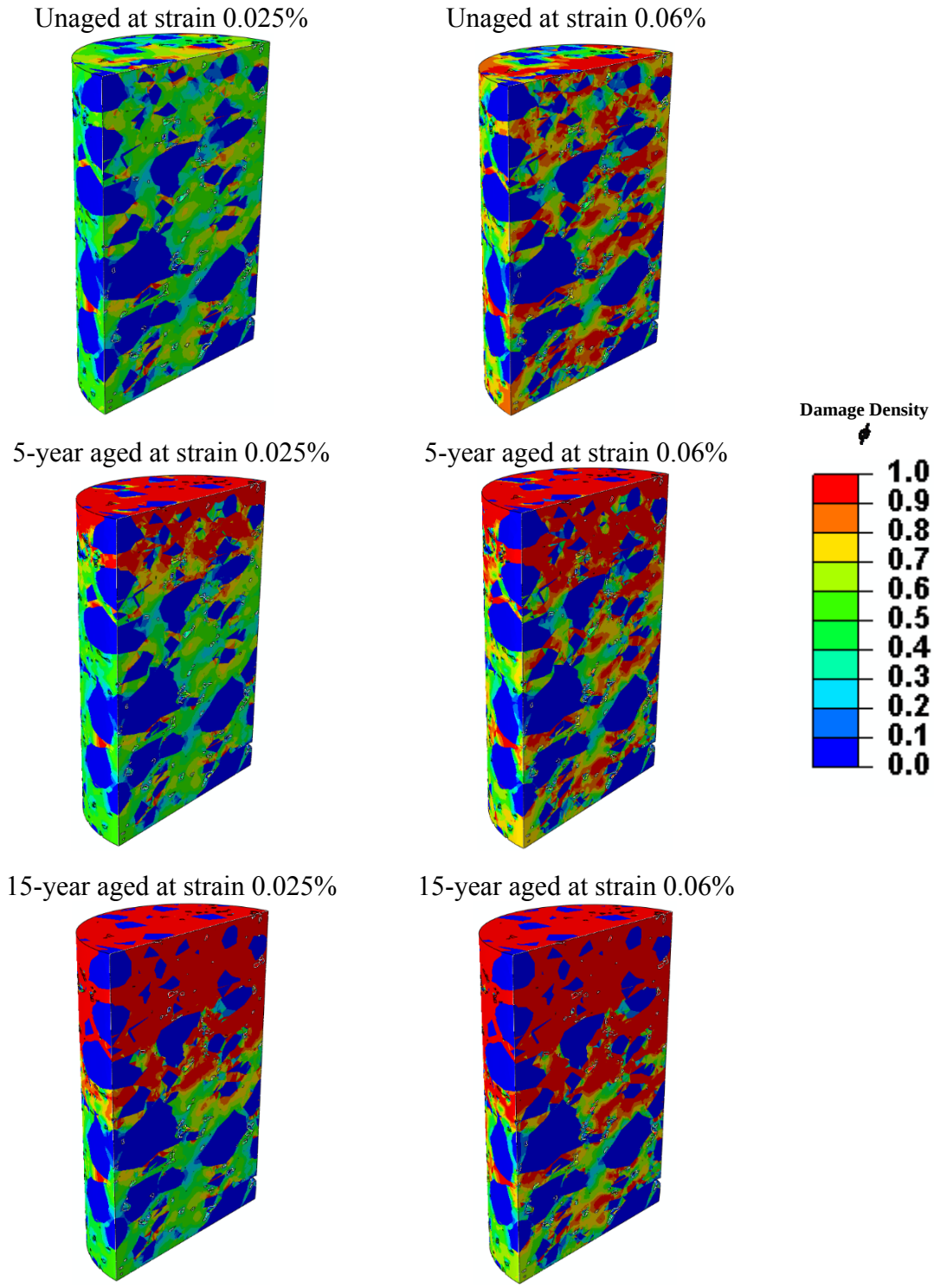

Figure 6.19. The damage density distribution at different aging times shown at two strain levels. The results correspond to the simulation with applied strain rate 5E-5/sec at 5°C.

6.3.3 Effect of Temperature

As discussed earlier, the asphalt concrete response is temperature-dependent, and asphalt oxidation occurs faster at higher temperatures. Therefore, to study the temperature effects on the mechanical behavior of the aged asphalt concrete, 3D simulations are conducted at 5°C and 19°C. In this case, the tensile strain load is applied at two different rates. The model parameters associated with different temperatures were previously described in Section 4. Figure 6.20(a) and Figure 6.20(b) represent the average stress-strain diagrams corresponding to strain rates $1\times10^{-4}/\sec$ and $5\times10^{-5}/\sec$, respectively. These figures clearly prove the dependency of the asphalt concrete response on the temperature even for the aged cases. The overall trend is that by increasing the temperature from 5°C and 19°C, the ultimate strength decreases. Moreover, comparing the 15-year aged material responses at two temperatures shows that the dependency of the mechanical response on the temperature decreases at longer aging times.

The damage density distributions are presented in Figure 6.21 and Figure 6.22 corresponding to different strain rates. These figures are plotted at the point where the material reached the ultimate strength. As seen in these figures, oxidative aging at the higher temperature has significant impact on the mechanical response, particularly damage density evolution. The reason is that the aging state variable evolves more rapidly at the higher temperature, making the mechanical material properties susceptible to producing more damage.

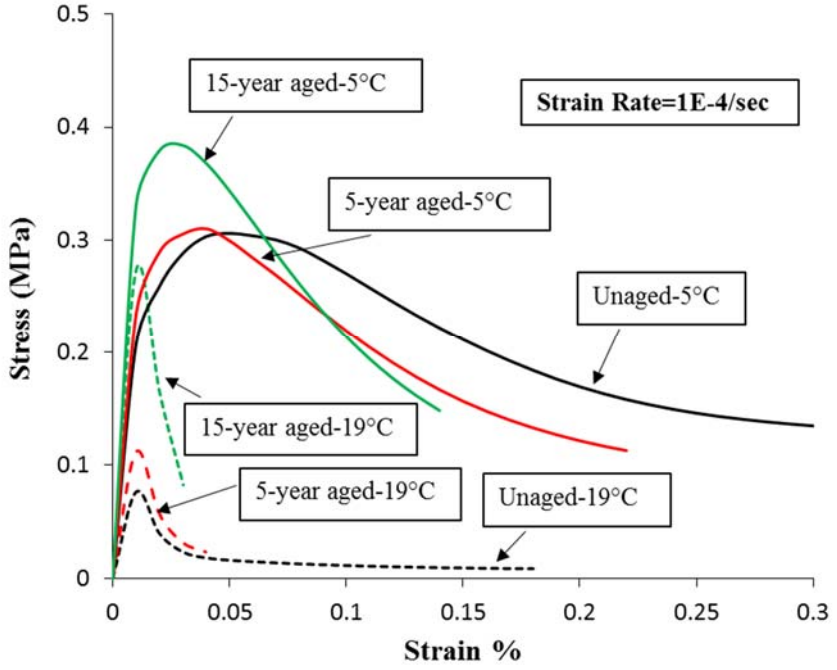

(a)

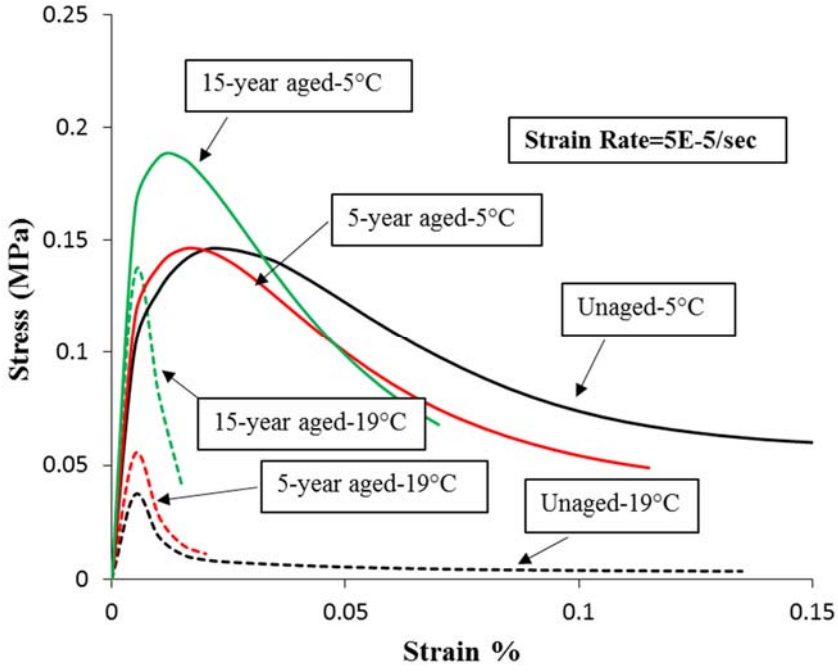

(b)

Figure 6.20. Comparing temperature dependency of the mechanical response of asphalt concrete under tensile strain rates of (a) 1E-4/sec and (b) 5E-5/sec, and at different aging times.

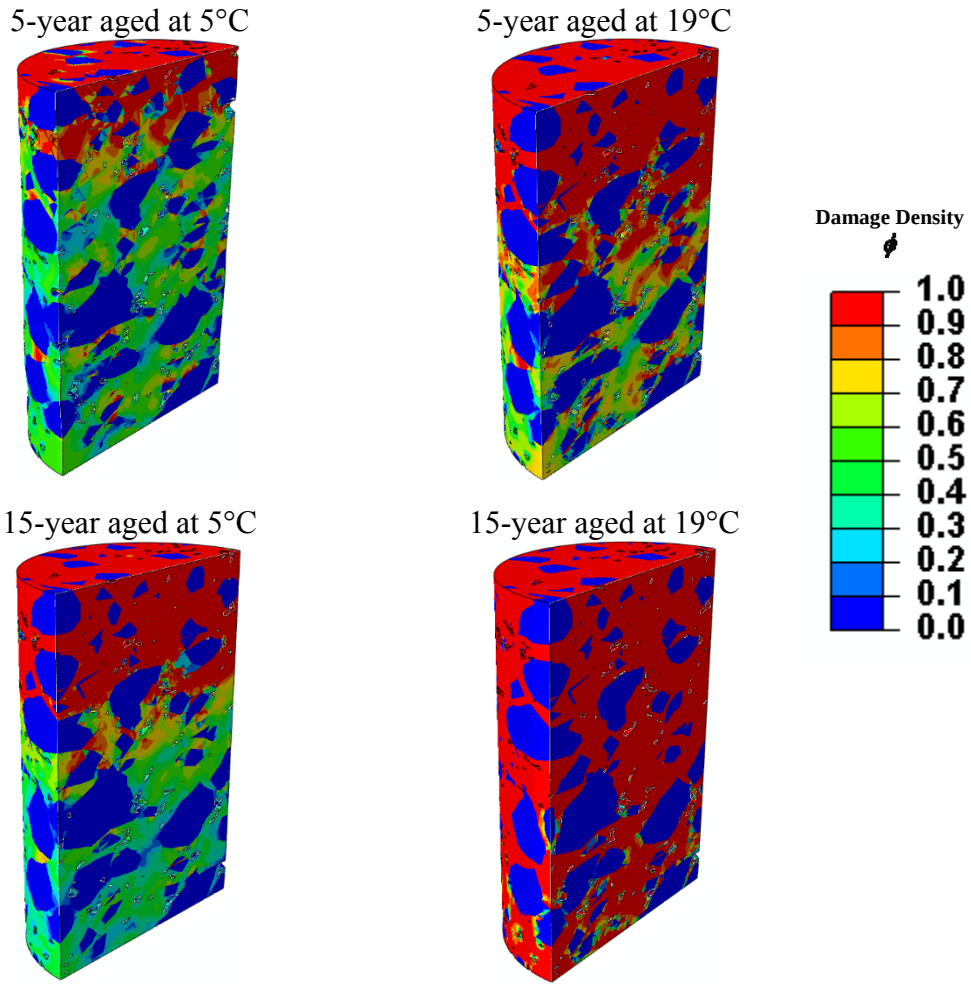

Figure 6.21. The damage density distribution at different aging times shown at the ultimate strength. The results correspond to the simulation with applied strain rate of 1E-4/sec.

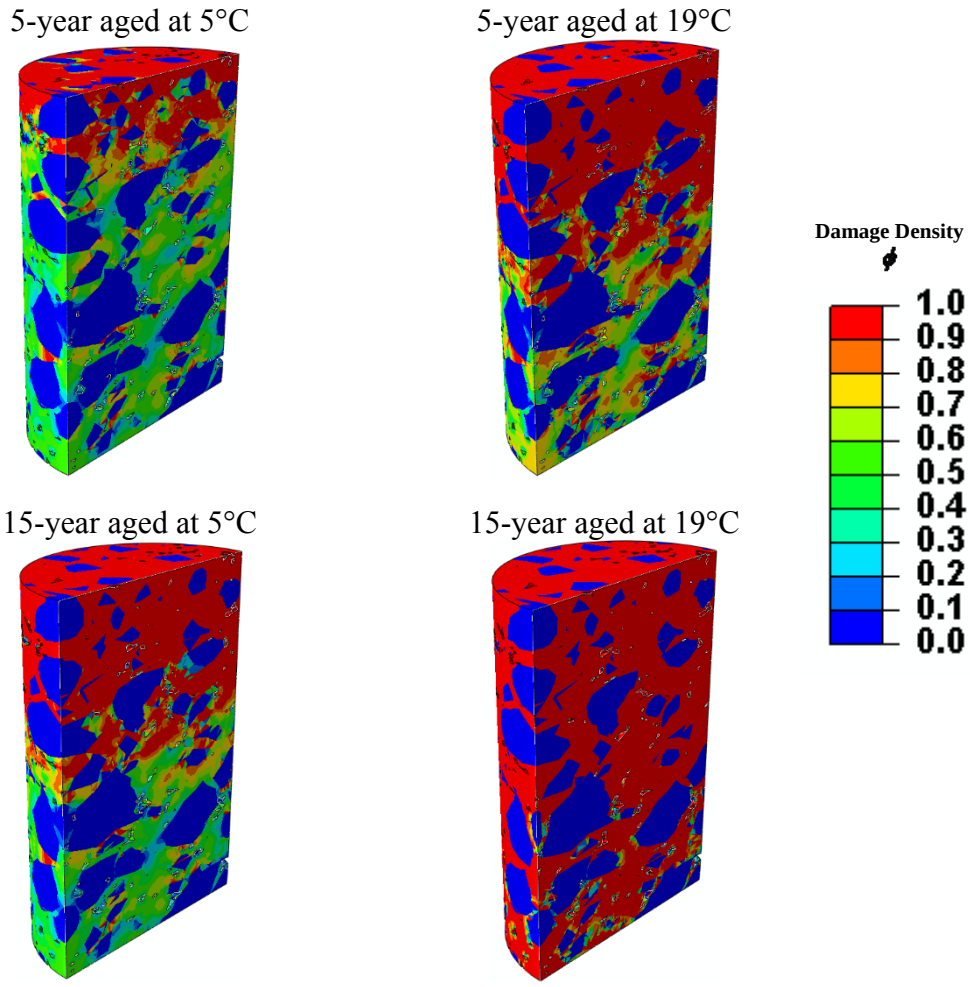

Figure 6.22. The damage density distribution at different aging times shown at the ultimate strength. The results correspond to the simulation with applied strain rate of 5E-5/sec.

6.3.4 Repeated Creep-Recovery Response

In order to investigate the capabilities of the model in simulating the cyclic loading, the repeated creep-recovery test at a constant compressive stress level is performed on the 3D microstructure at 5°C. The loading time is 0.7 sec followed by a 1.1-sec unloading period. The simulations are conducted on unaged and aged conditions. Figure 6.23(a) shows the stress history that is applied on the top boundary of the RVE, and Figure 6.23(b) represents the resultant strain response. It is expected that due to oxidative aging, the amount of strain response due to cyclic creep-recovery loading reduces, as this can be verified by experimental data such as those shown in Section 5. As shown in Figure 6.23(b), the finite element simulation on the asphalt microstructure using the coupled aging-viscoelastic-viscodamage constitutive relationship on the aged and unaged cases is able to predict the expected behavior. The amounts of accumulated strain during loading time and recovered strain during unloading time decrease as aging time increases.

Correspondingly, the distribution of the damage density variable is illustrated in Figure 6.24 at different loading times and aging conditions. At the unaged condition, the damage density variable initiates and propagates equally at different material points within the RVE. However, when oxygen diffusion from the top boundary is included in the simulations, the mode of distribution of the damage density significantly changes. The top layers of the RVE, which are mostly affected and degraded by oxygen diffusion, absorb a great deal of damage.

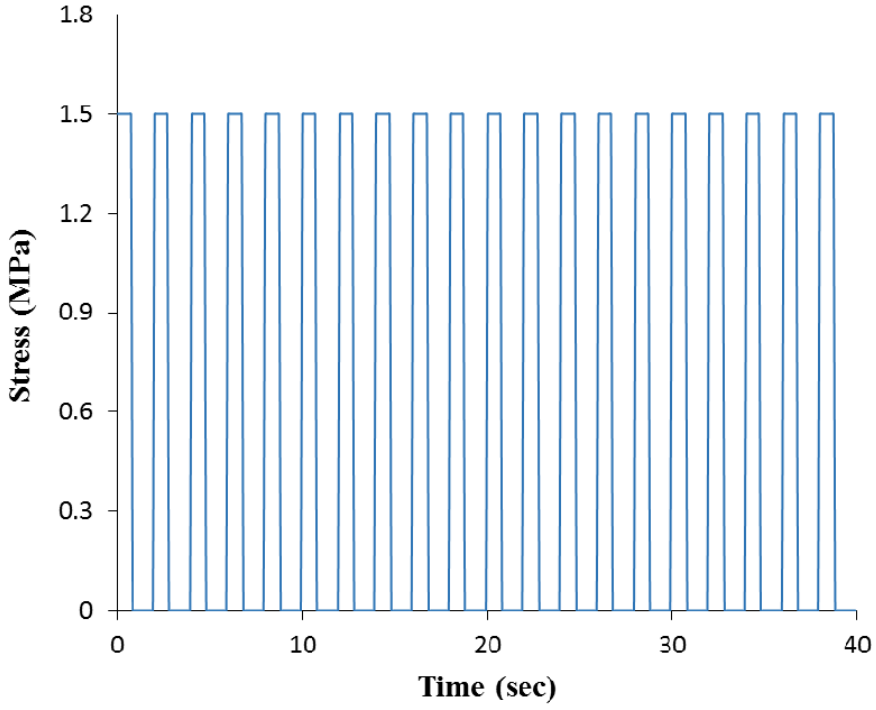

(a)

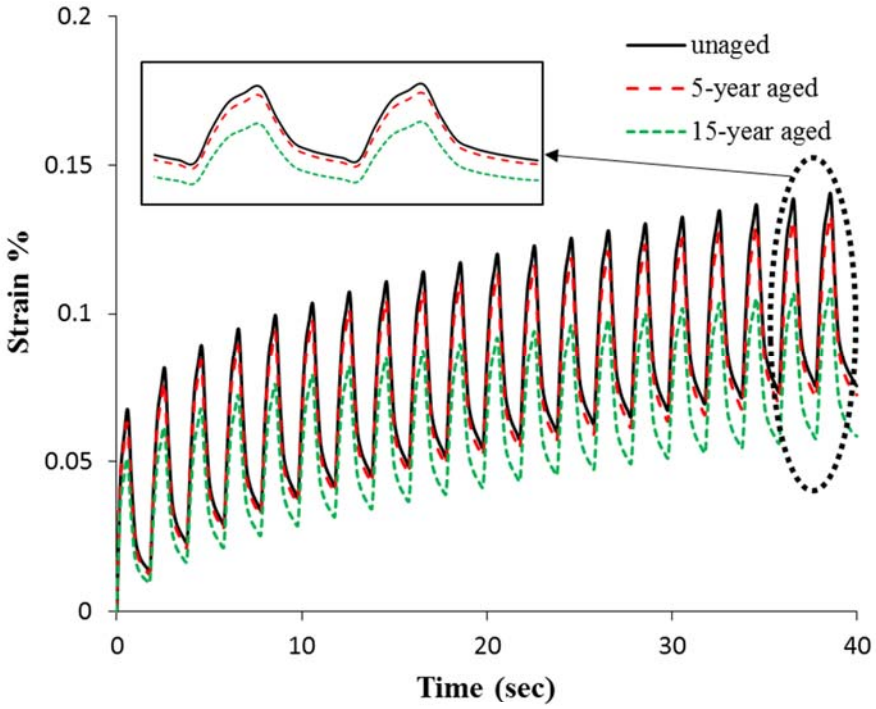

(b)

Figure 6.23. The repeated creep-recovery test simulated at 5°C and different aging times for the 3D microstructure. (a) The compressive stress-time diagram; (b) The strain-time response.

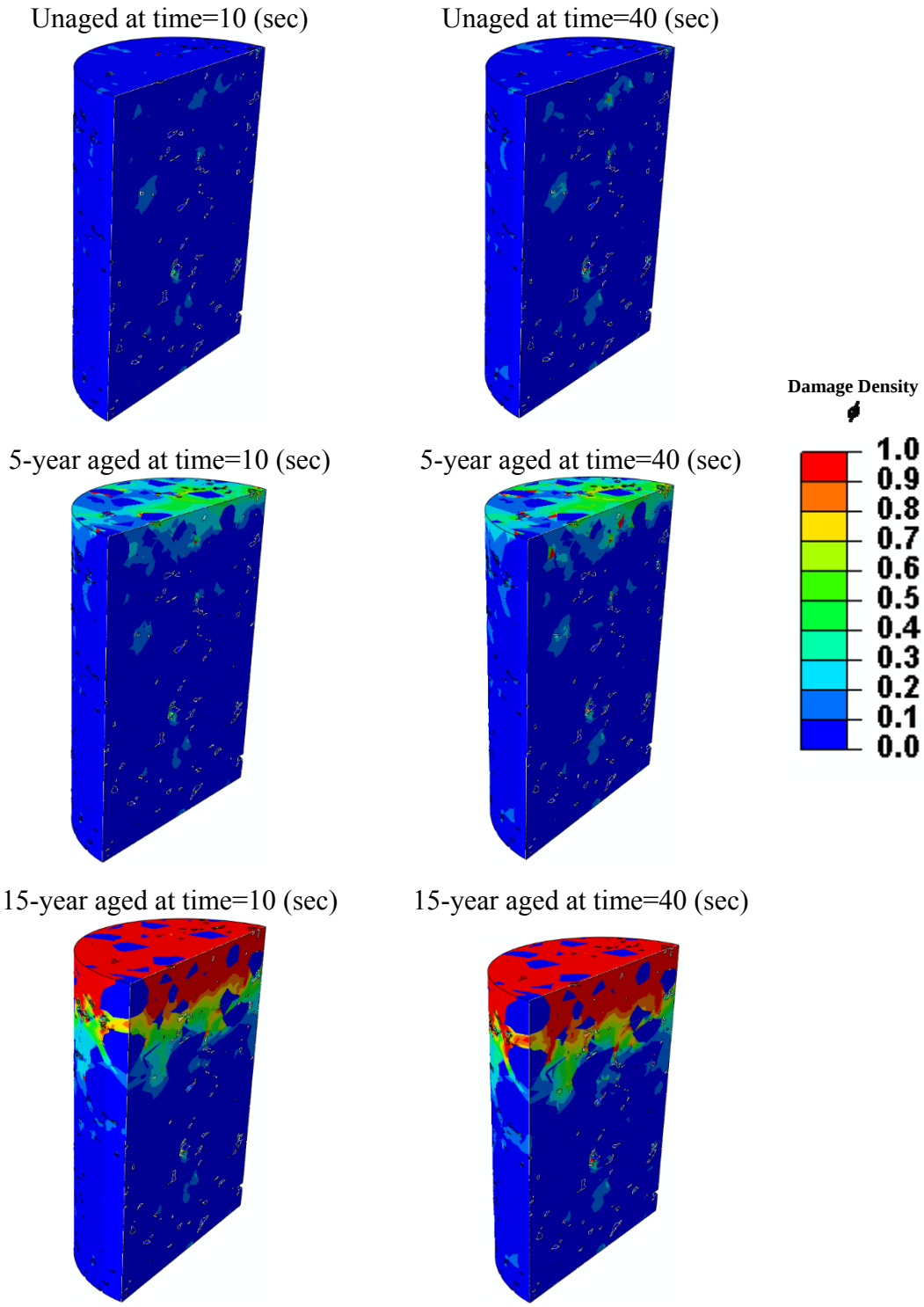

Figure 6.24. The damage density distribution during the repeated creep-recovery test at 5°C and different aging times, shown after 10 sec and 40 sec of loading. The constant compressive stress level of 1.5 MPa is applied during the loading intervals.

The microstructural finite element simulations presented for 2D and 3D cases suggest that the proposed oxidative aging-mechanical constitutive relationship is well-suited to micro-scale simulations of asphalt concrete. The simulations showed the propagation of the damage density within the microstructure occurs mainly in the matrix phase, being a weaker phase of asphalt binder and very fine aggregates. It is noted that the trend in the presented microstructural simulations for aged and unaged conditions is compatible with experimental observations, and this computational framework can be used to gain an insight toward the microstructural behavior of the aged asphalt concrete.

6.4 Simulation of 2D Pavement Structure in Macro-scale

The objective of this subsection is to apply the presented coupled aging-mechanical constitutive framework to predict the damage behavior of the aged pavement structure in macro-scale. The focus in this case is to investigate the capabilities of the aging constitutive relationship in capturing the performance of the pavement structure subjected to different aging times and repetitive loading. It was previously discussed that the oxidative aging has significant influence on the fatigue performance of asphalt concrete. Therefore, the simulations are conducted at lower temperatures to assure that the material behavior and the induced distress are governed by the viscodamage constitutive relationship, and the viscoplastic and healing effects are negligible. It should be noted that an accurate prediction of distress in pavements is a challenging task due to the complex nature of the loading conditions, the very large number of loading cycles, and the complicated constitutive behavior of the material. Even with the current power in computational analysis, conducting 3D finite element simulations of a pavement

structure subjected to millions of loading cycles and considering the realistic wheel tracking and environmental loading conditions seems impossible.

As a result, a simplified 2D axisymmetric finite element model is used in this work to simulate the behavior of the aged asphalt concrete pavement under cyclic pulse loading conditions. In order to consider the oxidative aging, the oxygen diffusion analysis is performed first using coupled diffusion-displacement analysis, and the mechanical pulse loading is applied on the top center of the axisymmetric model with 0.1 sec of loading and 0.4 sec of unloading times. The finite element model is illustrated in Figure 6.25.

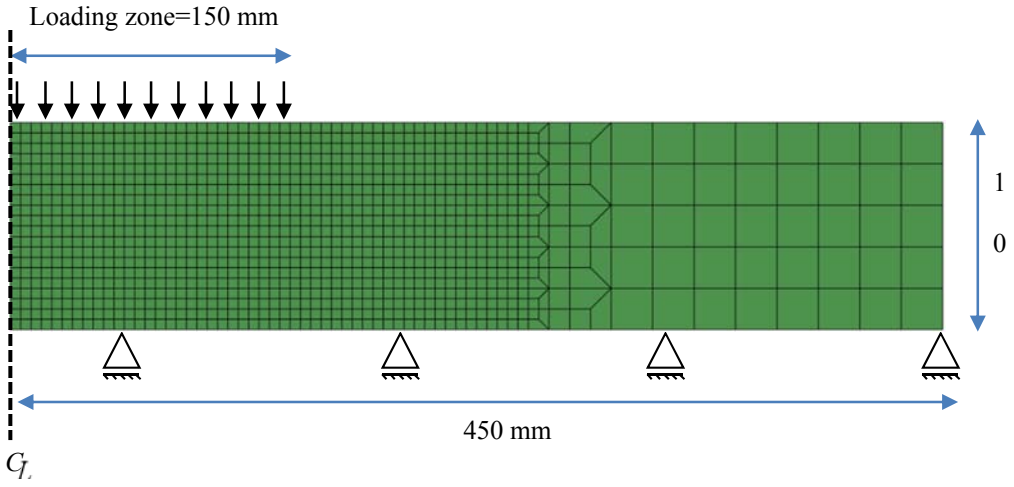

Figure 6.25. The finite element model of asphalt pavement structure and boundary conditions to perform two-dimensional simulations.

The oxygen diffusion analysis is conducted considering zero, 3-year, and 10-year aging times. The oxygen source is placed on the top surface of the asphalt concrete model and the side and the bottom boundaries are insulated. Figure 6.26(a) shows the oxygen diffusion analysis and the contours of the aging state variable within the pavement model. Since there is no additional oxygen flux at the side and bottom surfaces, oxygen diffuses uniformly, which resulted in uniform contours of the aging state variable. Figure 6.26(b) represents the variation of the aging state variable, A, through the thickness of the pavement model. This figure is in agreement with the observation of the oxidation that happens in the field, where the aging level is inversely proportional to the depth.

The resultant damage density distribution corresponding to different loading cycles and aging conditions is presented in Figure 6.27. It is noted that for clarity in presentation, the pavement model in these figures is mirrored at the center line. The damage density for the unaged pavement initiates from the bottom layers of the pavement model and propagates toward the upper layers. The damage density variable generally represents the micro-cracks and micro-damages in the asphalt concrete. Therefore, the evolving trend of this variable in the unaged case suggests that the cracks and damages in a zero-aged asphalt pavement form bottom–top cracks. On the other hand, when the pavement model is subjected to oxygen diffusion, the mode of damage density distribution changes. In this case, the damage variable originates from the top layers where the material points have been degraded due to oxygen diffusion. This

implies that cracks and damages in the aged asphalt pavement have top–bottom formations.

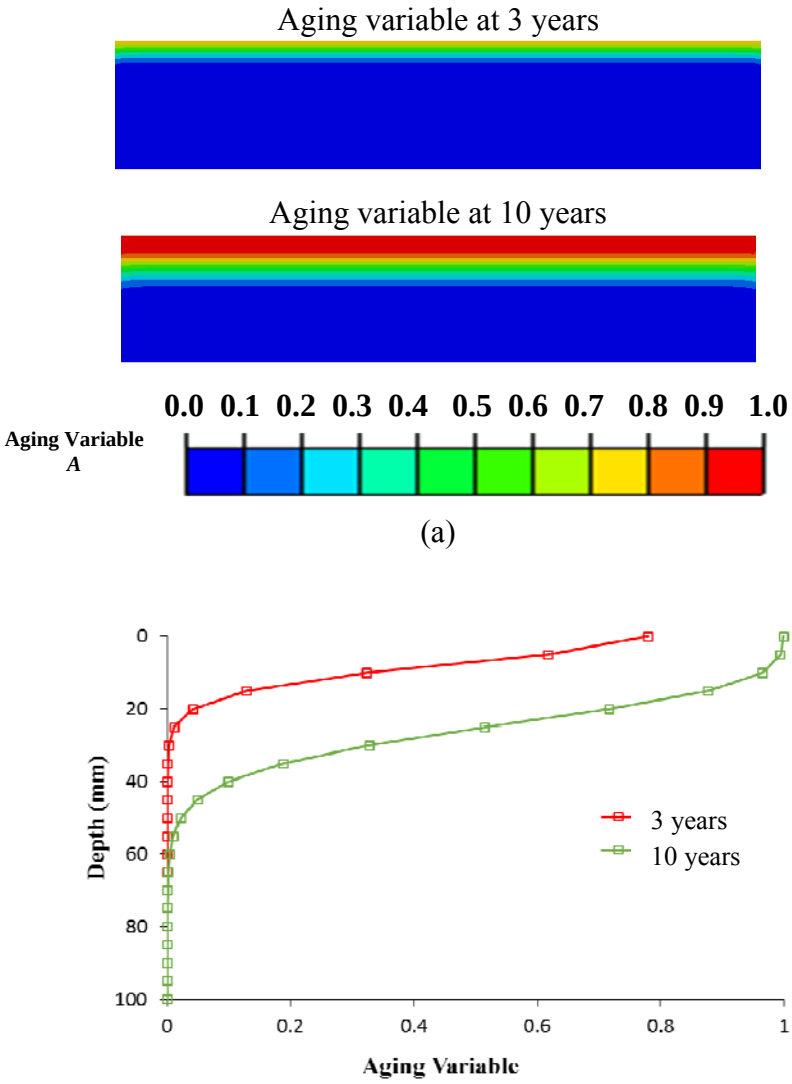

Figure 6.26. Two-dimensional oxygen diffusion simulation on pavement structure showing (a) aging variable contours and (b) variation of aging variable through the thickness. These simulations are based on several assumption: unit oxygen content on the top surface only and no oxygen consumption by reaction throughout the model; more information about these assumptions are given in subsection 4.2.1.

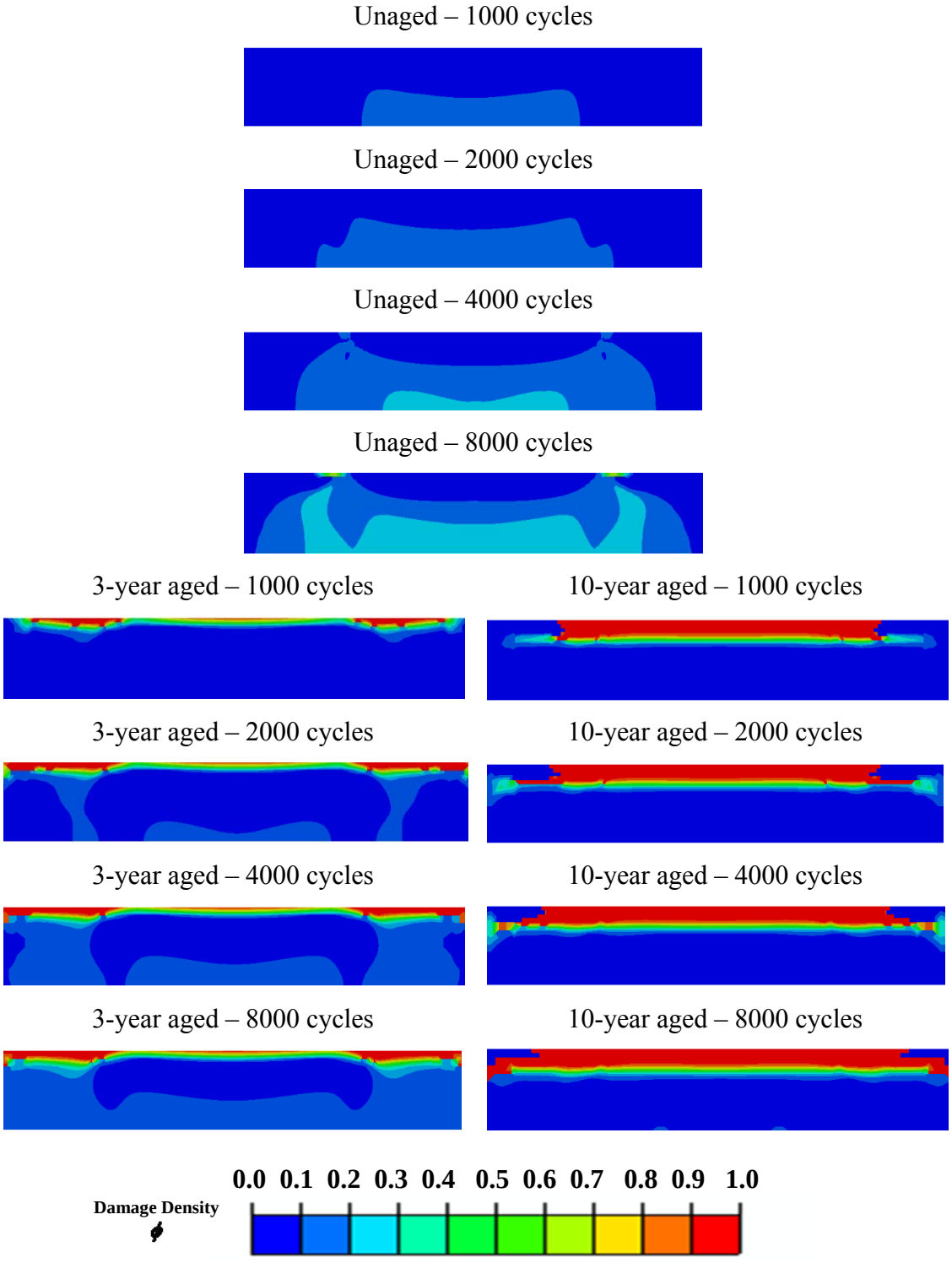

Figure 6.27. The comparison of the damage density distribution within the asphalt pavement model at different loading cycles and aging conditions.

6.5 Discussion

This section covered the finite element simulations performed on different asphalt concrete structures. The capabilities of the proposed oxidative aging constitutive relationship coupled to the viscoelastic-viscodamage constitutive relationship was investigated to simulate the aged asphalt concrete performance at multiple scales. The 2D and 3D asphalt concrete microstructures were constructed using X-ray CT images that include the aggregate, matrix, and air void phases.

In this section, the diffusion of oxygen in asphalt concrete is modeled using Fick's law. A unit oxygen concentration is introduced only on the top boundary and the only mechanism for oxygen transport is through diffusion that is driven by concentration gradient with assigning a constant diffusion coefficient throughout asphalt concrete. As discussed earlier, this study does not account for convective oxygen flow through the interconnected air voids. Therefore, the oxygen diffusion simulations in the pavement, as a function of time and depth, would be different than predictions obtained from models of oxygen transport previously presented (Glover et al., 2014). This limitation can be partially addressed by introducing oxygen concentration in air voids as part of boundary conditions. An example of this case is presented as Case 2 in subsection 6.2.5, where different air voids in the depth of asphalt concrete are assumed as oxygen sources.

The 2D and 3D microstructures were subjected to different loading scenarios and aging conditions at different temperatures, and at each case comparisons were made. The stress-strain diagrams showed that the oxidative aging increases the ultimate strength and stiffness of the microstructural models. However, it was shown that the aged

material behaves more brittle compared to the ductile behavior of the unaged asphalt concrete microstructure. The damage density contours in the 2D and 3D asphalt concrete microstructures were drawn and shown for different aged and unaged cases. It was observed that when the microstructure was subjected to oxygen diffusion, the trend of damage density initiation and evolution significantly changed and localized in the upper layers where the material points were affected by oxygen.

Furthermore, the pavement model of asphalt concrete was simulated at the macroscopic scale. The pavement model was first subjected to oxygen diffusion at different times and then thousands of loading cycles. It was shown that the proposed aging constitutive relationship reasonably predicts the aged pavement behavior such that the variation of the aging state variable was inversely proportional to the thickness of the pavement model. Moreover, comparing the damage density distribution for the unaged and aged conditions demonstrated that as the pavement model was subjected to more oxidative aging, the damage variable moved from bottom-up to top–bottom formation.

The results in this section show that the presented computational framework can be used to simulate the macroscopic thermo-chemo-mechanical response of asphalt concrete under different loading conditions, aging levels, and temperatures. It particularly allows one to conduct virtual experiments, which saves a great deal of resources and efforts. In fact, the proposed framework can be applied to guide and assist in beneficial designing of asphalt concrete microstructure in order to obtain and construct more sustainable material that lasts longer in the field.

Finally, the presented simulations are considered examples of utilizing the developed aging constitutive relationship in modeling the age hardening of asphalt concrete through usages of 2D and 3D microstructures. In additions, the aging constitutive relationship is used to simulate change in mechanical properties and response of pavement structure at macro-scale. In spite of the aforementioned limitations, the diffusion framework presented here can be also applied to model the diffusion problem in asphalt concrete when the interconnected air voids are sufficiently low, that the delivery of oxygen from the air voids to the adjoining binder is negligible. In addition, the model can be applied to other particulate composites in which oxygen diffusion is the main mechanism of transport.

7. CONCLUSIONS AND RECOMMENDATIONS

This study addresses the need in the asphalt pavement community to develop a constitutive modeling framework and a computational tool that uses a mechanistic-based oxidative aging relationship and includes it in a comprehensive model that is capable of describing the complex time-dependent, temperature-dependent, and stress-dependent behavior of asphalt concrete. Therefore, the main objectives of this dissertation were: (1) to develop a phenomenological mechanistic-based aging constitutive relationship that relates the hardening effects of oxidation to the mechanical behavior of asphalt concrete, and (2) to use the proposed constitutive modeling framework to efficiently predict the response of asphalt concrete and asphalt pavements subjected to aging and different loading conditions.

7.1 Conclusions

The phenomenon-based aging constitutive relationship is developed based on the evolution of the aging state variable. The aging relationship is a continuum-based constitutive equation that is motivated with the oxidation kinetics that occur at the molecular level. Therefore, the rates of change of the aging state variable and oxygen content are formulated as conjugate variables. In the aging constitutive equation, the aging state variable measures the changes in material properties, which are the increases in stiffness and viscosity as a result of oxidation. In order to capture the influence of aging on the mechanical response of the aged asphalt mixtures, the aging state variable is considered to affect the fundamental viscoelastic properties governing the stiffness and

viscosity of the material. In that, Schapery's viscoelastic theory is extended to account for the hardening effects of aging. The compliance terms and retardation times, which represent the transient response of asphalt concrete, are modified based on the time-dependent aging state variable. It is noted that the compliance terms are measures of stiffness, whereas the retardation times are the characteristic properties of viscoelastic materials being inversely related to viscosity of the material. This study proposes that both the compliance terms and the retardation times decrease with age. Therefore, the proposed relationship for the aged viscoelasticity predicts that the stiffness and viscosity of the aged material increase by decreasing the compliance terms and the retardation times. Since the viscoelastic theory is coupled to other mechanical components (such as damage and permanent deformation) of the material via PANDA, the predicted change in the viscoelastic properties due to the aging variable affects the overall mechanical behavior of asphalt concrete.

In order to ensure accuracy using the proposed aging model, the aging constitutive equation is calibrated against careful laboratory experiments and is subsequently validated against independent experimental data. A comprehensive methodology is developed and presented in this dissertation in order to identify the material parameters associated with the combined aging-mechanical constitutive relationships. The model calibration involves using the computational approach to estimate oxygen diffusivity, the dynamic modulus test to identify aging and linear viscoelastic parameters, the repeated creep-recovery test to extract nonlinear viscoelastic and viscoplastic material parameters, and the uniaxial constant strain test to calibrate

viscodamage parameters. In order to save the analysis time and increase the accuracy of the calibration procedure, the systematic approach presented in Section 44 was implemented in the MATLAB program and integrated with PANDA through the Panda Parameter Identifier (PPI) toolkit.

A computational approach is presented to obtain the effective oxygen diffusivity of asphalt concrete based on the oxygen diffusivity of its constituents (i.e., aggregate, asphalt binder, and air voids). The oxygen diffusivity of asphalt concrete is required to calculate the oxygen content distribution in the aged material. The oxygen transport is modeled using Fick's second law of diffusion. The diffusion simulations in material microstructures presented in this dissertation do not consider convective flow of oxygen in interconnected air voids, which is believed to be the main mechanism for oxygen to reach the internal structure. This limitation can be overcome partially by assigning oxygen concentration in air voids as part of boundary conditions.

Oxidative aging history term is incorporated in the aging constitutive relationship to implicitly account for the changes in the oxygen diffusivity of asphalt as well as the change in the rate of oxidative aging as the level of oxidation increases. It is noted that using Fick's second law to calculate oxygen content is an approximation because it does not account for the reaction term. However, in this study, the decreasing effect of chemical reaction on the diffusion rate, and subsequently decreasing the aging rate, is partially and indirectly considered via including the aging history term. Another approach is to incorporate such effects explicitly in the transport model. For example, one can use a non-Fickian diffusion model that takes into account the chemical potential

term, in which the diffusion rate of the material is affected by the chemical reactions occur due to oxidation of the asphalt components. However, this has not been done in this study, as the focus of the current research was on predicting the effect of aging on mechanical properties. All the model parameters in this study are calibrated against the set of ARC experimental data. The dynamic modulus test conducted for variously aged asphalt concrete specimens is used to calibrate the aging state variable at different ages. The dynamic modulus test data of the unaged material is used to identify linear viscoelastic parameters. The repeated creep-recovery test at variable stress levels conducted at a high temperature is used to obtain the nonlinear viscoelastic and viscoplastic material properties. The viscodamage parameters are determined using the uniaxial constant tensile strain rate test at a low temperature. Finally, the micro-damage healing material properties are identified by repeated creep-recovery test with variable resting times. All the material parameters are then used to validate the model predictions against other different tests that are not used in the calibration procedures.

The capability of the presented aging-mechanical constitutive relationship in predicting the mechanical response of the aged asphalt mixtures is validated against the ARC data. Several repeated creep-recovery tests at different stress level, aging time, temperature, and air void content are used to validate the combined aging-viscoelastic-viscoplastic behavior of asphalt concrete specimens. The model predictions are well in agreement with the experimental data. Furthermore, the capabilities of the aging-viscoelastic-viscodamage-healing constitutive relationship are investigated in predicting the repeated creep-recovery response when resting periods are different. It was shown

that the proposed constitutive modeling can reasonably predict the response of the aged asphalt concrete. Finally, the fatigue performance of the aged material is validated against the cyclic displacement-controlled test at different temperatures and strain amplitudes. The mechanical responses calculated by combined aging-viscoelastic-viscodamage constitutive relationship are in good agreement with the measured response of the utilized asphalt mixture.

Section 6 presented a framework to conduct finite element simulations on asphalt mixtures using coupled aging-mechanical material behavior at multiple scales. The 2D and 3D microstructures of asphalt concrete, which are constructed using X-ray CT images, consist of three phases: aggregate, matrix, and air void. In this case, it is assumed that the matrix phase in the microstructures behaves in accordance with the proposed aging-mechanical constitutive relationship. Since no independent experimental tests were conducted on asphalt binder, the material properties of asphalt binder in the matrix phase are based on assumptions. Hence, the presented results in this section are not compared to any experimental data and the focus was to investigate the capabilities of the proposed framework on simulating the anticipated macroscopic behavior of the aged asphalt mixture under different loading conditions. Therefore, different loading scenarios in tension and compression at various aging times are considered and applied to the microstructures. It was shown that the combined aging-viscoelastic-viscodamage constitutive relationship is capable of simulating the expected performance of the aged material, being the increase in stiffness and the brittleness. Moreover, the mode of damage density initiation and nucleation is computationally shown to be significantly

changed from unaged to aged cases. When the oxygen diffusion is included in the simulations, the damage density variable initiates and propagates mainly at the top layers of the microstructure where the material properties in these areas are affected by oxygen.

Consequently, the capabilities of the proposed constitutive modeling framework in simulating the fatigue performance of the aged material is investigated by 2D finite element simulations performed on the pavement structure on the macroscopic scale. The pulse loading up to 8000 cycles is applied on the unaged and 3- and 10-year aged cases. The computational results show that age-hardening increases the potential of the material to develop more damage compared to the unaged case. Moreover, the top–bottom damages are observed when the pavement model is subjected to oxygen diffusion from the top boundary normal to the pavement surface.

The oxygen diffusion in this study is simulated and approximated using Fick's second law of diffusion assuming a constant effective oxygen diffusivity for the asphalt mixture. Although the nonlinear evolution of the aging state variable is partially modeled via the aging history term, $(1-A)$, a more accurate transport model is required to precisely model the oxygen diffusion. The shortcoming of Fick's law stems from the fact that it does not account for the chemical potential and consumption of the oxygen as it diffuses in the asphalt mixture. Therefore, the proposed aging constitutive relationship in this study can be improved by employing more accurate transport models that take into account both diffusion and reaction terms in the oxygen transport problem to calculate more precise values for oxygen content with respect to time and position. However, this

issue has not addressed in this dissertation, as the focus was on predicting the effect of aging on mechanical properties. This will be the subject of future research in this area.

Overall, the following conclusions can be made through the subjects presented in this dissertation:

- The coupled continuum-based aging-mechanical constitutive framework provides a robust approach to model the effects of age-hardening on mechanical behavior of asphalt concrete.
- The oxidative aging constitutive relationship is an improvement over the previous approaches in modeling the aging effects on the mechanical behavior of asphalt concrete. It is consistent with the oxidation kinetics and is able to predict that the stiffness and viscosity of the aged material increase by decreasing the compliance terms and the retardation times.
- The presented process to identify the material parameters provides a simple and robust method to obtain the material properties that can be used to predict the mechanical response of the aged asphalt concrete under different loading scenarios.
- The microstructural simulation provides a well-suited computational tool to perform various virtual experiments with different aging and loading conditions.
- When the oxidative aging constitutive relationship is included, the finite element simulation is able to alter the damage density paradigm within the microstructural level. In this case, the damage density variable localizes and moves toward the material points that have been influenced by oxygen diffusion.

7.2 Recommendations and Future Research Areas

- *Integration of a more accurate oxygen transport model:* All the simulations presented in this dissertation assume that oxygen diffuses from the surface to the material microstructure. It is recommended that future work focuses on the development of a more accurate oxygen transport model that takes into account convective flow of oxygen through the interconnected air voids.
- *Incorporation of oxidative aging kinetics in transport model:* The oxygen transport model used in this study is Fick's second law that is only based on time and spatial coordination. However, it is known that the consumption of oxygen, as it diffuses in pavement and reacts with asphalt binder, plays a crucial role controlling the aging rate. Therefore, it is recommended to further develop the transport model based on the actual kinetics of oxidation and the fundamental properties that govern this reaction. Consequently, the developed aging constitutive relationship should be integrated with this advanced transport model to better predict the performance of aged pavements subjected to mechanical loading.
- *Consideration of the coupling between the environmental conditions and mechanical loading:* The effects of oxidative aging on the mechanical behavior of asphalt concrete is investigated and modeled in this work. An aged asphalt concrete is more susceptible to produce micro-cracks under mechanical loading. Consequently, the nucleation of these micro-cracks increases the porosity of pavements, allowing the air oxygen and moisture to reach more rapidly inside the

material layers. This coupling phenomenon contributes to more induced damage due to further mechanical loading. Therefore, consideration of the coupling between these mechanisms through robust constitutive modeling will enhance the predictions of the lifetime performance of asphalt pavement.

- *Investigation of the thermal coupling term:* The thermal coupling term in this study incorporates the effect of temperature variations on the rate of the aging state variable. However, there are no experimental data to calibrate the temperature-dependent parameters. It is suggested that asphalt concrete specimens be aged at different temperatures such that one will be able to identify the related parameters. The proper knowledge of the thermal coupling term enables one to effectively conduct the finite element simulations under realistic conditions in the case of considering temperature variations in the different layers of asphalt pavements.
- *Investigation of relationship between binder aging and mixture aging:* The developed constitutive model can be used to study the effect of aging on the rheological and mechanical behaviors of asphalt binders and asphalt mixtures. Therefore, it is recommended to investigate the relationship between the aging mechanisms of binder and their counterparts in asphalt mixtures. This offers a unique opportunity to better understand how various elements of the mixture (i.e. binder properties, binder content, aggregate type, aggregate distribution, air void distribution) affect the aging of the mixture and consequently the performance of asphalt pavements.

- *Extension of the constitutive modeling to the large deformation theories:* This study assumes the small deformation theories for asphalt concrete. However, in specific conditions, such as high temperatures, the asphalt concrete may undergo large deformation such that the small deformation theories may fail to reasonably predict the mechanical response. Furthermore, even at lower temperatures asphalt concrete may experience finite strains at high damage densities. Therefore, extending the current framework to large deformation theories will be helpful in analyzing the asphalt concrete at high temperatures or higher damage densities.
- *Extension of the damaged configuration for anisotropic cases:* The damage state variable (i.e., damage density) presented in this study is assumed to be isotropic. However, asphalt concrete is highly heterogeneous and anisotropic. As a result, the extension of the presented damaged configuration to the anisotropic cases will be beneficial to ensure the robustness of the constitutive relationships under different loading conditions.

REFERENCES

AASHTO TP4/T312, 2007. Standard Method for Preparing and Determining the Density of Hot Mix Asphalt (HMA) Specimens by Means of the Superpave Gyratory Compactor. American Association of State Highway and Transportation Officials, Washington D.C.

AASHTO TP 62, 2007. Test for Determining Dynamic Modulus of Hot Mix Asphalt (HMA). American Association of State Highway and Transportation Officials, Washington D.C.

Abu Al-Rub, R.K., Darabi, M.K., 2012. A Thermodynamic Framework for Constitutive Modeling of Time- and Rate-Dependent Materials. Part I: Theory, Int J Plasticity 34, 61-92.

Abu Al-Rub, R.K., Darabi, M.K., Kim, S.M., Little, D.N., Glover, C.J., 2013. Mechanistic-Based Constitutive Modeling of Oxidative Aging in Aging-Susceptible Materials and Its Effect on the Damage Potential of Asphalt Aoncrete, Constr Build Mater 41, 439-454.

Abu Al-Rub, R.K., Darabi, M.K., Little, D.N., Masad, E.A., 2010. A Micro-Damage Healing Model that Improves Prediction of Fatigue Life in Asphalt Mixes, Int J Eng Sci 48, 966-990.

Abu Al-Rub, R.K., Darabi, M.K., You, T., Masad, E.A., Little, D., 2011. A Unified Continuum Damage Mechanics Model for Predicting the Mechanical Response of Asphalt Mixtures and Pavements, International Journal of Roads and Airports 1, 68-84.

Adams, D.F., Crane, D.A., 1984. Finite-Element Micromechanical Analysis of a Unidirectional Composite Including Longitudinal Shear Loading, Comput Struct 18, 1153-1165.

Al-Azri, N.A., Jung, S.H., Lunsford, K.M., Ferry, A., Bullin, J.A., Davison, R.R., Glover, C.J., 2006. Binder Oxidative Aging in Texas Pavements - Hardening Rates, Hardening Susceptibilities, and Impact of Pavement Depth, Bituminous Materials and Nonbituminous Components of Bituminous Paving Mixtures 2006, 12-20.

Arao, Y., Yukie, O., Koyanagi, J., Takeda, S., Kawada, H., 2012. Simple Method for Obtaining Viscoelastic Parameters of Polymeric Materials by Incorporating Physical-Aging Effects, Mech Time-Depend Mat 16, 169-180.

ASTM D 2493-01, 2009. In Standard Test Method For Resilient Modulus of Bituminous Mixture. West Conshohocken, PA.

Beran, M., 1965. Statistical Continuum Theories, T Soc Rheol 9, 339-355.

Bhasin, A., Bommavaram, R., Greenfield, M.L., Little, D.N., 2011. Use of Molecular Dynamics to Investigate Self-Healing Mechanisms in Asphalt Binders, J Mater Civil Eng 23, 485-492.

Bykov, D.L., Martynova, E.D., 2011. Structure-Energy Analysis of Models of Nonlinearly Viscoelastic Materials with Several Aging and Viscosity Functions, Mech Solids+ 46, 52-61.

Carslaw, H.S., 1959. Conduction of Heat in Solids. Oxford, Clarendon Press, Oxford.

Chaboche, J.L., 2003. Damage Mechanics, in: Karihaloo, I.M.O.R. (Ed.), Comprehensive Structural Integrity. Pergamon, Oxford, pp. 213-284.

Chazal, C.F., Pitti, R.M., 2009. An Incremental Constitutive Law for Ageing Viscoelastic Materials: A Three-Dimensional Approach, Cr Mecanique 337, 30-33.

Chen, J.S., Huang, L.S., 2000. Developing an Aging Model to Evaluate Engineering Properties of Asphalt Paving Binders, Mater Struct 33, 559-565.

Coons, R.F., 1965. An Investigation of the Hardening of Asphalt Recovered from Pavements of Various Ages. Georgia Institute of Technology. Directed by Paul H. Wright.

Darabi, M.K., Abu Al-Rub, R.K., Little, D.N., 2012a. A Continuum Damage Mechanics Framework for Modeling Micro-Damage Healing, Int J Solids Struct 49, 492-513.

Darabi, M.K., Abu Al-Rub, R.K., Masad, E.A., Huang, C.W., Little, D.N., 2011. A Thermo-Viscoelastic-Viscoplastic-Viscodamage Constitutive Model for Asphaltic Materials, Int J Solids Struct 48, 191-207.

Darabi, M.K., Abu Al-Rub, R.K., Masad, E.A., Huang, C.W., Little, D.N., 2012b. A Modified Viscoplastic Model to Predict the Permanent Deformation of Asphaltic Materials Under Cyclic-Compression Loading at High Temperatures, Int J Plasticity 35, 100-134.

Darabi, M.K., Abu Al-Rub, R.K., Masad, E.A., Little, D.N., 2012c. A Thermodynamic Framework for Constitutive Modeling of Time- and Rate-Dependent Materials. Part II: Numerical Aspects and Application to Asphalt Concrete, Int J Plasticity 35, 67-99.

Darabi, M.K., Abu Al-Rub, R.K., Masad, E.A., Little, D.N., 2013. Constitutive Modeling of Fatigue Damage Response of Asphalt Concrete Materials with Consideration of Micro-Damage Healing, Int J Solids Struct 50, 2901-2913.

Di Benedetto, H., Mondher, N., Sauzeat, C., Olard, F., 2007. Three-Dimensional Thermo-Viscoplastic Behaviour of Bituminous Materials - The DBN Model, Road Mater Pavement 8, 285-315.

Domke, C.H., Davison, R.R., Glover, C.J., 1999. Effect of Oxidation Pressure on Asphalt Hardening Susceptibility, Transp Res Record, 114-121.

Domke, C.H., Davison, R.R., Glover, C.J., 2000. Effect of Oxygen Pressure on Asphalt Oxidation Kinetics, Ind Eng Chem Res 39, 592-598.

Gibiansky, L.V., Milton, G.W., 1993. On the Effective Viscoelastic Moduli of 2-Phase Media .1. Rigorous Bounds on the Complex Bulk Modulus, Proceedings of the Royal Society of London Series a-Mathematical Physical and Engineering Sciences 440, 163-188.

Glover, C.J., Han, R., Jin, X., Prapaitrakul, N., Cui, Y., Rose, A., Lawrence, J.J., Padigala, M., Arambula, E., Park, E.S., Martin, A.E., 2014. Evaluation of Binder Aging And Its Influence In Aging Of Hot Mix Asphalt Concrete: Technical Report. FHWA/TX-14/0-6009-2, Chapter 8.

Glover, C.J., Martin, A.E., Chowdhury, A., Han, R., Prapaitrakul, N., Jin, X., Lawrence, J., 2008. Evaluation of Binder Aging and Its Influence in Aging of Hot Mix Asphalt Concrete: Literature Review and Experimental Design, College Station, Tx, Texas Transportation Institute.

Guild, F.J., 1990. Internal Stresses in Heterogeneous Solids, Compos Sci Technol 38, 193-193.

Guo, Y.L., Wang, N., Bradshaw, R.D., Brinson, L.C., 2009. Modeling Mechanical Aging Shift Factors in Glassy Polymers During Nonisothermal Physical Aging. I. Experiments and KAHR-a(te) Model Prediction, J Polym Sci Pol Phys 47, 340-352.

Gusev, A.A., 1997. Representative Volume Element Size for Elastic Composites: A Numerical Study, J Mech Phys Solids 45, 1449-1459.

Haj-Ali, R.M., Muliana, A.H., 2004. A Multi-Scale Constitutive Formulation for the Nonlinear Viscoelastic Analysis of Laminated Composite Materials and Structures, Int J Solids Struct 41, 3461-3490.

Hajj, E.Y., Sebaaly, P.E., Weitzel, D., 2005. Fatigue Characteristics of Superpave and Hveem Mixtures, J Transp Eng-Asce 131, 302-310.

Han, R., Jin, X., Glover, C.J., 2013. Oxygen Diffusivity in Asphalts and Mastics, Petrol Sci Technol 31, 1563-1573.

Hashin, Z., Shtrikman, S., 1962. A Variational Approach to the Theory of the Effective Magnetic Permeability of Multiphase Materials, J Appl Phys 33, 3125-3131.

Herrington, P.R., 1998. Oxidation of Bitumen In The Presence Of a Constant Concentration of Oxygen, Petrol Sci Technol 16, 1061-1084.

Herrington, P.R., 2012. Diffusion and Reaction of Oxygen in Bitumen Films, Fuel 94, 86-92.

Herrington, P.R., Patrick, J.E., Ball, G.F.A., 1994. Oxidation of Roading Asphalts, Ind Eng Chem Res 33, 2801-2809.

Hintz, C., Velasquez, R., Li, Z., Bahia, H., 2011. Effect of Oxidative Aging on Binder Fatigue Performance, Asphalt Paving Technology 80, 527-547.

Huang, C.W., Abu Al-Rub, R.K., Masad, E.A., Little, D.N., 2011. Three-Dimensional Simulations of Asphalt Pavement Permanent Deformation Using a Nonlinear Viscoelastic and Viscoplastic Model, J Mater Civil Eng 23, 56-68.

Jeffrey, D.J., 1973. Conduction through a Random Suspension of Spheres, P Roy Soc Lond a Mat 335, 355-367.

Jin, X., Cui, Y., Glover, C.J., 2013. Modeling Asphalt Oxidation in Pavement With Field Validation, Petrol Sci Technol 31, 1398-1405.

Jin, X., Han, R.B., Cui, Y.C., Glover, C.J., 2011. Fast-Rate-Constant-Rate Oxidation Kinetics Model for Asphalt Binders, Ind Eng Chem Res 50, 13373-13379.

Juristyarini, P., Davison, R., Glover, C.J., 2011. Oxidation Hardening Kinetics of the Rheological Function G '/(eta '/G ') in Asphalts, Petrol Sci Technol 29, 2027-2036.

Kachanov, L.M., 1958. On Time to Rapture in Creep Conditions, Izviestia Akademii Nauk SSSR, Otdelenie Tekhnicheskikh Nauk (in Russian) 8, 26-31.

Kanit, T., Forest, S., Galliet, I., Mounoury, V., Jeulin, D., 2003. Determination of the Size of the Representative Volume Element for Random Composites: Statistical and Numerical Approach, Int J Solids Struct 40, 3647-3679.

Kliewer, J.E., Zeng, H.Y., Vinson, T.S., 1996. Aging and Low-Temperature Cracking of Asphalt Concrete Mixture, J Cold Reg Eng 10, 134-148.

Lado, F., Torquato, S., 1986. Effective Properties of 2-Phase Disordered Composite Media .1. Simplification of Bounds on the Conductivity and Bulk Modulus of Dispersions of Impenetrable Spheres, Phys Rev B 33, 3370-3378.

Lai, J., Bakker, A., 1996. 3-D Schapery Representation for Non-Linear Viscoelasticity and Finite Element Implementation, Comput Mech 18, 182-191.

Lau, C.K., Lunsford, K.M., Glover, C.J., Davison, R.R., Bullin, J.A., 1992. Reaction Rates and Hardening Susceptibilities as Determined from Pressure Oxygen Vessel Aging of Asphalts, 50-57.

Lee, D.Y., Huang, R.J., 1973. Weathering of Asphalts as Characterized by Infrared Multiple Internal Reflection Spectra, Appl Spectrosc 27, 435-440.

Lin, M.S., Lunsford, K.M., Glover, C.J., Davison, R.R., Bullin, J.A., 1995. The Effects of Asphaltenes on the Chemical and Physical Characteristics of Asphalt, in: Sheu, E., Mullins, O. (Eds.), Asphaltenes. Springer US, pp. 155-176.

Liu, M., Ferry, M.A., Davison, R.R., Glover, C.J., Bullin, J.A., 1998. Oxygen Uptake As Correlated To Carbonyl Growth in Aged Asphalts and Asphalt Corbett Fractions, Ind Eng Chem Res 37, 4669-4674.

Liu, M., Lunsford, K.M., Davison, R.R., Glover, C.J., Bullin, J.A., 1996. The Kinetics of Carbonyl Formation in Asphalt, Aiche J 42, 1069-1076.

Lu, X.H., Isacsson, U., 2002. Effect of Ageing on Bitumen Chemistry and Rheology, Constr Build Mater 16, 15-22.

Lunsford, K.M., (1994). The Effect of Temperature and Pressure on Laboratory Oxidized Asphalt Films with Comparison to Field Aging. (Volumes I and II). 9432726, Texas A&M University.

Martin, K.L., Davison, R.R., Glover, C.J., Bullin, J.A., 1990. Asphalt Aging in Texas Roads and Test Sections, Transp Res Record.

Masad, E., Dessouky, S., Little, D., 2007. Development of an Elastoviscoplastic Microstructural-Based Continuum Model to Predict Permanent Deformation in Hot Mix Asphalt, International Journal of Geomechanics 7, 119-130.

Masad, E., Huang, C.W., Airey, G., Muliana, A., 2008. Nonlinear Viscoelastic Analysis of Unaged and Aged Asphalt Binders, Constr Build Mater 22, 2170-2179.

Masad, E., Tashman, L., Little, D., Zbib, H., 2005. Viscoplastic Modeling of Asphalt Mixes with the Effects of Anisotropy, Damage and Aggregate Characteristics, Mech Mater 37, 1242-1256.

Masad, E.A., Huang, C.W., DAngelo, J., little, D.N., 2009. Characterization of Asphalt Binder Resistance to Permanent Deformation Based on Nonlinear Viscoelastic Analysis of Multiple Stress Creep Recovery (MSCR) Test, Journal of the Association of Asphalt Paving Technologists 78, 535-566.

Masson, R., Brenner, R., Castelnau, O., 2012. Incremental Homogenization Approach for Ageing Viscoelastic Polycrystals, Cr Mecanique 340, 378-386.

McCoy, J., 1976. On the Effective Thermal Conductivity of a Random Suspension of Spheres, International Journal of Engineering Science International Journal of Engineering Science 14, 7-18.

Miller, C.A., Torquato, S., 1990. Effective Conductivity of Hard-Sphere Dispersions, J Appl Phys 68, 5486-5493.

Odqvist, F.K.G., Hult, J., 1961. Some Aspects of Creep Rupture, Ark Fys 19, 379-382.

Pan, T.Y., Lu, Y., Wang, Z.Y., 2012a. Development of an Atomistic-Based Chemophysical Environment for Modelling Asphalt Oxidation, Polym Degrad Stabil 97, 2331-2339.

Pan, T.Y., Sun, L., Yu, Q.F., 2012b. An Atomistic-Based Chemophysical Environment for Evaluating Asphalt Oxidation and Antioxidants, J Mol Model 18, 5113-5126.

Park, S.W., Schapery, R.A., 1999. Methods of Interconversion between Linear Viscoelastic Material Functions. Part I - A Numerical Method Based On Prony Series, Int J Solids Struct 36, 1653-1675.

Pasricha, A., Dillard, D.A., Tuttle, M.E., 1997. Effect of Physical Aging and Variable Stress History on the Strain Response of Polymeric Composite, Compos Sci Technol 57, 1271-1279.

Pellinen, T.K., Witczak, M.W., 2002. Stress Dependent Master Curve Construction for Dynamic (Complex) Modulus, Journal of the Association of Asphalt Paving Technologists, Vol 71, 281-309.

Pellinen, T.K., Witczak, M.W., Bonaquist, R.F., 2004. Asphalt Mix Master Curve Construction Using Sigmoidal Fitting Function with Non-Linear Least Squares Optimization, Geotechnical Special Publication, 123 ed, pp. 83-101.

Perzyna, P., 1971. Thermodynamic Theory of Viscoplasticity, Advances in applied Mechanics 11, 313-354.

Petersen, J.C., Branthaver, J.F., Robertson, R.E., Harnsberger, P.M., Duvall, J.J., Ensley, E.K., 1993. Effects of Physicochemical Factors on Asphalt Oxidation Kinetics.

Petersen, J.C., Glaser, R., 2011. Asphalt Oxidation Mechanisms and the Role of Oxidation Products on Age Hardening Revisited, Road Mater Pavement 12, 795-819.

Petersen, J.C., Harnsberger, P.M., 1998. Asphalt Aging - Dual Oxidation Mechanism and Its Interrelationships with Asphalt Composition and Oxidative Age Hardening, Asphalt Mixture Components, 47-55.

Povirk, G.L., 1995. Incorporation of Microstructural Information into Models of 2-Phase Materials, Acta Metall Mater 43, 3199-3206.

Prapaitrakul, N., Han, R.B., Jin, X., Glover, C.J., 2009. A Transport Model of Asphalt Binder Oxidation in Pavements, Road Mater Pavement 10, 95-113.

Rabotnov, I.U.N., 1969. Creep Problems in Structural Members. North-Holland Pub. Co., Amsterdam, London.

Rahmani, E., Darabi, M.K., Abu Al-Rub, R.K., Kassem, E., Masad, E.A., Little, D.N., 2013. Effect of Confinement Pressure on the Nonlinear-Viscoelastic Response of Asphalt Concrete at High Temperatures, Constr Build Mater 47, 779-788.

Ruan, Y., Davison, R.R., Glover, C.J., 2003. An Investigation of Asphalt Durability: Relationships between Ductility and Rheological Properties for Unmodified Asphalts, Pet. Sci. Technol. 21, 231-254.

Schapery, R.A., 1966. A Theory of Non-linear Thermoviscoelasticity Based on Irreversible Thermodynamics. American Society of Mechanical Engineers.

Sensale, B., Partridge, P.W., Creus, G.J., 2001. General Boundary Elements Solution for Ageing Viscoelastic Structures, Int J Numer Meth Eng 50, 1455-1468.

Shakiba, M., Abu Al-Rub, R.K., Darabi, M.K., You, T., Masad, E.A., Little, D.N., 2013. Continuum Coupled Moisture-Mechanical Damage Model for Asphalt Concrete, Transp Res Record, 72-82.

Struik, L.C.E., 1977. Physical Aging in Plastics and Other Glassy Materials, Polym Eng Sci 17, 165-173.

Sun, C.T., Vaidya, R.S., 1996. Prediction of Composite Properties, From a Representative Volume Element, Compos Sci Technol 56, 171-179.

Tarefder, R.A., Arisa, I., 2011. Molecular Dynamic Simulations for Determining Change in Thermodynamic Properties of Asphaltene and Resin Because of Aging, Energ Fuel 25, 2211-2222.

Tashman, L., Masad, E., Little, D., Zbib, H., 2005. A Microstructure-Based Viscoplastic Model for Asphalt Concrete, Int J Plasticity 21, 1659-1685.

Walubita, L.F., Martin, A.E., Glover, C., Jung, S.H., Cleveland, G., Lytton, R.L., 2006. Fatigue Characterization of HMAC Mixtures Using Mechanistic Empirical and Calibrated Mechanistic Approaches Including the Effects of Aging, Asphalt Concrete, 103-114.

Weissberg, H.L., 1963. Effective Diffusion Coefficient in Porous Media, J Appl Phys 34, 2636-&.

Wong, C.P., Bollampally, R.S., 1999. Thermal Conductivity, Elastic Modulus, and Coefficient of Thermal Expansion of Polymer Composites Filled With Ceramic Particles for Electronic Packaging, J Appl Polym Sci 74, 3396-3403.

You, T.S., (2013). Two-and Three-Dimensional Microstructural Modeling of Asphalt Particulate Composite Materials using a Unified Viscoelastic-Viscoplastic-Viscodamage Constitutive Model. Doctoral dissertation, Texas A & M University. .

You, T.S., Abu Al-Rub, R.K., Darabi, M.K., Masad, E.A., Little, D.N., 2012. Three-Dimensional Microstructural Modeling of Asphalt Concrete Using a Unified Viscoelastic-Viscoplastic-Viscodamage Model, Constr Build Mater 28, 531-548.

Zhang, W.C., Evans, K.E., 1988. Numerical Prediction of the Mechanical-Properties of Anisotropic Composite-Materials, Comput Struct 29, 413-422.